



ATLAS Note

GROUP-2017-XX



30th April 2021

Draft version 0.1

1

2 **A Deep Learning Approach to Differential**
3 **Measurements of Higgs - Top Interactions in**
4 **Multilepton Final States**

5

The ATLAS Collaboration

6 Several theories Beyond the Standard Model modify the momentum spectrum of the Higgs
7 Boson, without significantly altering the overall rate of Higgs produced from top quark pairs.
8 A differential measurement of the Higgs transverse momentum provides a way to search for
9 these effects at the LHC. Because of the challenges inherent to reconstructing the Higgs in
10 multilepton final states, a deep learning approach is used to predict the momentum spectrum
11 of the Higgs for events where the Higgs Boson is produced from top quark pairs and decays
12 to final states that include multiple leptons. The regressed Higgs p_T is fit to data for events
13 with two or three leptons in the final state, and estimates of the sensitivity to variations in the
14 Higgs p_T spectrum are given.

© 2021 CERN for the benefit of the ATLAS Collaboration.

15 Reproduction of this article or parts of it is allowed as specified in the CC-BY-4.0 license.

16 **Contents**

17	I Introduction	4
18	1 Introduction	4
19	II Theoretical Motivation	7
20	2 The Standard Model and the Higgs Boson	7
21	2.1 The Forces and Particles of the Standard Model	7
22	2.2 The Higgs Mechanism	10
23	2.2.1 The Higgs Field	10
24	2.2.2 Electroweak Symmetry Breaking	12
25	2.3 $t\bar{t}H$ Production	15
26	2.4 WZ + Heavy Flavor Production	17
27	2.5 Extensions to the Standard Model	18
28	III The LHC and the ATLAS Detector	21
29	3 The LHC	21
30	4 The ATLAS Detector	24
31	4.1 Inner Detector	25
32	4.2 Calorimeters	27
33	4.3 Muon Spectrometer	28
34	4.4 Trigger System	29
35	IV Measurement of WZ + Heavy Flavor	30
36	5 Introduction	30
37	6 Data and Monte Carlo Samples	32
38	6.1 Data Samples	32
39	6.2 Monte Carlo Samples	32
40	7 Object Reconstruction	33
41	7.1 Light leptons	34
42	7.2 Jets	35
43	7.3 B-tagged Jets	35
44	7.4 Missing transverse energy	37
45	7.5 Overlap removal	37

46	8 Event Selection and Signal Region Definitions	38
47	8.1 Event Preselection	38
48	8.2 Fit Regions	41
49	8.3 Non-Prompt Lepton Estimation	42
50	8.3.1 $t\bar{t}$ Validation	43
51	8.3.2 Z+jets Validation	44
52	9 tZ Interference Studies and Separation Multivariate Analysis	44
53	10 Data and Monte Carlo Samples	48
54	10.1 Data Samples	48
55	10.2 Monte Carlo Samples	48
56	11 Object Reconstruction	49
57	11.1 Light leptons	50
58	11.2 Jets	51
59	11.3 B-tagged Jets	51
60	11.4 Missing transverse energy	53
61	11.5 Overlap removal	53
62	12 Event Selection and Signal Region Definitions	54
63	12.1 Event Preselection	54
64	12.2 Fit Regions	57
65	12.3 Non-Prompt Lepton Estimation	58
66	12.3.1 $t\bar{t}$ Validation	59
67	12.3.2 Z+jets Validation	60
68	13 tZ Interference Studies and Separation Multivariate Analysis	60
69	14 Systematic Uncertainties	64
70	15 Results	68
71	15.1 1-jet Fit Results	69
72	15.2 2-jet Fit Results	78
73	V Differential Studies of $t\bar{t}H$ Multilepton	87
74	16 Data and Monte Carlo Samples	87
75	16.1 Data Samples	88
76	16.2 Monte Carlo Samples	88
77	17 Object Reconstruction	91
78	17.1 Trigger Requirements	92
79	17.2 Light Leptons	92

80	17.3 Jets	93
81	17.4 B-tagged Jets	94
82	17.5 Missing Transverse Energy	94
83	17.6 Overlap removal	95
84	18 Higgs Momentum Reconstruction	95
85	18.1 Higgs Decay Product Identification	97
86	18.2 b-jet Identification	98
87	18.2.1 2lSS Channel	99
88	18.2.2 3l Channel	104
89	18.3 Higgs Reconstruction	107
90	18.3.1 2lSS Channel	108
91	18.3.2 3l Semi-leptonic Channel	112
92	18.3.3 3l Fully-leptonic Channel	116
93	18.4 p_T Prediction	120
94	18.4.1 2lSS Channel	121
95	18.4.2 3l Semi-leptonic Channel	124
96	18.4.3 3l Fully-leptonic Channel	128
97	18.5 3l Decay Mode	131
98	19 Signal Region Definitions	133
99	19.1 Pre-MVA Event Selection	134
100	19.2 Event MVA	139
101	19.3 Signal Region Definitions	147
102	20 Background Rejection MVA	150
103	20.1 Pre-MVA Event Selection	151
104	20.2 Event MVA	153
105	20.3 Signal Region Definitions	162
106	20.3.1 2lSS	163
107	20.3.2 3l – Semi – leptonic	163
108	20.3.3 3l – Fully – leptonic	163
109	21 Systematic Uncertainties	163
110	22 Results	170
111	22.1 Results - 80 fb^{-1}	171
112	22.2 Projected Results - 140 fb^{-1}	176
113	VI Conclusion	181
114	Appendices	188
115	.1 Non-prompt lepton MVA	188

116	.2	Non-prompt CR Modelling	193
117	.3	tZ Interference Studies	198
118	.4	Alternate tZ Inclusive Fit	202
119	.4.1	tZ Inclusive Fit	203
120	.4.2	Floating tZ	204
121	.5	DSID list	205
122	A	Machine Learning Models	228
123	A.1	Higgs Reconstruction Models	228
124	A.1.1	b-jet Identification Features - 2ISS	228
125	A.1.2	b-jet Identification Features - 3l	232
126	A.1.3	Higgs Reconstruction Features - 2ISS	237
127	A.1.4	Higgs Reconstruction Features - 3IS	242
128	A.1.5	Higgs Reconstruction Features - 3IF	247
129	A.2	Background Rejection MVAs	251
130	A.2.1	Background Rejection MVA Features - 2ISS	251
131	A.2.2	Background Rejection MVA Features - 3l	255
132	A.3	Alternate b-jet Identification Algorithm	260
133	A.4	Binary Classification of the Higgs p_T	261
134	A.5	Impact of Alternative Jet Selection	262

Part I**Introduction****1 Introduction**

138 Particle physics is an attempt to describe the fundamental building blocks of the universe and
139 their interactions. The Standard Model (SM) - our best current theory of fundamental particle
140 physics - does a remarkable job of that. All known fundamental particles and (almost) all of the
141 forces underlying their interactions can be explained by the SM, and the predictions from this
142 theory agree with experiment to an incredibly precise degree. This is especially true since the
143 Higgs Boson, the last piece of the SM predicted decades before, was finally discovered at the
144 Large Hadron Collider (LHC) in 2012.

145 Despite the success of the SM, there remains significant work to be done. For one, the
146 SM is incomplete: it fails to provide a description of gravity, to give an explanation for the
147 observation of Dark Matter, or to provide a mechanism for neutrinos to gain mass. Further, a
148 Higgs Boson with a mass of around 125 GeV, as observed at the LHC, gives rise to what is
149 known a hierarchy problem - such a low mass Higgs requires a seemingly unnatural level of “fine
150 tuning” that is unexplained by the SM.

151 A promising avenue for addressing these problems is to study the properties of the Higgs
152 Boson and the way it interacts with other particles, in part simply because these interactions

153 have not been measured before. Its interactions with the Top Quark are a particularly promising
154 place to look. Because the Higgs Field is responsible for allowing particle to acquire mass, the
155 strength of a particle's interaction with the Higgs Boson is proportional to its mass. As the most
156 massive of the fundamental particles, the Top Quark has the strongest coupling to the Higgs
157 Boson, meaning any new physics in the Higgs sector is likely to present itself most prominently
158 in its interaction with the Top Quark.

159 These interactions can be measured by directly by studying the production of a Higgs
160 Boson in association with a pair of Top Quarks ($t\bar{t}H$). While studies have been done measuring
161 the overall rate of $t\bar{t}H$ production, there are several theories of physics Beyond the Standard
162 Model (BSM) that would affect the kinematics of $t\bar{t}H$ production without altering its overall
163 rate. This dissertation attempts to make a differential measurement of the kinematics of the
164 Higgs Boson in $t\bar{t}H$ events in order to search for these BSM effects.

165 The proton-proton collision data collected by the ATLAS detector at the LHC from 2015-
166 2018 provides the opportunity to make this measurement for the first time. The unprecedented
167 energy achieved by the LHC during this period greatly increase the rate at which $t\bar{t}H$ events are
168 produced, and the large amount of data collected provides the necessary statistics for a differential
169 measurement to be performed.

170 A study of $t\bar{t}H$ events with multiple leptons in the final state is performed, using 139 fb^{-1}
171 of data from proton-proton collisions at an energy $\sqrt{s} = 13 \text{ TeV}$ collected by the ATLAS detector
172 from 2015-2018. Events are separated into channels based on the number of light leptons in the

173 final state - either two same-sign leptons, or three leptons. A deep neural network is used to
174 reconstruct the momentum of the Higgs Boson in each event. This momentum spectrum is fit to
175 data for each analysis channel in order to search for evidence of these BSM effects.

176 An additional study of WZ produced in association with a heavy flavor jet (including both
177 b-jets and charm jets) is also included. This process mimics the final state of $t\bar{t}H$ multilpjet
178 events, making it an irreducible background for that analysis. However, this process is poorly
179 understood, and difficult to simulate accurately, introducing large systematic uncertainties for
180 analyses that include it as a background. A measurement of WZ + heavy flavor in the fully
181 leptonic decay mode is performed in an attempt to reduce this uncertainty.

182 This dissertation begins with a brief explanation of the SM, its limitations, and the theor-
183 etical motivation behind this work in Part II. This is followed by a description of the LHC and
184 the ATLAS detector in Part III. Part IV details a measurement of WZ + heavy flavor. Studies
185 of differential measurements of $t\bar{t}H$ are then described in Part V, and preliminary results are
186 presented. Finally, the results of these studies are summarized in the conclusion, Part VI.

Part II**188 Theoretical Motivation****189 2 The Standard Model and the Higgs Boson**

190 The Standard Model of particle physics (SM) is a Quantum Field Theory (QFT) describing the
191 known fundamental particles and their interactions. It accounts for three of the four known
192 fundamental force - electromagnetism, the weak nuclear force, and the strong nuclear force, but
193 not gravity. Further, the SM describes a mechanism for combining the weak and electromagnetic
194 forces into a singular interaction, known as the electroweak force. It is a non-Abelian gauge
195 theory, invariant under the Lie Group $SU(3)_C \otimes SU(2)_L \otimes U(1)_Y$, where C refers to color
196 charge, L, the helicity of the particle, and Y, the hypercharge.

197 2.1 The Forces and Particles of the Standard Model

198 The SM particles, summarized in Figure 2.1, can be classified into two general categories based
199 on their spin: fermions, and bosons.

Standard Model of Elementary Particles

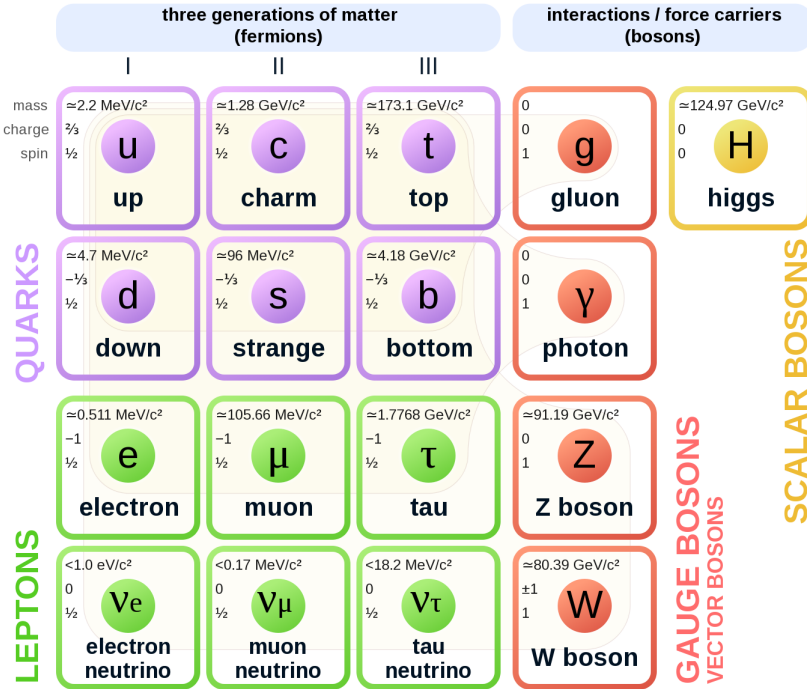


Figure 2.1: A summary of the particles of the Standard Model, including their mass, charge and spin, with the fermions listed on the left, and the bosons on the right. [1]

200 Fermions are particles with $\frac{1}{2}$ -integer spin, which according to the spin-statistics theorem,
 201 causes them to comply with the Pauli-exclusion principle. They can be separated into two groups,
 202 leptons and quarks, each of which consist of three generations of particles with increasing mass.

203 Leptons are fermions which interact via the electroweak force, but not the strong force.
 204 The three generation of leptons consist of the electron and electron neutrino, the muon and muon
 205 neutrino, the tau and tau neutrino. The quarks, by contrast, do interact via the strong force - which
 206 is to say they have color charge - in addition to the electroweak force. The three generations
 207 include the up and down quarks, the strange and charm quarks, and the top and bottom quarks.

208 Each of these generations form left-handed doublets invariant under SU(2) transfor-

209 mations. For the leptons these doublets are:

$$\begin{pmatrix} e^- \\ \nu_e \end{pmatrix}_L, \begin{pmatrix} \mu^- \\ \nu_\mu \end{pmatrix}_L, \begin{pmatrix} \tau^- \\ \nu_\tau \end{pmatrix}_L \quad (2.1)$$

210 And for the quarks:

$$\begin{pmatrix} u \\ d \end{pmatrix}_L, \begin{pmatrix} s \\ c \end{pmatrix}_L, \begin{pmatrix} t \\ b \end{pmatrix}_L \quad (2.2)$$

211 For both leptons and quarks, the heavier generations can decay into the lighter generation

212 of particles, while the first generation does not decay. Hence, ordinary matter generally consists

213 of this first generation of fermions - electrons, up quarks, and down quarks. Each of these

214 fermions has a corresponding anti-particle, which has an equal mass as its partner but opposite

215 charge. The fermions acquire their mass via the Higgs Mechanism, except for the neutrinos,

216 whose mass has been experimentally confirmed but is not accounted for in the SM.

217 Bosons, by contrast, have integer spin, and are therefore unconstrained by the Pauli-

218 exclusion principle. The SM includes two kinds of bosons: Gauge bosons, which are spin-1

219 particles that mediate the interactions between the fermions, and a single scalar, i.e. spin-0,

220 particle - the Higgs Boson. Of the gauge bosons, the W^+ , W^- and Z bosons - which are the

²²¹ mass eigenstates of the electroweak bosons - mediate the weak interaction, while the photon

²²² mediates the electric force, and the gluon mediates the strong force.

²²³ **2.2 The Higgs Mechanism**

²²⁴ A key feature of the SM is the gauge invariance of its Lagrangian. However, any terms added to

²²⁵ the Lagrangian giving mass to the the gauge bosons would violate this underlying symmetry of

²²⁶ the theory. This presents a clear problem with the theory: The experimental observation that the

²²⁷ W and Z bosons have mass seems to contradict the basic structure of the SM.

²²⁸ Rather than abandoning gauge invariance, an alternative way for particles to acquire mass

²²⁹ beyond adding a simple mass term to the Lagrangian was theorized by Higgs, Englert and Brout

²³⁰ in 1964 [2]. This procedure for introducing masses for the gauge bosons while preserving local

²³¹ gauge invariance, known as the Higgs mechanism, was incorporated into the electroweak theory

²³² by Weinberg in 1967 [3].

²³³ **2.2.1 The Higgs Field**

²³⁴ The Higgs mechanism introduces a complex scalar SU(2) doublet, Φ , with the form:

$$\Phi = \begin{pmatrix} \phi^+ \\ \phi^0 \end{pmatrix}_L \quad (2.3)$$

235 This field introduces a scalar potential to the Lagrangian of the form:

$$V(\Phi) = \mu^2 |\Phi^\dagger \Phi| + \lambda (|\Phi^\dagger \Phi|)^2 \quad (2.4)$$

236 Where μ and λ are free parameters of the new field. This represents the most general
 237 potential allowed while preserving $SU(2)_L$ invariance and renormalizability. In the case that
 238 $\mu^2 < 0$, this potential takes the form shown in Figure 2.2.

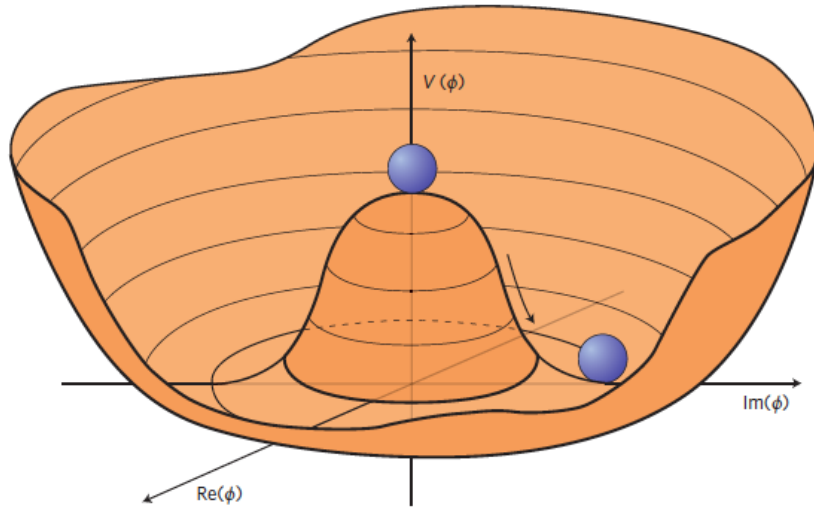


Figure 2.2: The value of the Higgs potential, $V(\Phi)$ as a function of Φ , for the case that $\mu^2 < 0$ [4].

239 The significant feature of this potential is that its minimum does not occur for a value of
 240 $\Phi = 0$. Instead, it is minimized when $|\Phi^\dagger \Phi| = -\mu^2/\lambda$. This means that in its ground state, the
 241 Higgs field takes on a non-zero value - referred to as a vacuum expectation value (VEV). So while
 242 the Higgs potential is globally symmetric, about the minimum this symmetry is broken. Since

²⁴³ the minimum is determined only by $\Phi^\dagger \Phi$, there is some ambiguity in the particular definition of

²⁴⁴ the VEV, but it is generally represented as

$$\langle \Phi \rangle = \frac{1}{\sqrt{2}} \begin{pmatrix} 0 \\ v \end{pmatrix} \quad (2.5)$$

²⁴⁵ The full value of Φ can be written as

$$\langle \Phi \rangle = \frac{1}{\sqrt{2}} \begin{pmatrix} 0 \\ v + H/\sqrt{2} \end{pmatrix} \quad (2.6)$$

²⁴⁶ with v being the value of the VEV, and H being the real value of the scalar field.

²⁴⁷ 2.2.2 Electroweak Symmetry Breaking

²⁴⁸ The Electroweak (EWK) interaction is described in the SM by a $SU(2)_L \otimes U(1)_Y$ gauge theory.

²⁴⁹ This theory predicts three $SU(2)_L$ gauge boson, $W_\mu^1, W_\mu^2, W_\mu^3$, and a single $U(1)_Y$ gauge boson,

²⁵⁰ B_μ . The couplings of these bosons to the Higgs field show up in the kinetic terms of the scalar

²⁵¹ field Φ in the Lagrangian:

$$(D_\mu \Phi)^\dagger (D^\mu \Phi) = |(\partial_\mu - \frac{i g}{2} W_\mu^a \sigma^a - \frac{i g'}{2} B_\mu Y) \phi|^2 \quad (2.7)$$

252 Here D_μ represents the covariant derivative required to preserve gauge invariance, g and
 253 g' represent coupling constant of the gauge bosons, σ^a denotes the Pauli matrices of $SU(2)$,
 254 and Y represents the hypercharge of $U(1)$. The terms in this interaction which contribute to the
 255 masses of the gauge bosons can be written as:

$$\frac{1}{2}(0, v) \left(\frac{g}{2} W_\mu^a \sigma^a - \frac{g'}{2} B_\mu \right)^2 \begin{pmatrix} 0 \\ v \end{pmatrix} \quad (2.8)$$

256 Expanding these terms into the mass eigenstates of the electroweak interaction yields four
 257 physical gauge bosons, two charged and two neutral, which are linear combinations of the fields
 258 W_μ^1 , W_μ^2 , W_μ^3 , and B_μ :

$$\begin{aligned} W_\mu^\pm &= \frac{1}{\sqrt{2}} (W_\mu^1 \pm i W_\mu^2) \\ Z^\mu &= \frac{1}{\sqrt{(g^2 + g'^2)}} (-g' B_\mu + g W_\mu^3) \\ A^\mu &= \frac{1}{\sqrt{(g^2 + g'^2)}} (g B_\mu + g' W_\mu^3) \end{aligned} \quad (2.9)$$

259 And the masses of these fields are given by:

$$\begin{aligned} M_W^2 &= \frac{1}{4} g^2 v^2 \\ M_Z^2 &= \frac{1}{4} (g^2 + g'^2) v^2 \\ M_A^2 &= 0 \end{aligned} \quad (2.10)$$

260 This produces exactly the particles we observe - three massive gauge bosons and a single
 261 massless photon. The massless photon represents the portion of the gauge symmetry, a single
 262 $U(1)$ of the electromagnetic force, that remains unbroken by the VEV.

263 Interactions with the Higgs field also lead to the generation of the fermion masses, which
 264 in the Lagrangian take the form:

$$-\lambda_\psi(\bar{\psi}_L \phi \psi_R + \bar{\psi}_R \phi^\dagger \psi_L) \quad (2.11)$$

265 After symmetry breaking has occurred and ϕ has taken on the value of the VEV as written
 266 in equation 2.5, the mass terms of the fermions become $\lambda_\psi v$. Written this way, the fermion
 267 masses are proportional to their Yukawa coupling to the VEV, λ_ψ .

268 Based on the equation 2.6, an additional mass term, $\mu^2 H^2$ arises from the potential $V(\Phi)$.
 269 This term can be understood as an excitation of the Higgs field, a scalar boson with mass $M_H = \mu$.
 270 This is the Higgs boson, which comes about as a natural prediction of electroweak symmetry
 271 breaking.

272 The fermions' Yukawa couplings to the VEV take the same form as the fermions' coupling
 273 to the Higgs boson - λ_ψ . Therefore, the strength of a fermion's interaction with the Higgs is
 274 directly proportional to its mass. We now have a model that predicts a Higgs boson with mass
 275 $M_H = \mu$, which interacts with the fermions with coupling strength λ_ψ . Because μ and λ_ψ are

²⁷⁶ free parameters of the theory, the mass of the Higgs boson and its interactions with the fermions

²⁷⁷ must be measured experimentally.

²⁷⁸ **2.3 $t\bar{t}H$ Production**

²⁷⁹ The strength of a particles interaction with the Higgs, given by its Yukawa coupling, is propor-
²⁸⁰ tionate to its mass. The top quark - as the heaviest known particle - has the strongest interaction,
²⁸¹ making this interaction particularly interesting to study. While several processes involve interac-
²⁸² tions between the Higgs and the top, some Higgs production modes include the top interaction
²⁸³ only as a part of a loop diagram, such as the gluon-gluon fusion diagram shown in Figure 2.3.

²⁸⁴ This process therefore only allows for an indirect probe of the Higgs-top Yukawa coupling, as
²⁸⁵ the flavor of the quark in this diagram is not unique.

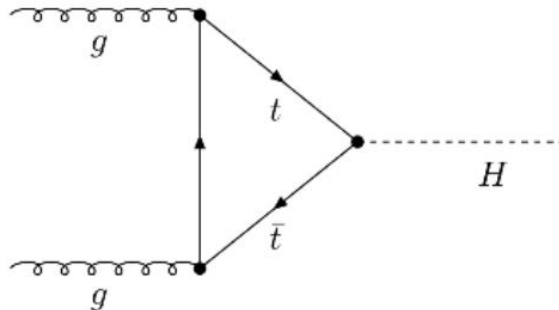


Figure 2.3: Diagram of a Higgs boson produced via gluon-gluon fusion.

²⁸⁶ Studying the Higgs produced in association with top quark pairs, $t\bar{t}H$, allows this interac-
²⁸⁷ tion to be measured directly. This process, as shown in Figure 2.4, involves a unique coupling
²⁸⁸ between the Higgs and the top, which can be identified by the top quark pair in the final state.

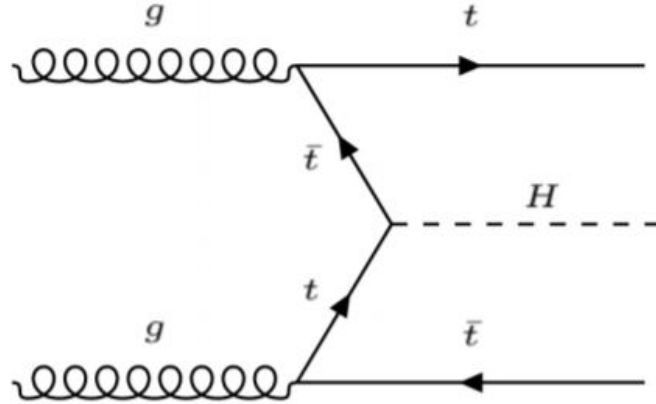


Figure 2.4: Diagram of a Higgs boson produced in association with a pair of top quarks.

289 The Higgs boson, as well as the top quarks, have very short lifetimes - on the order of
 290 10^{-22} s and 10^{-25} s respectively - meaning they can only be observed via their decay products.
 291 Measuring this process is therefore a matter of identifying events with final states consistent
 292 with $t\bar{t}H$ production. This thesis focuses on $t\bar{t}H$ events with multiple leptons in the final state,
 293 $t\bar{t}H - ML$. This includes $H \rightarrow W^+W^-$ events, where at least one of the W bosons decays
 294 leptonically.

295 While the branching ratio of $H \rightarrow W^+W^-$ is smaller than $H \rightarrow b\bar{b}$, it produces a clearer
 296 signal. On the other hand, $H \rightarrow \gamma\gamma$ produces the most easily identifiable signal, but has a much
 297 smaller branching ratio than $H \rightarrow W^+W^-$. Therefore, compared with other final states of $t\bar{t}H$,
 298 the $t\bar{t}H - ML$ channel is an attractive candidate for study, as it involves a good balance between
 299 statistical power and identifiability.

300 2.4 WZ + Heavy Flavor Production

301 Part IV is dedicated to a measurement of WZ produced in association with a heavy flavor jet
 302 - namely, a charm or b-jet - in the fully leptonic channel. In the instance that both the W
 303 and Z bosons decay leptonically, this process produces a final state similar to $t\bar{t}H$, making it
 304 an irreducible background for $t\bar{t}H$ – ML specifically, and any analysis that includes multiple
 305 leptons and b-tagged jets in the final state more broadly.

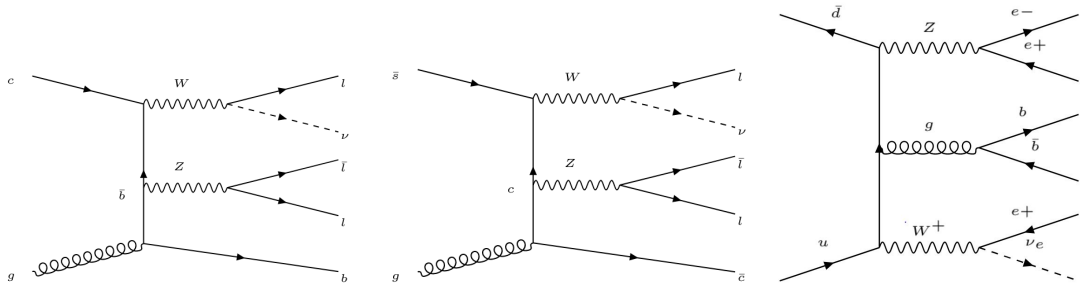


Figure 2.5: Example Feynman diagrams of WZ + heavy flavor production

306 The b-jets produced in this process can be thought of in two different ways: either as
 307 originating from the quark “sea” of the initial state hadrons, or as the result of a gluon from
 308 one the colliding protons splitting into $b\bar{b}$ pairs. However, the heavy flavor contribution to the
 309 parton distribution function (PDF) of the proton is uncertain, and simulations of this process
 310 disagree depending on which of these two approaches one considers. This makes WZ + heavy
 311 flavor difficult to accurately simulate, and introduces a large uncertainty for any analysis which
 312 includes it as a background, motivating a measurement of this process.

313 **2.5 Extensions to the Standard Model**

314 While the SM has been tested to great precision, particularly at the LHC, it is generally accepted
315 that it is only valid up to a certain energy scale. It is assumed that above a certain energy, at the
316 scale where something like a Grand Unified Theory (GUT) or quantum gravity become relevant,
317 the SM will not be applicable. Further, there are several experimental observations that the SM
318 fails to explain. For example, the SM predicts neutrinos to be massless, despite experimental
319 observation to the contrary, and fails to explain the observation of dark matter and dark energy.

320 Another example, relevant to the Higgs sector, is known as the hierarchy problem: large
321 quantum corrections to the Higgs mass from loop diagrams, such as those shown in Figure 2.6,
322 are many orders of magnitude larger than the Higgs mass itself. The observed value of the Higgs
323 mass therefore requires extremely precise cancellation between these corrections and the bare
324 mass of the Higgs, a cancellation which seems unnatural and suggests something missing in our
325 theoretical picture.

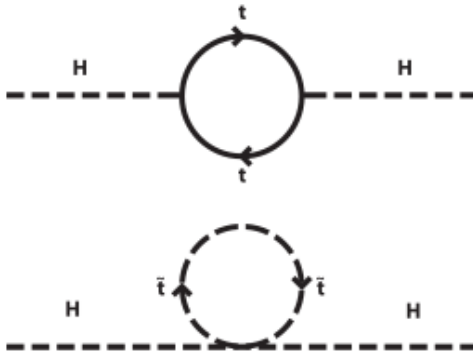


Figure 2.6: Above diagram is the leading order correction to the Higgs mass via a top quark loop, and below is the stop squark loop, coming from a supersymmetric extension of the SM, that provides a potential cancellation of the top diagram.

Because so many of the properties of the Higgs boson have not yet been studied, its interactions are a promising place to search for new physics that could resolve some of the limitations of the SM. As explained above, the interactions of the Higgs with the top quark, as in $t\bar{t}H$ production, are particularly interesting: As the most massive particle in the Standard Model, the top quark is the most strongly interacting with the Higgs. Therefore, any new physics effects are likely to be seen most prominently in this interaction.

These interactions can be measured directly by studying the production of a Higgs Boson in association with a pair of Top Quarks ($t\bar{t}H$). While this process has been observed by both the ATLAS [5] and CMS [6] collaborations, these analyses have focused on measuring the overall rate of $t\bar{t}H$ production. There are several theories of physics Beyond the Standard Model (BSM), however, that would affect the kinematics of $t\bar{t}H$ production without altering its overall rate [7].

338 An Effective Field Theory approach can be used to model the low energy effects of new,
 339 high energy physics, by parameterizing BSM effects as higher dimensional operators. These
 340 additional operators can then be added to the SM Lagrangian to write an effective Lagrangian
 341 that accounts for the effects of these higher energy physics. The lowest order of these that could
 342 contribute to Higgs-top couplings are dimension-six, as represented in Equation 2.12.

$$\mathcal{L}_{\text{eff}} = \mathcal{L}_{\text{SM}} + \frac{f}{\Lambda} O^6 \quad (2.12)$$

343 Here Λ represents the energy scale of the new physics, and f is a Wilson coefficient which
 344 represents the strength of the effective coupling. An experimental observation of any non-zero
 345 value of f would be a sign of BSM physics.

346 The addition of these operators can be shown to modify the transverse momentum (p_T)
 347 spectrum of the Higgs Boson in Higg-top interactions, without effecting the overall rate of $t\bar{t}H$
 348 production [8]. The possible impact of these higher order effects on the Higgs p_T spectrum are
 349 shown in Figure 2.7.

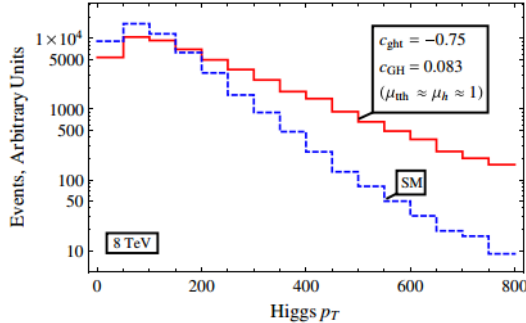


Figure 2.7: The momentum spectrum of the Higgs boson produced via top-quarks with (red) and without (blue) the presence of dimension-six operators.

350 This provides a clear, physics observable that could be used to search for evidence of
 351 BSM physics. The energy and luminosity produced by the LHC now make such a measurement
 352 possible. Reconstructing the momentum spectrum of the Higgs in $t\bar{t}H$ events therefore provides
 353 a means to search for new physics in the Higgs sector.

Part III

355 The LHC and the ATLAS Detector

356 3 The LHC

357 The Large Hadron Collider (LHC) is a particle accelerator consisting of a 27 km ring, designed
 358 to collide protons at high energy. Located outside of Geneva, Switzerland and buried about 100
 359 m underground, it consists of a ring of superconducting magnets which are used to accelerate

360 opposing beams of protons - or lead ions - which collide at the center of one of the various
361 detectors located around the LHC ring which record the result of these collisions. These
362 detectors include two general purpose detectors, ATLAS and CMS, which are designed to make
363 precision measurements of a broad range of physics phenomenon, and two more specialized
364 experiments, LHCb and ALICE, which are optimized to study b-quarks and heavy-ion physics,
365 respectively.

366 The LHC first began running in 2009 at a proton-proton center of mass energy of $\sqrt{s} = 8$
367 TeV. It operated at this energy from 2009 to 2012, known as Run 1, and data collected during
368 this period was used in discovering the Higgs Boson. The LHC began running again in 2015,
369 and collected data at an increased energy of $\sqrt{s} = 13$ TeV until 2018, a period referred to as Run
370 2.

371 The LHC consists of a chain of accelerators, which accelerate the protons to higher and
372 higher energies until they are injected into the main ring. This process is summarized in figure
373 3.1. Protons extracted from a tank of ionized hydrogen are fed into a linear accelerator, LINAC2,
374 where they reach an energy of 50 MeV. From there, they enter a series of three separate circular
375 accelerators, before being injected into the main accelerator ring at an energy of 450 GeV. Within
376 the main ring protons are separated into two separate beams moving in opposite directions,
377 and their energy is increased to their full collision energy. Radiofrequency cavities are used to
378 accelerate these particles and sort them into bunches. From 2015-2018, these bunches consisted
379 of around 100 billion protons each with an energy of 6.5 TeV per proton, which collided at a rate
380 of 40 MHz, or every 25 ns.

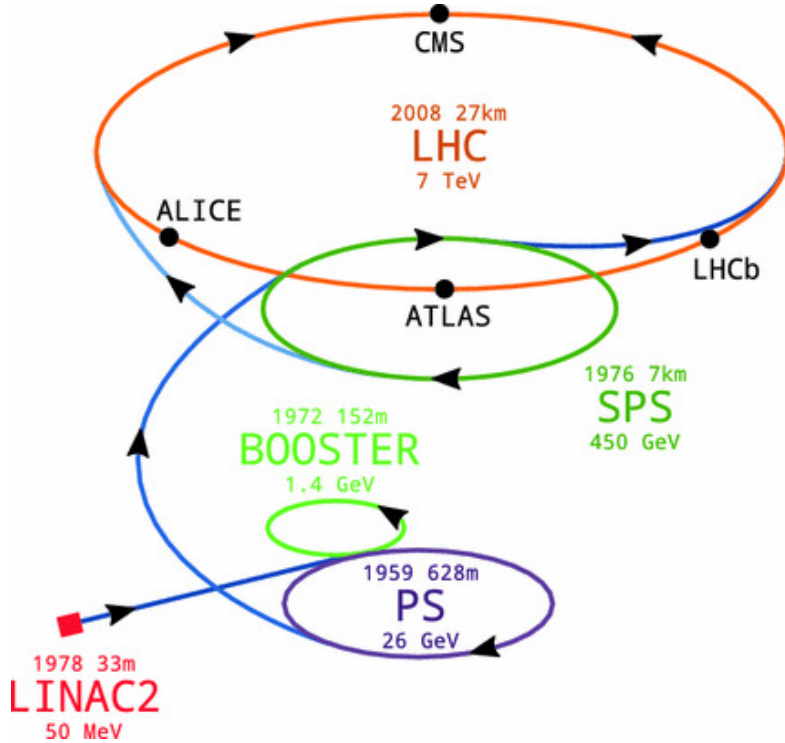


Figure 3.1: A summary of the accelerator chain used to feed protons into the LHC [9].

Because these proton bunches consist of a large number of particles, each bunch crossing consists of not just one, but several direct proton-proton collisions. The number of interactions that occur per bunch crossing, μ , is known as pileup. During Run 2, the average pileup for bunch crossings was around $\langle \mu \rangle = 35$, with values typically ranging between 10 and 70.

The amount of data collected by the LHC is measured in terms of luminosity, which is the ratio of the number of events detected per unit time, $\frac{dN}{dt}$, and the interaction cross-section, σ .

$$\mathcal{L} = \frac{1}{\sigma} \frac{dN}{dt} \quad (3.1)$$

387 The design luminosity of the LHC is $10^{34} \text{ cm}^{-2}\text{s}^{-1}$, however the LHC has achieved a
388 luminosity of over $2 \times 10^{34} \text{ cm}^{-2}\text{s}^{-1}$. The total luminosity is then this instantaneous luminosity
389 integrated over time.

$$\mathcal{L}_{\text{int}} = \int \mathcal{L} dt \quad (3.2)$$

390 The integrated luminosity collected by the ATLAS detector as of the end of 2018 is around
391 140 fb^{-1} , exceeding the expected integrated luminosity of 100 fb^{-1} .

392 4 The ATLAS Detector

393 ATLAS (a not terribly natural acronym for “A Toroidal LHC Apparatus”) is a general purpose
394 detector designed to maximize the detection efficiency of all physics objects, including leptons,
395 jets, and photons. This means it is capable of measuring all SM particles, with the exception of
396 neutrinos, the presence of which can be inferred based on missing transverse momentum. The
397 detector measures 44 m long, and 25 m tall.

398 The ATLAS detector consists of multiple concentric layers, each of which serves a different
399 purpose in reconstructing collisions. At the very center of the detector is the interaction point
400 where the proton beams of the LHC collide.

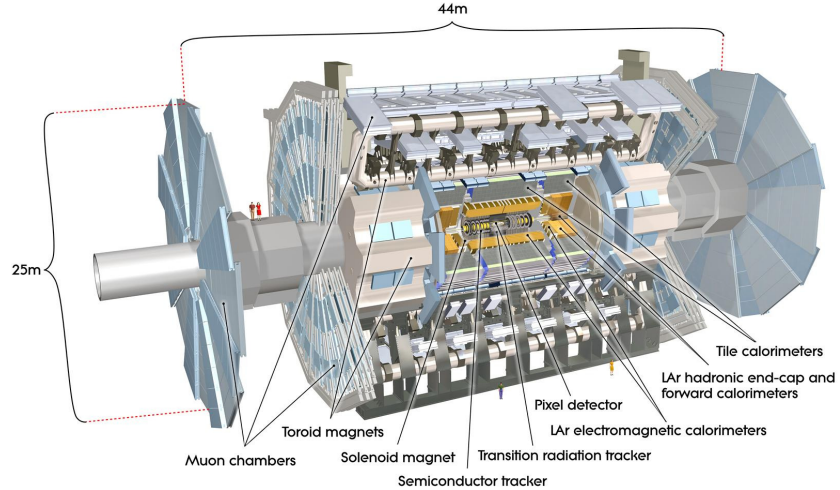


Figure 4.1: Cutaway view of the ATLAS detector, with labels of its major components [10].

401 4.1 Inner Detector

402 Just surrounding the interaction point is the Inner Detector, designed to track the path of charged
 403 particles moving through the detector. An inner solenoid surrounding the Innder Detector is
 404 used to produces a magnetic field of 2 T. This large magnetic field causes the path of charged
 405 particles moving through the Inner Detector to bend. Because this magnetic field is uniform and
 406 well known, it can be used in conjunction with the curvature of a particles path to measure its
 407 charge and momentum.

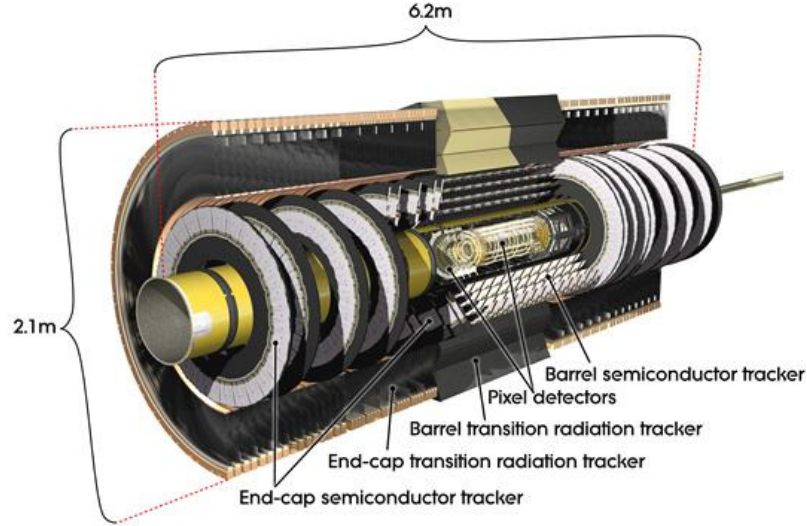


Figure 4.2: Cutaway view of the Inner Detector [11].

408 The Inner Detector consists of three components - the Pixel Detector, the Semi-Conductor
 409 Tracker (SCT), and the Transition Radiation Tracker (TRT). The Pixel Detector is the innermost
 410 of these, beginning just 33.25 mm away from the beam line. It consists of three silicon layers
 411 along the barrel, as well as three endcap layers, covering a range of $|\eta| < 2.5$.

412 The Semiconductor Tracker (SCT) is similar to the Pixel detector, but uses long strips of
 413 silicon rather than small pixels to cover a larger spatial area. It includes over 6 million readout
 414 strips, allowing the position of charged particles to be measured to an accuracy of $17 \mu\text{m}$.

415 The outermost component of the inner detector, the TRT consists of around 300,000 straw
 416 tubes filled with ionizable gas, which produces current through a wire in the center of each tube
 417 when a charged particle passes through. Between these staws are layers of material designed
 418 to produce transition radiation from ultrarelativistic particles as they pass through each material

419 boundary, amplifying the signal. The position uncertainty in the TRT is higher than the other
 420 two, on the order of 200 μm , but covering a much larger area.

421 **4.2 Calorimeters**

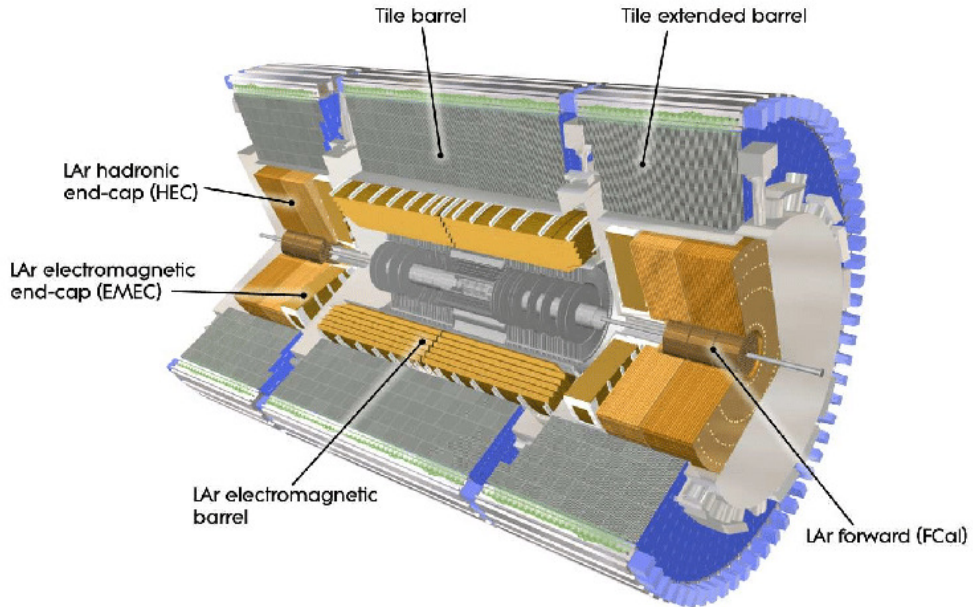


Figure 4.3: Cutaway view of the calorimeter system of the ATLAS detector [11].

422 Situated outside the Inner Detector are two concentric calorimeters. The inner calorimeter
 423 uses liquid argon (LAr) to measure the energy of particles that interact electromagnetically,
 424 which includes photons and any charged particle. The LAr calorimeter is made of heavy metals,
 425 primarily lead and copper, which causes electromagnetically interacting particles to shower,
 426 depositing their energy in the detector. The showering of the high energy particles that pass

427 through the calorimeter cause the liquid argon to ionize, and the ionized electrons are detected
428 by electronic readouts. The LAr calorimeter consists of around 180,000 readout channels.

429 The outer calorimeter measures the energy from particles that pass through the EM
430 calorimeter, and measures the energy of particles that interact via the strong force. This is
431 primarily hadrons. It is composed of steel plates designed to cause hadronic showering and
432 around 500,000 scintillating tiles as the active material. The signals from the hadronic calorimeter
433 are read out by photomultiplier tubes (PMTs).

434 **4.3 Muon Spectrometer**

435 Because muons are heavier than electrons and photons, and do not interact via the strong force,
436 they generally pass through the detector without being stopped by the calorimeters. The outermost
437 components of the detector are designed specifically to measure the energy and momentum of
438 muons produced in the LHC. The muon spectrometer consists of tracking and triggering systems.
439 The largest of the subdetectors, it extends from the outside of the calorimeter system, about a
440 4.25 m radius from the beam line, to a radius of 11 m. This large detector system is necessary
441 to accurately measure the momentum of muons, which is essential not only for measurements
442 involving the muons themselves, but also to accurately estimate the missing energy in each
443 event.

444 Two large toroidal magnets within the muon system generate a large magnetic field which
445 covers an area 26 m long with a radius of 10 m. Because the area covered by this magnet system

446 is so large, a uniform magnetic field like the one produced in the Inner Detector is impractical.
447 Instead, the magnetic field that exists in the muon spectrometer ranges between 2 T and 8 T, and
448 is much less uniform. The path of the muons passing through the spectrometer is bent by this
449 field, allowing their charge to be determined.

450 1200 tracking chambers are placed in the muon system in order to precisely measure the
451 tracks of muons with high spatial resolution. The path of the muons are tracked by Monitored
452 Drift Tubes, which are drift chambers formed by aluminum tubes and filled with ionizing gas.
453 These tubes produce a multi-layer spatial resolution on the order of 50 μm .

454 **4.4 Trigger System**

455 Because of the high collision rate and large amount of data collected by the various subdetectors,
456 ATLAS produces far more data than can actually be stored. Each event produces around 25 Mb
457 of raw data, which multiplied by the bunch crossing rate of 40 MHz, comes out to around a
458 petabyte of data every second. The information from every event cannot practically be stored,
459 therefore a sophisticated trigger system is employed in real time to determine whether events are
460 sufficiently interesting to be worth storing.

461 The trigger system in ATLAS involves multiple levels, each of which select out which
462 events move on to the next level of scrutiny. The level-1 trigger uses hardware information from
463 the calorimeters and muon spectrometer to select events that contain candidates for particles

⁴⁶⁴ commonly used in analysis, such as energetic leptons and jets. The level-1 trigger reduces the
⁴⁶⁵ rate of events from 40 MHz to around 100 kHz.

⁴⁶⁶ Events that pass the level-1 trigger move to the High-Level Trigger (HLT). The HLT takes
⁴⁶⁷ place outside of the detector in software, and looks for properties such as a large amount of
⁴⁶⁸ missing transverse energy, well defined leptons, and multiple high energy jets. Events that pass
⁴⁶⁹ the HLT are stored and used for analysis. Because the specifics of the HLT are determined by
⁴⁷⁰ software rather than hardware, the thresholds can be changed throughout the run of the detector
⁴⁷¹ in response to run conditions such as changes to pileup and luminosity. After the HLT is applied,
⁴⁷² the event rate is reduced to around 1000 per second, which are recorded for analysis.

⁴⁷³ **Part IV**

⁴⁷⁴ **Measurement of WZ + Heavy Flavor**

⁴⁷⁵ **5 Introduction**

⁴⁷⁶ The production of WZ in association with a heavy flavor jet represents an important background
⁴⁷⁷ for many major analyses. This includes any process with leptons and b-jets in the final state,
⁴⁷⁸ such as $t\bar{t}H$, $t\bar{t}W$, and $t\bar{t}Z$. While precise measurements have been made of WZ production
⁴⁷⁹ [12], WZ + heavy flavor remains poorly understood. This is largely because the QCD processes

480 involved in the production of the b-jet make it difficult to simulate accurately. This introduces a
481 large uncertainty for analyses that include this process as a background.

482 Motivated by its relevance to the $t\bar{t}H$ multilepton analysis, we perform a study of the fully
483 leptonic decay mode of this channel; that is, events where both the W and Z decay leptonically.
484 Because WZ has no associated jets at leading order, while the major backgrounds for this channel
485 tend to have high jet multiplicity, events with more than two jets are rejected. This gives a final
486 state signature of three leptons and one or two jets.

487 Events that meet this selection criteria are sorted into pseudo-continuous b-tagging regions
488 based on the DL1r b-tag score of their associated jets. This is done to separate WZ + b-jet events
489 from WZ + charm and WZ + light jets. These regions are fit to data in order to make a more
490 accurate estimate of the contribution of WZ + heavy-flavor, where heavy-flavor jets include
491 b-jets and charm jets. The full Run-2 dataset collected by the ATLAS detector, representing 139
492 fb^{-1} of data from pp collisions at $\sqrt{s} = 13 \text{ TeV}$, is used for this study.

493 Section 10 details the data and Monte Carlo (MC) samples used in the analysis. The
494 reconstruction of various physics objects is described in Section 11. Section 12 describes the
495 event selection applied to these samples, along the definitions of the various regions used in
496 the fit. The multivariate analysis techniques used to separate the tZ background from WZ +
497 heavy flavor are described in Section 13. Section 21 describes the various sources of systematic
498 uncertainties considered in the fit. Finally, the results of the analysis are summarized in Section
499 22, followed by a brief conclusion in Section ??.

500 **The current state of the analysis shows blinded results for the full 2018 dataset.**
501 **Regions containing >5% WZ+b events are blinded, and results are from Asimov, MC only**
502 **fits.**

503 **6 Data and Monte Carlo Samples**

504 **6.1 Data Samples**

505 This study uses a sample of proton-proton collision data collected by the ATLAS detector from
506 2015 through 2018 at an energy of $\sqrt{s} = 13$ TeV, which represents an integrated luminosity of
507 139 fb^{-1} . This data set was collected with a bunch crossing rate of 25 ns. All data used in this
508 analysis was verified by data quality checks.

509 **6.2 Monte Carlo Samples**

510 Several different generators were used to produce Monte Carlo simulations of the signal and
511 background processes. For all samples, the response of the ATLAS detector is simulated using
512 Geant4. The WZ signal samples are simulated using Sherpa 2.2.2 [13]. Specific information
513 about the Monte Carlo samples being used can be found in Table 21.

Table 1: The configurations used for event generation of signal and background processes, including the event generator, matrix element (ME) order, parton shower algorithm, and parton distribution function (PDF).

Process	Event generator	ME order	Parton Shower	PDF
WZ, VV	SHERPA 2.2.2	MEPS NLO	SHERPA	CT10
tZ	MG5_AMC	NLO	PYTHIA 8	CTEQ6L1
t̄tW	MG5_AMC (SHERPA 2.1.1)	NLO (LO multileg)	PYTHIA 8 (SHERPA)	NNPDF 3.0 NLO (NNPDF 3.0 NLO)
t̄t(Z/γ* → ll)	MG5_AMC	NLO	PYTHIA 8	NNPDF 3.0 NLO
t̄tH	MG5_AMC (MG5_AMC)	NLO (NLO)	PYTHIA 8 (HERWIG++)	NNPDF 3.0 NLO [14] (CT10 [15])
tHqb	MG5_AMC	LO	PYTHIA 8	CT10
tHW	MG5_AMC (SHERPA 2.1.1)	NLO (LO multileg)	HERWIG++ (SHERPA)	CT10 (NNPDF 3.0 NLO)
tWZ	MG5_AMC	NLO	PYTHIA 8	NNPDF 2.3 LO
t̄t̄, t̄t̄t̄	MG5_AMC	LO	PYTHIA 8	NNPDF 2.3 LO
t̄tW+W-	MG5_AMC	LO	PYTHIA 8	NNPDF 2.3 LO
t̄t	POWHEG-BOX v2 [16]	NLO	PYTHIA 8	NNPDF 3.0 NLO
t̄t̄γ	MG5_AMC	LO	PYTHIA 8	NNPDF 2.3 LO
s-, t-channel, Wt single top	POWHEG-BOX v1 [17]	NLO	PYTHIA 6	CT10
qqVV, VVV				
Z → l+l-	SHERPA 2.2.1	MEPS NLO	SHERPA	NNPDF 3.0 NLO

7 Object Reconstruction

514 All regions defined in this analysis share a common lepton, jet, and overall event preselection.

516 The selection applied to each physics object is detailed here; the event preselection, and the

517 selection used to define the various fit regions, is described in Section 12.

518 All events are required to be selected by dilepton triggers. The p_T thresholds of the

519 dilepton trigger on two electrons were 12 GeV in 2015, 17 GeV in 2016, and 24 GeV in 2017 and

520 2018, while for the dimuon triggers the p_T thresholds on the leading (sub-leading) muon were

521 18 GeV (8 GeV) in 2015, and 22 GeV (8 GeV) in 2016-2018. For the electron+muon triggers,
 522 the p_T thresholds on the electron (muon) were 17 GeV (14 GeV) for all datasets.

523 **7.1 Light leptons**

524 Electron candidates are reconstructed from energy clusters in the electromagnetic calorimeter
 525 that are associated with charged particle tracks reconstructed in the inner detector [18]. Electron
 526 candidates are required to have $p_T > 10$ GeV and $|\eta_{\text{cluster}}| < 2.47$. Muon candidates are
 527 reconstructed by combining inner detector tracks with track segments or full tracks in the muon
 528 spectrometer [19]. Muon candidates are required to have $p_T > 10$ GeV and $|\eta| < 2.5$. Candidates
 529 in the transition region between different electromagnetic calorimeter components, $1.37 <$
 530 $|\eta_{\text{cluster}}| < 1.52$, are rejected. A multivariate likelihood discriminant combining shower shape
 531 and track information is used to distinguish real electrons from hadronic showers (fake electrons).
 532 To further reduce the non-prompt electron contribution, the track is required to be consistent
 533 with originating from the primary vertex; requirements are imposed on the transverse impact
 534 parameter significance ($|d_0|/\sigma_{d_0} < 5$) and the longitudinal impact parameter ($|\Delta z_0 \sin \theta_\ell| < 0.5$
 535 mm). Electron candidates are required to pass TightLH identification.

536 Muon candidates are reconstructed by combining inner detector tracks with track segments
 537 or full tracks in the muon spectrometer [19]. Muon candidates are required to have $p_T > 10$ GeV
 538 and $|\eta| < 2.5$. The longitudinal impact parameter is the same for both electrons and muons, while

539 muons are required to pass a slightly tighter transverse impact parameter, $|d_0|/\sigma_{d_0} < 3$. Muons
 540 are also required to pass Medium ID requirements.

541 Leptons are additionally required to pass a non-prompt BDT selection developed by the
 542 $t\bar{t}H$ multilepton/ $t\bar{t}W$ analysis group. This BDT and the WPs used are summarized in Appendix
 543 .1, and described in detail in [20]. Optimized working points and scale factors for this BDT are
 544 taken from that analysis.

545 7.2 Jets

546 Jets are reconstructed from calibrated topological clusters built from energy deposits in the
 547 calorimeters [21], using the anti- k_t algorithm with a radius parameter $R = 0.4$. Particle Flow, or
 548 PFlow, jets are used in the analysis, which are hadronic objects reconstructed using information
 549 from both the tracker and the calorimeter. Jets with energy contributions likely arising from noise
 550 or detector effects are removed from consideration [22], and only jets satisfying $p_T > 25$ GeV
 551 and $|\eta| < 2.5$ are used in this analysis. For jets with $p_T < 60$ GeV and $|\eta| < 2.4$, a jet-track
 552 association algorithm is used to confirm that the jet originates from the selected primary vertex,
 553 in order to reject jets arising from pileup collisions [23].

554 7.3 B-tagged Jets

555 In order to make a measurement of $WZ +$ heavy flavor it is necessary to distinguish these events
 556 from $WZ +$ light jets. For this purpose, the DL1r b-tagging algorithm is used to distinguish

557 heavy flavor jets from lighter ones. The DL1r algorithm uses jet kinematics, particularly jet
 558 vertex information, as input for a neural network which assigns each jet a score designed to
 559 reflect how likely that jet is to have originated from a b-quark.

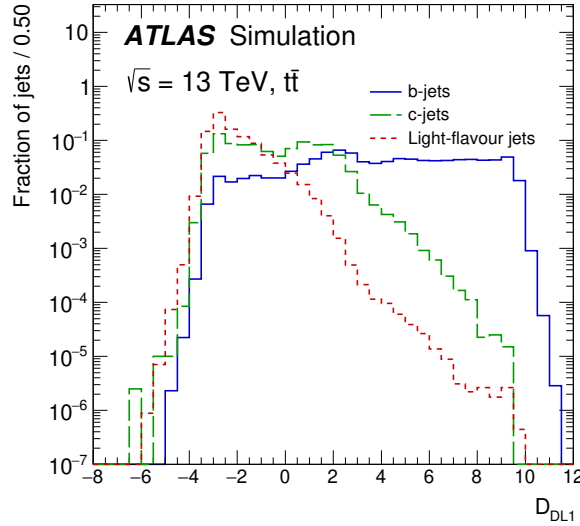


Figure 7.1: Output distribution of the DL1r algorithm for b-jets, charm jets, and light jets

560 From the output of the BDT, calibrated working points (WPs) are developed based on the
 561 efficiency of truth b-jets at particular values of the DL1r algorithm. The working points used in
 562 this analysis are summarized in Table 8.

WP	none	loose	medium	tight	tightest
b eff.	-	85%	77%	70%	60%

Table 2: B-tagging Working Points by tightness and b-jet efficiency

563 A tighter WP will accept fewer b-jets, but reject a higher fraction of charm and light jets.
 564 Generally, analyses that include b-jets will use a fixed working point, for example, requiring that

565 a jet pass the 70% threshold. By instead treating these working point as bins, e.g. events with
566 jets that fall between the 85% and 77% WPs fall into one bin, while events with jets passing the
567 60% WP fall into another, and looking at the full psuedo-continuous DL1r spectrum of the jets,
568 additional information can be gained. The psuedo-continuous b-tag spectrum is used in this case
569 to separate out WZ + b, WZ + charm, and WZ + light.

570 **7.4 Missing transverse energy**

571 Missing transverse momentum (E_T^{miss}) is used as part of the event selection. The missing
572 transverse momentum vector is defined as the inverse of the sum of the transverse momenta of
573 all reconstructed physics objects as well as remaining unclustered energy, the latter of which is
574 estimated from low- p_T tracks associated with the primary vertex but not assigned to a hard object,
575 with object definitions taken from [24]. Light leptons considered in the E_T^{miss} reconstruction are
576 required to have $p_T > 10$ GeV, while jets are required to have $p_T > 20$ GeV.

577 **7.5 Overlap removal**

578 To avoid double counting objects and remove leptons originating from decays of hadrons, overlap
579 removal is performed in the following order: any electron candidate within $\Delta R = 0.1$ of another
580 electron candidate with higher p_T is removed; any electron candidate within $\Delta R = 0.1$ of a muon
581 candidate is removed; any jet within $\Delta R = 0.3$ of an electron candidate is removed; if a muon

582 candidate and a jet lie within $\Delta R = \min(0.4, 0.04 + 10[\text{GeV}]/p_T(\text{muon}))$ of each other, the jet
 583 is kept and the muon is removed.

584 This algorithm is applied to the preselected objects. The overlap removal procedure is
 585 summarized in Table 24.

Keep	Remove	Cone size (ΔR)
electron	electron (low p_T)	0.1
muon	electron	0.1
electron	jet	0.3
jet	muon	$\min(0.4, 0.04 + 10[\text{GeV}]/p_T(\text{muon}))$
electron	tau	0.2

Table 3: Summary of the overlap removal procedure between electrons, muons, and jets.

586 8 Event Selection and Signal Region Definitions

587 Event are required to pass a preselection described in Section 12.1 and summarized in Table 10.
 588 Those that pass this preselection are divided into various fit regions described in Section 12.2,
 589 based on the number of jets in the event, and the b-tag score of those jets.

590 8.1 Event Preselection

591 Events are required to include exactly three reconstructed light leptons passing the requirement
 592 described in 11.1, which have a total charge of ± 1 .

593 The leptons are ordered in the analysis code as 0, 1, and 2. Lepton 0 is the lepton whose
 594 charge is opposite the other two. Lepton 1 is the lepton closest to the opposite charge lepton, i.e.
 595 the smallest ΔR , leaving lepton 2 as the lepton further from the opposite charge lepton. Lepton
 596 0 is required to have $p_T > 10$ GeV, while the same sign leptons, 1 and 2, are required to have
 597 $p_T > 20$ GeV to reduce the contribution of non-prompt leptons.

598 The invariant mass of at least one pair of opposite sign, same flavor leptons is required
 599 to fall within 10 GeV of the mass of the Z boson, 91.2 GeV. Events where one of the opposite
 600 sign pairs have an invariant mass less than 12 GeV are rejected in order to suppress low mass
 601 resonances.

602 An additional requirement is placed on the missing transverse energy, $E_T^{\text{miss}} > 20$ GeV,
 603 and the transverse mass of the W candidate, $m(E_T^{\text{miss}} + l_{\text{other}}) > 30$ GeV, where E_T^{miss} is the
 604 missing transverse energy, and l_{other} is the lepton not included in the Z-candidate.

605 Events are required to have one or two reconstructed jets passing the selection described
 606 in Section 11.2. Events with more than two jets are rejected in order to reduce the contribution
 607 of backgrounds such as $t\bar{t}Z$ and $t\bar{t}W$, which tend to have higher jet multiplicity.

Event Selection

- Exactly three leptons with charge ± 1
 - Two same-charge leptons with $p_T > 20$ GeV
 - One opposite charge lepton with $p_T > 10$ GeV
 - $m(l^+l^-)$ within 10 GeV of 91.2 GeV
 - Transverse mass of W-candidate, $m_T(E_T^{\text{miss}} + \text{lep}_{\text{other}}) > 30$ GeV
 - Missing transverse energy, $E_T^{\text{miss}} > 20$ GeV
 - One or two jets with $p_T > 25$ GeV
-

Table 4: Summary of the selection applied to events for inclusion in the fit

608 The event yields in the preselection region for both data and Monte Carlo are summarized
 609 in Table 12.1, which shows good agreement between data and Monte Carlo, and demonstrates
 610 that this region consists primarily of WZ events. The WZ events are split into WZ + b, WZ +
 611 c, and WZ + l based on the truth flavor of the associated jet in the event. In this ordering b-jet
 612 supersede charm, which supersides light. That is, WZ + l events contain no charm and no b jets
 613 at truth level, WZ + c contain at least one truth charm and no b-jets, and WZ + b contains at least
 614 one truth b-jet.

Process	Events
WZ + b	167.6 ± 6.5
WZ + c	1080 ± 40
WZ + l	7220 ± 310
Other VV	850 ± 140
$t\bar{t}W$	16.8 ± 2.3
$t\bar{t}Z$	115 ± 17
rare Top	2.2 ± 0.1
Single top	0.10 ± 0.45
Three top	0.01 ± 0.01
Four top	0.02 ± 0.01
$t\bar{t}WW$	0.23 ± 0.05
Z + jets	600 ± 260
V + γ	37 ± 54
tZ	190 ± 70
tW	5.5 ± 1.2
WtZ	25.8 ± 1.1
VVV	26.2 ± 0.9
VH	94 ± 7
t \bar{t}	108.68 ± 8
t $\bar{t}H$	4.3 ± 0.5
Total	10600 ± 530
Data	10574

Table 5: Event yields in the preselection region at 139.0 fb^{-1}

615 Here Other VV represents diboson processes other than WZ, and consists predominantly

616 of $ZZ \rightarrow ll\bar{l}\bar{l}$ events where one of the leptons is not reconstructed.

617 8.2 Fit Regions

618 Once preselection has been applied, the remaining events are categorized into one of twelve
619 orthogonal regions. The regions used in the fit are summarized in Table 12.

Table 6: A list of the regions used in the fit and the selection used for each.

Region	Selection
1j, <85%	$N_{\text{jets}} = 1, n\text{Jets}_{\text{DL1r}_85} = 0$
1j, 85%-77%	$N_{\text{jets}} = 1, n\text{Jets}_{\text{DL1r}_85} = 1, n\text{Jets}_{\text{DL1r}_77} = 0$
1j, 77%-70%	$N_{\text{jets}} = 1, n\text{Jets}_{\text{DL1r}_77} = 1, n\text{Jets}_{\text{DL1r}_70} = 0$
1j, 70%-60%	$N_{\text{jets}} = 1, n\text{Jets}_{\text{DL1r}_70} = 1, n\text{Jets}_{\text{DL1r}_60} = 0$
1j, >60%	$N_{\text{jets}} = 1, n\text{Jets}_{\text{DL1r}_60} = 1, tZ \text{ BDT} > 0.725$
1j tZ CR	$N_{\text{jets}} = 1, n\text{Jets}_{\text{DL1r}_60} = 1, tZ \text{ BDT} < 0.725$
2j, <85%	$N_{\text{jets}} = 2, n\text{Jets}_{\text{DL1r}_85} = 0$
2j, 85%-77%	$N_{\text{jets}} = 2, n\text{Jets}_{\text{DL1r}_85} \geq 1, n\text{Jets}_{\text{DL1r}_77} = 0$
2j, 77%-70%	$N_{\text{jets}} = 2, n\text{Jets}_{\text{DL1r}_77} \geq 1, n\text{Jets}_{\text{DL1r}_70} = 0$
2j, 70%-60%	$N_{\text{jets}} = 2, n\text{Jets}_{\text{DL1r}_70} \geq 1, n\text{Jets}_{\text{DL1r}_60} = 0$
2j, >60%	$N_{\text{jets}} = 2, n\text{Jets}_{\text{DL1r}_60} \geq 1, tZ \text{ BDT} > 0.725$
2j tZ CR	$N_{\text{jets}} = 2, n\text{Jets}_{\text{DL1r}_60} \geq 1, tZ \text{ BDT} < 0.725$

620 The working points discussed in Section 11.3 are used to separate events into fit regions
621 based on the highest working point reached by a jet in each event. Because the background
622 composition differs significantly based on the number of b-jets, events are further subdivided
623 into 1-jet and 2-jet regions in order to minimize the impact of background uncertainties.

624 An unfolding procedure is performed to account for differences in the number of recon-
625 structed jets compared to the number of truth jets in each event. In order to account for migration

626 of WZ+1-jet and WZ+2-jet events between the 1-jet and 2-jet bins at reco level, the signal
627 samples are separated based on the number of truth jets. Events with 0 jets or more than 3 jets at
628 truth level, yet fall within one of the categories listed in Table 12, are categorized as WZ + other,
629 and treated as a background. The composition of the number of truth jets in each reco jet bin is
630 taken from MC, with uncertainties in these estimates described in detail in Section 21.

631 An additional tZ control region is created based on the BDT described in Section 13. The
632 region with 1-jet passing the 60% working point is split in two - a signal enriched region of
633 events with a BDT score greater than 0.03, and a tZ control region including events with less
634 than 0.03. This cutoff is arrived at by performing an Asimov fit with a variety of cutoffs, and
635 selecting the value that produces the highest significance for the measurement of WZ + b.

636 **8.3 Non-Prompt Lepton Estimation**

637 Two processes act as sources of non-prompt leptons appear in the analysis: $t\bar{t}$ and Z+jet
638 production both produce two prompt leptons, and each contribute to the 31 region when an
639 additional non-prompt lepton appears in the event. The contribution of these processes is
640 estimated with Monte Carlo simulations, which are validated using enriched control regions.

641 The modelling in the Z+jets and $t\bar{t}$ CRs is further validated for each of the pseudo-
642 continuous b-tag regions used in the analysis. The relevant lepton p_T spectrum in each b-tag
643 region is shown in Appendix .2 for these CRs after the correction factors derived below have
644 been applied.

645 **8.3.1 $t\bar{t}$ Validation**

646 $t\bar{t}$ events can produce two prompt leptons from the decay of each of the tops. These top decays
 647 produce two b-quarks, the decay of which can produce additional non-prompt leptons, which
 648 occasionally pass the event preselection. In order to validate that the Monte Carlo accurately
 649 simulates this process accurately, the MC prediction in a non-prompt $t\bar{t}$ enriched control region
 650 is compared to data.

651 The $t\bar{t}$ control region is similar to the preselection region - three leptons meeting the
 652 criteria described in Section 12 are required, and the requirements on E_T^{miss} remain the same.
 653 However, the selection requiring a lepton pair form a Z-candidate are reversed. Events where the
 654 invariant mass of any two opposite sign, same flavor leptons falls within 10 GeV of 91.2 GeV are
 655 rejected. This ensures the $t\bar{t}$ control region is orthogonal to the preselection region.

656 Further, because the jet multiplicity of $t\bar{t}$ events tends to be higher than WZ, the number
 657 of jets in each event is required to be greater than 1. As b-jets are almost invariably produced
 658 from top decays, at least one b-tagged jet passing the 70% DL1r WP in each event is required.

659 Data is compared to MC predictions in the region for a variety of kinematic variable, as well
 660 as various b-tag WPs. A constant normalization discrepancy between data and MC predictions
 661 of approximately 10% is found, which is accounted for by applying a constant correction factor
 662 of 0.9 to the $t\bar{t}$ MC prediction. As data and MC are found to agree within 20% for each of
 663 the b-tag WPs considered, a 20% systematic uncertainty on the $t\bar{t}$ prediction is included for the
 664 analysis.

665 **8.3.2 Z+jets Validation**

666 Similar to $t\bar{t}$, a non-prompt Z +jets control region is produced in order to validate the MC
 667 predictions. The lepton requirements remain the same as the preselection region. Because no
 668 neutrinos are present for this process, the E_T^{miss} cut is reversed, requiring $E_T^{\text{miss}} < 30 \text{ GeV}$. This
 669 also ensures this control region is orthogonal to the preselection region. Further, the number of
 670 jets in each event is required to be greater than or equal to one.

671 While there is general agreement between data and MC within statistical uncertainty, the
 672 shape of the p_T spectrum of the lepton from the W is found to differ. To account for this
 673 discrepancy, a variable correction factor is applied to Z +jets. χ^2 minimization of the W lepton
 674 p_T spectrum is performed to derive a correction factor of $1.53 - 6.6 * 10^{-6}(\text{lep_Pt_W})$.

675 The uncertainty in the $Z + \text{jets}$ prediction is evaluated by comparing data to MC for each
 676 of the continuous b-tag WPs. For each of the regions considered, the data falls within 25% of
 677 the MC prediction once this correction factor has been applied. Therefore, a 25% systematic
 678 uncertainty is applied to $Z + \text{jets}$ in the analysis.

679 **9 tZ Interference Studies and Separation Multivariate Analysis**

680 An important process to consider in this analysis is tZ : the top almost always decays into a W
 681 boson and b-quark, and when both the W and Z decay leptonically, this gives three leptons and
 682 a heavy flavor jet in the final state. Because tZ can produce a final state identical to the signal,

683 it represents a predominant background in the most signal enriched regions. That is, the region
684 with one jet passing the 60% DL1r WP. Therefore, a boosted decision tree (BDT) algorithm is
685 trained using XGBoost [28] to separate WZ + heavy flavor from tZ. The result of this BDT is
686 used to create a tZ enriched region in the fit, reducing its impact on the measurement of WZ +
687 heavy flavor.

688 The following kinematic variables are used as inputs to train this BDT:

- 689 • The invariant mass of the reconstructed top candidate
690 • p_T of each of the leptons, jet
691 • The invariant mass of each combination of lepton pairs, $M(l\bar{l})$
692 • E_T^{miss}
693 • Distance between each combination of leptons, $\Delta R(l\bar{l})$
694 • Distance between each lepton and the jet, $\Delta R(lj)$

695 Here the top candidate is reconstructed based on the procedure described in section 6.1 of
696 [27]. Broadly, the mass of the top quark candidate is reconstructed from the jet, the lepton not
697 included in the Z-candidate, and a reconstructed neutrino. In the case that there is one jet in the
698 event, there is only possible b-jet candidate. For events with two jets, the jet with the highest
699 DL1r score is used.

700 The training samples included only events meeting the requirements of the 1-jet, >60%
701 region, i.e. passing all the selection described in section 12 and having exactly one jet which
702 passes the tightest (60%) DL1r working point. A sample of 20,000 background (tZ) and signal
703 (WZ+b) Monte Carlo events are used to train the BDT. And additional 5,000 events are reserved
704 for testing the model, in order to prevent over-fitting. A total of 750 decision trees with a
705 maximum depth of 6 branches are used to build the model. These parameters are chosen
706 empirically, by training several models with different parameters and selecting the one that gave
707 the best separation for the test sample.

708 The results of the BDT training are shown in figure 13.1. The output scores for both signal
709 and background events is shown on the left. The right shows the receiving operating characteristic
710 (ROC) curve that results from the MVA. The ROC curve represents the background rejection
711 as a function of signal efficiency, where each point on the curve represents a different response
712 score. The ROC curve of the BDT is compared to the performance of using an optimal set of flat
713 selections on the same set of input variables.

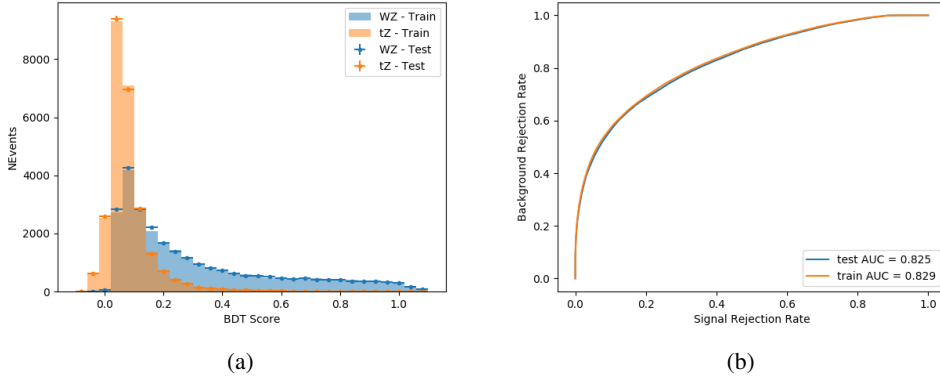


Figure 9.1: Distribution of the BDT response for signal and background events on the left, the ROC curve for the BDT on the right.

714 The relative important of each input feature in the model, measured by how often they
 715 appeared in the decision trees, is shown in figure 13.2.

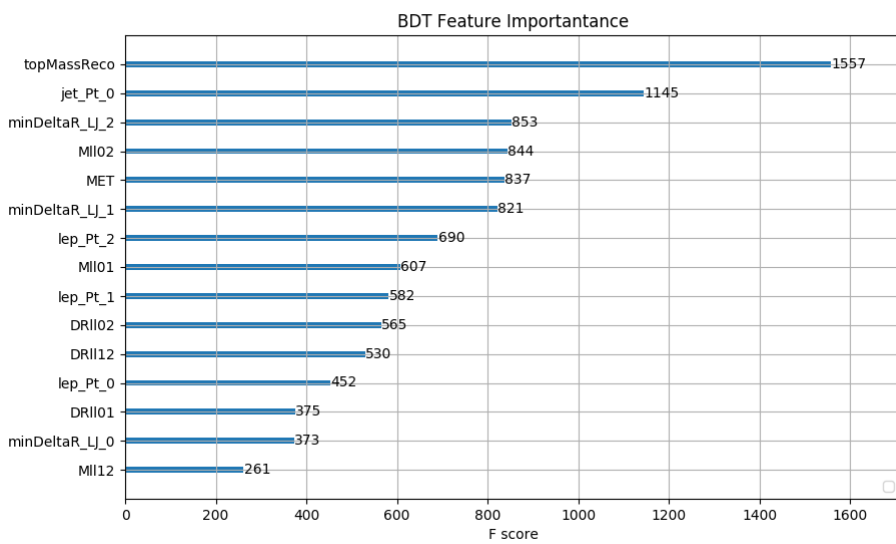


Figure 9.2: Relative importance of each input feature in the model.

716 These results suggest that some amount of separation can be achieved between these two
717 processes, with a high BDT score selecting a set of events that is pure in $WZ + b$. A BDT score
718 of 0.725 is selected as a cutoff, where events with scores higher than this form a signal enriched
719 region, and events with scores lower than this form a $t\bar{Z}$ control region. This cutoff is selected by
720 varying the value of this cutoff in stat-only Asimov fits, and selecting the value that minimizes
721 the statistical uncertainty on $WZ + b$.

722 **10 Data and Monte Carlo Samples**

723 **10.1 Data Samples**

724 This study uses a sample of proton-proton collision data collected by the ATLAS detector from
725 2015 through 2018 at an energy of $\sqrt{s} = 13$ TeV, which represents an integrated luminosity of
726 139 fb^{-1} . This data set was collected with a bunch crossing rate of 25 ns. All data used in this
727 analysis was verified by data quality checks.

728 **10.2 Monte Carlo Samples**

729 Several different generators were used to produce Monte Carlo simulations of the signal and
730 background processes. For all samples, the response of the ATLAS detector is simulated using
731 Geant4. The WZ signal samples are simulated using Sherpa 2.2.2 [13]. Specific information
732 about the Monte Carlo samples being used can be found in Table 21.

Table 7: The configurations used for event generation of signal and background processes, including the event generator, matrix element (ME) order, parton shower algorithm, and parton distribution function (PDF).

Process	Event generator	ME order	Parton Shower	PDF
WZ, VV	SHERPA 2.2.2	MEPS NLO	SHERPA	CT10
tZ	MG5_AMC	NLO	PYTHIA 8	CTEQ6L1
t̄tW	MG5_AMC (SHERPA 2.1.1)	NLO (LO multileg)	PYTHIA 8 (SHERPA)	NNPDF 3.0 NLO (NNPDF 3.0 NLO)
t̄t(Z/γ* → ll)	MG5_AMC	NLO	PYTHIA 8	NNPDF 3.0 NLO
t̄tH	MG5_AMC (MG5_AMC)	NLO (NLO)	PYTHIA 8 (HERWIG++)	NNPDF 3.0 NLO [14] (CT10 [15])
tHqb	MG5_AMC	LO	PYTHIA 8	CT10
tHW	MG5_AMC (SHERPA 2.1.1)	NLO (LO multileg)	HERWIG++ (SHERPA)	CT10 (NNPDF 3.0 NLO)
tWZ	MG5_AMC	NLO	PYTHIA 8	NNPDF 2.3 LO
t̄t̄t, t̄t̄t̄t	MG5_AMC	LO	PYTHIA 8	NNPDF 2.3 LO
t̄tW+W-	MG5_AMC	LO	PYTHIA 8	NNPDF 2.3 LO
t̄t	POWHEG-BOX v2 [16]	NLO	PYTHIA 8	NNPDF 3.0 NLO
t̄tγ	MG5_AMC	LO	PYTHIA 8	NNPDF 2.3 LO
s-, t-channel, Wt single top	POWHEG-BOX v1 [17]	NLO	PYTHIA 6	CT10
qqVV, VVV				
Z → l+l-	SHERPA 2.2.1	MEPS NLO	SHERPA	NNPDF 3.0 NLO

11 Object Reconstruction

734 All regions defined in this analysis share a common lepton, jet, and overall event preselection.

735 The selection applied to each physics object is detailed here; the event preselection, and the

⁷³⁶ selection used to define the various fit regions, is described in Section 12.

All events are required to be selected by dilepton triggers. The p_T thresholds of the

738 dilepton trigger on two electrons were 12 GeV in 2015, 17 GeV in 2016, and 24 GeV in 2017 and

739 2018, while for the dimuon triggers the p_T thresholds on the leading (sub-leading) muon were

⁷⁴⁰ 18 GeV (8 GeV) in 2015, and 22 GeV (8 GeV) in 2016-2018. For the electron+muon triggers,
⁷⁴¹ the p_T thresholds on the electron (muon) were 17 GeV (14 GeV) for all datasets.

⁷⁴² **11.1 Light leptons**

⁷⁴³ Electron candidates are reconstructed from energy clusters in the electromagnetic calorimeter
⁷⁴⁴ that are associated with charged particle tracks reconstructed in the inner detector [18]. Electron
⁷⁴⁵ candidates are required to have $p_T > 10$ GeV and $|\eta_{\text{cluster}}| < 2.47$. Muon candidates are
⁷⁴⁶ reconstructed by combining inner detector tracks with track segments or full tracks in the muon
⁷⁴⁷ spectrometer [19]. Muon candidates are required to have $p_T > 10$ GeV and $|\eta| < 2.5$. Candidates
⁷⁴⁸ in the transition region between different electromagnetic calorimeter components, $1.37 <$
⁷⁴⁹ $|\eta_{\text{cluster}}| < 1.52$, are rejected. A multivariate likelihood discriminant combining shower shape
⁷⁵⁰ and track information is used to distinguish real electrons from hadronic showers (fake electrons).
⁷⁵¹ To further reduce the non-prompt electron contribution, the track is required to be consistent
⁷⁵² with originating from the primary vertex; requirements are imposed on the transverse impact
⁷⁵³ parameter significance ($|d_0|/\sigma_{d_0} < 5$) and the longitudinal impact parameter ($|\Delta z_0 \sin \theta_\ell| < 0.5$
⁷⁵⁴ mm). Electron candidates are required to pass TightLH identification.

⁷⁵⁵ Muon candidates are reconstructed by combining inner detector tracks with track segments
⁷⁵⁶ or full tracks in the muon spectrometer [19]. Muon candidates are required to have $p_T > 10$ GeV
⁷⁵⁷ and $|\eta| < 2.5$. The longitudinal impact parameter is the same for both electrons and muons, while

758 muons are required to pass a slightly tighter transverse impact parameter, $|d_0|/\sigma_{d_0} < 3$. Muons
 759 are also required to pass Medium ID requirements.

760 Leptons are additionally required to pass a non-prompt BDT selection developed by the
 761 $t\bar{t}H$ multilepton/ $t\bar{t}W$ analysis group. This BDT and the WPs used are summarized in Appendix
 762 .1, and described in detail in [20]. Optimized working points and scale factors for this BDT are
 763 taken from that analysis.

764 11.2 Jets

765 Jets are reconstructed from calibrated topological clusters built from energy deposits in the
 766 calorimeters [21], using the anti- k_t algorithm with a radius parameter $R = 0.4$. Particle Flow, or
 767 PFlow, jets are used in the analysis, which are hadronic objects reconstructed using information
 768 from both the tracker and the calorimeter. Jets with energy contributions likely arising from noise
 769 or detector effects are removed from consideration [22], and only jets satisfying $p_T > 25$ GeV
 770 and $|\eta| < 2.5$ are used in this analysis. For jets with $p_T < 60$ GeV and $|\eta| < 2.4$, a jet-track
 771 association algorithm is used to confirm that the jet originates from the selected primary vertex,
 772 in order to reject jets arising from pileup collisions [23].

773 11.3 B-tagged Jets

774 In order to make a measurement of $WZ +$ heavy flavor it is necessary to distinguish these events
 775 from $WZ +$ light jets. For this purpose, the DL1r b-tagging algorithm is used to distinguish

776 heavy flavor jets from lighter ones. The DL1r algorithm uses jet kinematics, particularly jet
 777 vertex information, as input for a neural network which assigns each jet a score designed to
 778 reflect how likely that jet is to have originated from a b-quark.

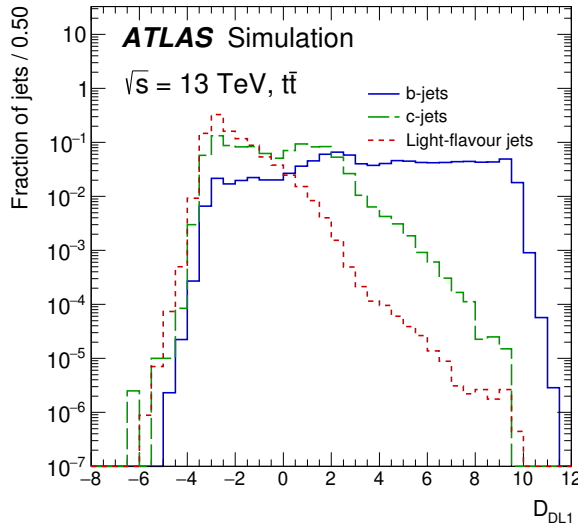


Figure 11.1: Output distribution of the DL1r algorithm for b-jets, charm jets, and light jets

779 From the output of the BDT, calibrated working points (WPs) are developed based on the
 780 efficiency of truth b-jets at particular values of the DL1r algorithm. The working points used in
 781 this analysis are summarized in Table 8.

WP	none	loose	medium	tight	tightest
b eff.	-	85%	77%	70%	60%

Table 8: B-tagging Working Points by tightness and b-jet efficiency

782 A tighter WP will accept fewer b-jets, but reject a higher fraction of charm and light jets.
 783 Generally, analyses that include b-jets will use a fixed working point, for example, requiring that

784 a jet pass the 70% threshold. By instead treating these working point as bins, e.g. events with
785 jets that fall between the 85% and 77% WPs fall into one bin, while events with jets passing the
786 60% WP fall into another, and looking at the full psuedo-continuous DL1r spectrum of the jets,
787 additional information can be gained. The psuedo-continuous b-tag spectrum is used in this case
788 to separate out $WZ + b$, $WZ + \text{charm}$, and $WZ + \text{light}$.

789 **11.4 Missing transverse energy**

790 Missing transverse momentum (E_T^{miss}) is used as part of the event selection. The missing
791 transverse momentum vector is defined as the inverse of the sum of the transverse momenta of
792 all reconstructed physics objects as well as remaining unclustered energy, the latter of which is
793 estimated from low- p_T tracks associated with the primary vertex but not assigned to a hard object,
794 with object definitions taken from [24]. Light leptons considered in the E_T^{miss} reconstruction are
795 required to have $p_T > 10$ GeV, while jets are required to have $p_T > 20$ GeV.

796 **11.5 Overlap removal**

797 To avoid double counting objects and remove leptons originating from decays of hadrons, overlap
798 removal is performed in the following order: any electron candidate within $\Delta R = 0.1$ of another
799 electron candidate with higher p_T is removed; any electron candidate within $\Delta R = 0.1$ of a muon
800 candidate is removed; any jet within $\Delta R = 0.3$ of an electron candidate is removed; if a muon

801 candidate and a jet lie within $\Delta R = \min(0.4, 0.04 + 10[\text{GeV}]/p_T(\text{muon}))$ of each other, the jet
 802 is kept and the muon is removed.

803 This algorithm is applied to the preselected objects. The overlap removal procedure is
 804 summarized in Table 24.

Keep	Remove	Cone size (ΔR)
electron	electron (low p_T)	0.1
muon	electron	0.1
electron	jet	0.3
jet	muon	$\min(0.4, 0.04 + 10[\text{GeV}]/p_T(\text{muon}))$
electron	tau	0.2

Table 9: Summary of the overlap removal procedure between electrons, muons, and jets.

805 12 Event Selection and Signal Region Definitions

806 Event are required to pass a preselection described in Section 12.1 and summarized in Table 10.
 807 Those that pass this preselection are divided into various fit regions described in Section 12.2,
 808 based on the number of jets in the event, and the b-tag score of those jets.

809 12.1 Event Preselection

810 Events are required to include exactly three reconstructed light leptons passing the requirement
 811 described in 11.1, which have a total charge of ± 1 .

812 The leptons are ordered in the analysis code as 0, 1, and 2. Lepton 0 is the lepton whose
 813 charge is opposite the other two. Lepton 1 is the lepton closest to the opposite charge lepton, i.e.
 814 the smallest ΔR , leaving lepton 2 as the lepton further from the opposite charge lepton. Lepton
 815 0 is required to have $p_T > 10$ GeV, while the same sign leptons, 1 and 2, are required to have
 816 $p_T > 20$ GeV to reduce the contribution of non-prompt leptons.

817 The invariant mass of at least one pair of opposite sign, same flavor leptons is required
 818 to fall within 10 GeV of the mass of the Z boson, 91.2 GeV. Events where one of the opposite
 819 sign pairs have an invariant mass less than 12 GeV are rejected in order to suppress low mass
 820 resonances.

821 An additional requirement is placed on the missing transverse energy, $E_T^{\text{miss}} > 20$ GeV,
 822 and the transverse mass of the W candidate, $m(E_T^{\text{miss}} + l_{\text{other}}) > 30$ GeV, where E_T^{miss} is the
 823 missing transverse energy, and l_{other} is the lepton not included in the Z-candidate.

824 Events are required to have one or two reconstructed jets passing the selection described
 825 in Section 11.2. Events with more than two jets are rejected in order to reduce the contribution
 826 of backgrounds such as $t\bar{t}Z$ and $t\bar{t}W$, which tend to have higher jet multiplicity.

Event Selection

- Exactly three leptons with charge ± 1
 - Two same-charge leptons with $p_T > 20$ GeV
 - One opposite charge lepton with $p_T > 10$ GeV
 - $m(l^+l^-)$ within 10 GeV of 91.2 GeV
 - Transverse mass of W-candidate, $m_T(E_T^{\text{miss}} + \text{lep}_{\text{other}}) > 30$ GeV
 - Missing transverse energy, $E_T^{\text{miss}} > 20$ GeV
 - One or two jets with $p_T > 25$ GeV
-

Table 10: Summary of the selection applied to events for inclusion in the fit

827 The event yields in the preselection region for both data and Monte Carlo are summarized
 828 in Table 12.1, which shows good agreement between data and Monte Carlo, and demonstrates
 829 that this region consists primarily of WZ events. The WZ events are split into WZ + b, WZ +
 830 c, and WZ + l based on the truth flavor of the associated jet in the event. In this ordering b-jet
 831 supersede charm, which supersides light. That is, WZ + l events contain no charm and no b jets
 832 at truth level, WZ + c contain at least one truth charm and no b-jets, and WZ + b contains at least
 833 one truth b-jet.

Process	Events
WZ + b	167.6 ± 6.5
WZ + c	1080 ± 40
WZ + l	7220 ± 310
Other VV	850 ± 140
$t\bar{t}W$	16.8 ± 2.3
$t\bar{t}Z$	115 ± 17
rare Top	2.2 ± 0.1
Single top	0.10 ± 0.45
Three top	0.01 ± 0.01
Four top	0.02 ± 0.01
$t\bar{t}WW$	0.23 ± 0.05
Z + jets	600 ± 260
V + γ	37 ± 54
tZ	190 ± 70
tW	5.5 ± 1.2
WtZ	25.8 ± 1.1
VVV	26.2 ± 0.9
VH	94 ± 7
t \bar{t}	108.68 ± 8
t $\bar{t}H$	4.3 ± 0.5
Total	10600 ± 530
Data	10574

Table 11: Event yields in the preselection region at 139.0 fb^{-1}

834 Here Other VV represents diboson processes other than WZ, and consists predominantly

⁸³⁵ of $ZZ \rightarrow llll$ events where one of the leptons is not reconstructed.

⁸³⁶ 12.2 Fit Regions

⁸³⁷ Once preselection has been applied, the remaining events are categorized into one of twelve
⁸³⁸ orthogonal regions. The regions used in the fit are summarized in Table 12.

Table 12: A list of the regions used in the fit and the selection used for each.

Region	Selection
1j, <85%	$N_{\text{jets}} = 1, n\text{Jets_DL1r_85} = 0$
1j, 85%-77%	$N_{\text{jets}} = 1, n\text{Jets_DL1r_85} = 1, n\text{Jets_DL1r_77}=0$
1j, 77%-70%	$N_{\text{jets}} = 1, n\text{Jets_DL1r_77} = 1, n\text{Jets_DL1r_70}=0$
1j, 70%-60%	$N_{\text{jets}} = 1, n\text{Jets_DL1r_70} = 1, n\text{Jets_DL1r_60}=0$
1j, >60%	$N_{\text{jets}} = 1, n\text{Jets_DL1r_60} = 1, tZ \text{ BDT} > 0.725$
1j tZ CR	$N_{\text{jets}} = 1, n\text{Jets_DL1r_60} = 1, tZ \text{ BDT} < 0.725$
2j, <85%	$N_{\text{jets}} = 2, n\text{Jets_DL1r_85} = 0$
2j, 85%-77%	$N_{\text{jets}} = 2, n\text{Jets_DL1r_85} >= 1, n\text{Jets_DL1r_77}=0$
2j, 77%-70%	$N_{\text{jets}} = 2, n\text{Jets_DL1r_77} >= 1, n\text{Jets_DL1r_70}=0$
2j, 70%-60%	$N_{\text{jets}} = 2, n\text{Jets_DL1r_70} >= 1, n\text{Jets_DL1r_60}=0$
2j, >60%	$N_{\text{jets}} = 2, n\text{Jets_DL1r_60} >= 1, tZ \text{ BDT} > 0.725$
2j tZ CR	$N_{\text{jets}} = 2, n\text{Jets_DL1r_60} >= 1, tZ \text{ BDT} < 0.725$

⁸³⁹ The working points discussed in Section 11.3 are used to separate events into fit regions
⁸⁴⁰ based on the highest working point reached by a jet in each event. Because the background
⁸⁴¹ composition differs significantly based on the number of b-jets, events are further subdivided
⁸⁴² into 1-jet and 2-jet regions in order to minimize the impact of background uncertainties.

⁸⁴³ An unfolding procedure is performed to account for differences in the number of recon-
⁸⁴⁴ structed jets compared to the number of truth jets in each event. In order to account for migration

845 of WZ+1-jet and WZ+2-jet events between the 1-jet and 2-jet bins at reco level, the signal
 846 samples are separated based on the number of truth jets. Events with 0 jets or more than 3 jets at
 847 truth level, yet fall within one of the categories listed in Table 12, are categorized as WZ + other,
 848 and treated as a background. The composition of the number of truth jets in each reco jet bin is
 849 taken from MC, with uncertainties in these estimates described in detail in Section 21.

850 An additional tZ control region is created based on the BDT described in Section 13. The
 851 region with 1-jet passing the 60% working point is split in two - a signal enriched region of
 852 events with a BDT score greater than 0.03, and a tZ control region including events with less
 853 than 0.03. This cutoff is arrived at by performing an Asimov fit with a variety of cutoffs, and
 854 selecting the value that produces the highest significance for the measurement of WZ + b.

855 **12.3 Non-Prompt Lepton Estimation**

856 Two processes act as sources of non-prompt leptons appear in the analysis: $t\bar{t}$ and Z+jet
 857 production both produce two prompt leptons, and each contribute to the 31 region when an
 858 additional non-prompt lepton appears in the event. The contribution of these processes is
 859 estimated with Monte Carlo simulations, which are validated using enriched control regions.

860 The modelling in the Z+jets and $t\bar{t}$ CRs is further validated for each of the pseudo-
 861 continuous b-tag regions used in the analysis. The relevant lepton p_T spectrum in each b-tag
 862 region is shown in Appendix .2 for these CRs after the correction factors derived below have
 863 been applied.

864 **12.3.1 $t\bar{t}$ Validation**

865 $t\bar{t}$ events can produce two prompt leptons from the decay of each of the tops. These top decays
866 produce two b-quarks, the decay of which can produce additional non-prompt leptons, which
867 occasionally pass the event preselection. In order to validate that the Monte Carlo accurately
868 simulates this process accurately, the MC prediction in a non-prompt $t\bar{t}$ enriched control region
869 is compared to data.

870 The $t\bar{t}$ control region is similar to the preselection region - three leptons meeting the
871 criteria described in Section 12 are required, and the requirements on E_T^{miss} remain the same.
872 However, the selection requiring a lepton pair form a Z-candidate are reversed. Events where the
873 invariant mass of any two opposite sign, same flavor leptons falls within 10 GeV of 91.2 GeV are
874 rejected. This ensures the $t\bar{t}$ control region is orthogonal to the preselection region.

875 Further, because the jet multiplicity of $t\bar{t}$ events tends to be higher than WZ, the number
876 of jets in each event is required to be greater than 1. As b-jets are almost invariably produced
877 from top decays, at least one b-tagged jet passing the 70% DL1r WP in each event is required.

878 Data is compared to MC predictions in the region for a variety of kinematic variable, as well
879 as various b-tag WPs. A constant normalization discrepancy between data and MC predictions
880 of approximately 10% is found, which is accounted for by applying a constant correction factor
881 of 0.9 to the $t\bar{t}$ MC prediction. As data and MC are found to agree within 20% for each of
882 the b-tag WPs considered, a 20% systematic uncertainty on the $t\bar{t}$ prediction is included for the
883 analysis.

884 **12.3.2 Z+jets Validation**

885 Similar to $t\bar{t}$, a non-prompt Z +jets control region is produced in order to validate the MC
886 predictions. The lepton requirements remain the same as the preselection region. Because no
887 neutrinos are present for this process, the E_T^{miss} cut is reversed, requiring $E_T^{\text{miss}} < 30 \text{ GeV}$. This
888 also ensures this control region is orthogonal to the preselection region. Further, the number of
889 jets in each event is required to be greater than or equal to one.

890 While there is general agreement between data and MC within statistical uncertainty, the
891 shape of the p_T spectrum of the lepton from the W is found to differ. To account for this
892 discrepancy, a variable correction factor is applied to Z +jets. χ^2 minimization of the W lepton
893 p_T spectrum is performed to derive a correction factor of $1.53 - 6.6 * 10^{-6}(\text{lep}_\text{Pt}_W)$.

894 The uncertainty in the $Z + \text{jets}$ prediction is evaluated by comparing data to MC for each
895 of the continuous b-tag WPs. For each of the regions considered, the data falls within 25% of
896 the MC prediction once this correction factor has been applied. Therefore, a 25% systematic
897 uncertainty is applied to $Z + \text{jets}$ in the analysis.

898 **13 tZ Interference Studies and Separation Multivariate Analysis**

899 An important process to consider in this analysis is tZ : the top almost always decays into a W
900 boson and b-quark, and when both the W and Z decay leptonically, this gives three leptons and
901 a heavy flavor jet in the final state. Because tZ can produce a final state identical to the signal,

902 it represents a predominant background in the most signal enriched regions. That is, the region
903 with one jet passing the 60% DL1r WP. Therefore, a boosted decision tree (BDT) algorithm is
904 trained using XGBoost [28] to separate WZ + heavy flavor from tZ. The result of this BDT is
905 used to create a tZ enriched region in the fit, reducing its impact on the measurement of WZ +
906 heavy flavor.

907 The following kinematic variables are used as inputs to train this BDT:

- 908 • The invariant mass of the reconstructed top candidate
- 909 • p_T of each of the leptons, jet
- 910 • The invariant mass of each combination of lepton pairs, $M(l\bar{l})$
- 911 • E_T^{miss}
- 912 • Distance between each combination of leptons, $\Delta R(l\bar{l})$
- 913 • Distance between each lepton and the jet, $\Delta R(lj)$

914 Here the top candidate is reconstructed based on the procedure described in section 6.1 of
915 [27]. Broadly, the mass of the top quark candidate is reconstructed from the jet, the lepton not
916 included in the Z-candidate, and a reconstructed neutrino. In the case that there is one jet in the
917 event, there is only possible b-jet candidate. For events with two jets, the jet with the highest
918 DL1r score is used.

919 The training samples included only events meeting the requirements of the 1-jet, >60%
920 region, i.e. passing all the selection described in section 12 and having exactly one jet which
921 passes the tightest (60%) DL1r working point. A sample of 20,000 background (tZ) and signal
922 (WZ+b) Monte Carlo events are used to train the BDT. And additional 5,000 events are reserved
923 for testing the model, in order to prevent over-fitting. A total of 750 decision trees with a
924 maximum depth of 6 branches are used to build the model. These parameters are chosen
925 empirically, by training several models with different parameters and selecting the one that gave
926 the best separation for the test sample.

927 The results of the BDT training are shown in figure 13.1. The output scores for both signal
928 and background events is shown on the left. The right shows the receiving operating characteristic
929 (ROC) curve that results from the MVA. The ROC curve represents the background rejection
930 as a function of signal efficiency, where each point on the curve represents a different response
931 score. The ROC curve of the BDT is compared to the performance of using an optimal set of flat
932 selections on the same set of input variables.

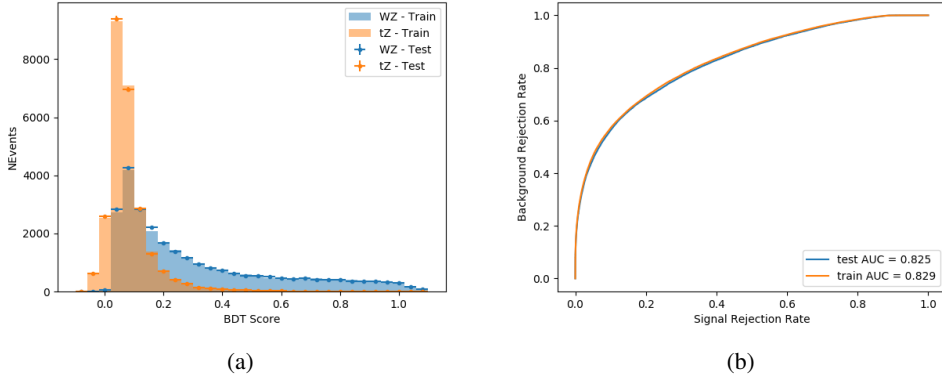


Figure 13.1: Distribution of the BDT response for signal and background events on the left, the ROC curve for the BDT on the right.

933 The relative important of each input feature in the model, measured by how often they
 934 appeared in the decision trees, is shown in figure 13.2.

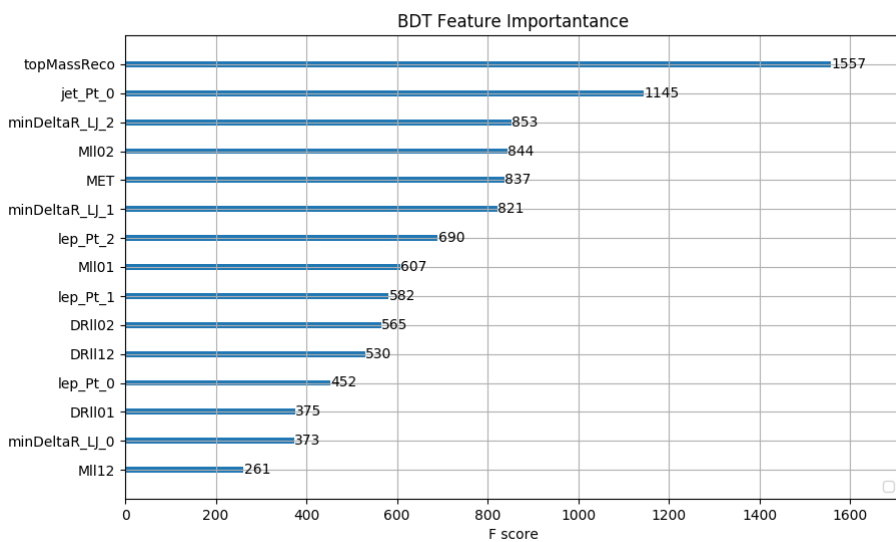


Figure 13.2: Relative importance of each input feature in the model.

935 These results suggest that some amount of separation can be achieved between these two
936 processes, with a high BDT score selecting a set of events that is pure in $WZ + b$. A BDT score
937 of 0.725 is selected as a cutoff, where events with scores higher than this form a signal enriched
938 region, and events with scores lower than this form a $t\bar{Z}$ control region. This cutoff is selected by
939 varying the value of this cutoff in stat-only Asimov fits, and selecting the value that minimizes
940 the statistical uncertainty on $WZ + b$.

941 **14 Systematic Uncertainties**

942 The systematic uncertainties that are considered are summarized in Table 44. These are imple-
943 mented in the fit either as a normalization factors or as a shape variation or both in the signal
944 and background estimations. The numerical impact of each of these uncertainties is outlined in
945 Section 22.

Table 13: Sources of systematic uncertainty considered in the analysis.

Systematic uncertainty	Components
Luminosity	1
Pileup reweighting	1
Physics Objects	
Electron	6
Muon	15
Jet energy scale	28
Jet energy resolution	8
Jet vertex fraction	1
Jet flavor tagging	131
E_T^{miss}	3
Total (Experimental)	194
Signal Modeling	
Shape modelling	3
Renormalization and factorization scales	5
nJet Migration	5
Background Modeling	
Cross section	15
Renormalization and factorization scales	12
Total (Signal and background modeling)	35
Total (Overall)	230

946 The uncertainty in the combined integrated luminosity is derived from a calibration of the

947 luminosity scale performed for 13 TeV proton-proton collisions [29], [30].

948 The experimental uncertainties are related to the reconstruction and identification of light

949 leptons and b-tagging of jets, and to the reconstruction of E_T^{miss} . The sources which contribute to

950 the uncertainty in the jet energy scale (JES) [31] are decomposed into uncorrelated components

951 and treated as independent sources of uncertainty in the analysis. These are treated as 30

952 nuisance parameters included in the fit. A similar approach is used for the jet energy resolution

953 (JER) uncertainty, which is decomposed into 8 JER uncertainty components included as NPs in
954 the fit.

955 The uncertainties in the b-tagging efficiencies measured in dedicated calibration analyses
956 [32] are also decomposed into uncorrelated components. The large number of components for
957 b-tagging is due to the calibration of the distribution of the MVA discriminant.

958 Theoretical uncertainties applied to MC predictions, including cross section, PDF, and scale
959 uncertainties are taken from theory calculations, with the exception of non-prompt and dibo-
960 son backgrounds. The cross-section uncertainty on tZ is taken from [33]. Derivation of the
961 non-prompt background uncertainties, Z+jets and tt>, are explained in Section 12.3. These
962 normalization uncertainties are chosen so as to account for the complete uncertainty in the
963 non-prompt contribution, and therefore no additional modelling uncertainties are considered for
964 Z+jets and tt>.

965 The other VV + heavy flavor processes (namely VV+b and VV+charm, which primarily
966 consist of ZZ events) are also poorly understood, because these processes involve the same
967 physics as WZ + heavy flavor, and have also not been measured. Therefore, a conservative 50%
968 uncertainty is applied to those samples. While this uncertainty is large, it is found to have little
969 impact on the significance of the final result.

970 The theory uncertainties applied to the predominate background estimates are summarized
971 in Table 48.

Process	X-section [%]
tZ	X-sec: ± 15.2 QCD Scale: $^{+5.2}_{-1.3}$ PDF($+\alpha_S$): ± 1.2
t̄t H (aMC@NLO+Pythia8)	QCD Scale: $^{+5.8}_{-9.2}$ PDF($+\alpha_S$): ± 3.6
t̄t Z (aMC@NLO+Pythia8)	QCD Scale: $^{+9.6}_{-11.3}$ PDF($+\alpha_S$): ± 4
t̄t W (aMC@NLO+Pythia8)	QCD Scale: $^{+12.9}_{-11.5}$ PDF($+\alpha_S$): ± 3.4
VV + b/charm (Sherpa 2.2.1)	± 50
VV + light (Sherpa 2.2.1)	± 6
t̄t	± 20
Z + jets	± 25
Others	± 50

Table 14: Summary of theoretical uncertainties for MC predictions in the analysis.

972 Additional signal uncertainties are estimated by comparing estimates from the nominal Sherpa
 973 WZ samples with alternate WZ samples generated with Powheg+PYTHIA8. Separate systemat-
 974 ics are included in the fit for WZ + b, WZ + charm and WZ + light, where the distribution among
 975 each of the fit regions is varied based on the prediction of the Powheg sample.

976 A similar approach is taken to account for uncertainties in migrations between the number of
 977 reco and truth jets. The fraction of events with 1 truth jet which fall into the 1 jet bin versus the
 978 2 jet bin at reco level is compared for Sherpa and Powheg. The same is done for events with 2
 979 truth jets. A systematic is included where events are shifted between the 1-jet and 2-jet regions
 980 based on the differences between these two shapes. This is done independently for each of the
 981 WZ + b, WZ + charm, and WZ + light templates.

982 Additional systematics are included to account for the uncertainty in the contamination of
983 0 jet and 3 or more jet events (as defined at truth level) in the 1 and 2 reco jet bins. Because these
984 events fall outside the scope of this measurement, these events are included as a background.
985 As such, a normalization, rather than a shape, uncertainty is applied for this background. The
986 number of WZ events with 0-jets and $>=3$ -jets in the reconstructed 1-jet and 2-jet regions are
987 compared for Sherpa and Powheg, and these differences are taken as separate normalization
988 systematics on the yield of WZ+0-jet and WZ+ $>=3$ -jet events.

989 15 Results

990 A separate maximum-likelihood fit is performed over the 1-jet and 2-jet fit regions in order to
991 extract the best-fit value of the WZ + b-jet and WZ + charm jet contributions. The WZ + b,
992 WZ + charm and WZ + light contributions are allowed to float, with the remaining background
993 contributions are held fixed. **The current fit strategy treats the WZ + b-jet contribution as**
994 **the parameter of interest, with the normalization of the WZ + charm and the WZ + light**
995 **contributions taken as systematic uncertainties. This could however be adjusted, depending**
996 **on whether it is decided the goal of the analysis should be to measure WZ+b specifically or**
997 **WZ + heavy flavor overall.** The result of the fit is used to extract the cross-section of WZ +
998 heavy-flavor production.

999 A maximum likelihood fit to data is performed simultaneously in the regions described
1000 in Section 12. The parameters μ_{WZ+b} , $\mu_{WZ+charm}$, $\mu_{WZ+light}$, where $\mu = \sigma_{\text{observed}}/\sigma_{\text{SM}}$, are

1001 extracted from the fit.

1002 The Asimov fit for 1-jet events gives an expected μ value of $1.00^{+0.37}_{-0.35}(\text{stat})^{+0.24}_{-0.22}(\text{sys})$ for
1003 WZ + b. The fitted cross-section modifiers for WZ + charm and WZ + light are $1.00 \pm 0.17 \pm 0.15$
1004 and $1.00 \pm 0.04 \pm 0.07$, respectively.

1005 The expected cross-section of WZ+b with 1 associated jet obtained from the fit is
1006 $1.74^{+0.65}_{-0.61}(\text{stat})^{+0.42}_{-0.37}(\text{sys})$ fb with an expected significance of 2.2σ . The expected cross-sectin
1007 of WZ + charm is measured to be $14.6 \pm 2.5(\text{stat}) \pm 2.1(\text{sys})$ fb, with a correlation of -0.23.

1008 For 2-jet events, the fit gives an expected μ value of $1.00^{+0.34}_{-0.33}(\text{stat})^{+0.29}_{-0.28}(\text{sys})$ for WZ +
1009 b. The fitted cross-section modifiers for WZ + charm and WZ + light are $1.00 \pm 0.17 \pm 0.15$ and
1010 $1.00 \pm 0.04 \pm 0.08$, respectively.

1011 The expected WZ + b cross-section in the 2-jet region is $2.46^{+0.83}_{-0.81}(\text{stat})^{+0.073}_{-0.68}(\text{sys})$ fb
1012 with an expected significance of 2.6σ . The 2-jet expected cross-section of WZ + charm is
1013 $12.7 \pm 2.2(\text{stat}) \pm 2.0(\text{sys})$ fb, and the correlation between WZ + charm and WZ + b is -0.26.

1014 15.1 1-jet Fit Results

1015 **The results of the fit are currently blinded.**

1016 The pre-fit yields in each of the regions used in the fit are shown in Table 15.1, and
1017 summarized in Figure 15.1.

Sample	1j, <85% WP	1j, 77%-85% WP	1j, 70%-77% WP	1j, 60%-70% WP	1j, >60% WP	tZ CR
WZ + b - 1j	8.1 ± 1.6	4.7 ± 0.5	4.6 ± 0.4	5.1 ± 0.4	18.2 ± 2.4	4.8 ± 0.6
WZ + c - 1j	260 ± 22	81 ± 6	43.1 ± 3.6	25.8 ± 2.6	9.4 ± 1.8	2.9 ± 0.6
WZ + l - 1j	3090 ± 250	91 ± 13	17 ± 3	4.9 ± 1.6	1.3 ± 0.4	0.2 ± 0.1
WZ + b - 2j	1.10 ± 0.37	0.44 ± 0.11	0.39 ± 0.06	0.62 ± 0.14	2.1 ± 0.5	0.59 ± 0.14
WZ + c - 2j	21 ± 5	5.6 ± 1.2	3.0 ± 0.7	2.0 ± 0.5	0.70 ± 0.20	0.30 ± 0.08
WZ + l - 2j	250 ± 60	5.7 ± 1.6	0.73 ± 0.53	0.31 ± 0.15	0.07 ± 0.06	0.01 ± 0.01
WZ - Other	13 ± 5	1.4 ± 0.4	0.42 ± 0.08	0.2 ± 0.01	0.30 ± 0.05	0.67 ± 0.15
Other VV	6.2 ± 0.6	0.2 ± 0.4	0.2 ± 0.04	0.07 ± 0.1	0.1 ± 0.1	0.1 ± 0.2
ZZ	336 ± 26	17.8 ± 2.1	4.3 ± 0.6	1.7 ± 0.5	0.36 ± 0.08	0.10 ± 0.03
t̄W	1.1 ± 0.2	0.2 ± 0.1	0.3 ± 0.1	0.4 ± 0.1	1.5 ± 0.3	0.7 ± 0.2
t̄Z	6.8 ± 1.2	1.4 ± 0.3	1.0 ± 0.2	1.2 ± 0.2	4.4 ± 0.8	3.2 ± 0.6
Z + jets	169 ± 38	8.9 ± 1.9	3.7 ± 0.8	3.3 ± 0.7	3.2 ± 0.7	0.8 ± 0.17
V + γ	45 ± 28	1.9 ± 2.4	0.1 ± 0.1	0.02 ± 0.01	1.0 ± 0.9	0.02 ± 0.03
tZ	24.3 ± 4.3	5.5 ± 1.1	4.1 ± 0.8	5.9 ± 1.1	10.7 ± 2.0	23 ± 4
tW	1.4 ± 0.8	0.2 ± 0.5	0.0 ± 0.2	0.7 ± 0.6	0.26 ± 0.42	0.39 ± 0.41
WtZ	2.3 ± 1.2	0.6 ± 0.3	0.3 ± 0.21	0.27 ± 0.2	1.1 ± 0.7	0.6 ± 0.5
VVV	12.4 ± 0.5	0.93 ± 0.06	0.35 ± 0.03	0.13 ± 0.02	0.14 ± 0.03	0.02 ± 0.01
VH	40 ± 6	2.6 ± 1.4	0.9 ± 0.8	0.7 ± 0.8	0.5 ± 0.6	0.0 ± 0.0
t̄t	12.1 ± 1.6	2.9 ± 0.6	2.5 ± 0.5	2.8 ± 0.5	11.2 ± 1.4	10.9 ± 1.5
t̄tH	0.24 ± 0.03	0.05 ± 0.01	0.04 ± 0.01	0.06 ± 0.01	0.20 ± 0.03	0.13 ± 0.02
Total	5010 ± 260	227 ± 24	88 ± 12	57 ± 8	76 ± 16	53 ± 8

Table 15: Pre-fit yields in each of the 1-jet fit regions.

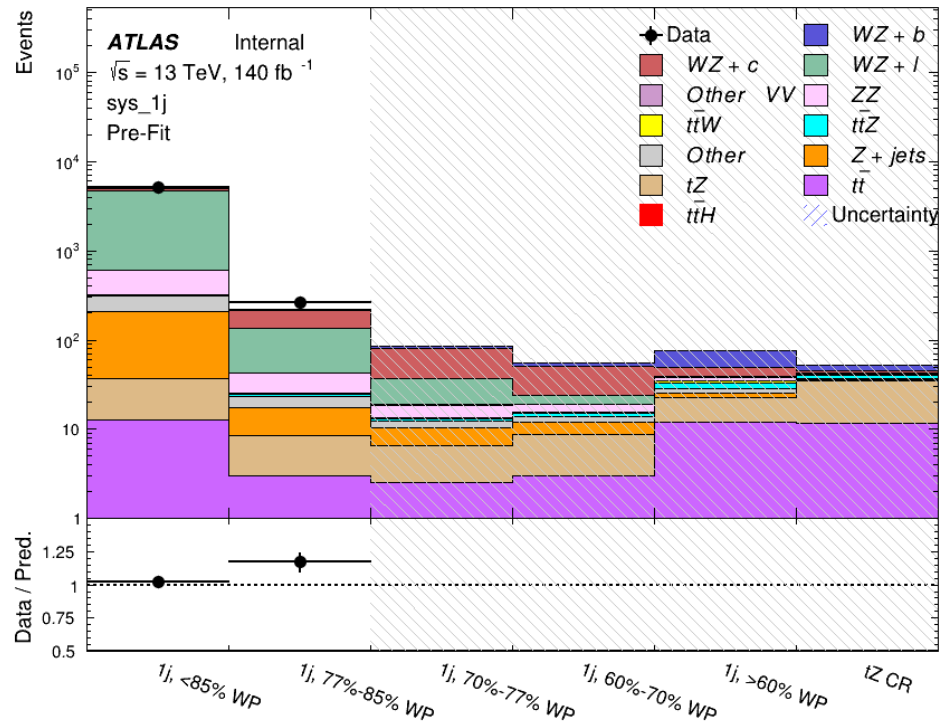


Figure 15.1: Pre-fit summary of the 1-jet fit regions.

1019

The post-fit yields in each region are summarized in Figure 15.1.

1020

	1j, <85% WP	1j, 77%-85% WP	1j, 70%-77% WP	1j, 60%-70% WP	1j, >60% WP	tZ CR
WZ + b	8.1 ± 4.9	4.7 ± 2.0	4.6 ± 2.0	5.1 ± 2.1	18 ± 10	5.0 ± 2.5
WZ + c	260 ± 60	80 ± 14	43 ± 7	26 ± 5	9.4 ± 2.3	2.9 ± 0.7
WZ + l	3090 ± 130	90 ± 11	17.3 ± 2.8	4.9 ± 1.6	1.3 ± 0.4	0.23 ± 0.1
WZ + b - 2j	1.10 ± 0.37	0.44 ± 0.11	0.39 ± 0.06	0.62 ± 0.14	2.1 ± 0.5	0.59 ± 0.1
WZ + c - 2j	21 ± 5	5.6 ± 1.2	3.0 ± 0.7	2.0 ± 0.5	0.70 ± 0.20	0.30 ± 0.0
WZ + l - 2j	250 ± 60	5.7 ± 1.6	0.73 ± 0.53	0.31 ± 0.15	0.07 ± 0.06	0.01 ± 0.0
WZ - Other	13 ± 5	1.4 ± 0.4	0.42 ± 0.08	0.2 ± 0.01	0.30 ± 0.05	0.67 ± 0.1
Other VV	6.2 ± 0.6	0.92 ± 0.07	0.02 ± 0.01	0.01 ± 0.01	0.01 ± 0.01	0.01 ± 0.0
ZZ	346 ± 57	19 ± 5	4.3 ± 0.8	2.7 ± 0.5	2.4 ± 0.1	2.1 ± 0.6
t̄tW	1.09 ± 0.21	0.2 ± 0.1	0.1 ± 0.1	0.4 ± 0.1	1.5 ± 0.3	0.1 ± 0.2
t̄tZ	6.8 ± 1.2	1.4 ± 0.3	1.0 ± 0.2	1.2 ± 0.2	4.4 ± 0.7	3.2 ± 0.5
rare Top	0.14 ± 0.04	0.04 ± 0.02	0.04 ± 0.0	0.1 ± 0.03	0.14 ± 0.04	0.15 ± 0.0
t̄tWW	0.04 ± 0.03	0.01 ± 0.02	0.01 ± 0.01	0.01 ± 0.01	0.01 ± 0.02	0.01 ± 0.0
Z + jets	169 ± 37	8.9 ± 1.9	3.7 ± 0.8	3.3 ± 0.7	3.2 ± 0.7	0.8 ± 0.2
W + jets	0.01 ± 0.01	0.01 ± 0.0				
V + γ	46 ± 28	1.9 ± 2.4	0.1 ± 0.1	0.0 ± 0.2	1.0 ± 0.9	0.0 ± 0.0
tZ	24 ± 4	5.5 ± 1.0	4.1 ± 0.8	5.9 ± 1.1	10.7 ± 1.8	23.3 ± 3.7
tW	1.37 ± 0.82	0.18 ± 0.26	0.01 ± 0.12	0.67 ± 0.64	0.26 ± 0.42	0.39 ± 0.4
WtZ	2.3 ± 1.2	0.6 ± 0.3	0.3 ± 0.2	0.3 ± 0.2	1.1 ± 0.6	0.6 ± 0.3
VVV	12.4 ± 0.4	0.9 ± 0.1	0.4 ± 0.1	0.13 ± 0.02	0.14 ± 0.03	0.02 ± 0.0
VH	40 ± 6	2.6 ± 1.4	0.9 ± 0.8	0.7 ± 0.8	0.4 ± 0.6	0.01 ± 0.0
t̄t	12.1 ± 1.6	2.9 ± 0.6	2.5 ± 0.5	2.8 ± 0.5	11.2 ± 1.5	10.9 ± 1.4
t̄tH	0.24 ± 0.03	0.05 ± 0.01	0.04 ± 0.01	0.06 ± 0.01	0.20 ± 0.03	0.13 ± 0.0
Total	5100 ± 110	227 ± 12	87 ± 6	56.7 ± 4.4	76 ± 9	52.5 ± 4.2

Table 16: Post-fit yields in each of the 1-jet fit regions.

1021

A post-fit summary plot of the 1-jet fitted regions is shown in Figure 15.2:

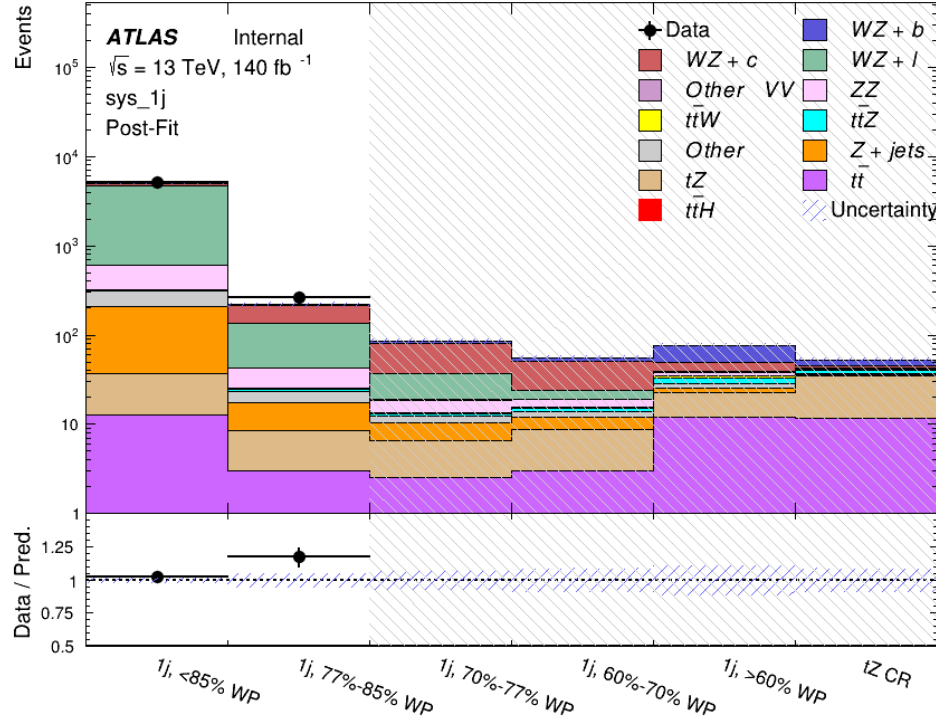


Figure 15.2: Post-fit summary of the 1-jet fit regions.

1022 As described in Section 21, there are 226 systematic uncertainties that are considered
 1023 as NPs in the fit. These NPs are constrained by Gaussian or log-normal probability density
 1024 functions. The latter are used for normalisation factors to ensure that they are always positive.
 1025 The expected number of signal and background events are functions of the likelihood. The prior
 1026 for each NP is added as a penalty term, decreasing the likelihood as it is shifted away from its
 1027 nominal value.

1028 The impact of each NP is calculated by performing the fit with the parameter of interest held
 1029 fixed, varied from its fitted value by its uncertainty, and calculating $\Delta\mu$ relative to the baseline

¹⁰³⁰ fit. The impact of the most significant sources of systematic uncertainties is summarized in Table

¹⁰³¹ [17](#).

Uncertainty Source	$\Delta\mu$	
WZ + light cross-section	0.13	-0.12
WZ + charm cross-section	-0.10	0.12
Jet Energy Scale	0.08	0.13
tZ cross-section	-0.10	0.10
Jet Energy Resolution	-0.10	0.10
Luminosity	-0.08	0.09
Other Diboson + b cross-section	-0.07	0.07
Flavor tagging	0.05	0.05
t <bar>t</bar>	-0.05	0.05
WZ cross-section - QCD scale	-0.04	0.03
Total Systematic Uncertainty	0.28	0.32

Table 17: Summary of the most significant sources of systematic uncertainty on the measurement of WZ + b with exactly one associated jet.

¹⁰³² The ranking and impact of those nuisance parameters with the largest contribution to the

¹⁰³³ overall uncertainty is shown in Figure [15.3](#).

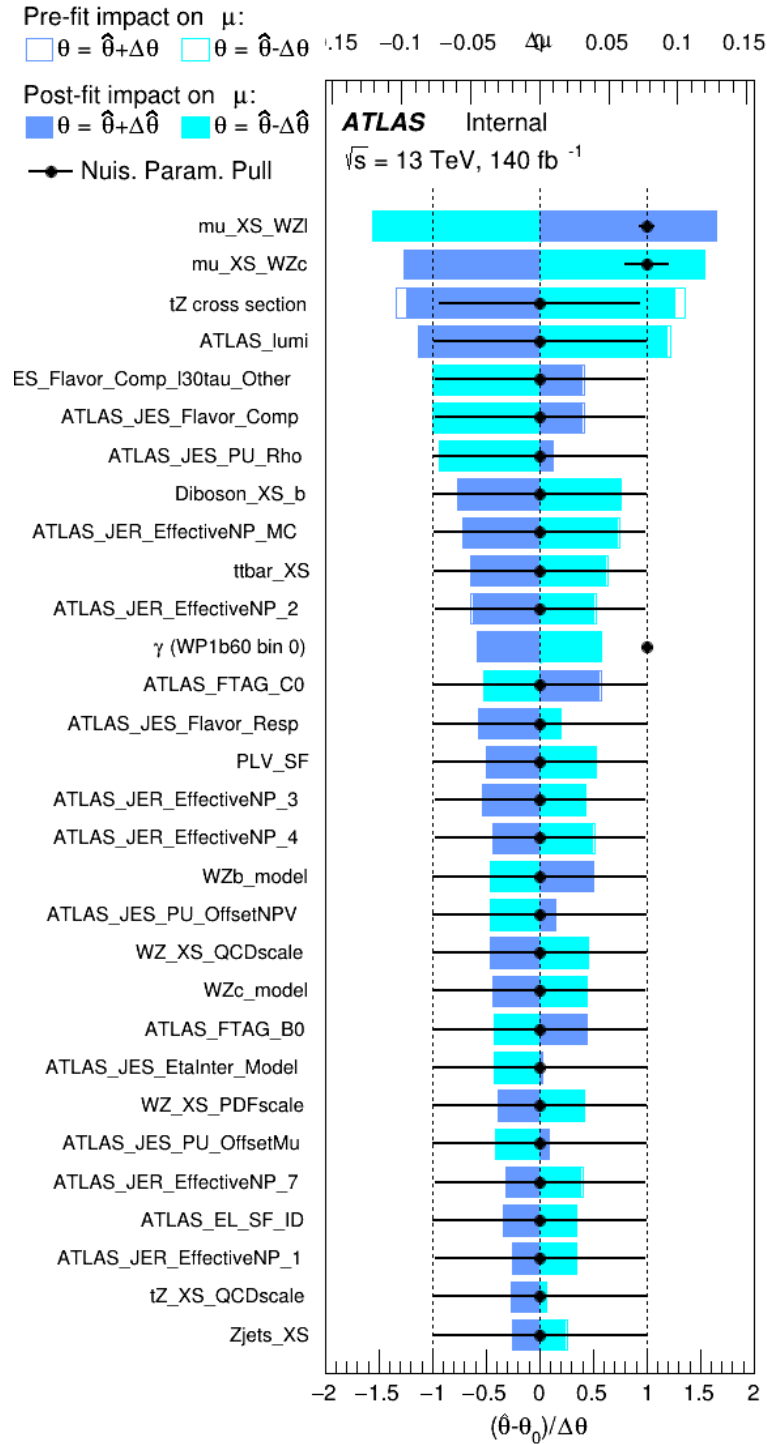


Figure 15.3: Impact of systematic uncertainties on the signal-strength of $WZ + b$ for events with exactly one jet

1034 The large impact of the Jet Energy Scale and Jet Flavor Tagging is unsurprising, as the
 1035 shape of the fit regions depends heavily on the modeling of the jets. The other major sources
 1036 of uncertainty come from background modelling and cross-section uncertainty. The pie charts
 1037 in Figure 15.4 show that for the modelling uncertainties that contribute most correspond to the
 1038 most significant backgrounds.

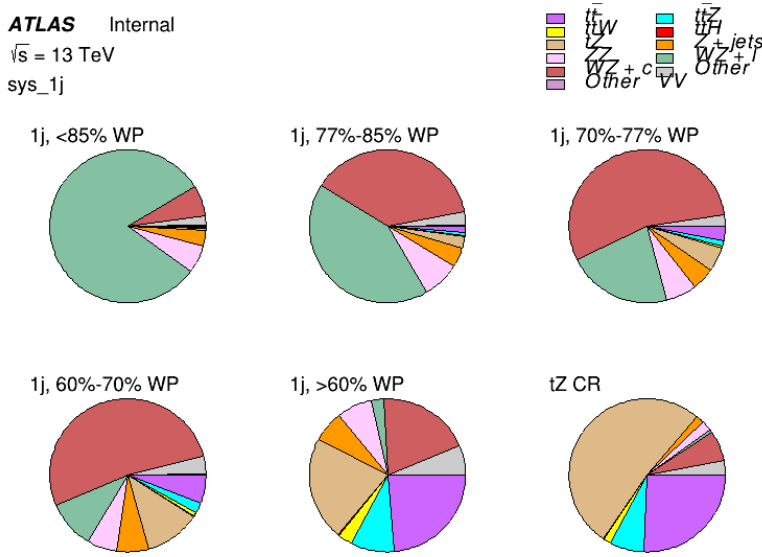


Figure 15.4: Post-fit background composition of the fit regions.

1039 The correlations between these nuisance parameters are summarized in Figure 15.5.

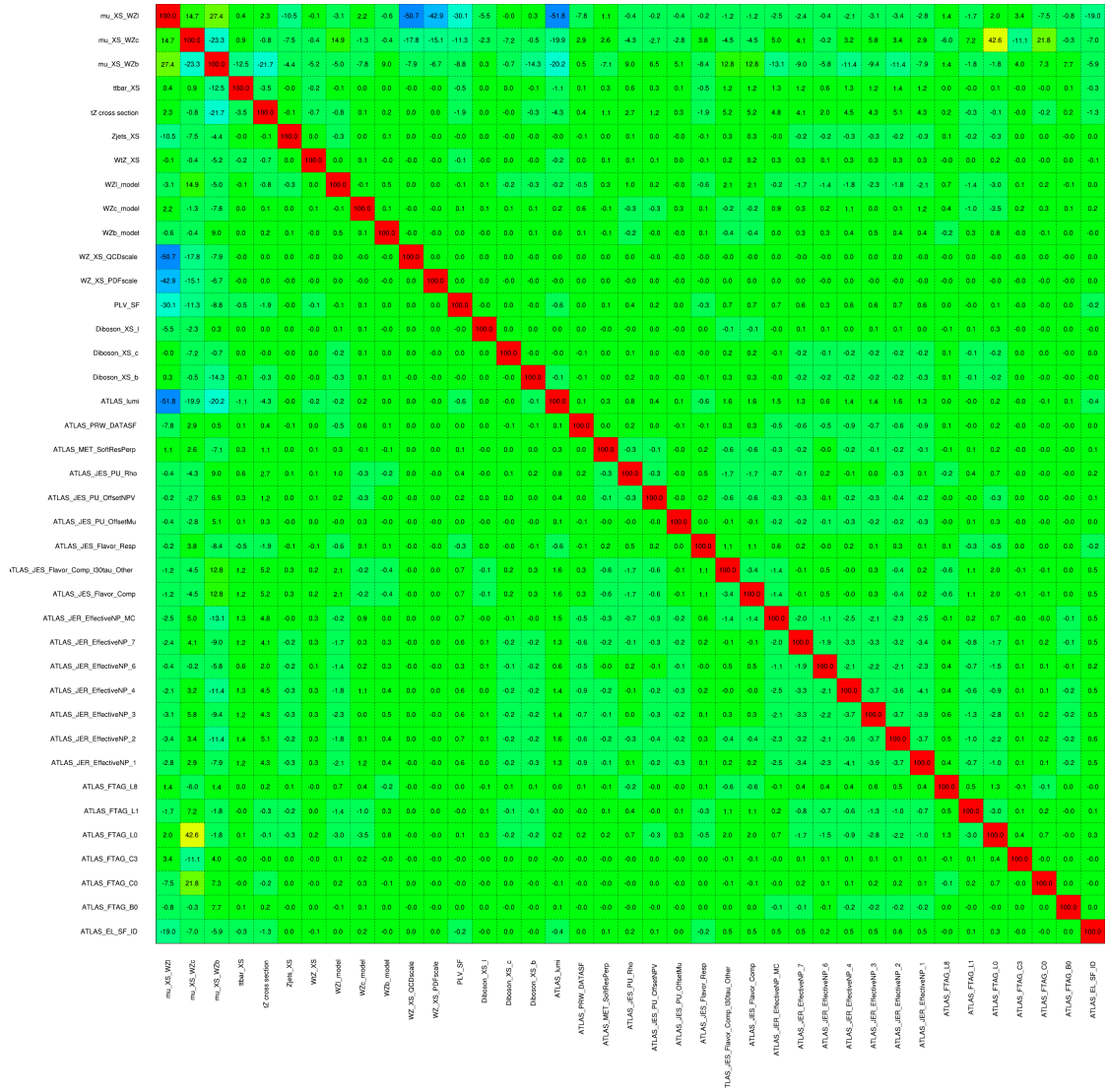


Figure 15.5: Correlations between nuisance parameters

1040 The negative correlations between $\mu_{WZ+charm}$ and μ_{WZ+b} and $\mu_{WZ+light}$ are expected:
1041 WZ + charm is present in both the WZ + b and WZ + light enriched regions, therefore increasing
1042 the fraction of charm requires increasing the fraction of WZ + b and WZ + light. This reasoning
1043 also explains the positive correlation between μ_{WZ+b} and $\mu_{WZ+light}$.

1044 Two of the major backgrounds in the region with the highest purity of WZ + b are tZ and
1045 Other VV + b, explaining the negative correlations between μ_{WZ+b} and the tZ cross section, and
1046 the VV + b cross section.

1047 The high correlation between the luminosity and $\mu_{WZ+light}$ arises from the fact that the
1048 uncertainty on $\mu_{WZ+light}$ is very low (around 4%). Small changes in luminosity cause a change
1049 in the yield of WZ + light that is large compared to its uncertainty, producing a large correlation
1050 between these two parameters.

1051 **15.2 2-jet Fit Results**

1052 **The results of the fit are currently blinded.**

1053 Pre-fit yields in each of the 2-jet fit regions are shown in Figure 15.2.

	2j, <85% WP	2j, 77%-85% WP	2j, 70%-77% WP	2j, 60%-70% WP	2j, >60% WP	tZ CR 2j
WZ + b - 2j	3.1 ± 1.6	6.7 ± 0.5	5.6 ± 0.4	8.0 ± 0.6	31 ± 2	14 ± 1
WZ + c - 2j	180 ± 20	54 ± 6	41 ± 3	24 ± 3	11 ± 2	4.8 ± 0.6
WZ + l - 2j	1250 ± 150	90 ± 14	18 ± 3	5.8 ± 1.4	1.4 ± 0.4	0.25 ± 0.1
WZ + b - 1j	3.4 ± 0.6	1.52 ± 0.35	1.58 ± 0.23	1.95 ± 0.39	6.7 ± 1.1	1.9 ± 0.6
WZ + c - 1j	56 ± 14	17.6 ± 4.0	8.6 ± 2.2	6.3 ± 1.8	3.0 ± 0.9	0.7 ± 0.2
WZ + l - 1j	427 ± 120	24 ± 7	4.7 ± 2.3	1.6 ± 0.7	0.3 ± 0.2	0.01 ± 0.0
WZ - Other	129 ± 29	6.1 ± 4.6	1.2 ± 0.3	0.3 ± 0.2	2.9 ± 0.5	3.6 ± 0.6
Other VV	7.63 ± 0.63	0.6 ± 0.5	0.16 ± 0.03	0.01 ± 0.01	0.1 ± 0.1	0.1 ± 0.1
ZZ	135 ± 20	14.1 ± 3.2	4.7 ± 0.8	4.0 ± 0.6	4.1 ± 0.7	3.1 ± 0.5
t̄tW	0.8 ± 0.2	0.4 ± 0.1	0.5 ± 0.1	0.7 ± 0.2	4.3 ± 0.6	3.9 ± 0.6
t̄tZ	14.7 ± 2.2	5.6 ± 0.8	4.5 ± 0.7	6.5 ± 1.1	25.4 ± 4.0	21.9 ± 3.4
rare Top	0.14 ± 0.04	0.07 ± 0.03	0.03 ± 0.02	0.09 ± 0.03	0.37 ± 0.07	0.6 ± 0.1
t̄tWW	0.04 ± 0.03	0.02 ± 0.02	0.01 ± 0.01	0.01 ± 0.00	0.03 ± 0.03	0.01 ± 0.0
Z + jets	110.0 ± 22.9	9.6 ± 2.0	2.1 ± 0.50	1.6 ± 0.4	5.1 ± 1.1	1.5 ± 0.3
W + jets	0.0 ± 0.0	0.0 ± 0.0	0.0 ± 0.0	0.0 ± 0.0	0.0 ± 0.0	0.0 ± 0.0
V + γ	25 ± 18	0.5 ± 0.2	0.1 ± 0.1	0.1 ± 0.1	0.0 ± 0.02	0.05 ± 0.0
tZ	15.9 ± 2.9	6.9 ± 1.3	5.1 ± 1.0	8.0 ± 1.5	18.7 ± 3.2	36.4 ± 6.1
tW	0.9 ± 0.7	0.2 ± 0.3	0.0 ± 0.1	0.0 ± 0.0	0.8 ± 0.6	0.2 ± 0.2
WtZ	4.9 ± 2.5	1.5 ± 0.8	1.1 ± 0.6	1.3 ± 0.7	4.6 ± 2.4	3.3 ± 1.7
VVV	7.4 ± 0.3	1.0 ± 0.1	0.4 ± 0.1	0.2 ± 0.1	0.13 ± 0.03	0.04 ± 0.0
VH	19.5 ± 4.2	2.8 ± 1.6	0.7 ± 0.7	0.1 ± 0.2	0.0 ± 0.0	0.0 ± 0.0
t̄t	0.7 ± 0.4	0.1 ± 0.1	0.05 ± 0.06	0.15 ± 0.13	0.8 ± 0.5	2.3 ± 1.2
t̄t	6.8 ± 1.0	2.4 ± 0.5	1.8 ± 0.4	3.3 ± 0.6	8.4 ± 1.2	13.6 ± 1.1
t̄tH	0.4 ± 0.1	0.2 ± 0.1	0.16 ± 0.02	0.23 ± 0.03	0.94 ± 0.11	1.03 ± 0.1
Total	2580 ± 160	229 ± 24	89 ± 13	69 ± 11	120 ± 15	108 ± 11

Table 18: Pre-fit yields in each of the 2-jet fit regions.

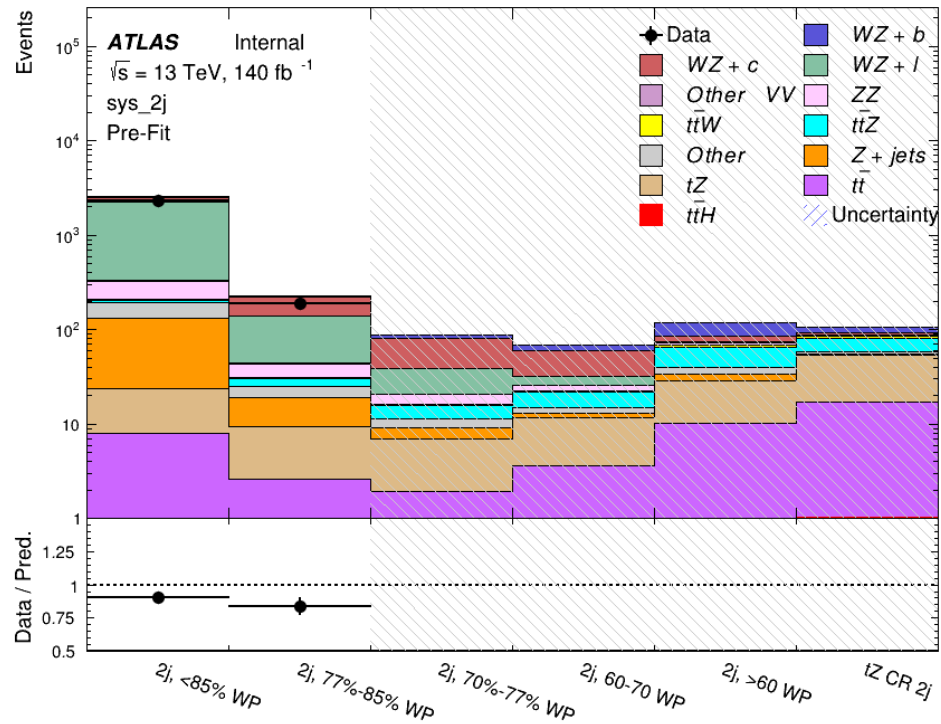


Figure 15.6: Pre-fit summary of the 2-jet fit regions.

1054

The post-fit yields in each region are summarized in Figure 15.2.

	2j, <85% WP	2j, 77%-85% WP	2j, 70%-77% WP	2j, 60%-70% WP	2j, >60% WP	tZ CR 2j
WZ + b	13 ± 6	6.7 ± 2.9	5.8 ± 2.5	8.0 ± 3.5	31 ± 13	14 ± 5
WZ + c	260 ± 60	77 ± 15	41 ± 8	26 ± 5	10.9 ± 2.4	4.8 ± 1.1
WZ + l	1860 ± 90	90 ± 12	17.6 ± 2.8	5.8 ± 1.3	1.4 ± 0.4	0.3 ± 0.2
WZ + b - 1j	3.4 ± 0.6	1.52 ± 0.35	1.58 ± 0.23	1.95 ± 0.39	6.7 ± 1.1	1.9 ± 0.6
WZ + c - 1j	56 ± 14	17.6 ± 4.0	8.6 ± 2.2	6.3 ± 1.8	3.0 ± 0.9	0.7 ± 0.2
WZ + l - 1j	427 ± 120	24 ± 7	4.7 ± 2.3	1.6 ± 0.7	0.3 ± 0.2	0.01 ± 0.0
WZ - Other	129 ± 29	6.1 ± 4.6	1.2 ± 0.3	0.3 ± 0.2	2.9 ± 0.5	3.6 ± 0.6
Other VV	7.6 ± 0.6	0.3 ± 0.3	0.3 ± 0.1	0.1 ± 0.06	0.03 ± 0.02	0.1 ± 0.1
ZZ	145 ± 30	11.3 ± 4.4	2.7 ± 1.6	1.0 ± 0.3	4.0 ± 0.1	2.4 ± 0.1
t̄tW	0.8 ± 0.2	0.4 ± 0.1	0.54 ± 0.12	0.74 ± 0.15	4.3 ± 0.6	3.9 ± 0.6
t̄tZ	14.7 ± 2.2	5.6 ± 0.8	4.5 ± 0.7	6.5 ± 1.0	25.4 ± 3.9	21.9 ± 3.0
rare Top	0.14 ± 0.04	0.07 ± 0.03	0.03 ± 0.02	0.09 ± 0.03	0.4 ± 0.1	0.6 ± 0.1
t̄tWW	0.04 ± 0.03	0.02 ± 0.02	0.01 ± 0.01	0.01 ± 0.01	0.03 ± 0.03	0.01 ± 0.0
Z + jets	110 ± 23	9.6 ± 2.0	2.1 ± 0.5	1.6 ± 0.4	5.1 ± 1.1	1.5 ± 0.3
W + jets	0.0 ± 0.0	0.0 ± 0.0				
V + γ	25 ± 19	0.5 ± 0.2	0.1 ± 0.1	0.13 ± 0.14	0.0 ± 0.02	0.05 ± 0.0
tZ	15.9 ± 2.7	6.9 ± 1.2	5.1 ± 0.9	8.0 ± 1.4	18.7 ± 3.0	36 ± 6
tW	0.1 ± 0.7	0.2 ± 0.3	0.0 ± 0.1	0.0 ± 0.0	0.8 ± 0.6	0.2 ± 0.2
WtZ	4.9 ± 2.5	1.5 ± 0.8	1.1 ± 0.6	1.3 ± 0.7	4.6 ± 2.3	3.3 ± 1.7
VVV	7.4 ± 0.3	1.0 ± 0.1	0.36 ± 0.03	0.19 ± 0.03	0.13 ± 0.03	0.04 ± 0.0
VH	19 ± 4	2.8 ± 1.6	0.7 ± 0.7	0.1 ± 0.2	0.0 ± 0.0	0.0 ± 0.0
t̄t	6.8 ± 1.0	2.4 ± 0.5	1.8 ± 0.4	3.3 ± 0.6	8.4 ± 1.2	13.6 ± 1.7
t̄tH	0.40 ± 0.05	0.19 ± 0.03	0.16 ± 0.02	0.23 ± 0.03	0.94 ± 0.11	1.03 ± 0.1
Total	2580 ± 60	229 ± 11	89 ± 6	69.1 ± 4.1	120 ± 10	108 ± 6

Table 19: Post-fit yields in each of the 2-jet fit regions.

1055

A post-fit summary of the fitted regions is shown in Figure 15.7:

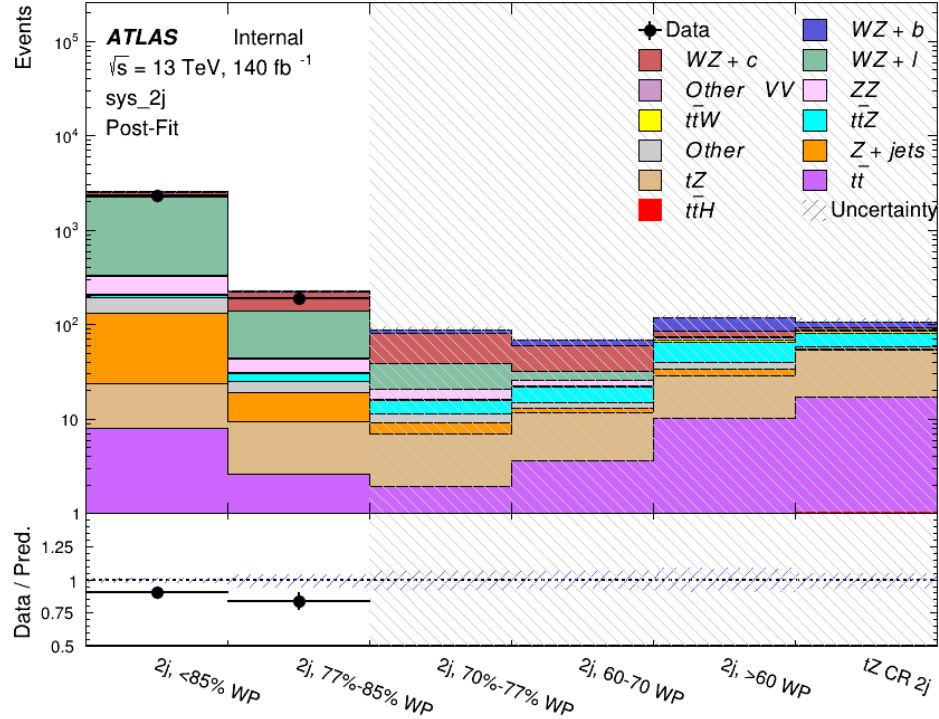


Figure 15.7: Post-fit summary of the fit over 2-jet regions.

1056 The same set of systematic uncertainties consider for the 1-jet fit are included in the 2-jet
 1057 fit as well. The impact of the most significant systematic uncertainties is summarized in Table
 1058 20.

Uncertainty Source	$\Delta\mu$	
WZ + c cross-section	-0.1	0.14
Luminosity	-0.11	0.12
tZ cross-section	-0.11	0.11
Jet Energy Scale	-0.11	0.11
ttZ cross-section - QCD scale	-0.08	0.09
WZ + l cross-section	0.08	-0.07
WtZ cross-section	-0.07	0.07
Flavor tagging	0.05	0.05
Other VV + b cross-section	-0.05	0.05
Jet Energy Resolution	-0.04	0.04
Total	0.29	0.31

Table 20: Summary of the most significant sources of systematic uncertainty on the measurement of WZ + b 2-jet events.

1059 The ranking and impact of those nuisance parameters with the largest contribution to the
 1060 overall uncertainty is shown in Figure 15.8.

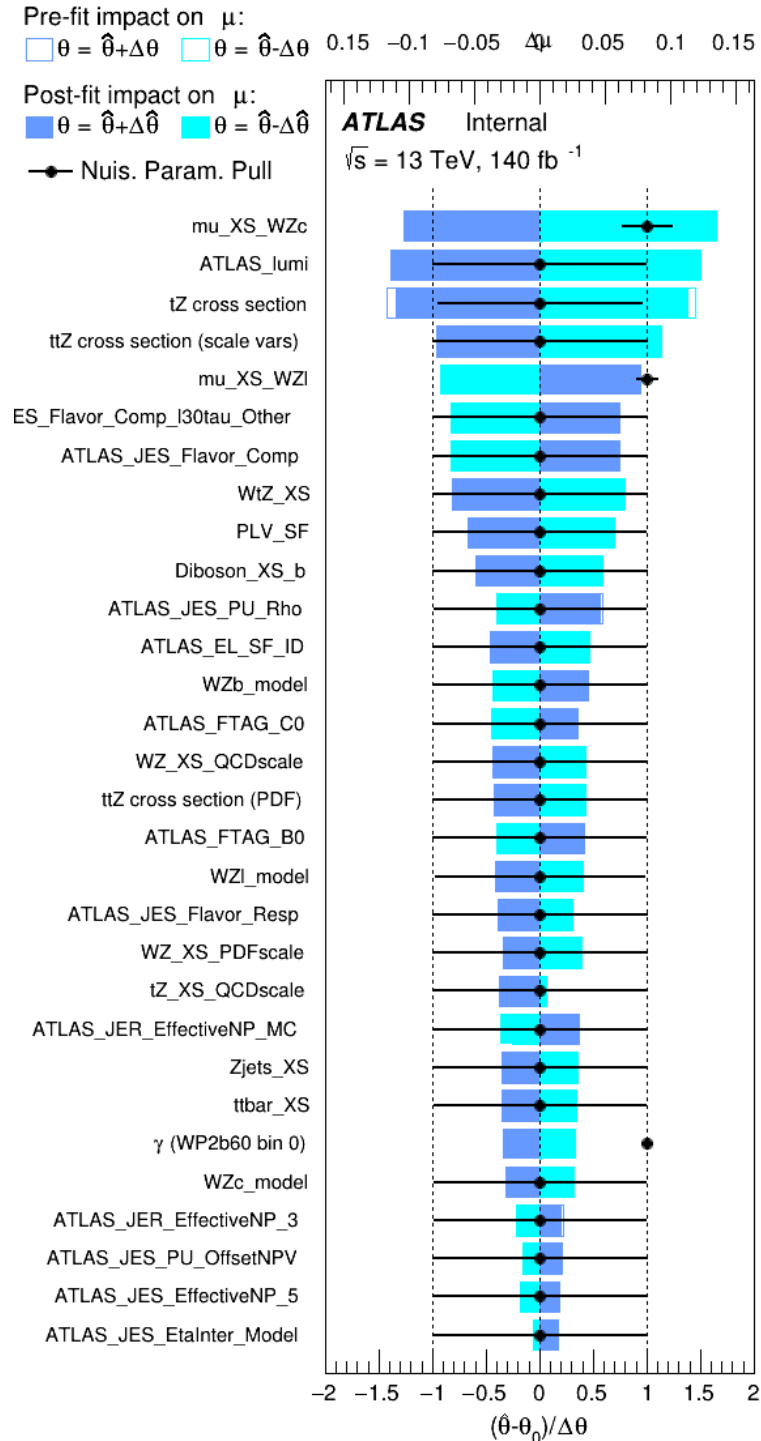


Figure 15.8: Impact of systematic uncertainties on the signal-strength of $WZ + b$ in 2-jet events.

1061 The large impact of the Jet Energy Scale and Jet Flavor Tagging is unsurprising, as the
 1062 shape of the fit regions depends heavily on the modeling of the jets. The other major sources
 1063 of uncertainty come from background modelling and cross-section uncertainty. The pie charts
 1064 in Figure 15.9 show that for the modelling uncertainties that contribute most correspond to the
 1065 most significant backgrounds.

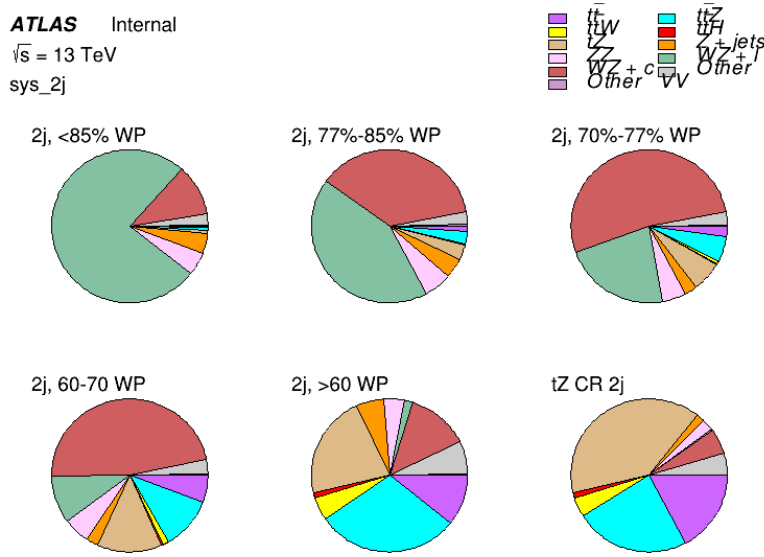


Figure 15.9: Post-fit background composition of the 2-jet fit regions.

1066 The correlations between these nuisance parameters are summarized in Figure 15.10.



Figure 15.10: Correlations between nuisance parameters in the 2-jet fit

1067

As in the 1-jet case, no significant, unexpected correlations are found between nuisance

parameters.

1069 Part V**1070 Differential Studies of $t\bar{t}H$ Multilepton****1071 16 Data and Monte Carlo Samples**

1072 For both data and Monte Carlo (MC) simulations, samples were prepared in the `xAOD` format,
1073 which was used to produce a `xAOD` based on the `HIGG8D1` derivation framework. This framework
1074 was designed for the main $t\bar{t}H$ multi-lepton analysis. Because this analysis targets events with
1075 multiple light leptons, as well as tau hadrons, this framework skims the dataset of any events that
1076 do not meet at least one of the following requirements:

- 1077 • at least two light leptons within a range $|\eta| < 2.6$, with leading lepton $p_T > 15$ GeV and
1078 subleading lepton $p_T > 5$ GeV
- 1079 • at least one light lepton with $p_T > 15$ GeV within a range $|\eta| < 2.6$, and at least two hadronic
1080 taus with $p_T > 15$ GeV.

1081 Samples were then generated from these `HIGG8D1` derivations using `AnalysisBase` version
1082 21.2.127. A ptag of `p4133` was used for MC samples, and `p4134` for data.

1083 16.1 Data Samples

1084 The study uses proton-proton collision data collected by the ATLAS detector from 2015 through
1085 2018, which represents an integrated luminosity of 139 fb^{-1} and an energy of $\sqrt{s} = 13 \text{ TeV}$. All
1086 data used in this analysis was included in one of the following Good Run Lists:

- 1087 • data15_13TeV.periodAllYear_DetStatus-v79-repro20-02_DQDefects-00-02-02
1088 _PHYS_StandardGRL_All_Good_25ns.xml
- 1089 • data16_13TeV.periodAllYear_DetStatus-v88-pro20-21_DQDefects-00-02-04
1090 _PHYS_StandardGRL_All_Good_25ns.xml
- 1091 • data17_13TeV.periodAllYear_DetStatus-v97-pro21-13_Unknown_PHYS_StandardGRL
1092 _All_Good_25ns_Triggerno17e33prim.xml
- 1093 • data18_13TeV.periodAllYear_DetStatus-v102-pro22-04_Unknown_PHYS_StandardGRL
1094 _All_Good_25ns_Triggerno17e33prim.xml

1095 16.2 Monte Carlo Samples

1096 Several Monte Carlo (MC) generators were used to simulate both signal and background pro-
1097 cesses. For all of these, the effects of the ATLAS detector are simulated in Geant4. The specific
1098 event generator used for each of these MC samples is listed in Table 21.

Table 21: The configurations used for event generation of signal and background processes, including the event generator, matrix element (ME) order, parton shower algorithm, and parton distribution function (PDF).

Process	Event generator	ME order	Parton Shower	PDF
t̄H	MG5_AMC (MG5_AMC)	NLO (NLO)	PYTHIA 8 (HERWIG++)	NNPDF 3.0 NLO [14] (CT10 [15])
t̄W	MG5_AMC (SHERPA 2.1.1)	NLO (LO multileg)	PYTHIA 8 (SHERPA)	NNPDF 3.0 NLO (NNPDF 3.0 NLO)
t̄(Z/γ* → ll)	MG5_AMC	NLO	PYTHIA 8	NNPDF 3.0 NLO
VV	SHERPA 2.2.2	MEPS NLO	SHERPA	CT10
t̄t	POWHEG-BOX v2 [16]	NLO	PYTHIA 8	NNPDF 3.0 NLO
t̄γ	MG5_AMC	LO	PYTHIA 8	NNPDF 2.3 LO
tZ	MG5_AMC	LO	PYTHIA 6	CTEQ6L1
tHqb	MG5_AMC	LO	PYTHIA 8	CT10
tHW	MG5_AMC (SHERPA 2.1.1)	NLO (LO multileg)	HERWIG++ (SHERPA)	CT10 (NNPDF 3.0 NLO)
tWZ	MG5_AMC	NLO	PYTHIA 8	NNPDF 2.3 LO
t̄t̄, t̄t̄t̄	MG5_AMC	LO	PYTHIA 8	NNPDF 2.3 LO
t̄W+W-	MG5_AMC	LO	PYTHIA 8	NNPDF 2.3 LO
s-, t-channel, Wt single top	POWHEG-BOX v1 [17]	NLO	PYTHIA 6	CT10
qqVV, VVV				
Z → l+l-	SHERPA 2.2.1	MEPS NLO	SHERPA	NNPDF 3.0 NLO

1099 As explained in detail in [5], the t̄W contribution predicted by MC is found disagree
 1100 significantly with what is observed in data. While an effort is currently being undertaken to
 1101 measure t̄W more accurately, the approach used by the 80 fb⁻¹ t̄H analysis is used for this
 1102 analysis: A normalization factor of 1.68 is applied to the MC estimate of t̄W. Additionally,
 1103 systematic uncertainties are applied to account for this modelling discrepancy, as outlined in
 1104 Section 21.

1105 While the main t̄H analysis uses a more sophisticated data-driven approach to estimating
 1106 the contribution of events with non-prompt leptons (or "fakes"), at the time of this note this

1107 strategy has not been completely developed for the full Run-2 dataset. Therefore, the non-prompt
1108 contribution is estimated with MC, while applying normalization corrections and systematic
1109 uncertainties derived from data driven techniques developed for the 80 fb^{-1} $t\bar{t}H/t\bar{t}W$ analysis
1110 [5]. The primary contribution to the non-prompt lepton background is from $t\bar{t}$ production, with
1111 $V+jets$ and single-top as much smaller sources. Likelihood fits over several control regions
1112 enriched with these non-prompt backgrounds are fit to data in order to derive normalization
1113 factors for these backgrounds. The specific normalization factors and uncertainties applied to
1114 the non-prompt contributions are listed in Section 21.

1115 The specific DSIDs used in the analysis are listed below:

Sample	DSID
t̄H	345873-5, 346343-5
VV	364250-364254, 364255, 363355-60, 364890
t̄W	413008
t̄Z	410156, 410157, 410218-20
low mass t̄Z	410276-8
Rare Top	410397, 410398, 410399
single Top	410658-9, 410644-5
three Top	304014
four Top	410080
t̄WW	410081
Z + jets	364100-41
low mass Z + jets	364198-215
W + jets	364156-97
Vγ	364500-35
tZ	410560
tW	410013-4
WtZ	410408
VVV	364242-9
VH	342284-5
WtH	341998
t̄tγ	410389
t̄t	410470

Table 22: List of Monte Carlo samples by data set ID used in the analysis.

¹¹¹⁶ 17 Object Reconstruction

¹¹¹⁷ All analysis channels considered in this note share a common object selection for leptons and

¹¹¹⁸ jets, as well as a shared trigger selection.

1119 **17.1 Trigger Requirements**

1120 Events are required to be selected by dilepton triggers, as summarized in Table 23.

Dilepton triggers (2015)	
$\mu\mu$ (asymm.)	HLT_mu18_mu8noL1
ee (symm.)	HLT_2e12_lhloose_L12EM10VH
$e\mu, \mu e$ (\sim symm.)	HLT_e17_lhloose_mu14
Dilepton triggers (2016)	
$\mu\mu$ (asymm.)	HLT_mu22_mu8noL1
ee (symm.)	HLT_2e17_lhvloose_nod0
$e\mu, \mu e$ (\sim symm.)	HLT_e17_lhloose_nod0_mu14
Dilepton triggers (2017)	
$\mu\mu$ (asymm.)	HLT_mu22_mu8noL1
ee (symm.)	HLT_2e24_lhvloose_nod0
$e\mu, \mu e$ (\sim symm.)	HLT_e17_lhloose_nod0_mu14
Dilepton triggers (2018)	
$\mu\mu$ (asymm.)	HLT_mu22_mu8noL1
ee (symm.)	HLT_2e24_lhvloose_nod0
$e\mu, \mu e$ (\sim symm.)	HLT_e17_lhloose_nod0_mu14

Table 23: List of lowest p_T -threshold, un-prescaled dilepton triggers used for 2015-2018 data taking.

1121 **17.2 Light Leptons**

1122 Electron candidates are reconstructed from energy clusters in the electromagnetic calorimeter
1123 that are associated with charged particle tracks reconstructed in the inner detector [18]. Electron
1124 candidates are required to have $p_T > 10$ GeV and $|\eta_{\text{cluster}}| < 2.47$. Candidates in the transition
1125 region between different electromagnetic calorimeter components, $1.37 < |\eta_{\text{cluster}}| < 1.52$, are
1126 rejected. A multivariate likelihood discriminant combining shower shape and track information

1127 is used to distinguish prompt electrons from nonprompt leptons, such as those originating from
 1128 hadronic showers. Electron candidate are also required to pass TightLH identification.

1129 To further reduce the non-prompt contribution, the track of each electron is required to
 1130 originate from the primary vertex; requirements are imposed on the transverse impact parameter
 1131 significance ($|d_0|/\sigma_{d_0}$) and the longitudinal impact parameter ($|\Delta z_0 \sin \theta_\ell|$).

1132 Muon candidates are reconstructed by combining inner detector tracks with track segments
 1133 or full tracks in the muon spectrometer [19]. Muon candidates are required to have $p_T > 10$ GeV
 1134 and $|\eta| < 2.5$. Muons are required to Medium ID requirements.

1135 All leptons are required to pass a non-prompt BDT selection developed by the main
 1136 $t\bar{t}H - ML/t\bar{t}W$ analysis, described in detail in [5]. Optimized working points and scale factors
 1137 for this BDT are taken from that analysis. This BDT and the WPs used are summarized in
 1138 Appendix .1,

1139 17.3 Jets

1140 Jets are reconstructed from calibrated topological clusters built from energy deposits in the
 1141 calorimeters [21], using the anti- k_t algorithm with a radius parameter $R = 0.4$. Particle Flow, or
 1142 PFlow, jets are used in the analysis, which are hadronic objects reconstructed using information
 1143 from both the tracker and the calorimeter. Jets with energy contributions likely arising from noise
 1144 or detector effects are removed from consideration [22], and only jets satisfying $p_T > 25$ GeV

1145 and $|\eta| < 2.5$ are used in this analysis. For jets with $p_T < 60$ GeV and $|\eta| < 2.4$, a jet-track
1146 association algorithm is used to confirm that the jet originates from the selected primary vertex,
1147 in order to reject jets arising from pileup collisions [23].

1148 17.4 B-tagged Jets

1149 Each analysis channel used in this analysis includes b-jets in the final state. These are identified
1150 using the DL1r b-tagging algorithm, which uses jet vertex and kinematic information to distin-
1151 guish heavy and light flavored jets. These features are used as inputs to a neural network, the
1152 output of which is used to form calibrated working points (WPs) based on how likely a jet is to
1153 have originated from a b-quark. This analysis uses the 70% DL1r WP - implying an efficiency of
1154 70% for truth b-jets - for selecting b-tagged jets.

1155 17.5 Missing Transverse Energy

1156 Because all $t\bar{t}H - ML$ channels considered include multiple neutrinos, missing transverse
1157 energy (E_T^{miss}) is present in each event. The missing transverse momentum vector is defined as
1158 the inverse of the sum of the transverse momenta of all reconstructed physics objects as well
1159 as remaining unclustered energy, the latter of which is estimated from low- p_T tracks associated
1160 with the primary vertex but not assigned to a hard object [24].

1161 17.6 Overlap removal

1162 To avoid double counting objects and remove leptons originating from decays of hadrons, overlap
 1163 removal is performed in the following order: any electron candidate within $\Delta R = 0.1$ of another
 1164 electron candidate with higher p_T is removed; any electron candidate within $\Delta R = 0.1$ of a muon
 1165 candidate is removed; any jet within $\Delta R = 0.3$ of an electron candidate is removed; if a muon
 1166 candidate and a jet lie within $\Delta R = \min(0.4, 0.04 + 10[\text{GeV}]/p_T(\text{muon}))$ of each other, the jet
 1167 is kept and the muon is removed.

1168 This algorithm is applied to the preselected objects. The overlap removal procedure is
 1169 summarized in Table 24.

Keep	Remove	Cone size (ΔR)
electron	electron (low p_T)	0.1
muon	electron	0.1
electron	jet	0.3
jet	muon	$\min(0.4, 0.04 + 10[\text{GeV}]/p_T(\text{muon}))$
electron	tau	0.2

Table 24: Summary of the overlap removal procedure between electrons, muons, and jets.

1170 18 Higgs Momentum Reconstruction

1171 Reconstructing the momentum of the Higgs boson is a particular challenge for channels with
 1172 leptons in the final state: Because all channels include at least two neutrinos in the final state, the
 1173 Higgs can never be fully reconstructed. However, the momentum spectrum can be well predicted
 1174 by a neural network when provided with the four-vectors of the Higgs Boson decay products, as

1175 shown in Section 18.1. With this in mind, several layers of MVAs are used to reconstruction the
1176 Higgs momentum.

1177 The first layer is a model designed to select which jets are most likely to be the b-jets that
1178 came from the top decay, detailed in Section 18.2. As described in Section 18.3, the kinematics
1179 of these jets and possible Higgs decay products are fed into the second layer, which is designed
1180 to identify the decay products of the Higgs Boson itself. The kinematics of the particles this
1181 layer identifies as most likely to have originated from the Higgs decay are then fed into yet
1182 another neural-network, which predicts the momentum of the Higgs (18.4). For the 3l channel,
1183 an additional MVA is used to determine the decay mode of the Higgs boson in the 3l channel
1184 (18.5).

1185 Models are trained on Monte Carlo simulations of $t\bar{t}H$ events generated using MG5_AMC.
1186 Specifically, events DSIDs 346343-5, 345873-5, and 345672-4 are used for training in order to
1187 increase the statistics of the training sample.

1188 For all of these models, the Keras neural network framework, with Tensorflow 2.0 as the
1189 backend, is used, and the number of hidden layers and nodes are determined using grid search
1190 optimization. Each neural network uses the LeakyReLU activation function, a learning rate of
1191 0.01, and the Adam optimization algorithm, as alternatives are found to either decrease or have
1192 no impact on performance. Batch normalization is applied after each layer in order to stabilize
1193 the model and decrease training time. For the classification algorithms (b-jet matching, Higgs
1194 reconstruction, and 3l decay identification) binary-cross entropy is used as the loss function,

1195 while the p_T reconstruction algorithm uses MSE.

1196 The specific inputs features used for each model are arrived at through a process of trial
1197 and error - features considered potentially useful are tried, and those that are found to increase
1198 performance are included. While each model includes a relatively large number of features,
1199 some using upwards of 30, this inclusive approach is found to maximize the performance of each
1200 model while decreasing the variance compared to a reduced number of inputs. Each input feature
1201 is validated by comparing MC simulations to 80 fb^{-1} of data, as shown in the sections below.

1202 **18.1 Higgs Decay Product Identification**

1203 Machine Learning algorithms are trained to identify the decay products of the Higgs Boson using
1204 MC simulations of $t\bar{t}H$ events. The kinematics of the reconstructed physics objects, as well as
1205 event level variables, are used as inputs, with the parent ID taken from the truth record used to
1206 label the data. The objects considered include light leptons and jets.

1207 Reconstructed physics objects are matched to particle level objects, in order to identify the
1208 parent particle of these reconstructed objects. Reconstructed jets are matched to truth jets based
1209 on the requirements that the reco jet and truth jet fall within $\Delta R < 0.4$, and the two objects have
1210 a p_T that agrees within 10%. Truth level and reco level leptons are required to have the same
1211 flavor, a $\Delta R < 0.1$, and p_T that agree within 10%. Events where no match can be found between
1212 the particle level decay products of the Higgs and the reconstructed objects are not included in
1213 training.

1214 Leptons considered as possible Higgs and top decay candidates are required to pass the
1215 selection described in Section 17.2. For jets, however, it is found that a large fraction that
1216 originate from either the top decay or the Higgs decay fall outside the selection described in
1217 Section 17.3. Specifically, jets from the Higgs decay tend to be soft, with 32% having $p_T <$
1218 25 GeV. Therefore jets with $p_T < 15$ GeV are considered as possible candidates in the models
1219 described below. By contrast, less than 5% of the jets originating from the Higgs fall below
1220 this p_T threshold. The jets are found to be well modeled even down to this low p_T threshold,
1221 as shown in Section 20.1. The impact of using different p_T selection for the jet candidates is
1222 considered in detail in Section A.5. As they are expected to originate from the primary vertex,
1223 jets are also required to pass a JVT cut.

1224 18.2 b-jet Identification

1225 Including the kinematics of the b-jets that originate from the top decay is found to improve the
1226 identification of the Higgs decay products, and improve the accuracy with which the Higgs
1227 momentum can be reconstructed. Because these b-jets are reconstructed by the detector with
1228 high efficiency (just over 90% of the time), and can be identified relatively consistently, the first
1229 step in reconstructing the Higgs is selecting the b-jets from the top decay.

1230 Exactly two b-jets are expected in the final state of $t\bar{t}H - ML$ events. However, in both
1231 the 3l and 2lSS channels, only one or more b-tagged jets are required (where the 70% DL1r b-tag
1232 working point is used). Therefore, for events which have exactly one, or more than two, b-tagged

1233 jets, deciding which combination of jets correspond to the top decay is non-trivial. Further,
1234 events with 1 b-tagged jet represent just over half of all $t\bar{t}H - ML$ events. Of those, both b-jets
1235 are reconstructed by the detector 75% of the time. Therefore, rather than adjusting the selection
1236 to require exactly 2 b-tagged jets, and losing more than half of the signal events, a neural network
1237 is used to predict which pair of jets is most likely to correspond to truth b-jets.

1238 Once the network is trained, all possible pairings of jets are fed into the model, and the pair
1239 of jets with the highest output score are taken to be b-jets in successive steps of the analysis.

1240 **18.2.1 2lSS Channel**

1241 For the 2lSS channel, the input features shown in Table 25 are used for training. Here j_0 and j_1
1242 are the two jet candidates, while l_0 and l_1 are the two leptons in the event, both ordered by p_T . jet
1243 DL1r is an integer corresponding to the calibrated b-tagging working points reached by each jet,
1244 where 5 represents the tightest working point and 1 represents the loosest. The variables nJets
1245 DL1r 60% and nJets DL1r 85% represent the number of jets in the event passing the 60% and
1246 85% b-tag working points, respectively.

jet p_T 0	jet p_T 1	Lepton p_T 0
Lepton p_T 1	jet η 0	jet η 1
$\Delta R(j_0)(j_1)$	$M(j_0 j_1)$	$\Delta R(l_0)(j_0)$
$\Delta R(l_0)(j_1)$	$\Delta R(l_1)(j_0)$	$\Delta R(l_1)(j_1)$
$M(l_0 j_0)$	$M(l_0 j_1)$	$M(l_1 j_0)$
$M(l_1 j_1)$	jet DL1r 0	jet DL1r 1
nJets OR DL1r 85	nJets OR DL1r 60	$\Delta R(j_0 l_0)(j_1 l_1)$
$\Delta R(j_0 l_1)(j_1 l_0)$	$p_T(j_0 j_1 l_0 l_1 E_T^{\text{miss}})$	$M(j_0 j_1 l_0 l_1 E_T^{\text{miss}})$
$\Delta\phi(j_0)(E_T^{\text{miss}})$	$\Delta\phi(j_1)(E_T^{\text{miss}})$	HT jets
nJets	E_T^{miss}	

Table 25: Input features used in the b-jet identification algorithm for the 2lSS channel

1247 As there are far more incorrect combinations than correct ones, by a factor of more than
 1248 20:1, the training set is resampled to reduce the fraction of incorrect combinations. A random
 1249 sample of 5 million incorrect entries are used for training, along with close 1 million correct
 1250 entries. 10% of the dataset is set aside for testing, leaving around 5 million datapoints for
 1251 training.

1252 The difference between the distributions for a few of these features for the "correct" (i.e.
 1253 both jets are truth b-jets), and "incorrect" combinations are shown in Figure 18.1. The correct and
 1254 incorrect contributions are scaled to the same integral, so as to better demonstrate the differences
 1255 in the distributions.

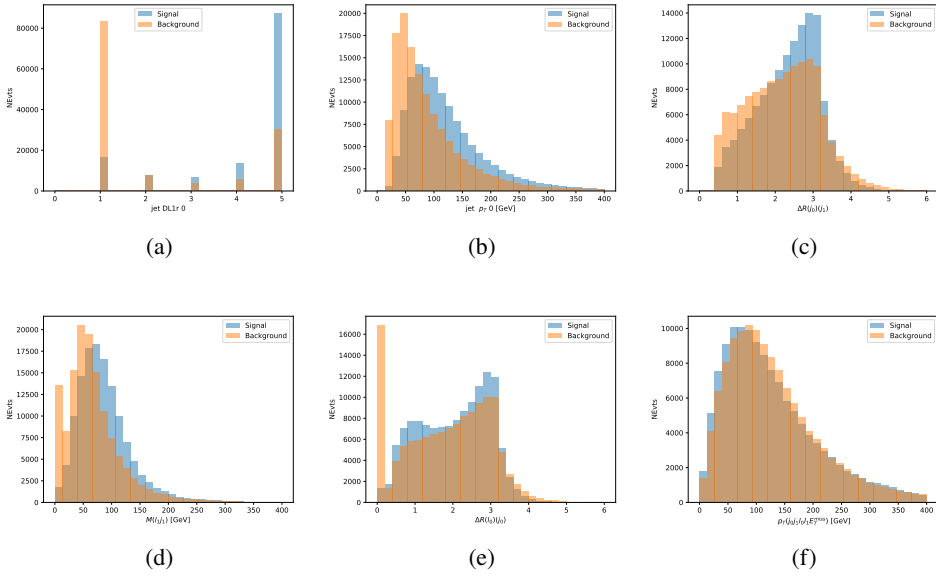


Figure 18.1: Input features for top2lSS training. The signal in blue represents events where both jet candidates are truth b-jets from top decays, and the orange is all other combinations. Each are scaled to the same number of events. (a) shows the DL1r working point of leading jet, (b) shows the p_T of the leading jet, (c) shows the ΔR of the two jets, (d) the invariant mass of lepton 1 and jet 1, (e) the ΔR of lepton 0 and jet 0, and (f) the p_T of both jets, both leptons, and the E_T^{miss} .

1256 The modeling of these inputs is validated against data, with Figure 18.2 showing good
 1257 general agreement between data and MC. Plots for the complete list of features can found in
 1258 Section A.

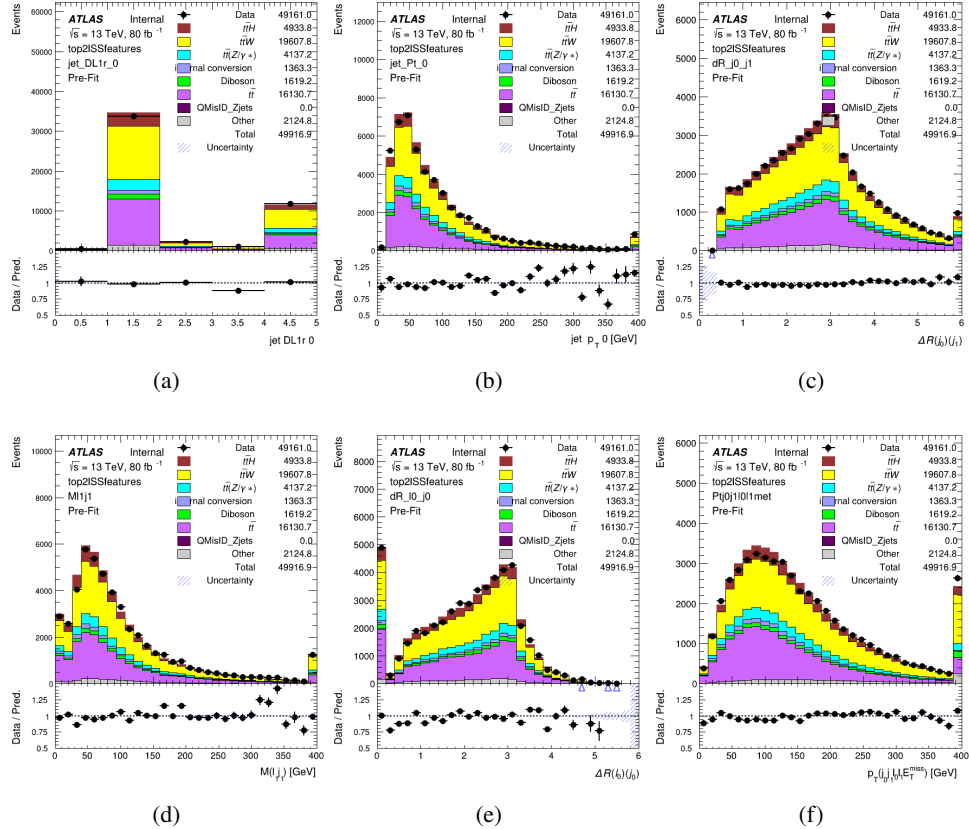


Figure 18.2: Data/MC comparisons of input features for top2ISS training for 80 fb^{-1} of data. (a) shows the DL1r working point of leading jet, (b) shows the p_T of the leading jet, (c) shows the ΔR of the two jets, (d) the invariant mass of lepton 1 and jet 1, (e) the ΔR of lepton 0 and jet 0, and (f) the p_T of both jets, both leptons, and the E_T^{miss} .

1259 Based on the results of grid search evaluation, the optimal architecture is found to include
1260 5 hidden layers with 40 nodes each. No regularizer or dropout is added to the network, as
1261 overfitting is found to not be an issue. The output score distribution as well as the ROC curve for
1262 the trained model are shown in Figure 18.2.1. The model is found to identify the correct pairing
1263 of jets for 73% of 2lSS signal events on test data.

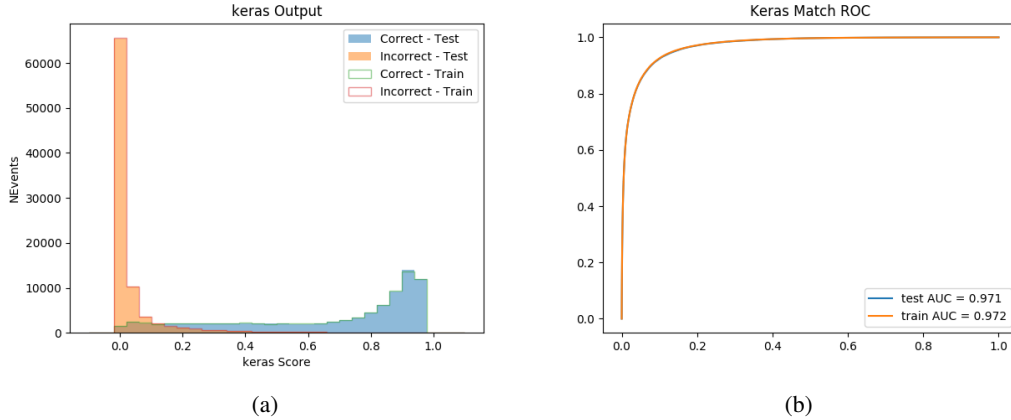


Figure 18.3: Results of the b-jet identification algorithm for the 2lSS channel, showing (a) the output score of the NN for correct and incorrect combinations of jets. (b) the ROC curve of the output, showing background rejection as a function of signal efficiency

1264 For point of comparison, a "naive" approach to identify b-jets is used as well: The two
 1265 jets which pass the highest DL1r b-tag working point are assumed to be the b-jets from the top
 1266 decay. In the case that multiple jets meet the same b-tag working point, the jet with higher p_T is
 1267 used. This method identifies the correct jet pair 65% of the time.

1268 The accuracy of the model for different values of n-bjets, compared to this naive approach,
 1269 is shown in Table 26.

b-jet Selection	Neural Network	Naive
1 b-jet	58.6%	42.1%
2 b-jets	88.4%	87.1%
≥ 3 b-jets	61.7%	53.3%
Overall	73.9%	67.2%

Table 26: Accuracy of the NN in identifying b-jets from tops in 2lSS events, overall and split by the number of b-tagged jets in the event, compared to the accuracy of taking the two highest b-tagged jets.

1270 18.2.2 3l Channel

¹²⁷¹ The input features used in the 3l channel are listed in Table 27, with the same naming convention
¹²⁷² as the 2lSS channel.

jet p_T 0	jet p_T 1	jet η 0
jet η 1	Lepton p_T 0	Lepton p_T 1
Lepton p_T 2	$\Delta R(j_0)(j_1)$	$M(j_0 j_1)$
$\Delta R(l_0)(j_0)$	$\Delta R(l_1)(j_0)$	$\Delta R(l_2)(j_0)$
$\Delta R(l_0)(j_1)$	$\Delta R(l_1)(j_1)$	$\Delta R(l_2)(j_1)$
$M(l_0 j_0)$	$M(l_1 j_0)$	$M(l_2 j_0)$
$M(l_0 j_1)$	$M(l_1 j_1)$	$M(l_2 j_1)$
$\Delta R(j_0 l_0)(j_1 l_1)$	$\Delta R(j_0 l_0)(j_1 l_2)$	$\Delta R(j_0 l_1)(j_1 l_0)$
$\Delta R(j_0 l_2)(j_1 l_0)$	jet DL1r 0	jet DL1r 1
$p_T(j_0 j_1 l_0 l_1 l_2 E_T^{\text{miss}})$	$M(t j_0 j_1 l_0 l_1 l_2 E_T^{\text{miss}})$	$\Delta\phi(j_0)(E_T^{\text{miss}})$
$\Delta\phi(j_1)(E_T^{\text{miss}})$	HT Lepton	HT jets
nJets	E_T^{miss}	nJets OR DL1r 85
nJets OR DL1r 60		

Table 27: Input features for the b-jet identification algorithm in the 3l channel.

¹²⁷³ A few of these features are shown in Figure 18.4, comparing the distributions for correct
¹²⁷⁴ and incorrect combinations of jets.

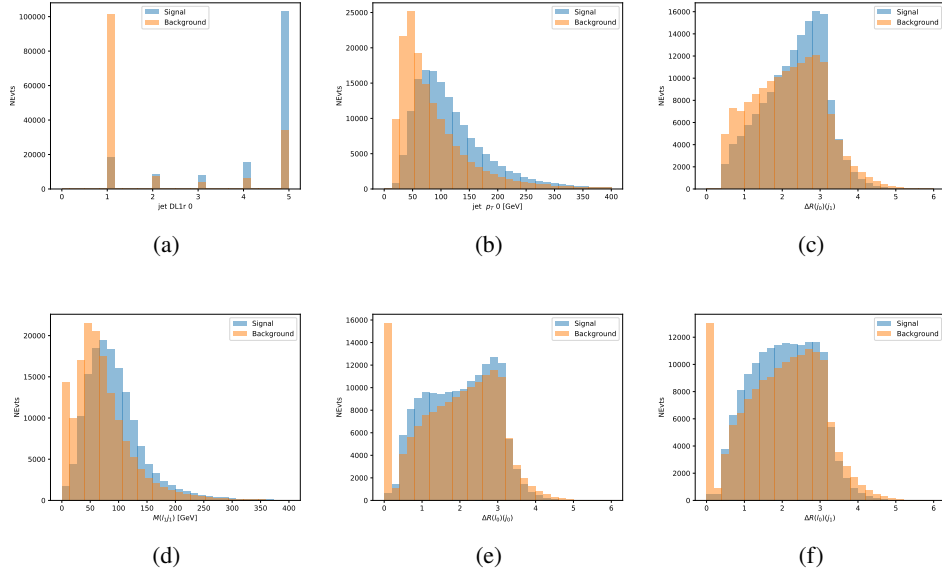


Figure 18.4: Input features for top3l training. The signal in blue represents events where both jet candidates are truth b-jets from top decays, and the orange is all other combinations. Scaled to the same number of events. (a) show the DL1r WP of jet 0, (b) the p_T of jet 0, (c) ΔR between jet 0 and jet 1, (d) the invariant mass of lepton 1 and jet 1, (e) ΔR between lepton 0 and jet 0, and (f) ΔR between lepton 0 and jet 1

1275

The modeling of these inputs is validated against data, with Figure 18.5 showing good

1276

general agreement between data and MC. Plots for the complete list of features can found in

1277

[Section A](#).

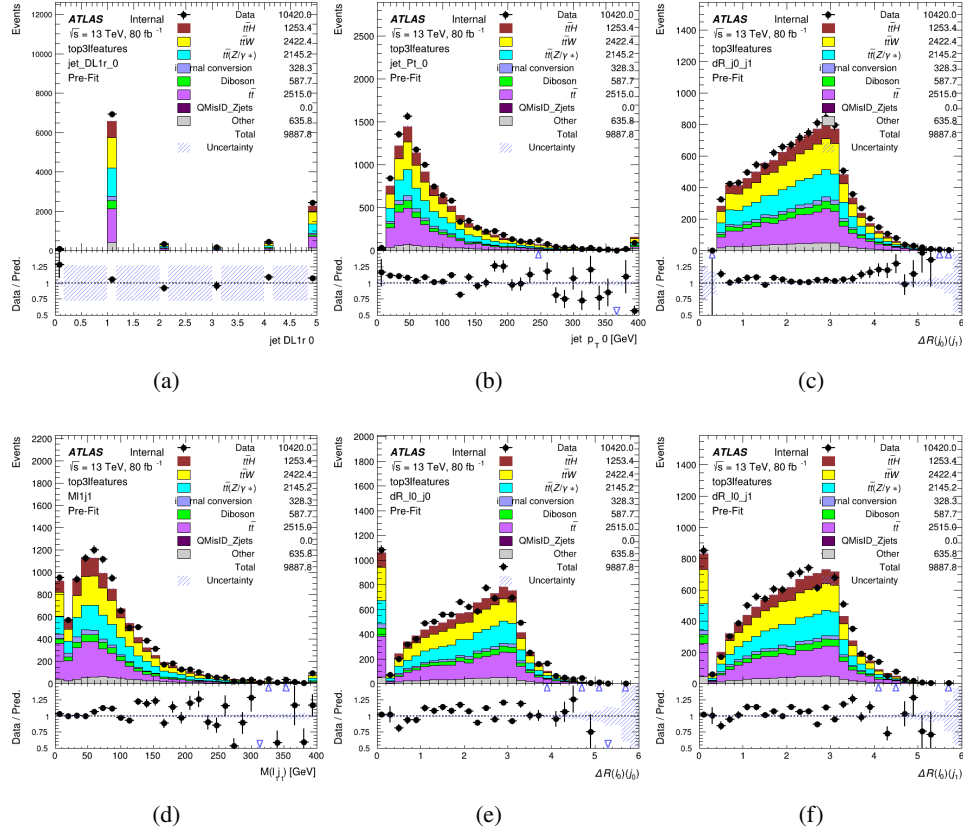


Figure 18.5: Data/MC comparisons of input features for top3l training for 80 fb^{-1} of data. (a) show the DL1r WP of jet 0, (b) the p_T of jet 0, (c) ΔR between jet 0 and jet 1, (d) the invariant mass of lepton 1 and jet 1, (e) ΔR between lepton 0 and jet 0, and (f) ΔR between lepton 0 and jet 1

Again, the dataset is downsized to reduce the ratio of correct and incorrect combination from 20:1, to 5:1. Around 7 million events are used for training, with 10% set aside for testing. Based on the results of grid search evaluation, the optimal architecture is found to include 5 hidden layers with 60 nodes each. The output score distribution as well as the ROC curve for the trained model are shown in Figure 18.2.2.

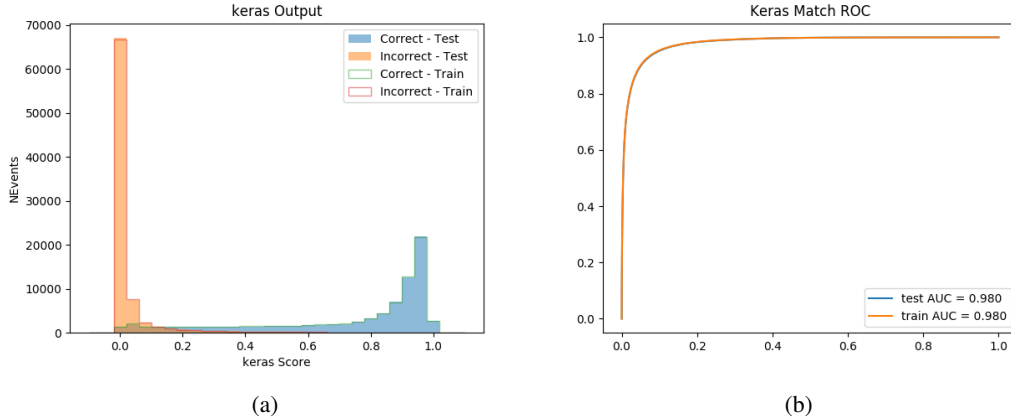


Figure 18.6: Results of the b-jet identification algorithm for the 3l channel, showing (a) the output score of the NN for correct and incorrect combinations of jets. (b) the ROC curve of the output, showing background rejection as a function of signal efficiency

1283 This procedure is found to identify the correct pairing of jets for nearly 80% of 3l signal
 1284 events. The accuracy of the model is summarized in Table 28.

Table 28: Accuracy of the NN in identifying b-jets from tops, compared to the naive method of taking the highest b-tagged jets.

	NN	Naive
1 b-jet	69.0%	48.9%
2 b-jets	89.6%	88.3%
≥ 3 b-jets	55.7%	52.3%
Overall	79.8%	70.2%

1285 18.3 Higgs Reconstruction

1286 Techniques similar to the b-jet identification algorithms are employed to select the decay products
 1287 of the Higgs: kinematics of all possible combinations of reconstructed objects are fed into a neural
 1288 network to determine which of those is most likely to be the decay products of the Higgs.

1289 Again separate models are used for the 2lSS and 3l channels, while the 3l channel has now
1290 been split into two: $t\bar{t}H$ events with three leptons in the final state include both instances where
1291 the Higgs decays into a lepton (and a neutrino) and a pair of jets, and instances where the Higgs
1292 decays to two leptons.

1293 3l events are therefore categorized as either semi-leptonic (3lS) or fully-leptonic (3lF). In
1294 the semi-leptonic case the reconstructed decay products consist of two jets and a single lepton.
1295 For the fully-leptonic case, the decay products include 2 of the three leptons associated with the
1296 event. For training the models, events are separated into these two categories using truth level
1297 information. A separate MVA, described in Section 18.5, is used to make this distinction at reco
1298 level and determine which model to use.

1299 For all channels, the models described in Section 18.2 are used to identify b-jet candidates,
1300 whose kinematics are used to identify the Higgs decay products. These jets are not considered
1301 as possible candidates for the Higgs decay, justified by the fact that these models are found to
1302 misidentify jets from the Higgs decay as jets from the top decay less than 1% of the time.

1303 18.3.1 2lSS Channel

1304 For the 2lSS channel, the Higgs decay products include one light lepton and two jets. The neural
1305 network is trained on the kinematics of different combinations of leptons and jets, as well as the
1306 b-jets identified in Section 18.2, with the specific input features listed in Table 29.

Lepton p_T H	Lepton p_T T	jet p_T 0
jet p_T 1	top p_T 0	top p_T 1
top η 0	top η 1	jet η 0
jet η 1	jet Phi 0	jet Phi 1
Lepton η H	Lepton heta T	$\Delta R(j_0)(j_1)$
$\Delta R(l_H)(j_0)$	$\Delta R(l_H)(j_1)$	$M(j_0 j_1)$
$M(l_H j_0)$	$M(l_H j_1)$	$\Delta R(l_H)(b_0)$
$\Delta R(l_H)(b_1)$	$\Delta R(l_T)(b_0)$	$\Delta R(l_T)(b_1)$
$\Delta R(j_0 j_1)(l_H)$	$\Delta R(j_0 j_1)(l_T)$	$\Delta R(j_0 j_1)(b_0)$
$\Delta R(j_0 j_1)(b_1)$	$\Delta R(j_0)(b_0)$	$\Delta R(j_0)(b_1)$
$\Delta R(j_1)(b_0)$	$\Delta R(j_1)(b_1)$	$M(j_0 j_1 l_H)$
$p_T(j_0 j_1 l_H l_T b_0 b_1 E_T^{\text{miss}})$	topScore	E_T^{miss}
nJets	HT jets	

Table 29: Input features used to identify the Higgs decay products in 2ISS events

1307 Here j_0 and j_1 , and l_H are the jet and lepton decay candidates, respectively. The other
 1308 lepton in the event is labeled l_T , as it is assumed to have come from the decay of one of the top
 1309 quarks. b_0 and b_1 are the two b-jets identified by the b-jet identification algorithm. The b-jet
 1310 Reco Score is the output of the b-jet reconstruction algorithm.

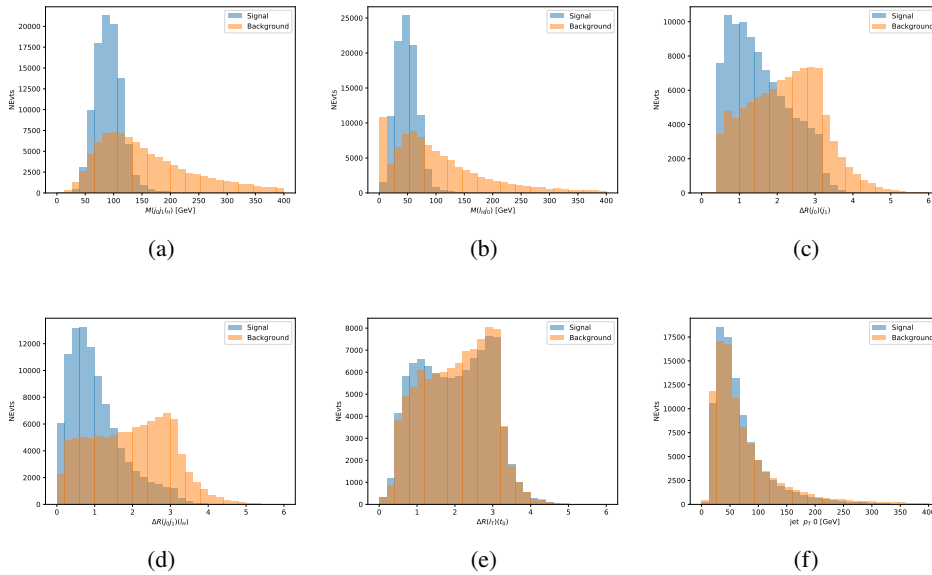


Figure 18.7: Input features for higgs2lSS training. The signal in blue represents events where both jet candidates are truth b-jets from top decays, and the orange is all other combinations. Scaled to the same number of events. (a) shows the invariant mass of the two jet candidates and the lepton candidate, (b) the invariant mass of jet 0 and the lepton candidate, (c) ΔR between the jet candidates, (d) ΔR between jet 0 + jet 1 and the lepton candidate, (e) ΔR between the lepton from the top and the leading b-jet, (f) the p_T of jet 0.

1311 The modeling of these inputs is validated against data, with Figure 18.2 showing good
 1312 general agreement between data and MC. Plots for the complete list of features can found in
 1313 Section A.

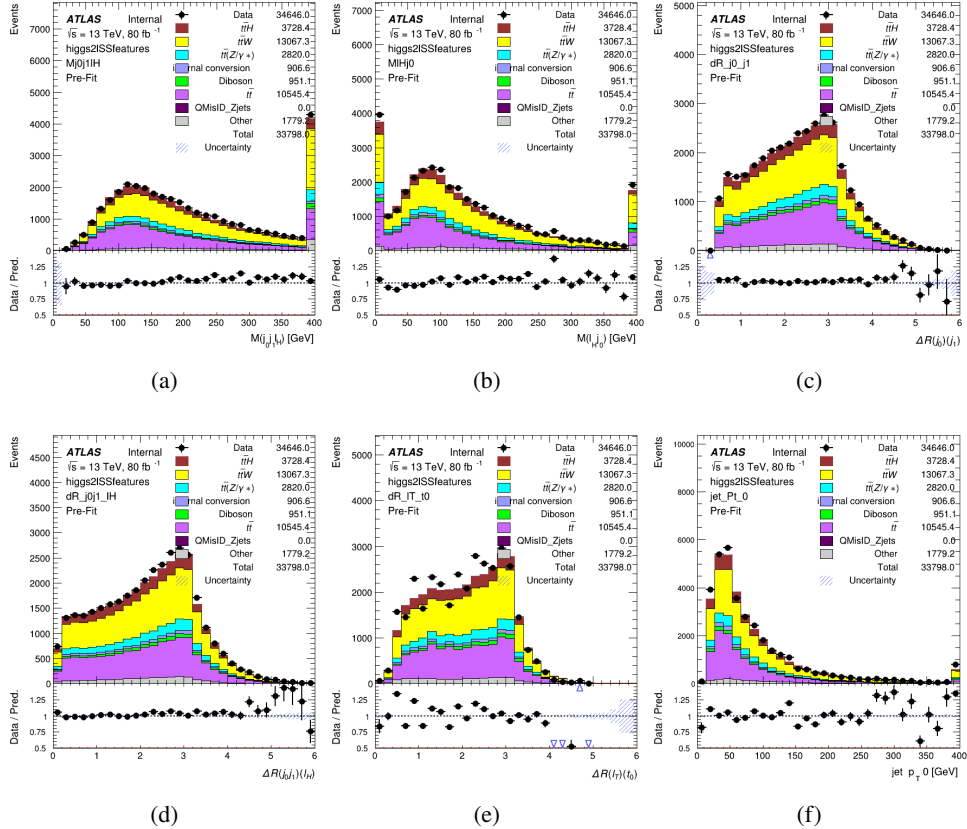


Figure 18.8: Data/MC comparisons of input features for higgs2lSS training for 80 fb^{-1} of data. (a) shows the invariant mass of the two jet candidates and the lepton candidate, (b) the invariant mass of jet 0 and the lepton candidate, (c) ΔR between the jet candidates, (d) ΔR between jet 0 + jet 1 and the lepton candidate, (e) ΔR between the lepton from the top and the leading b-jet, (f) the p_T of jet 0.

1314 A neural network consisting of 7 hidden layers with 60 nodes each is trained on around 2
 1315 million events, with an additional 200,000 reserved for testing the model. In order to compensate
 1316 for large number of incorrect combinations, these have been downsampled such that the correct
 1317 combinations represent over 10% of the training set. The output of the NN is summarized in
 1318 Figure 18.3.1.

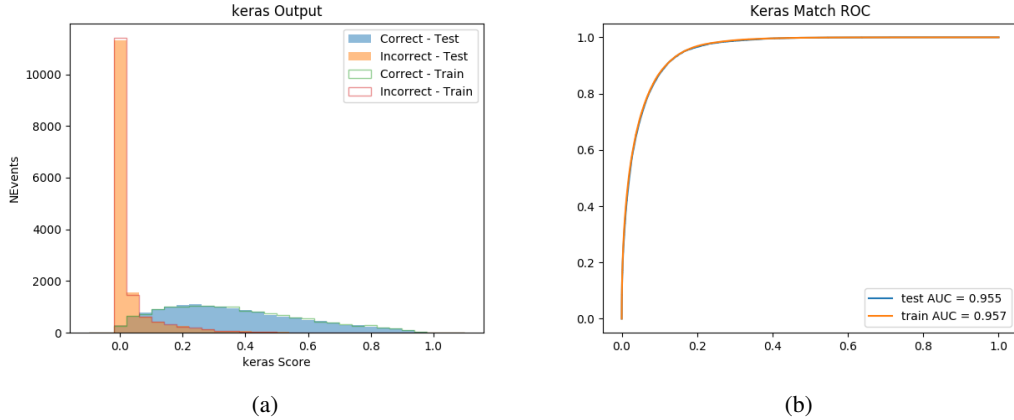


Figure 18.9: Result of the Higgs reconstruction algorithm in the 2lSS channel, showing (a) the output score of the NN for correct and incorrect combinations of jets scaled to an equal number of events, and (b) the ROC curve of the output, showing background rejection as a function of signal efficiency

1319 The neural network identifies the correct combination 55% of the time. It identifies the
 1320 correct lepton 85% of the time, and selects the correct lepton and at least one of the correct jets
 1321 81% of the time.

1322 18.3.2 3l Semi-leptonic Channel

1323 For 3l $t\bar{t}H$ where the Higgs decay semi-leptonically, the decay products include one of the three
 1324 leptons and two jets. In this case, the other two leptons originated from the decay of the tops,
 1325 meaning the opposite-sign (OS) lepton cannot have come from the Higgs. This leaves only the two
 1326 same-sign (SS) leptons as possible Higgs decay products.

Lepton $p_T H$	Lepton $p_T T_0$	Lepton $p_T T_1$
jet $p_T 0$	jet $p_T 1$	top $p_T 0$
top $p_T 1$	jet $\eta 0$	jet $\eta 1$
jet $\phi 0$	jet $\phi 1$	$\Delta R(j_0)(j_1)$
$M(j_0 j_1)$	$\Delta R(l_H)(j_0)$	$\Delta R(l_H)(j_1)$
$\Delta R(j_0 j_1)(l_H)$	$\Delta R(j_0 j_1)(l_{T_1})$	$\Delta R(l_{T_0})(l_{T_1})$
$\Delta R(l_H)(l_{T_1})$	$M(j_0 j_1 l_{T_0})$	$M(j_0 j_1 l_{T_1})$
$M(j_0 j_1 l_H)$	$\Delta R(j_0 j_1 l_H)(l_{T_0})$	$\Delta R(j_0 j_1 l_H)(l_{T_1})$
$\Delta\phi(j_0 j_1 l_H)(E_T^{\text{miss}})$	$p_T(j_0 j_1 l_H l_{T_0} l_{T_1} b_0 b_1 E_T^{\text{miss}})$	$M(j_0 j_1 b_0)$
$M(j_0 j_1 b_1)$	$\Delta R(l_{T_0})(b_0)$	$\Delta R(l_{T_0})(b_1)$
$\Delta R(l_{T_1})(b_0)$	$\Delta R(l_{T_1})(b_1)$	$\Delta R(j_0)(b_0)$
$\Delta R(j_0)(b_1)$	$\Delta R(j_1)(b_0)$	$\Delta R(j_1)(b_1)$
topScore	MET	HT jets
nJets		

Table 30: Input features used to identify the Higgs decay products in 3lS events

1327 Here j_0 and j_1 , and l_H are the jet and lepton decay candidates, respectively. The other
 1328 two leptons in the event are labeled as l_{T0} and l_{T1} . b_0 and b_1 are the two b-jets identified by
 1329 the b-jet identification algorithm. The b-jet Reco Score is the output of the Higgs reconstruction
 1330 algorithm.

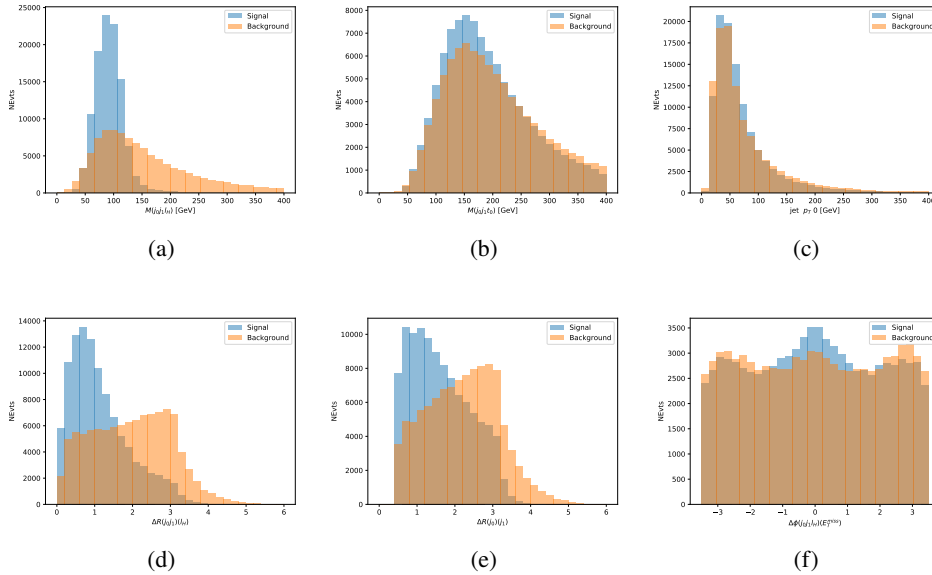


Figure 18.10: Input features for higgs3lS training. The signal in blue represents events where both jet candidates are truth b-jets from top decays, and the orange is all other combinations. Scaled to the same number of events.

1331 The modeling of these inputs is validated against data, with Figure 18.11 showing good
 1332 general agreement between data and MC. Plots for the complete list of features can found in
 1333 appendix A.1.

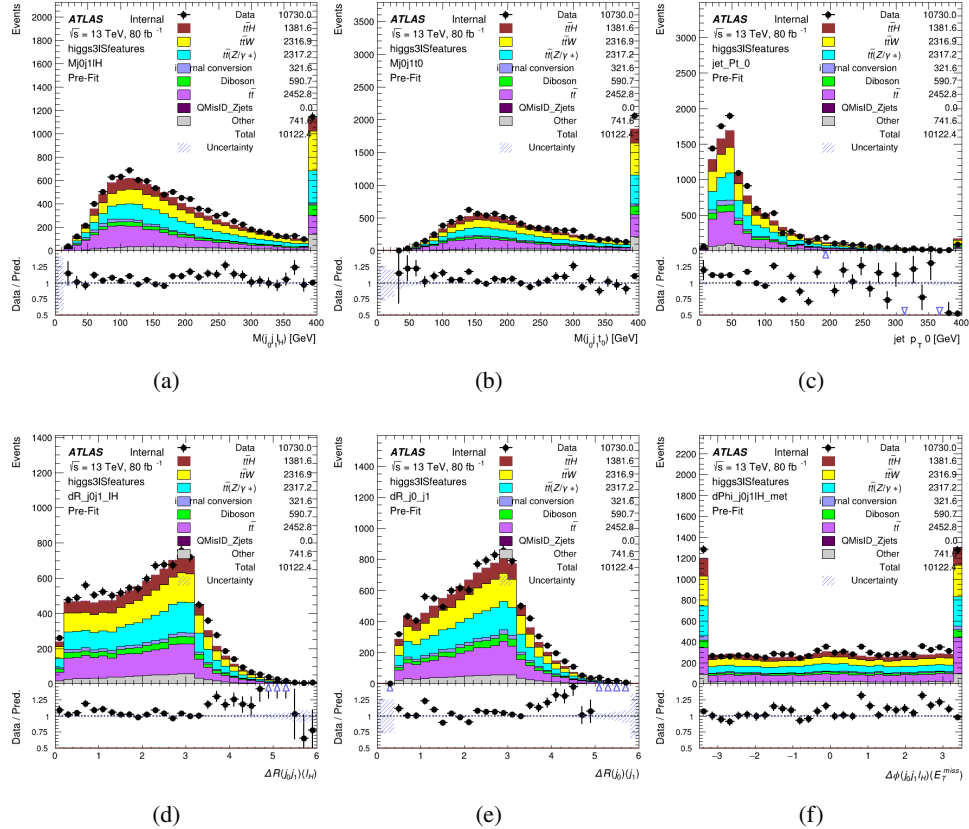


Figure 18.11: Data/MC comparisons of input features for higgs3IS training for 80 fb^{-1} of data.

1334 A neural network of 7 hidden layers with 70 nodes each is trained on 1.8 million events.

1335 Once again, incorrect combinations are downsampled, such that the correct combinations are
 1336 around 10% of the training set. 10% of the dataset is reserved for testing. The output of the NN
 1337 is summarized in Figure 18.3.2.

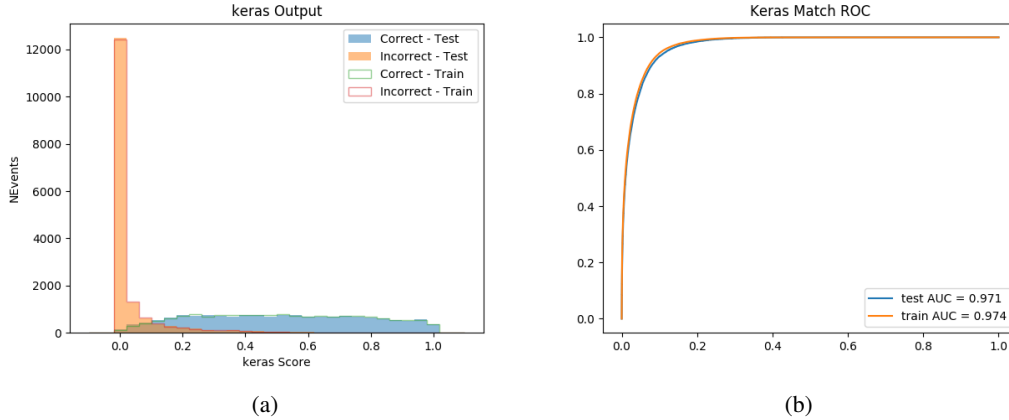


Figure 18.12: Results of the Higgs reconstruction algorithm in the 3lS channel, showing (a) the output score of the NN for correct and incorrect combinations of jets, scaled to an equal number of entries.,. (b) the ROC curve of the output, showing background rejection as a function of signal efficiency

1338 The neural network identifies the correct combination 64% of the time. It identifies the
 1339 correct lepton 85% of the time, and selects the correct lepton and at least one of the correct jets
 1340 83% of the time.

1341 18.3.3 3l Fully-leptonic Channel

1342 In the fully-leptonic 3l case, the goal is identify which two of the three leptons originated from
 1343 the Higgs decay. Since one of these two must be the OS lepton, this problem is reduced to
 1344 determining which of the two SS leptons originated from the Higgs. The kinematics of both
 1345 possibilities are used for training, one where the SS lepton from the Higgs is correctly labeled,
 1346 and one where it is not.

Lepton $p_T H_1$	Lepton $p_T H_0$	Lepton $p_T T$
top $p_T 0$	top $p_T 1$	$\Delta\phi(l_{H_1})(E_T^{\text{miss}})$
$\Delta\phi(l_T)(E_T^{\text{miss}})$	$M(l_{H_0}l_{H_1})$	$M(l_{H_1}l_T)$
$M(l_{H_0}l_T)$	$\Delta R(l_{H_0})(l_{H_1})$	$\Delta R(l_{H_1})(l_T)$
$\Delta R(l_{H_0})(l_T)$	$\Delta R(l_{H_0}l_{H_1})(l_T)$	$\Delta R(l_{H_0}l_T)(l_{H_1})$
$\Delta R(l_{H_0}l_{H_1})(b_0)$	$\Delta R(l_{H_0}l_{H_1})(b_1)$	$\Delta R(l_{H_0}b_0)$
$M(l_{H_0}b_0)$	$\Delta R(l_{H_0}b_1)$	$M(l_{H_0}b_1)$
$\Delta R(l_{H_1}b_0)$	$M(l_{H_1}b_0)$	$\Delta R(l_{H_1}b_1)$
$M(l_{H_1}b_1)$	E_T^{miss}	topScore

Table 31: Input features used to identify the Higgs decay products in 3lF events

1347 Here l_{H0} and l_{H1} are the Higgs decay candidates. The other lepton in the event is labeled
 1348 l_T . b_0 and b_1 are the two b-jets identified by the b-jet identification algorithm. The b-jet Reco
 1349 Score is the output of the Higgs reconstruction algorithm.

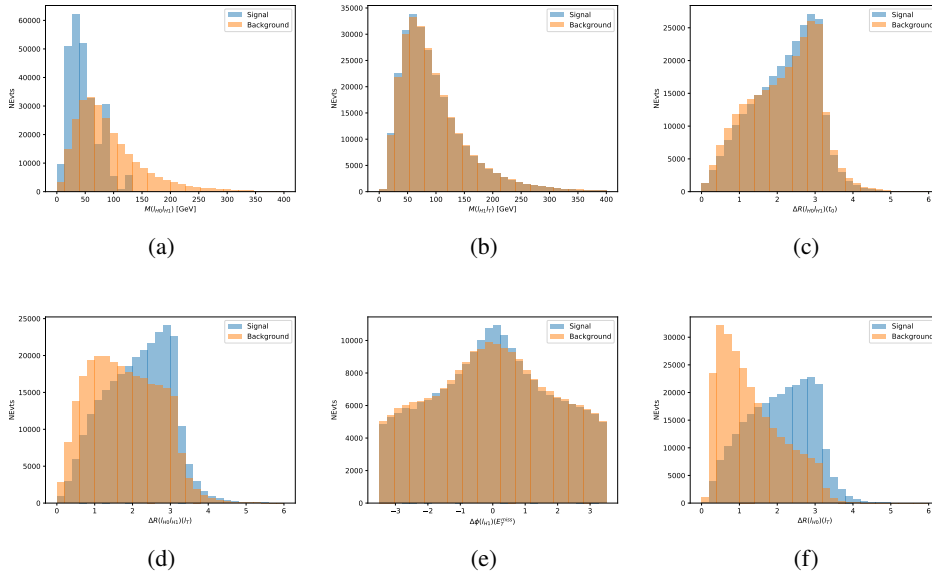


Figure 18.13: Input features for higgs3IF training. The signal in blue represents events where both jet candidates are truth b-jets from top decays, and the orange is all other combinations. Scaled to the same number of events.

1350 The modeling of these inputs is validated against data, with Figure 18.14 showing good
 1351 general agreement between data and MC. Plots for the complete list of features can found in
 1352 Section A.

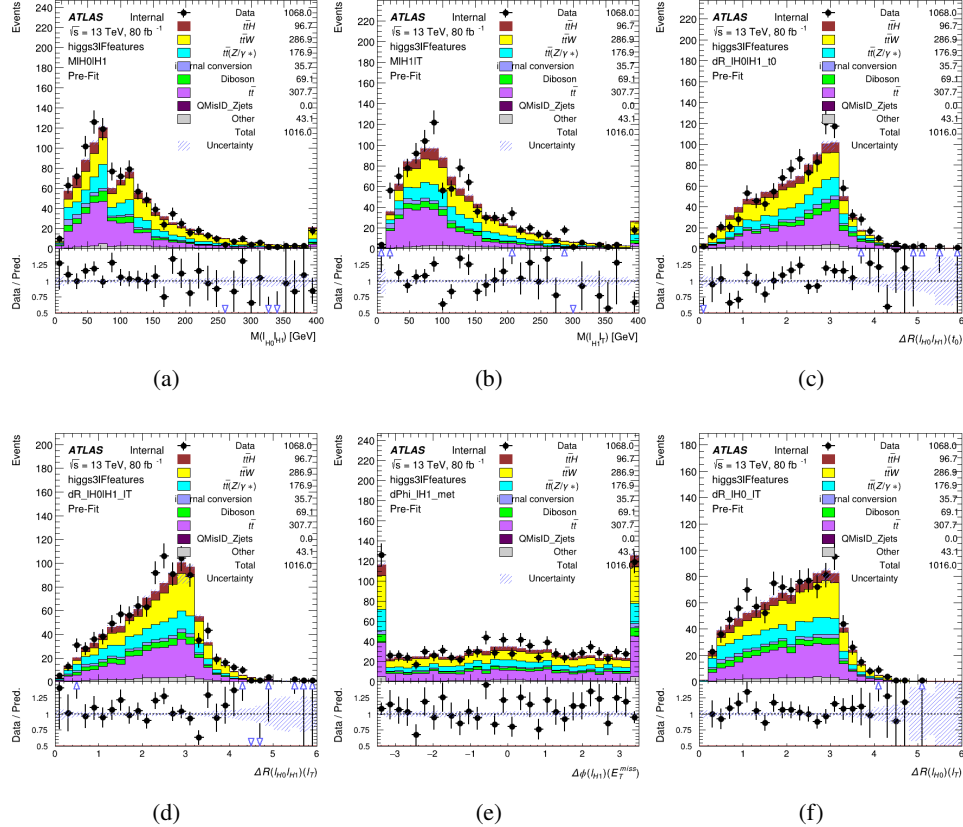


Figure 18.14: Data/MC comparisons of input features for higgs3IF training for 80 fb^{-1} of data.

1353 A neural network consisting of 5 nodes and 60 hidden units is trained on 800,000 events,
 1354 with 10% of the dataset reserved for testing. The output of the model is summarized in Figure
 1355 [18.3.3.](#)

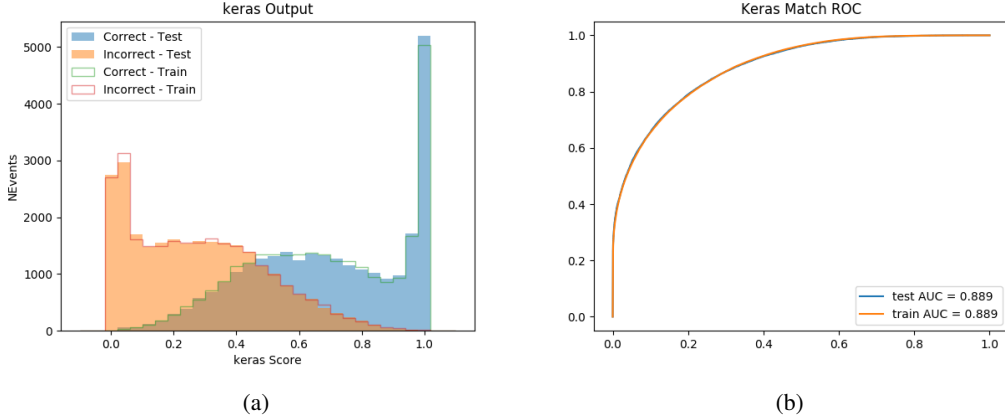


Figure 18.15: (a) the output score of the NN for correct and incorrect combinations of jets. (a) the ROC curve of the output, showing background rejection as a function of signal efficiency

1356 The correct lepton is identified by the model for 80% of events in the testing data set.

1357 18.4 p_T Prediction

1358 Once the most probable decay products have been identified, their kinematics are used as inputs
 1359 to a regression model which attempts to predict the momentum of the Higgs Boson. Once again,
 1360 a DNN is used. Input variables representing the b-jets and leptons not from the Higgs decay
 1361 are included as well, as these are found to improve performance. The truth p_T of the Higgs,
 1362 as predicted by MC, are used as labels. Separate models are built for each channel - 2lSS, 3l
 1363 Semi-leptonic and 3l Fully-leptonic.

1364 As a two-bin fit is targeted for the final result, some metrics evaluating the performance
 1365 of the models aim to show how well it distinguished between "high p_T " and "low p_T " events. A

1366 cutoff point of 150 GeV is used to define these two categories.

1367 Because the analysis uses a two bin fit of the Higgs p_T , the momentum reconstruction
1368 could be treated as a binary classification problem, rather than a regression problem. This
1369 approach is explored in detail in Section A.4, and is found not to provide any significant increase
1370 in sensitivity. The regression approach is used because it provides more flexibility for future
1371 analyses, as it is independent of the cutoff between high and low p_T , as well as the number of
1372 bins. Further, a regression allows the output of the neural network to be more clearly understood,
1373 as it can be directly compared to a physics observable.

1374 **18.4.1 2lSS Channel**

1375 The input variables listed in Table 32 are used to predict the Higgs p_T in the 2lSS channel. Here
1376 j_0 and j_1 are the two jets identified as Higgs decay products. The lepton identified as originating
1377 from the Higgs is labeled l_H , while the other lepton is labeled l_T , as it is assumed to have come
1378 from the decay of one of the top quarks. b_0 and b_1 are the two b-jets identified by the b-jet
1379 identification algorithm. The Higgs Reco Score and b-jet Reco Score are the outputs of the Higgs
1380 reconstruction algorithm, and the b-jet identification algorithm, respectively.

HT	$M(j_0 j_1)$	$M(j_0 j_1 l_H)$
$M(l_H j_0)$	$M(l_H j_1)$	$p_T(b_0 b_1)$
$p_T(j_0 j_1 l_H)$	$\Delta\phi(j_0 j_1 l_H)(E_T^{\text{miss}})$	$\Delta R(j_0)(j_1)$
$\Delta R(j_0 j_1)(l_H)$	$\Delta R(j_0 j_1 l_H)(l_T)$	$\Delta R(j_0 j_1 l_H)(b_0)$
$\Delta R(j_0 j_1 l_H)(b_1)$	$\Delta R(l_H)(j_0)$	$\Delta R(l_H)(b_0)$
$\Delta R(l_H)(b_1)$	$\Delta R(l_T)(b_0)$	$\Delta R(l_T)(b_1)$
$\Delta R(b_0)(b_1)$	Higgs Reco Score	jet η 0
jet η 1	jet Phi 0	jet Phi 1
jet p_T 0	jet p_T 1	Lepton η H
Lepton ϕ H	Lepton p_T H	Lepton p_T T
E_T^{miss}	nJets	b-jet Reco Score
b-jet p_T 0	b-jet p_T 1	

Table 32: Input features for reconstructing the Higgs p_T spectrum for 2lSS events

1381 The optimal neural network architecture for this channel is found to consist of 7 hidden
 1382 layers with 60 nodes each. The inputdata set includes 1.2 million events, 10% of which is used
 1383 for testing, the other 90% for training. Training is found to converge after around 150 epochs.

1384 To evaluate the performance of the model, the predicted p_T spectrum is compared to the
 1385 truth Higgs p_T in Figure 18.16. In order to visualize the model performance more clearly, in (a)
 1386 of that figure, the color of each point is determined by Kernal Density Estimation (KDE). The
 1387 color shown represents the logarithm of the output from KDE, to counteract the large number of
 1388 low p_T events. For that same reason, each column of the histogram shown in (b) of Figure 18.16
 1389 is normalized to unity. This plot therefore demonstrates what the model predicts for each slice
 1390 of truth p_T .

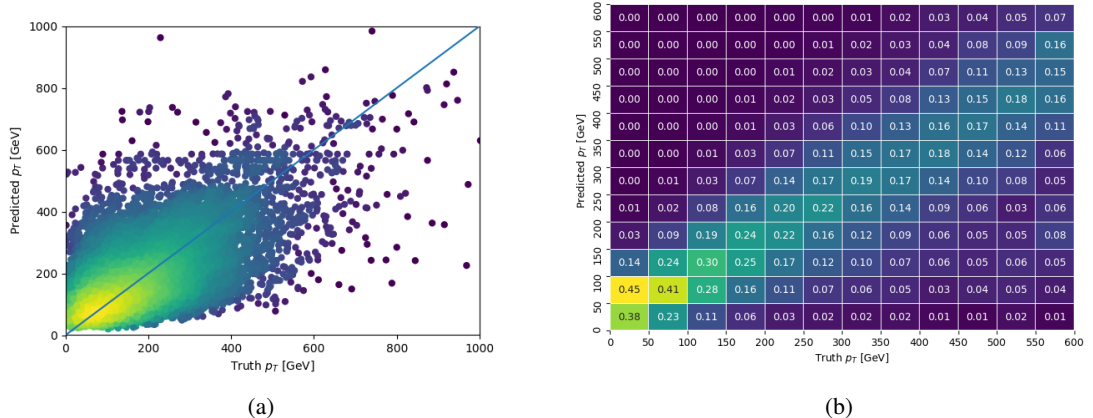


Figure 18.16: The regressed Higgs momentum spectrum as a function of the truth p_T for 2lSS $t\bar{t}H$ events in (a) a scatterplot, where the color of each point represents the log of the point density, based on Gaussian Kernal Density Estimation, and (b) a histogram where each column has been normalized to one.

1391 We are also interested in how well the model distinguishes between events with $p_T < 150$

1392 GeV and >150 GeV. Figure 18.17 demonstrates the NN output for high and low p_T events based
 1393 on this cutoff.

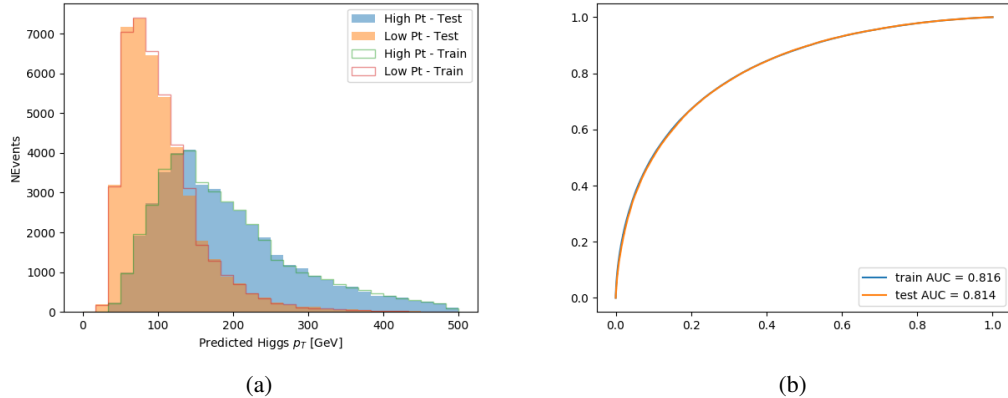


Figure 18.17: (a) shows the reconstructed Higgs p_T for 2lSS events with truth $p_T > 150$ GeV and < 150 GeV, while (b) shows the ROC curve for those two sets of events.

1394 **18.4.2 3l Semi-leptonic Channel**

1395 The following input features are used to predict the Higgs p_T for events in the 3lS channel:

HT jets	MET	$M(j_0 j_1)$
$M(j_0 j_1 l_H)$	$M(j_0 j_1 l_{T0})$	$M(j_0 j_1 l_{T1})$
$M(j_0 j_1 b_0)$	$M(j_0 j_1 b_1)$	$M(b_0 l_{T0})$
$M(b_0 l_{T1})$	$M(b_1 l_{T0})$	$M(b_1 l_{T1})$
$\Delta\phi(j_0 j_1 l_H)(E_T^{\text{miss}})$	$\Delta R(j_0)(j_1)$	$\Delta R(j_0 j_1)(l_H)$
$\Delta R(j_0 j_1)(l_{T1})$	$\Delta R(j_0 j_1)(b_0)$	$\Delta R(j_0 j_1)(b_1)$
$\Delta R(j_0 j_1 l_H)(l_{T0})$	$\Delta R(j_0 j_1 l_H)(l_{T1})$	$\Delta R(j_0 j_1 l_H)(b_0)$
$\Delta R(j_0 j_1 l_H)(b_1)$	$\Delta R(l_H)(j_0)$	$\Delta R(l_H)(j_1)$
$\Delta R(l_H)(l_{T1})$	$\Delta R(l_{T0})(l_{T1})$	$\Delta R(l_{T0})(b_0)$
$\Delta R(l_{T0})(b_1)$	$\Delta R(l_{T1})(b_0)$	$\Delta R(l_{T1})(b_1)$
higgsScore	jet η 0	jet η 1
jet ϕ 0	jet ϕ 1	jet p_T 0
jet p_T 1	Lepton η H	Lepton ϕ H
Lepton p_T H	Lepton p_T T0	Lepton p_T T1
nJets	topScore	b-jet p_T 0
b-jet p_T 1		

Table 33: Input features for reconstructing the Higgs p_T spectrum for 3lS events

Again, j_0 and j_1 are the two jets identified as Higgs decay products, ordered by p_T . The lepton identified as originating from the Higgs is labeled l_H , while the other two leptons are labeled l_{T0} and l_{T1} . b_0 and b_1 are the two b-jets identified by the b-jet identification algorithm. The Higgs Reco Score and b-jet Reco Score are the outputs of the Higgs reconstruction algorithm, and the b-jet identification algorithm, respectively.

The optimal neural network architecture for this channel is found to consist of 7 hidden layers with 80 nodes each. The inputdata set includes one million events, 10% of which is used for testing, the other 90% for training. Training is found to converge after around 150 epochs.

To evaluate the performance of the model, the predicted p_T spectrum is compared to the truth Higgs p_T in Figure 18.18. Once again, (a) of 18.18 shows a scatterplots of predicted vs truth p_T , where the color of each point corresponds to the log of the relative KDE at that point. Each column of the the histogram in (b) is normalized to unity, to better demonstrate the output of the NN for each slice of truth p_T .

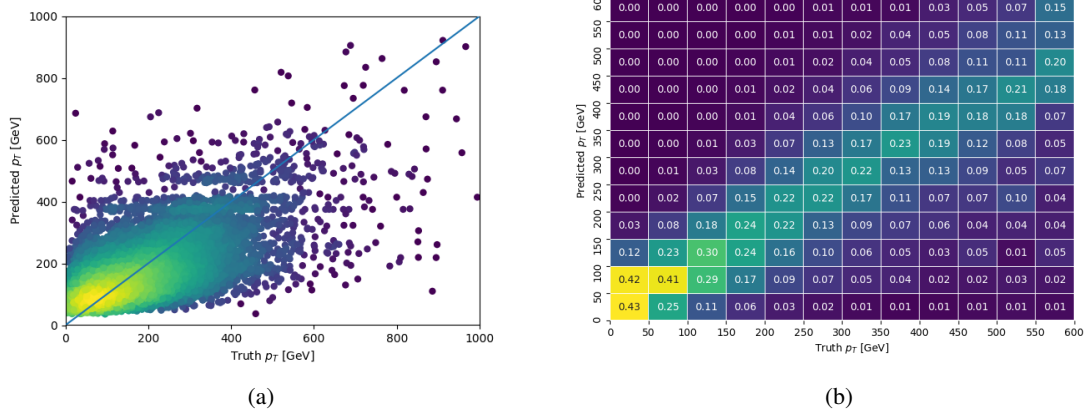


Figure 18.18: The regressed Higgs momentum spectrum as a function of the truth p_T for 3lS $t\bar{t}H$ events in (a) a scatterplot, where the color of each point represents the log of the point density, based on Gaussian Kernel Density Estimation, and (b) a histogram where each column has been normalized to one.

1409 Figure 18.19 shows (a) the output of the NN for events with truth p_T less than and greater
 1410 than 150 GeV and (b) the ROC curve demonstrating how well the NN distinguishes high and low
 1411 p_T events.

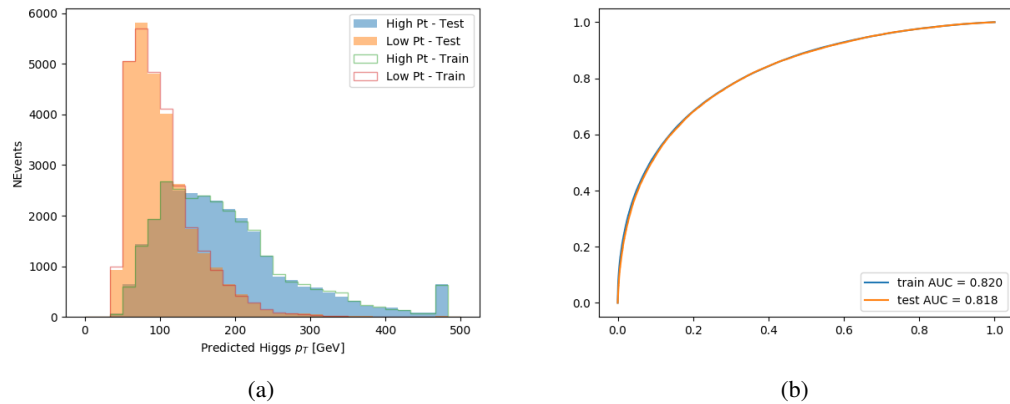


Figure 18.19: (a) shows the reconstructed Higgs p_T for 3lS events with truth $p_T > 150$ GeV and < 150 GeV, while (b) shows the ROC curve for those two sets of events.

¹⁴¹² **18.4.3 3l Fully-leptonic Channel**

¹⁴¹³ The features listed in 34 are used to construct a model for predictin the Higgs p_T for 3lF events.

HT	$M(l_{H0}l_{H1})$	$M(l_{H0}l_T)$
$M(l_{H0}b_0)$	$M(l_{H0}b_1)$	$M(l_{H1}l_T)$
$M(l_{H1}b_0)$	$M(l_{H1}b_1)$	$\Delta R(l_{H0})(l_{H1})$
$\Delta R(l_{H0})(l_T)$	$\Delta R(l_{H0}l_{H1})(l_T)$	$\Delta R(l_{H0}l_T)(l_{H1})$
$\Delta R(l_{H1})(l_T)$	$\Delta R(l_{H0}b_0)$	$\Delta R(l_{H0}b_1)$
$\Delta R(l_{H1}b_1)$	$\Delta R(l_{H1}b_0)$	higgsScore
Lepton η H_0	Lepton η H_1	Lepton η T
Lepton p_T H_0	Lepton p_T H_1	Lepton p_T T
E_T^{miss}	topScore	b-jet p_T 0
b-jet p_T 1		

Table 34: Input features for reconstructing the Higgs p_T spectrum for 3lF events

1414 l_{H0} and l_{H1} represent the two leptons identified by the Higgs reconstruction model as
 1415 originating from the Higgs, while l_T is the other lepton in the event. The Higgs Reco Score and
 1416 b-jet Reco Score are the outputs of the Higgs reconstruction algorithm, and b-jet identification
 1417 algorithm, respectively.

1418 The optimal neural network architecture for this channel is found to consist of 5 hidden
 1419 layers with 40 nodes each. The input data set includes 400,000 events, 10% of which is used for
 1420 testing, the other 90% for training. Training is found to converge after around 150 epochs.

1421 The predicted transverse momentum, as a function of the truth p_T , is shown in Figure
 1422 [18.20](#).

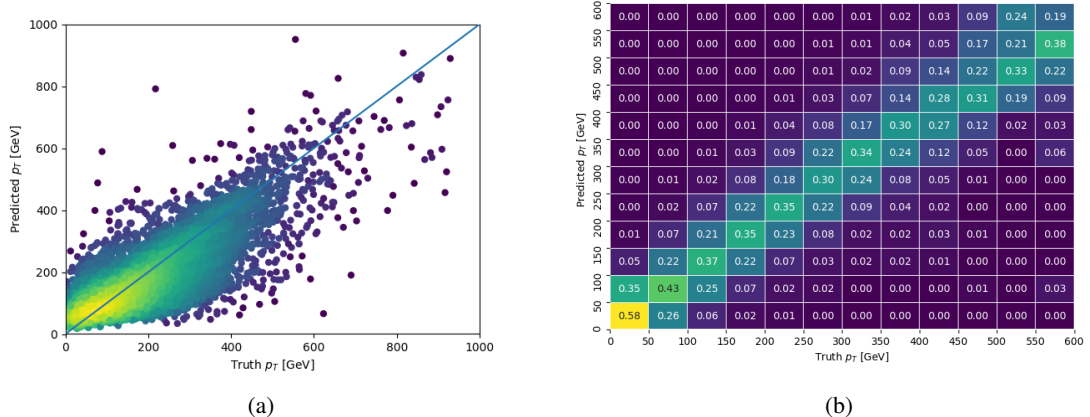


Figure 18.20: The regressed Higgs momentum spectrum as a function of the truth p_T for 3lF $t\bar{t}H$ events in (a) a scatterplot, where the color of each point represents the log of the point density, based on Gaussian Kernel Density Estimation, and (b) a histogram where each column has been normalized to one.

1423 When split into high and low p_T , based on a cutoff of 150 GeV, the

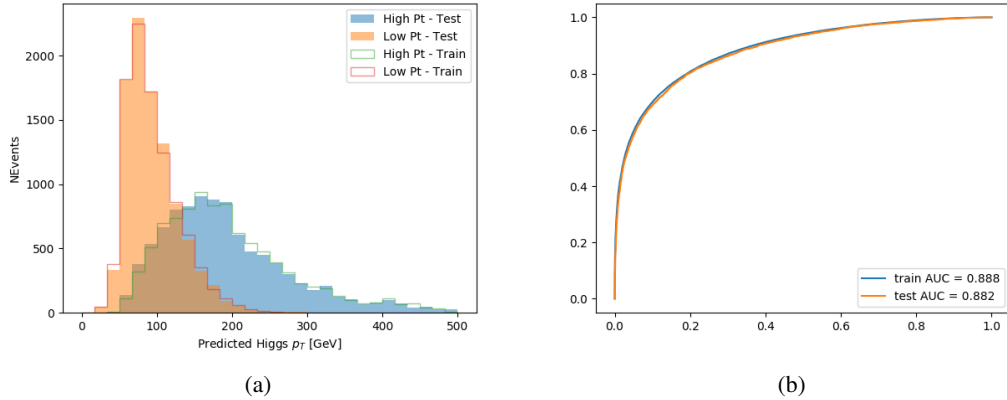


Figure 18.21: (a) shows the reconstructed Higgs p_T for 3lF events with truth $p_T > 150$ GeV and < 150 GeV, while (b) shows the ROC curve for those two sets of events.

18.5 3l Decay Mode

In the 3l channel, there are two possible ways for the Higgs to decay, both involving intermediate W boson pairs: Either both W bosons decay leptonically, in which case the reconstructed decay consists of two leptons (referred as the fully-leptonic 3l channel), or one W decays leptonically and the other hadronically, giving two jets and one lepton in the final state (referred to as the semi-leptonic 3l channel). In order to accurately reconstruct the Higgs, it is necessary to identify which of these decays took place for each 3l event.

The kinematics of each event, along with the output scores of the Higgs and top reconstruction algorithms, are used to distinguish these two possible decay modes. The particular inputs used are listed in Table 35.

HT jets	$M(l_0 t_0)$	$M(l_0 t_1)$
$M(l_1 t_0)$	$M(l_1 t_1)$	$M(l_0 l_1)$
$M(l_0 l_2)$	$M(l_1 l_2)$	$\Delta R(l_0 t_0)$
$\Delta R(l_0 t_1)$	$\Delta R(l_1 t_0)$	$\Delta R(l_1 t_1)$
$\Delta R(l l_0 1)$	$\Delta R(l l_0 2)$	$\Delta R(l l_1 2)$
Lepton η 0	Lepton η 1	Lepton η 2
Lepton ϕ 0	Lepton ϕ 1	Lepton ϕ 2
Lepton p_T 0	Lepton p_T 1	Lepton p_T 2
E_T^{miss}	nJets	nJets OR DL1r 60
nJets OR DL1r 85	score3lF	score3lS
topScore	total charge	

Table 35: Input features used to distinguish semi-leptonic and fully-leptonic Higgs decays in the 3l channel.

1434 Here l_0 is the opposite charge lepton, l_1 and l_2 are the two SS leptons order by ΔR
 1435 from lepton 0. score3lF and score3lS are the outputs of the 3lS and 3lF Higgs reconstruction
 1436 algorithms, while topScore is the output of the b-jet identification algorithm.

1437 A neural network with 5 hidden layers, each with 50 nodes, is trained to distinguish these
 1438 two decay modes. The output of the model is summarized in Figure 18.22.

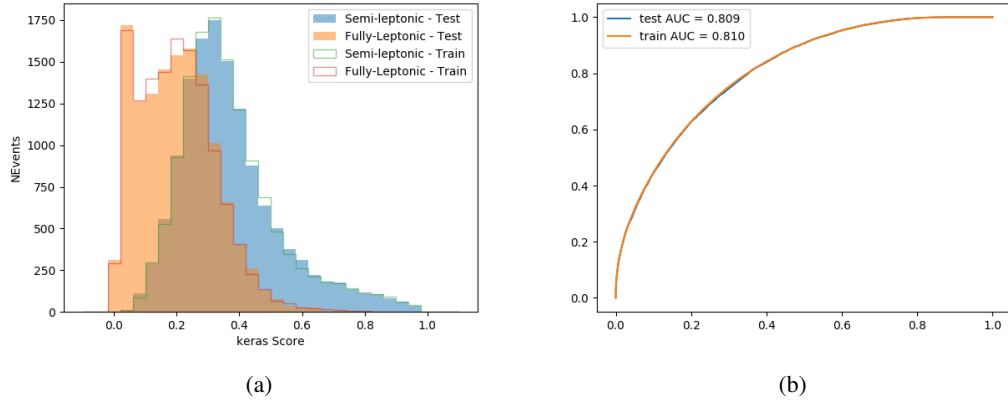


Figure 18.22: (a) shows the output of the decay separation NN for Semi-leptonic (blue) and Fully-leptonic (orange) 3l events, scaled to equal area. (b) shows the ROC curve for those two sets of events.

1439 A cutoff of 0.23 is determined to be optimal for separating 3lS and 3lF in the fit.

1440 19 Signal Region Definitions

1441 Events are divided into two channels based on the number of leptons in the final state: one with
 1442 two same-sign leptons, the other with three leptons. The 3l channel includes events where both
 1443 leptons originated from the Higgs boson as well as events where only one of the leptons

1444 19.1 Pre-MVA Event Selection

1445 A preselection is applied to define orthogonal analysis channels based on the number of leptons

1446 in each event. For the 2lSS channel, the following preselection is used:

- 1447
- Two very tight, same-charge, light leptons with $p_T > 20 \text{ GeV}$

- 1448
- ≥ 4 reconstructed jets, ≥ 1 b-tagged jets

- 1449
- No reconstructed tau candidates

1450 The event yield after the 2lSS preselection has been applied, for MC and data at 80 fb^{-1} ,

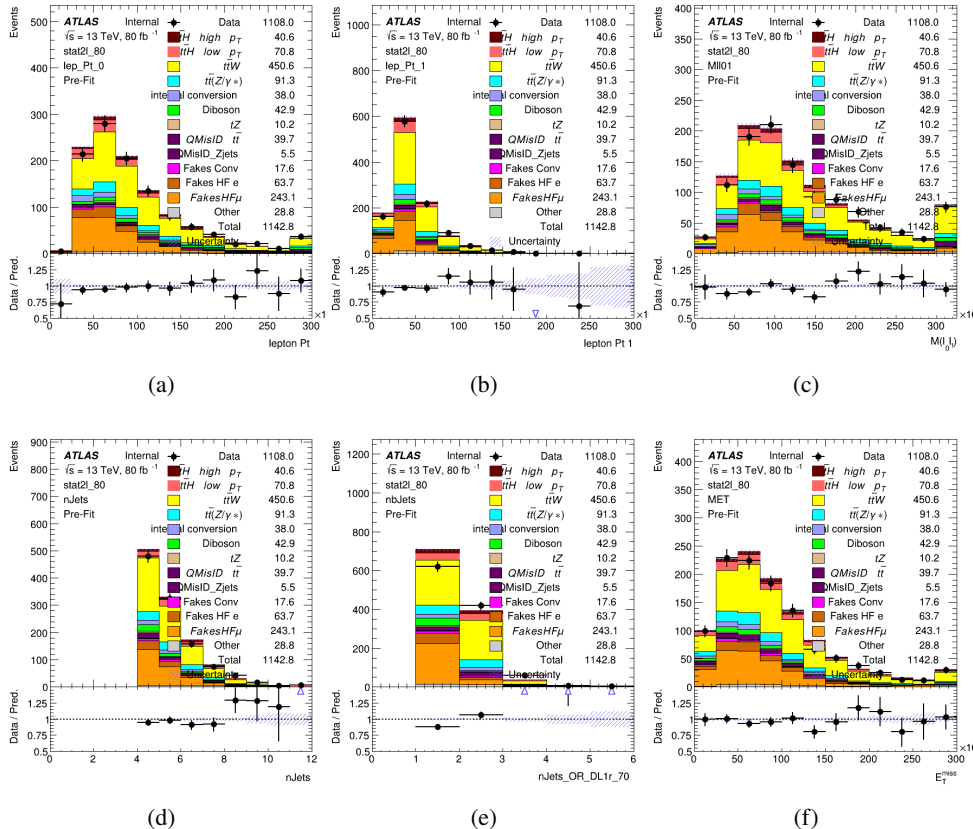
1451 is shown in Table 36.

	Yields
t̄H high p _T	36.19 ± 0.23
t̄H low p _T	63.58 ± 0.31
t̄W	440.64 ± 2.32
t̄Z/γ	91.84 ± 0.79
t̄lllowmass	8.47 ± 0.28
rareTop	24.2099 ± 0.40
VV	38.7927 ± 0.55
tZ	3e-05 ± 5.47-06
QMISID t̄	39.90 ± 2.36
QMISID Zjets	5.49 ± 0.67
t̄ int. conv.	12.74 ± 1.40
t̄ + γ int. conv.	12.09 ± 0.58
t̄ Conv.	13.55 ± 1.43
t̄ + γ Conv.	5.35 ± 0.38
t̄ HF e	59.92 ± 2.89
t̄ + γ HF e	0.51 ± 0.15
t̄ HF μ	224.57 ± 5.62
t̄ + γ HF μ	1.60 ± 0.23
Z + jets internal conv	3e-05 ± 5.47e-06
Z + jets conv	0.62 ± 0.21
Z + jets HF e	0.14 ± 0.13
Z + jets HF μ	0.82 ± 0.26
Single top Conv	2.27 ± 0.53
Single top HF e	2.33 ± 0.50
Single top HF μ	11.12 ± 1.07
Three top	2.22 ± 0.02
Four top	13.09 ± 0.16
t̄WW	10.985 ± 0.30
tW	3e-05 ± 5.47-06
WtZ	9.07 ± 0.44
VVV	0.30 ± 0.04
VH	0.59 ± 1.55
Total	1133.11 ± 7.69
Data	1108

Table 36: Event yield in the 2ISS preselection region.

1452

Figure 20.1. Good general agreement is found.

Figure 19.1: Data/MC comparisons of the 2lSS pre-selection region. (a) and (b) show the p_T of leptons 0 and 1, (c) shows the invariant mass of lepton 0 and 1, (d) shows the jet multiplicity, (e) the b-tagged jet multiplicity, and (f) the missing transverse energy.

1453

For the 3l channel, the following selection is applied:

1454

- Three light leptons with total charge ± 1
- Same charge leptons are required to be very tight, with $p_T > 20 \text{ GeV}$
- Opposite charge lepton must be loose, with $p_T > 10 \text{ GeV}$

1455

1457 • ≥ 2 reconstructed jets, ≥ 1 b-tagged jets

1458 • No reconstructed tau candidates

1459 • $|M(l^+l^-) - 91.2 \text{ GeV}| > 10 \text{ GeV}$ for all opposite-charge, same-flavor lepton pairs

1460 The event yield after the 3l preselection has been applied, for MC and data at 80 fb^{-1} , is

1461 shown in Table 19.1.

	Yields
t̄H high p _T	18.40 ± 0.13
t̄H low p _T	29.91 ± 0.16
t̄W	134.22 ± 1.25
t̄Z/γ	88.47 ± 0.73
t̄lllowmass	2.77 ± 0.16
rareTop	15.05 ± 0.32
VV	34.54 ± 0.54
tZ	2e-05 ± 4.47-06
QMisID t̄t	1.80 ± 0.59
QMisID Zjets	0.02 ± 0.02
t̄t internal conversion	4.34 ± 0.43
t̄t + γ internal conversion	5.83 ± 0.42
t̄t Conv.	4.71 ± 0.45
t̄t + γ Conv.	2.64 ± 0.27
t̄t HF e	27.44 ± 1.05
t̄t + γ HF e	0.27 ± 0.11
t̄t HF μ	89.21 ± 1.92
t̄t + γ HF μ	0.94 ± 0.16
Z + jets conv	0.09 ± 0.19
Z + jets HF e	0.25 ± 0.15
Z + jets HF μ	2.41 ± 0.95
Single top Conv	0.58 ± 0.61
Single top HF e	1.50 ± 0.43
Single top HF μ	4.62 ± 0.85
Three top	0.96 ± 0.02
Four top	5.58 ± 0.10
t̄WW	5.45 ± 0.21
WtZ	8.71 ± 0.42
VVV	0.81 ± 0.02
Total	492.14 ± 3.22
Data	535

Table 37: Yields of the analysis

1462

Comparisons of kinematic distributions for data and MC in this region are shown in Figure

1463

20.2.

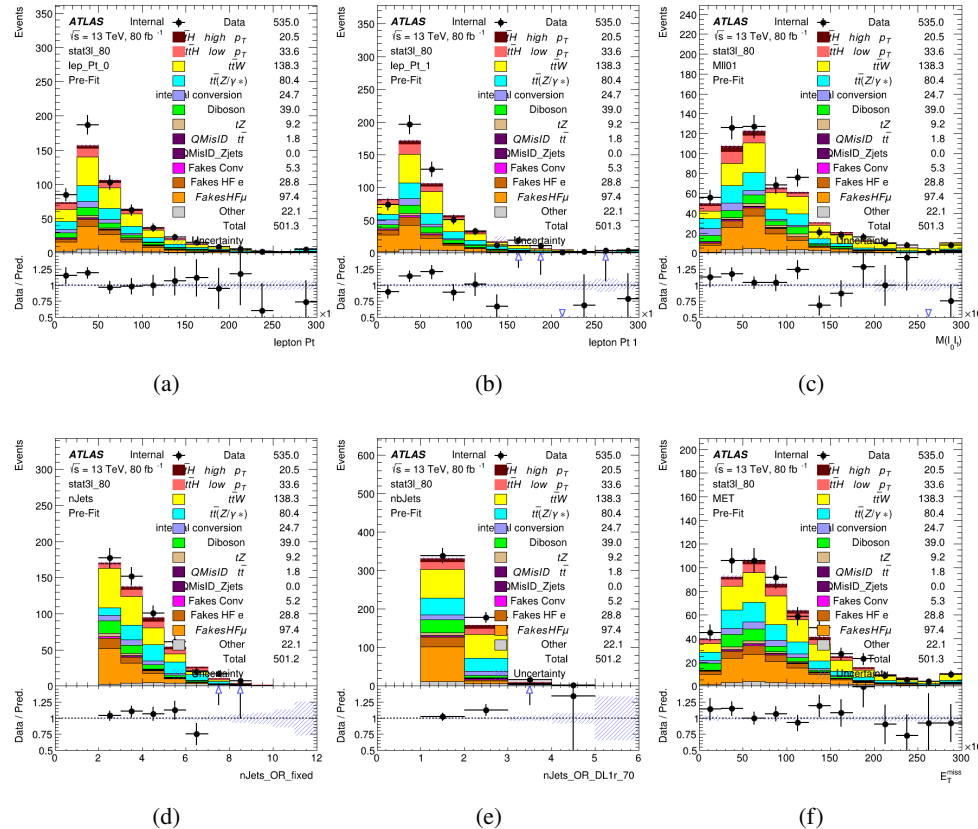


Figure 19.2: Data/MC comparisons of the 3l pre-selection region. (a) and (b) show the p_T of leptons 0 and 1, (c) shows the invariant mass of lepton 0 and 1, (d) shows the jet multiplicity, (e) the b-tagged jet multiplicity, and (f) the missing transverse energy.

1464

19.2 Event MVA

1465

Separate multi-variate analysis techniques (MVAs) are used in order to distinguish signal events

1466

from background for each analysis channel - 2lSS, 3l semi-leptonic (3lS), and 3l fully leptonic

1467

(3lF). In particular, Boosted Decision Tree (BDT) algorithms are produced with XGBoost

1468 [xgboost] are trained using the kinematics of signal and background events derived from Monte
1469 Carlo simulations. Events are weighted in the BDT training by the weight of each Monte Carlo
1470 event.

1471 Because the background composition differs for events with a high reconstructed Higgs p_T
1472 compared to events with low reconstructed Higgs p_T , separate MVAs are produced for high and
1473 low p_T regions. This is found to provide better significance than attempting to build an inclusive
1474 model, as demonstrated in appendix A.2. A cutoff of 150 GeV is used. This gives a total of 6
1475 background rejection MVAs - explicitly, 2lSS high p_T , 2lSS low p_T , 3lS high p_T , 3lS low p_T ,
1476 3lF high p_T , and 3lF low p_T .

1477 The following features are used in both the high and low p_T 2lSS BDTs:

HT	$M(\text{lep}, E_T^{\text{miss}})$	$M(l_0 l_1)$
binHiggs p_T 2ISS	$\Delta R(l_0)(l_1)$	diLepton type
higgsRecoScore	jet η 0	jet η 1
jet ϕ 0	jet ϕ 1	jet p_T 0
jet p_T 1	Lepton η 0	Lepton η 1
Lepton ϕ 0	Lepton ϕ 1	Lepton p_T 0
Lepton p_T 1	E_T^{miss}	$\min \Delta R(l_0)(\text{jet})$
$\min \Delta R(l_1)(\text{jet})$	$\min \Delta R(\text{Lepton})(\text{bjet})$	mjjMax frwdJet
nJets	nJets OR DL1r 60	nJets OR DL1r 70
nJets OR DL1r 85	topRecoScore	

Table 38: Input features used to distinguish signal and background events in the 2ISS channel.

1478

While for each of the 31 BDTs, the features listed below are used for training:

$M(\text{lep}, E_T^{\text{miss}})$	$M(l_0 l_1)$	$M(l_0 l_1 l_2)$
$M(l_0 l_2)$	$M(l_1 l_2)$	$\text{binHiggs } p_T \text{ 3lF}$
$\text{binHiggs } p_T \text{ 3lS}$	$\Delta R(l_0)(l_1)$	$\Delta R(l_0)(l_2)$
$\Delta R(l_1)(l_2)$	decayScore	higgsRecoScore3lF
higgsRecoScore3lS	$\text{jet } \eta \text{ 0}$	$\text{jet } \eta \text{ 1}$
$\text{jet } \phi \text{ 0}$	$\text{jet } \phi \text{ 1}$	$\text{jet } p_T \text{ 0}$
$\text{jet } p_T \text{ 1}$	$\text{Lepton } \eta \text{ 0}$	$\text{Lepton } \eta \text{ 1}$
$\text{Lepton } \eta \text{ 2}$	$\text{Lepton } \phi \text{ 0}$	$\text{Lepton } \phi \text{ 1}$
$\text{Lepton } \phi \text{ 2}$	$\text{Lepton } p_T \text{ 0}$	$\text{Lepton } p_T \text{ 1}$
$\text{Lepton } p_T \text{ 2}$	E_T^{miss}	$\min \Delta R(l_0)(\text{jet})$
$\min \Delta R(l_1)(\text{jet})$	$\min \Delta R(l_2)(\text{jet})$	$\min \Delta R(\text{Lepton})(\text{bjet})$
$mjj\text{Max frwdJet}$	$n\text{Jets}$	$n\text{Jets OR DL1r 60}$
$n\text{Jets OR DL1r 70}$	$n\text{Jets OR DL1r 85}$	topScore

Table 39: Input features used to distinguish signal and background events in the 3l channel.

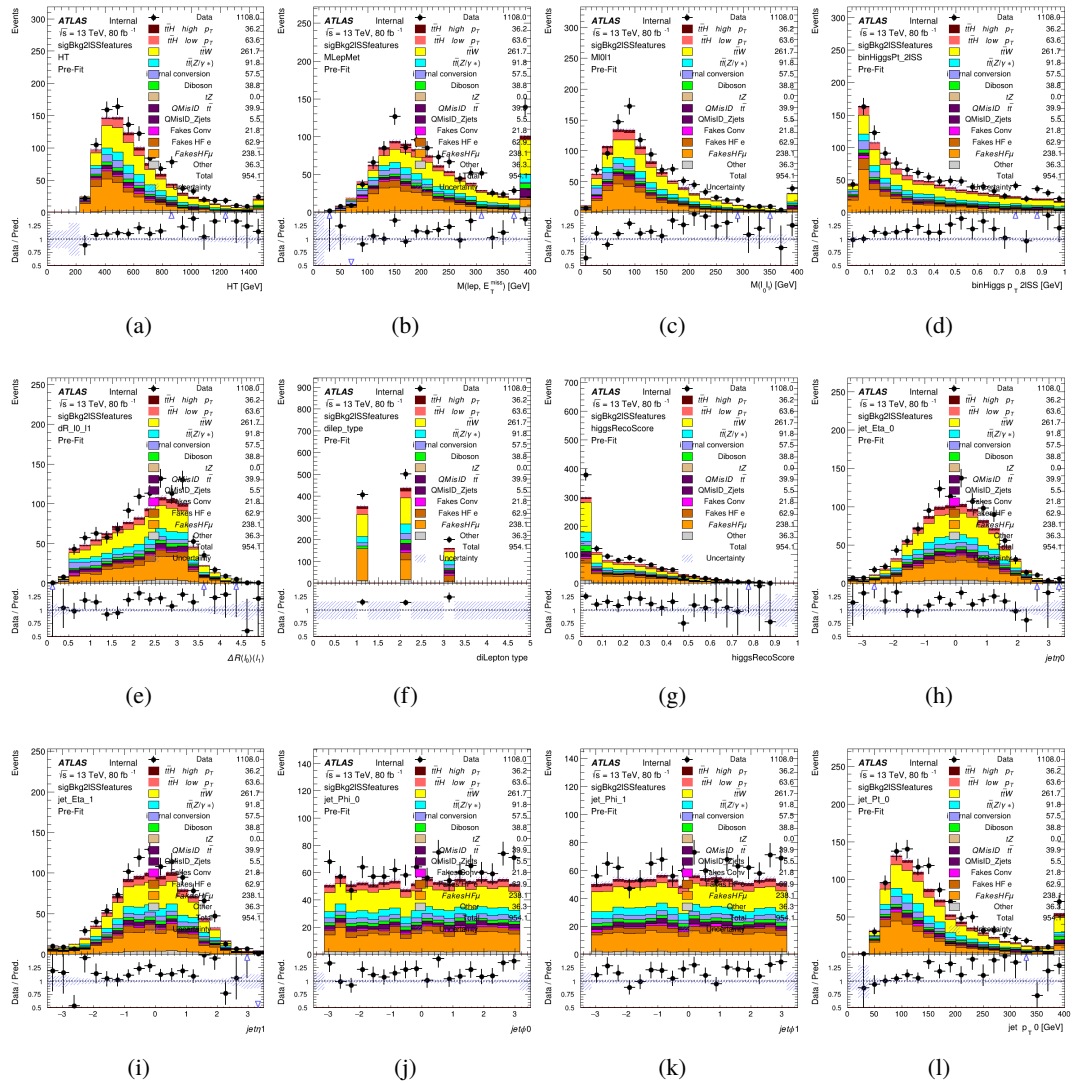


Figure 19.3:

1479

The BDTs are produced with a maximum tree depth of 6, using AUC as the target loss

1480 function.

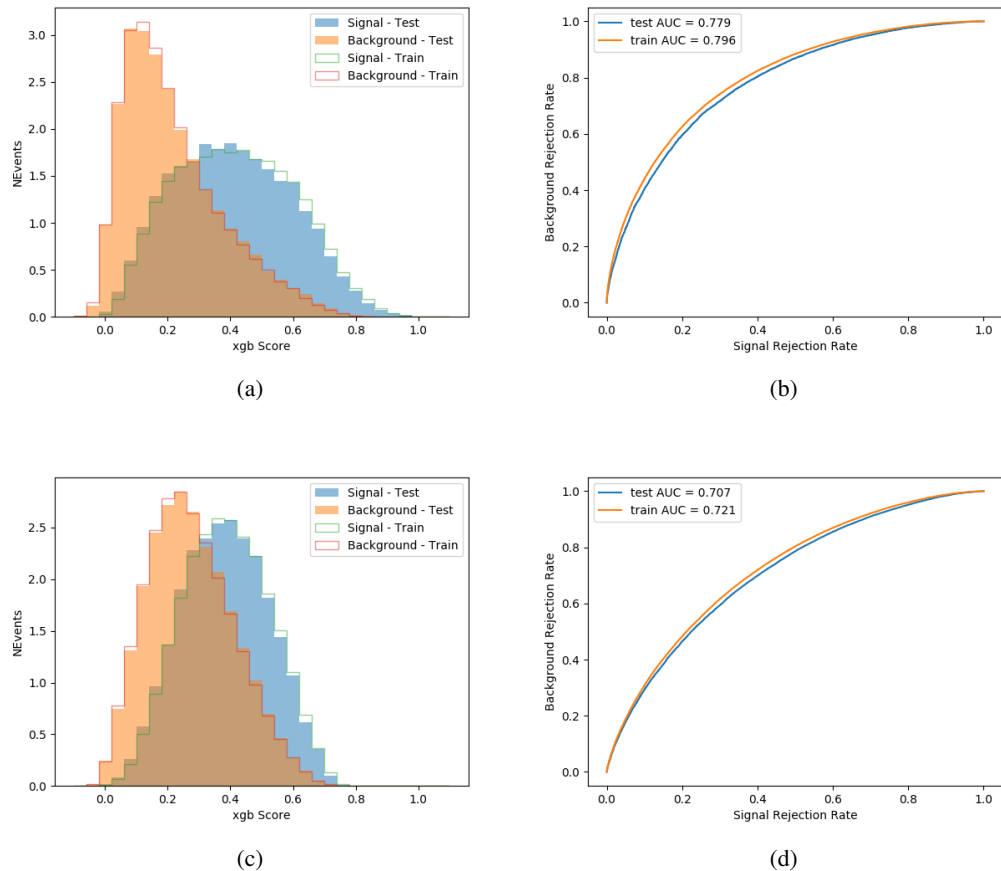


Figure 19.4:

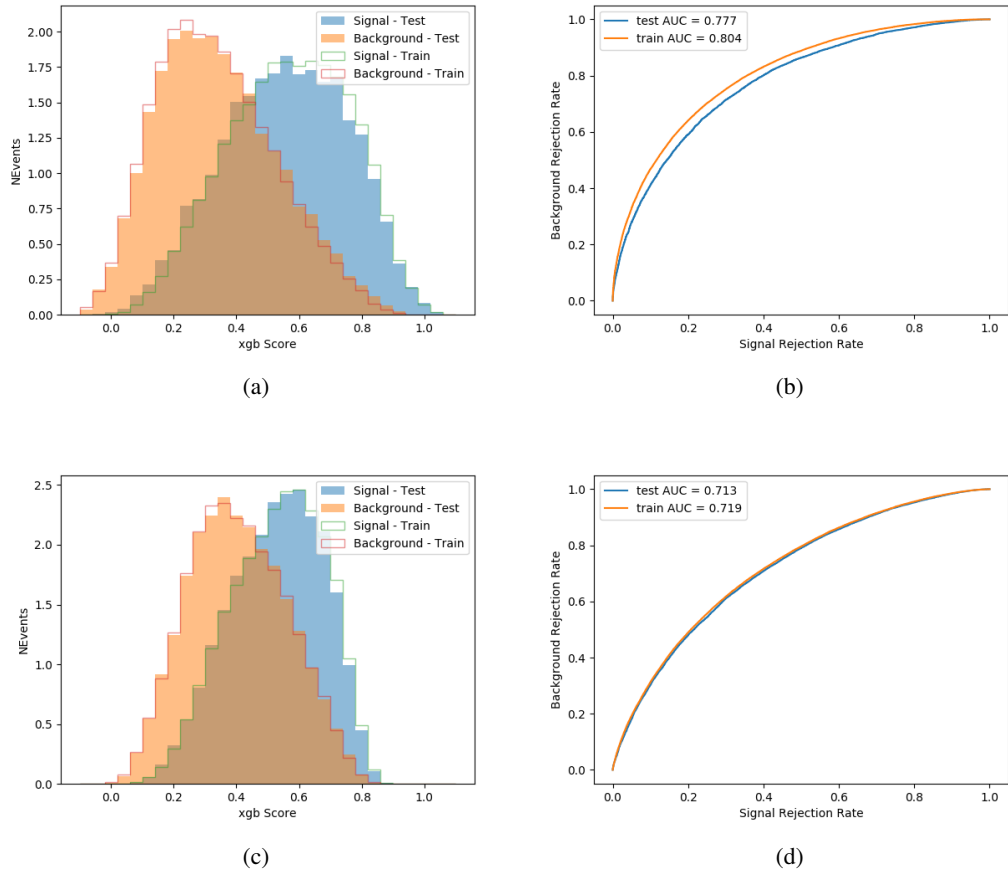


Figure 19.5:

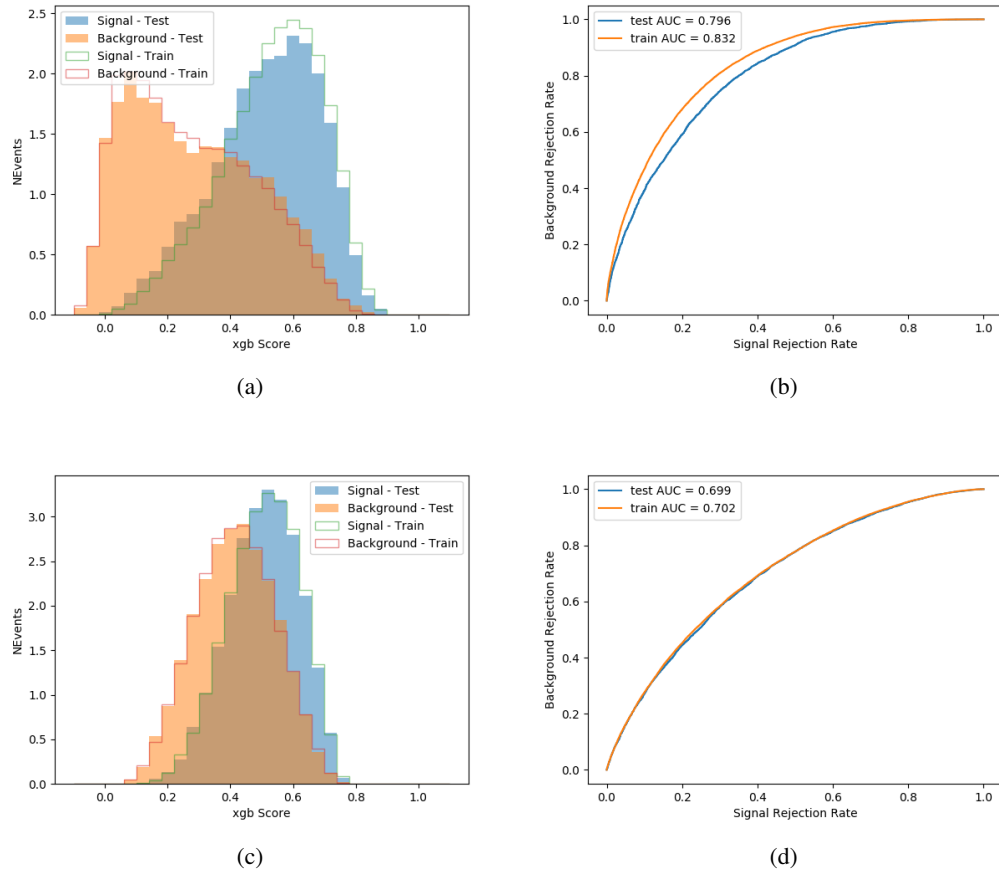


Figure 19.6:

1481 Output distributions of each MVA comparing MC prediction to data at 80 fb^{-1} are shown
 1482 in figures [19.7-19.2](#).

1483 **19.3 Signal Region Definitions**

1484 Once pre-selection has been applied, channels are further refined based on the MVAs described
 1485 above. The output of the model described in Section [18.5](#) is used to separate the three channel

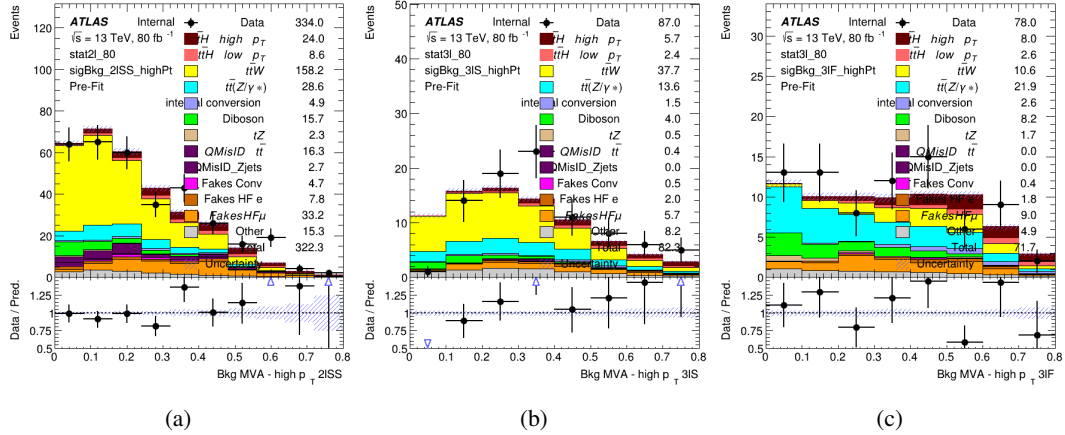


Figure 19.7: Output score of the high p_T BDTs in the (a) 2ISS, (b) 3IS, and (c) 3IF channels

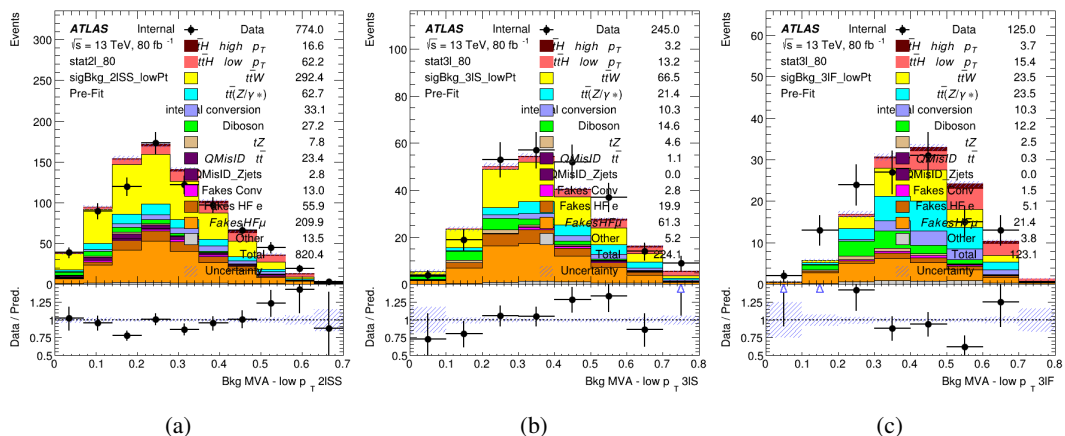


Figure 19.8: Output score of the low p_T BDTs in the (a) 2ISS, (b) 3IS, and (c) 3IF channels

¹⁴⁸⁶ into two - Semi-leptonic and Fully-leptonic - based on the predicted decay mode of the Higgs
¹⁴⁸⁷ boson. This leaves three orthogonal signal regions - 2lSS, 3lS, and 3lF.

¹⁴⁸⁸ For each event, depending on the number of leptons as well as whether the p_T of the Higgs
¹⁴⁸⁹ is predicted to be high (> 150 GeV) or low (< 150 GeV), a cut on the appropriate background
¹⁴⁹⁰ rejection MVA is applied. The particular cut values, listed in Table 40, are determined by
¹⁴⁹¹ maximizing S/\sqrt{B} in each region.

Channel	BDT Score
2lSS high p_T	0.36
2lSS low p_T	0.34
3lS high p_T	0.51
3lS low p_T	0.43
3lF high p_T	0.33
3lF low p_T	0.41

Table 40: Cutoff values on background rejection MVA score applied to signal regions.

¹⁴⁹² The event preselection and MVA selection define the three signal regions. These signal
¹⁴⁹³ region definitions are summarized in Table 41.

Region	Selection
2ISS	Two same charge tight leptons with $p_T > 20 \text{ GeV}$ $N_{\text{jets}} \geq 4, N_{\text{b-jets}} \geq 1$ b-tagged jets Zero τ_{had} $H_{p_T}^{\text{pred}} > 150 \text{ GeV}$ and BDT score > 0.36 or $H_{p_T}^{\text{pred}} < 150 \text{ GeV}$ and BDT score > 0.34
3IS	Three light leptons with total charge ± 1 Two tight SS leptons, $p_T > 20 \text{ GeV}$ One loose OS lepton, $p_T > 10 \text{ GeV}$ $N_{\text{jets}} \geq 2, N_{\text{b-jets}} \geq 1$ b-tagged jets Zero τ_{had} $ M(l^+l^-) - 91.2 \text{ GeV} > 10 \text{ GeV}$ for all OSSF lepton pairs Decay NN Score < 0.23 $H_{p_T}^{\text{pred}} > 150 \text{ GeV}$ and BDT score > 0.51 or $H_{p_T}^{\text{pred}} > 150 \text{ GeV}$ and BDT score > 0.43
3IF	Three light leptons with total charge ± 1 Two tight SS leptons, $p_T > 20 \text{ GeV}$ One loose OS lepton, $p_T > 10 \text{ GeV}$ $N_{\text{jets}} \geq 2, N_{\text{b-jets}} \geq 1$ b-tagged jets Zero τ_{had} $ M(l^+l^-) - 91.2 \text{ GeV} > 10 \text{ GeV}$ for all OSSF lepton pairs Decay NN Score > 0.23 $H_{p_T}^{\text{pred}} > 150 \text{ GeV}$ and BDT score > 0.33 or $H_{p_T}^{\text{pred}} > 150 \text{ GeV}$ and BDT score > 0.41

Table 41: Selection applied to define the three signal regions used in the fit.

20 Background Rejection MVA

1494 Events are divided into two channels based on the number of leptons in the final state: one with
 1495 two same-sign leptons, the other with three leptons. The 3l channel includes events where both
 1496 leptons originated from the Higgs boson as well as events where only one of the leptons
 1497

1498 20.1 Pre-MVA Event Selection

1499 A preselection is applied to define orthogonal analysis channels based on the number of leptons
 1500 in each event. For the 2lSS channel, the following preselection is used:

- 1501 • Two very tight, same-charge, light leptons with $p_T > 20$ GeV

- 1502 • ≥ 4 reconstructed jets, ≥ 1 b-tagged jets

- 1503 • No reconstructed tau candidates

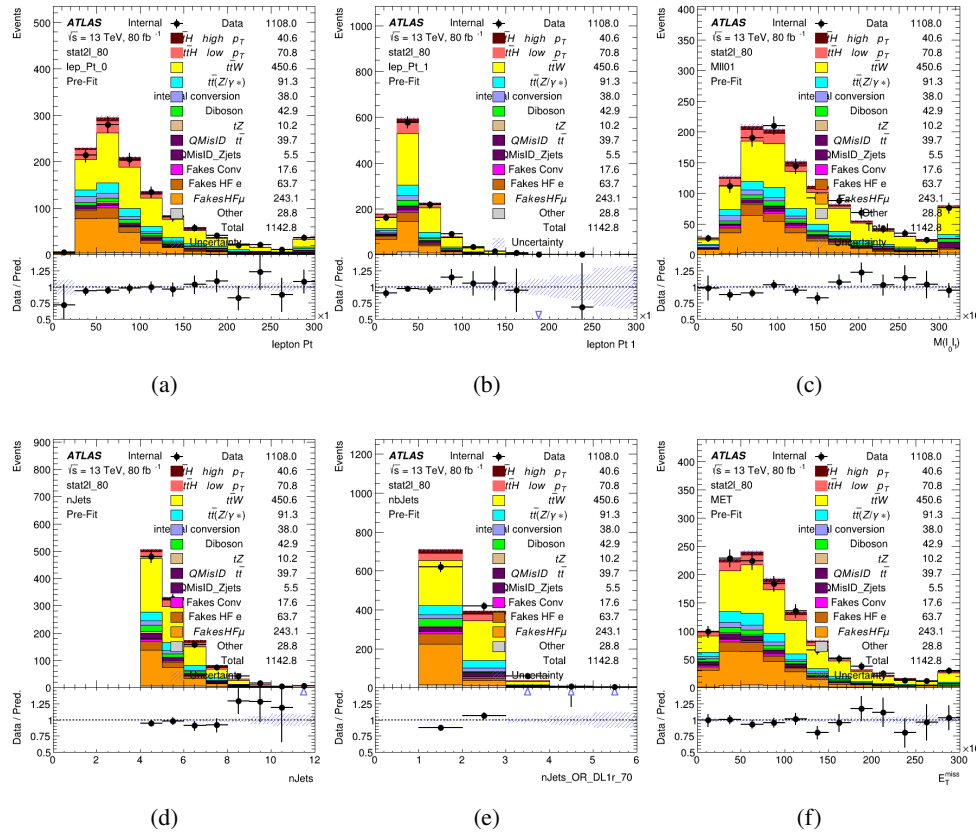


Figure 20.1:

1504 For the 31 channel, the following selection is applied:

1505 • Three light leptons with total charge ± 1

1506 • Same charge leptons are required to be very tight, with $p_T > 20 \text{ GeV}$

1507 • Opposite charge lepton must be loose, with $p_T > 10 \text{ GeV}$

1508 • $>= 2$ reconstructed jets, $>= 1$ b-tagged jets

1509 • No reconstructed tau candidates

1510 • $|M(l^+l^-) - 91.2 \text{ GeV}| > 10 \text{ GeV}$ for all opposite-charge, same-flavor lepton pairs

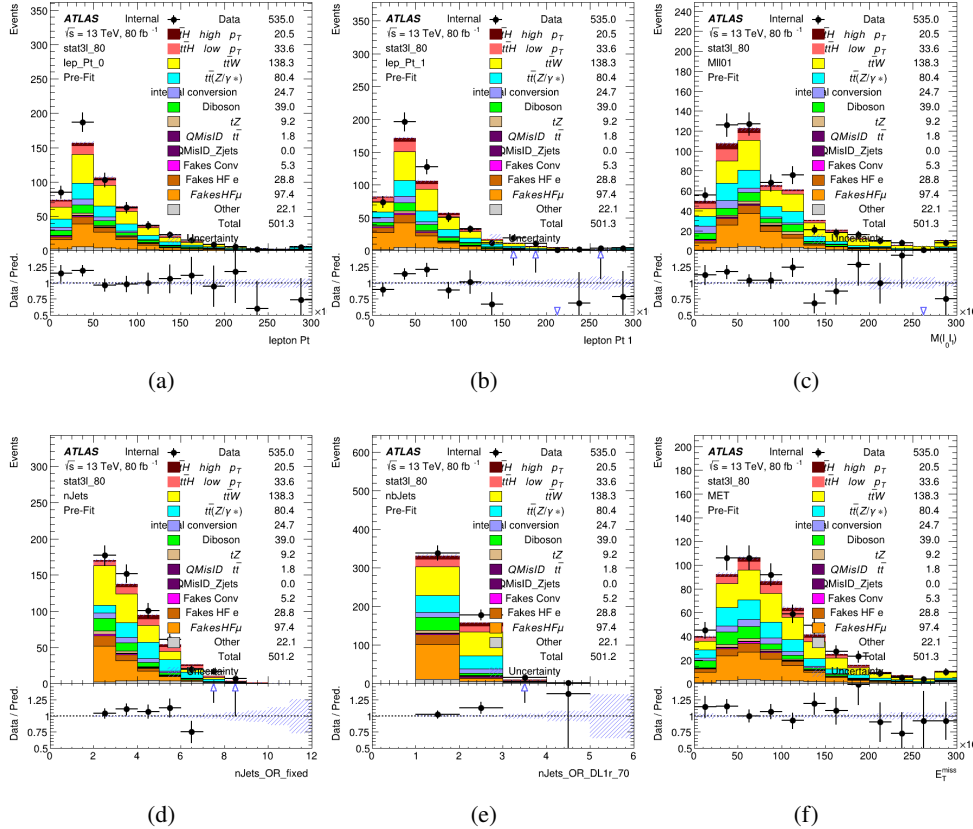


Figure 20.2:

20.2 Event MVA

Separate multi-variate analysis techniques (MVAs) are used in order to distinguish signal events from background for each analysis channel - 2lSS, 3l semi-leptonic (3lS), and 3l fully leptonic (3lF). In particular, Boosted Decision Tree (BDT) algorithms are produced with XGBoost [xgboost] are trained using the kinematics of signal and background events derived from Monte Carlo simulations. Events are weighted in the BDT training by the weight of each Monte Carlo

1517 event.

1518 Because the background composition differs for events with a high reconstructed Higgs p_T
1519 compared to events with low reconstructed Higgs p_T , separate MVAs are produced for high and
1520 low p_T regions. This is found to provide better significance than attempting to build an inclusive
1521 model, as demonstrated in appendix A.2. A cutoff of 150 GeV is used. This gives a total of 6
1522 background rejection MVAs - explicitly, 2lSS high p_T , 2lSS low p_T , 3lS high p_T , 3lS low p_T ,
1523 3lF high p_T , and 3lF low p_T .

1524 The following features are used in both the high and low p_T 2lSS BDTs:

HT	$M(\text{lep}, E_T^{\text{miss}})$	$M(l_0 l_1)$
binHiggs p_T 2ISS	$\Delta R(l_0)(l_1)$	diLepton type
higgsRecoScore	jet η 0	jet η 1
jet ϕ 0	jet ϕ 1	jet p_T 0
jet p_T 1	Lepton η 0	Lepton η 1
Lepton ϕ 0	Lepton ϕ 1	Lepton p_T 0
Lepton p_T 1	E_T^{miss}	$\min \Delta R(l_0)(\text{jet})$
$\min \Delta R(l_1)(\text{jet})$	$\min \Delta R(\text{Lepton})(\text{bjet})$	mjjMax frwdJet
nJets	nJets OR DL1r 60	nJets OR DL1r 70
nJets OR DL1r 85	topRecoScore	

Table 42: Input features used to distinguish signal and background events in the 2ISS channel.

1525

While for each of the 31 BDTs, the features listed below are used for training:

$M(\text{lep}, E_T^{\text{miss}})$	$M(l_0 l_1)$	$M(l_0 l_1 l_2)$
$M(l_0 l_2)$	$M(l_1 l_2)$	$\text{binHiggs } p_T \text{ 3lF}$
$\text{binHiggs } p_T \text{ 3lS}$	$\Delta R(l_0)(l_1)$	$\Delta R(l_0)(l_2)$
$\Delta R(l_1)(l_2)$	decayScore	higgsRecoScore3lF
higgsRecoScore3lS	$\text{jet } \eta \text{ 0}$	$\text{jet } \eta \text{ 1}$
$\text{jet } \phi \text{ 0}$	$\text{jet } \phi \text{ 1}$	$\text{jet } p_T \text{ 0}$
$\text{jet } p_T \text{ 1}$	$\text{Lepton } \eta \text{ 0}$	$\text{Lepton } \eta \text{ 1}$
$\text{Lepton } \eta \text{ 2}$	$\text{Lepton } \phi \text{ 0}$	$\text{Lepton } \phi \text{ 1}$
$\text{Lepton } \phi \text{ 2}$	$\text{Lepton } p_T \text{ 0}$	$\text{Lepton } p_T \text{ 1}$
$\text{Lepton } p_T \text{ 2}$	E_T^{miss}	$\min \Delta R(l_0)(\text{jet})$
$\min \Delta R(l_1)(\text{jet})$	$\min \Delta R(l_2)(\text{jet})$	$\min \Delta R(\text{Lepton})(\text{bjet})$
$mjj\text{Max frwdJet}$	$n\text{Jets}$	$n\text{Jets OR DL1r 60}$
$n\text{Jets OR DL1r 70}$	$n\text{Jets OR DL1r 85}$	topScore

Table 43: Input features used to distinguish signal and background events in the 3l channel.

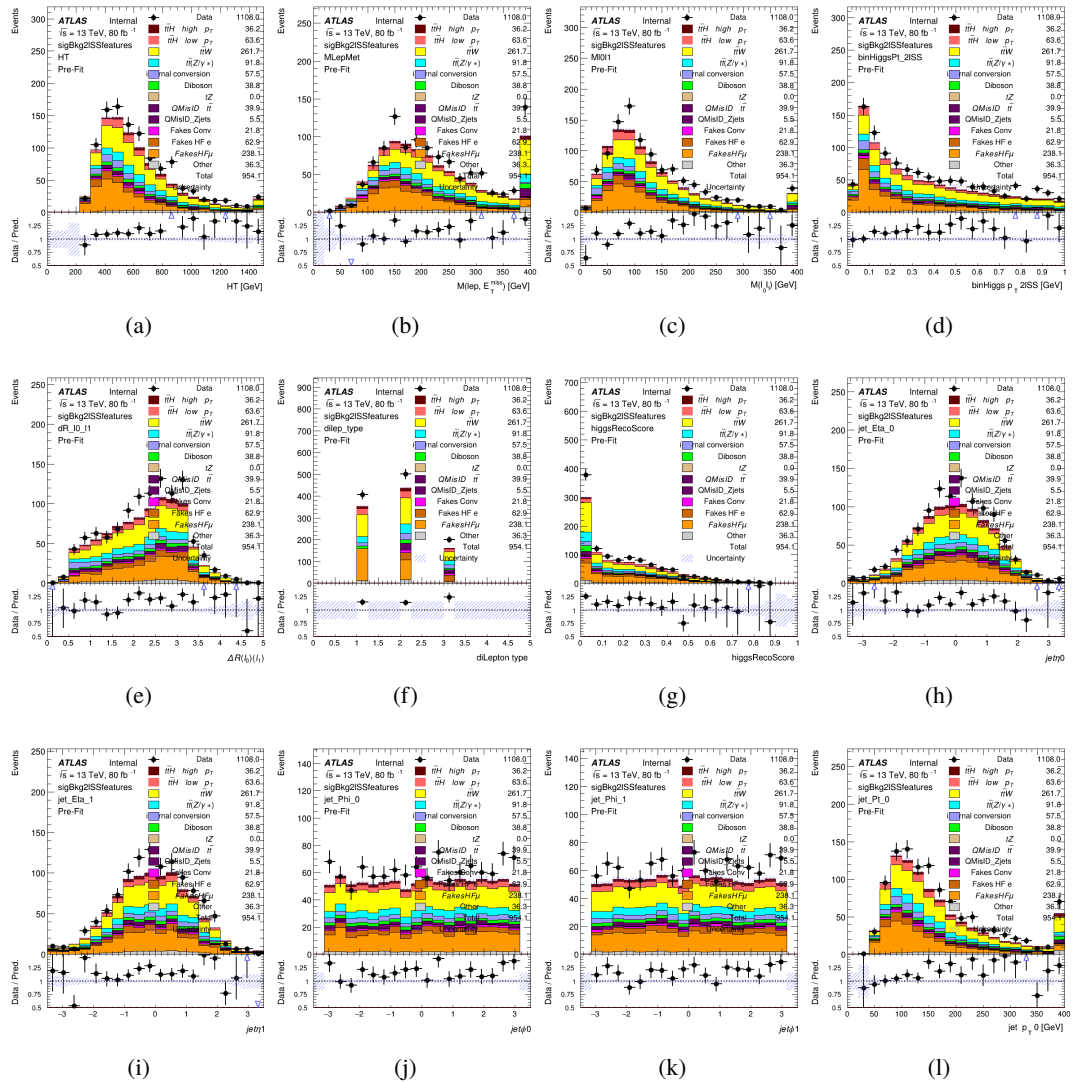


Figure 20.3:

1526

The BDTs are produced with a maximum tree depth of 6, using AUC as the target loss

function.

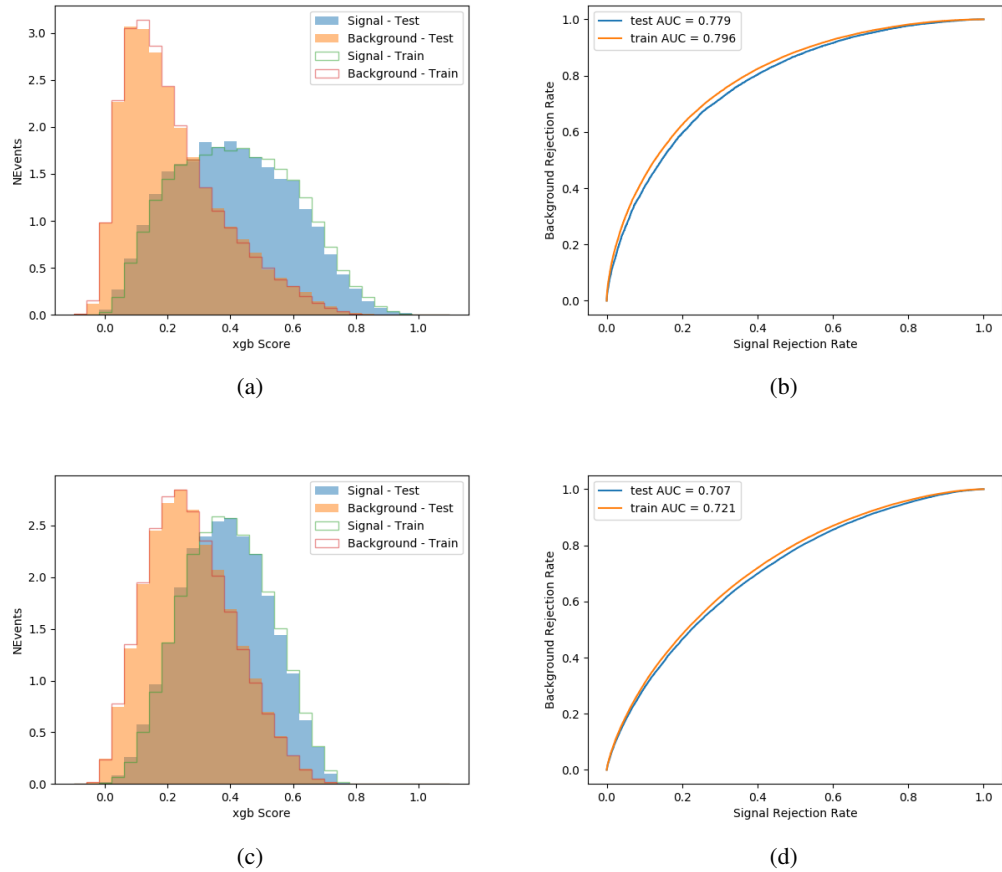


Figure 20.4:

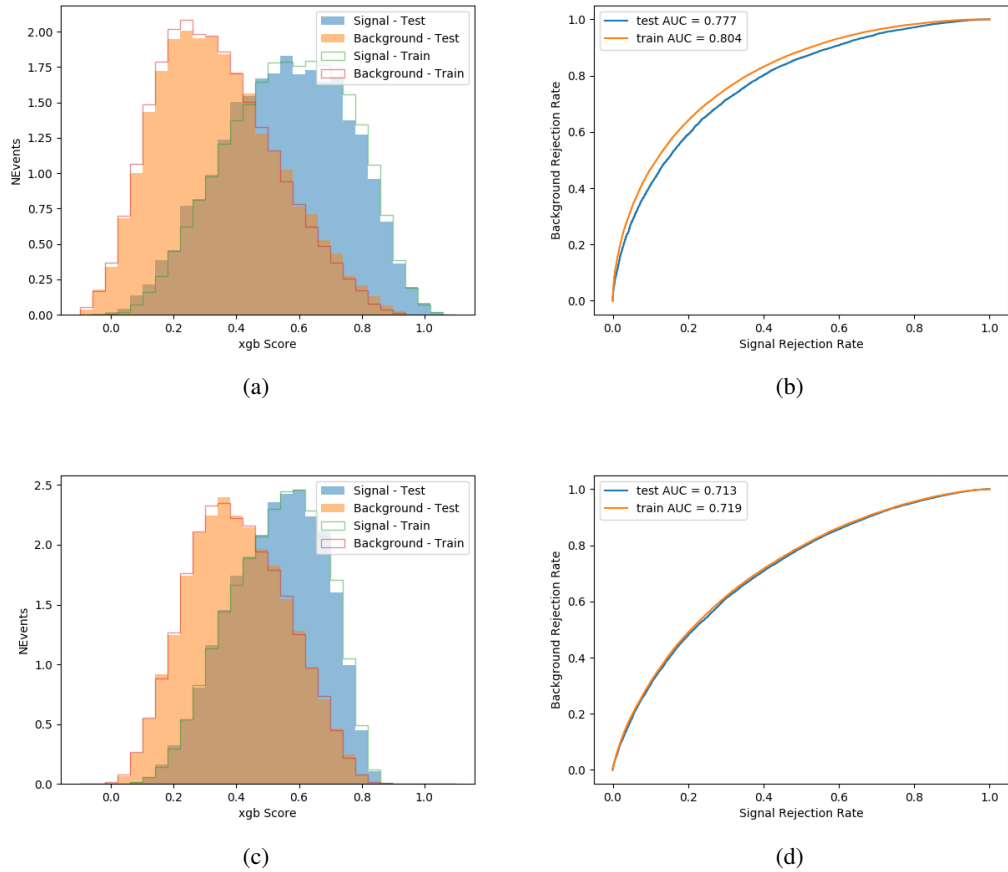


Figure 20.5:

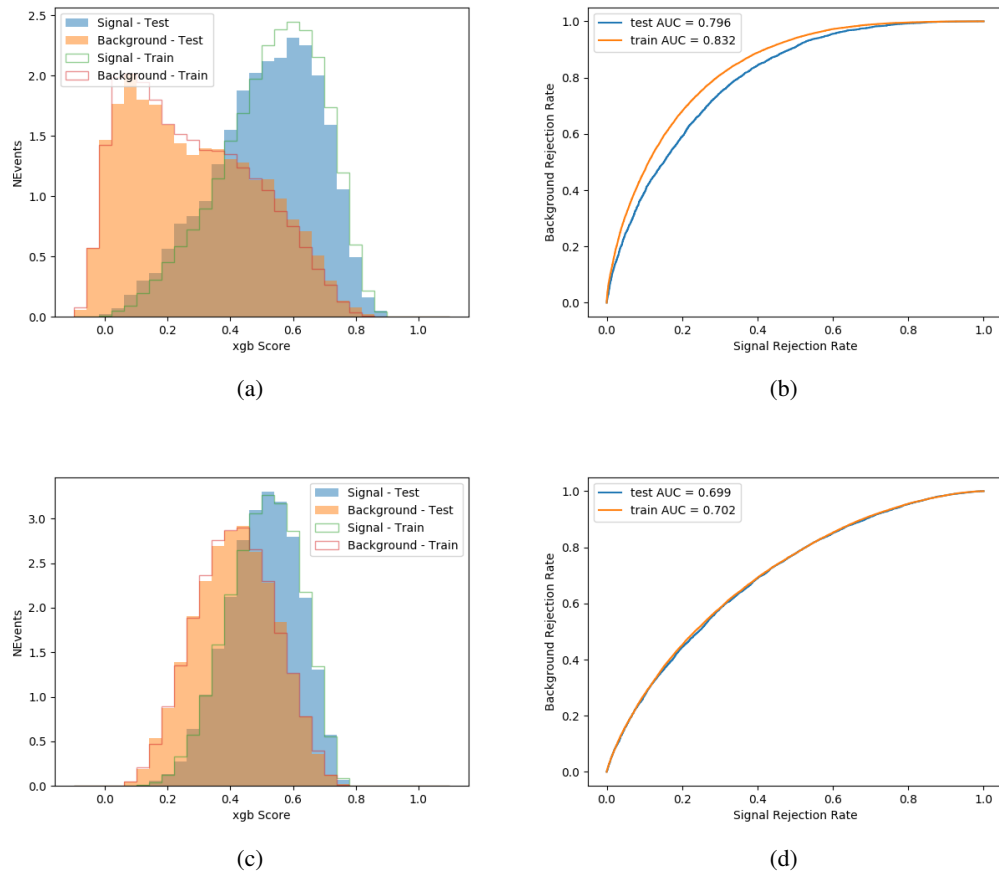


Figure 20.6:

1528

Output distributions of each MVA comparing MC prediction to data at 80 fb^{-1} are shown

1529

in Figure 20.2.

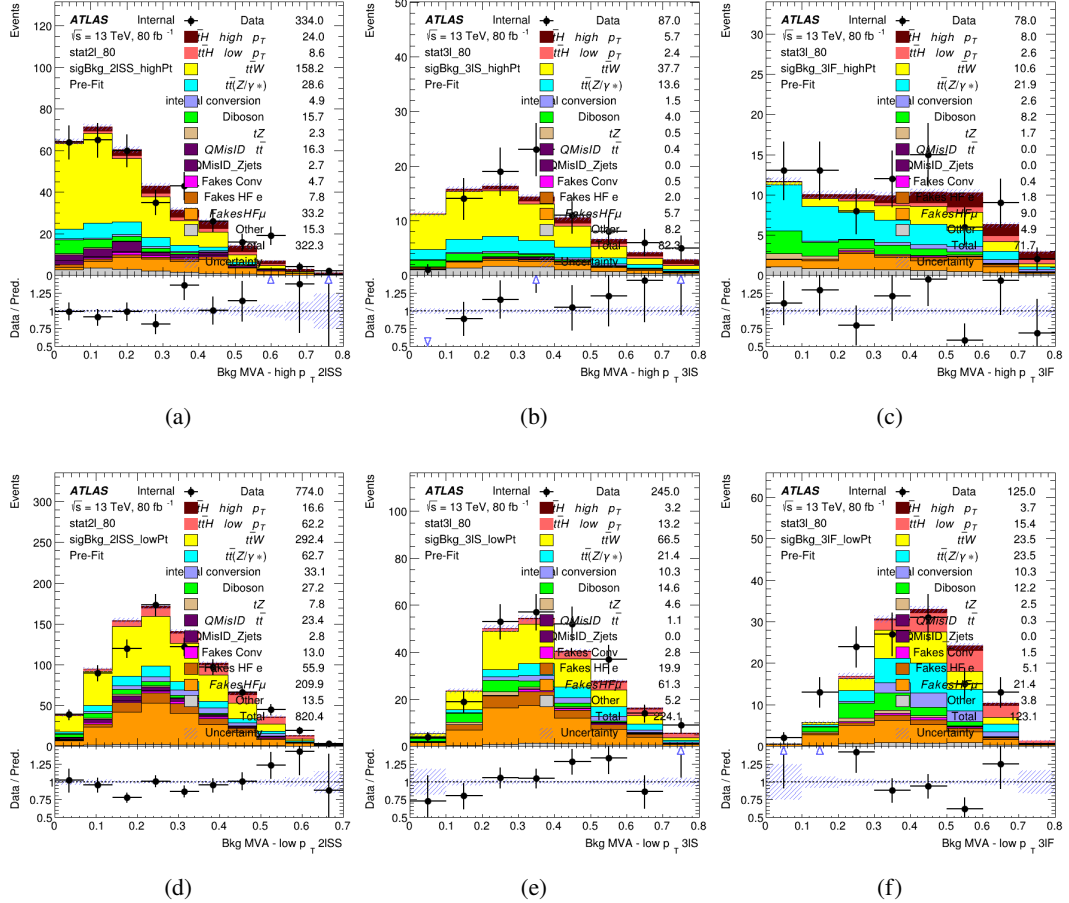


Figure 20.7: scores

1530 20.3 Signal Region Definitions

1531 Once pre-selection has been applied, channels are further refined based on the MVAs described
 1532 above. The output of the model described in Section 18.5 is used to separate the three channel
 1533 into two - Semi-leptonic and Fully-leptonic - based on the predicted decay mode of the Higgs
 1534 boson.

1535 For each event, depending on the channel as well as the predicted p_T of the Higgs derived
1536 from the algorithm described in Section 18.4, a cut on the appropriate background rejection
1537 algorithm is applied. The specific selection used, and the event yield in each channel after this
1538 selection has been applied, is summarized below.

1539 **20.3.1 2lSS**

1540 **20.3.2 3l – Semi – leptonic**

1541 **20.3.3 3l – Fully – leptonic**

1542 **21 Systematic Uncertainties**

1543 The systematic uncertainties that are considered are summarized in Table 44. These are imple-
1544 mented in the fit either as a normalization factors or as a shape variation or both in the signal
1545 and background estimations. The numerical impact of each of these uncertainties is outlined in
1546 section 22.

Table 44: Sources of systematic uncertainty considered in the analysis. Some of the systematic uncertainties are split into several components, as indicated by the number in the rightmost column.

Systematic uncertainty	Components
Luminosity	1
Pileup reweighting	1
Physics Objects	
Electron	6
Muon	15
Jet energy scale and resolution	28
Jet vertex fraction	1
Jet flavor tagging	131
E_T^{miss}	3
Total (Experimental)	186
Background Modeling	
Cross section	24
Renormalization and factorization scales	10
Parton shower and hadronization model	2
Shower tune	4
Total (Signal and background modeling)	40
Background Modeling	
Cross section	24
Renormalization and factorization scales	10
Parton shower and hadronization model	2
Shower tune	4
Total (Signal and background modeling)	40
Total (Overall)	226

¹⁵⁴⁷ The uncertainty in the combined 2015+2016 integrated luminosity is derived from a
¹⁵⁴⁸ calibration of the luminosity scale using x-y beam-separation scans performed in August 2015
¹⁵⁴⁹ and May 2016 [29].

¹⁵⁵⁰ The experimental uncertainties are related to the reconstruction and identification of light
¹⁵⁵¹ leptons and b-tagging of jets, and to the reconstruction of E_T^{miss} . The TOTAL electron ID
¹⁵⁵² correlation model is used, corresponding to 1 electron ID systematic. Electron ID is found to be

1553 a subleading systematic that is unconstrained by the fit, making it an appropriate choice for this
1554 analysis.

1555 The sources which contribute to the uncertainty in the jet energy scale [31] are decom-
1556 posed into uncorrelated components and treated as independent sources in the analysis. The
1557 CategoryReduction model is used to account for JES uncertainties, which decomposes the uncer-
1558 tainties into 30 nuisance parameters included in the fit. The SimpleJER model is used to account
1559 for jet energy resolution (JER) uncertainties, and 8 JER uncertainty components unclued as
1560 NPs in the fit.

1561 The uncertainties in the b-tagging efficiencies measured in dedicated calibration analyses
1562 [32] are also decomposed into uncorrelated components. The large number of components for
1563 b-tagging is due to the calibration of the distribution of the BDT discriminant.

1564 The systematic uncertainties associated with the signal and background processes are
1565 accounted for by varying the cross-section of each process within its uncertainty.

1566 The full list of systematic uncertainties considered in the analysis is summarized in Tables
1567 45, 46 and 47.

1568

Experimental Systematics on Leptons and E_T^{miss}			
Type	Description	Systematics Name	Application
Trigger			
Scale Factors	Trigger Efficiency	lepSFTrigTight_MU(EL)_SF_Trigger_STAT(SYST)	Event Weight
Muons			
Efficiencies	Reconstruction and Identification	lepSFObjTight_MU_SF_ID_STAT(SYST)	Event Weight
	Isolation	lepSFObjTight_MU_SF_Isol_STAT(SYST)	Event Weight
	Track To Vertex Association	lepSFObjTight_MU_SF_TTVA_STAT(SYST)	Event Weight
p_T Scale	p_T Scale	MUONS_SCALE	p_T Correction
Resolution	Inner Detector Energy Resolution	MUONS_ID	p_T Correction
	Muon Spectrometer Energy Resolution	MUONS_MS	p_T Correction
Electrons			
Efficiencies	Reconstruction	lepSFObjTight_EL_SF_ID	Event Weight
	Identification	lepSFObjTight_EL_SF_Reco	Event Weight
	Isolation	lepSFObjTight_EL_SF_Isol	Event Weight
Scale Factor	Energy Scale	EG_SCALE_ALL	Energy Correction
Resolution	Energy Resolution	EG_RESOLUTION_ALL	Energy Correction
E_T^{miss}			
Soft Tracks Terms	Resolution	MET_SoftTrk_ResoPerp	p_T Correction
	Resolution	MET_SoftTrk_ResoPara	p_T Correction
	Scale	MET_SoftTrk_ScaleUp	p_T Correction
	Scale	MET_SoftTrk_ScaleDown	p_T Correction

Table 45: Summary of experimental systematics considered for leptons and E_T^{miss} . Includes type, description, name of systematic as used in the fit, and mode of application. The mode of application indicates the systematic evaluation, e.g. as an overall event re-weighting (Event Weight) or rescaling (p_T Correction).

Experimental Systematics on Jets			
Type	Origin	Systematics Name	Application
Jet Vertex Tagger		JVT	Event Weight
Energy Scale	Calibration Method	JET_21NP_ JET_EffectiveNP_1-19	p _T Correction p _T Correction
	η inter-calibration	JET_EtaIntercalibration_Modelling JET_EtaIntercalibration_NonClosure JET_EtaIntercalibration_TotalStat	p _T Correction p _T Correction p _T Correction
	High p _T jets	JET_SingleParticle_HighPt	p _T Correction
	Pile-Up	JET_Pileup_OffsetNPV JET_Pileup_OffsetMu JET_Pileup_PtTerm JET_Pileup_RhoTopology	p _T Correction p _T Correction p _T Correction p _T Correction
	Non Closure	JET_PunchThrough_MC15	p _T Correction
	Flavour	JET_Flavor_Response JET_BJES_Response JET_Flavor_Composition	p _T Correction p _T Correction p _T Correction
Resolution		JET_JER_SINGLE_NP	Event Weight

Table 46: Jet systematics take into account effects of jets calibration method, η inter-calibration, high p_T jets, pile-up, and flavor response. They are all diagonalised into effective parameters.

Experimental Systematics on b-tagging		
Type	Origin	Systematic Name
Scale Factors	DL1r b-tagger efficiency on b originated jets in bins of η	DL1r_Continuous_EventWeight_B0-29
	DL1r b-tagger efficiency on c originated jets in bins of η	DL1r_Continuous_EventWeight_C0-19
	DL1r b-tagger efficiency on light flavoured originated jets in bins of η and p_T	DL1r_Continuous_EventWeight_Light0-79
	DL1r b-tagger extrapolation efficiency	DL1r_Continuous_EventWeight_extrapolation DL1r_Continuous_EventWeight_extrapolation_from_charm

Table 47: Summary of experimental systematics to be included for b-tagging of jets in the analysis, using the continuous DL1r tagging algorithm. All of the b-tagging related systematics are applied as event weights. From left: type, description, and the name of systematic used in the fit.

1569 As mentioned in Section 16.2, a normalization corrections and uncertainties on the estim-
 1570 ates of non-prompt leptons backgrounds are derived using data driven techniques, decribed in
 1571 detail in [5]. These are derived from a likelihood fit over various non-prompt enriched control
 1572 regions, targeting several sources of non-prompt light leptons separately: external conversion
 1573 electrons, internal conversion electrons, electrons from heavy flavor decays, and muons from
 1574 heavy flavor decays.

1575 The normalization factor and uncertainty applied to each source of non-prompt leptons is
 1576 summarized in Table 21

Processs	
NF_e^{ExtCO}	1.70 ± 0.51
NF_e^{IntCO}	0.75 ± 0.26
NF_e^{HF}	1.09 ± 0.32
NF_{μ}^{HF}	1.28 ± 0.17

1577 In addition to those derived from the control regions, several additional uncertainties are
 1578 assigned to the non-prompt lepton background. An additional 25% uncertainty on material
 1579 conversions is assigned, based on the comparison between data and MC in a region where a
 1580 loose electron fails the photon conversion veto. A shape uncertainty of 15% (6%) is assigned to
 1581 the HF non-prompt electron (muon) background based on a comparison between data and MC
 1582 where the second leading electron (muon) is only required to be loose. As the contribution from
 1583 light non-prompt leptons is small, about 10% percent of the contribution from HF non-prompt
 1584 leptons, it is derived from the agreement between data and simulation in a LF enriched region at
 1585 low values of the non-prompt lepton BDT. The resulting uncertainty is 100%, and is taken to be
 1586 uncorrelated between internal and material conversions.

1587 Theoretical uncertainties applied to MC predictions, including cross section, PDF, and
 1588 scale uncertainties are taken from theory calculations for the predominate prompt backgrounds.
 1589 Following the nominal $t\bar{t}H - ML$ analysis, a 50% uncertainty is applied to Diboson to account
 1590 for the large uncertainty in estimating $VV +$ heavy flavor. The other “rare” background processes
 1591 - including tZ , rare top processes, $ttWW$, WtZ , VVV , $tHjb$ and WtH - are assigned an overall
 1592 50% normalization uncertainty as well. The theory uncertainties applied to the MC estimates

1593 are summarized in Table 48.

Process	X-section [%]
t̄H (aMC@NLO+Pythia8)	QCD Scale: $^{+5.8}_{-9.2}$ PDF($+\alpha_S$): ± 3.6
t̄Z (aMC@NLO+Pythia8)	QCD Scale: $^{+9.6}_{-11.3}$ PDF($+\alpha_S$): ± 4
t̄W (aMC@NLO+Pythia8)	QCD Scale: $^{+12.9}_{-11.5}$ PDF($+\alpha_S$): ± 3.4
tHjb (aMC@NLO+Pythia8)	QCD Scale: $^{+6.5}_{-14.9}$ PDF($+\alpha_S$): ± 3.7
WtH (aMC@NLO+Pythia8)	QCD Scale: $^{+5.0}_{-6.7}$ PDF($+\alpha_S$): ± 6.3
VV (Sherpa 2.2.1)	± 50
Others	± 50

Table 48: Summary of theoretical uncertainties for MC predictions in the analysis.

1594 Additional uncertainties to account for t̄W mismodelling are also applied. These include
 1595 a “Generator” uncertainty, based on a comparison between the nominal Sherpa 2.2.5 sample,
 1596 and the formerly used aMC@NLO sample, and an “Extra radiation” uncertainty, which includes
 1597 renormalisation and factorisation scale variations of the Sherpa 2.2.5 sample.

1598 22 Results

1599 A maximum likelihood fit is performed simultaneously over the reconstructed Higgs p_T spectrum
 1600 in the three signal regions, 2lSS, 3lS, and 3lF. The signal is split into high and low p_T samples,
 1601 based on whether the truth p_T of the Higgs is above or below 150 GeV. The parameters $\mu_{t\bar{t}H\text{high}p_T}$
 1602 and $\mu_{t\bar{t}H\text{low}p_T}$, where $\mu = \sigma_{\text{observed}}/\sigma_{\text{SM}}$, are extracted from the fit, signifying the difference

₁₆₀₃ between the observed value and the theory prediction. Unblinded results are shown for the 80
₁₆₀₄ fb^{-1} data set, as well as MC only projections of results using the full Run-2, 140 fb^{-1} dataset.

₁₆₀₅ As described in Section 21, there are 229 systematic uncertainties that are considered
₁₆₀₆ as NPs in the fit. These NPs are constrained by Gaussian or log-normal probability density
₁₆₀₇ functions. The latter are used for normalisation factors to ensure that they are always positive.
₁₆₀₈ The expected number of signal and background events are functions of the likelihood. The prior
₁₆₀₉ for each NP is added as a penalty term, decreasing the likelihood as it is shifted away from its
₁₆₁₀ nominal value.

₁₆₁₁ 22.1 Results - 80 fb^{-1}

₁₆₁₂ As the data collected from 2015-2017 has been unblinded for $t\bar{t}H - \text{ML}$ channels, representing 80
₁₆₁₃ fb^{-1} , those events are unblinded. The predicted Higgs p_T spectrum is fit to data simultaneously
₁₆₁₄ in each of the three signal regions shown in Figure 22.1.

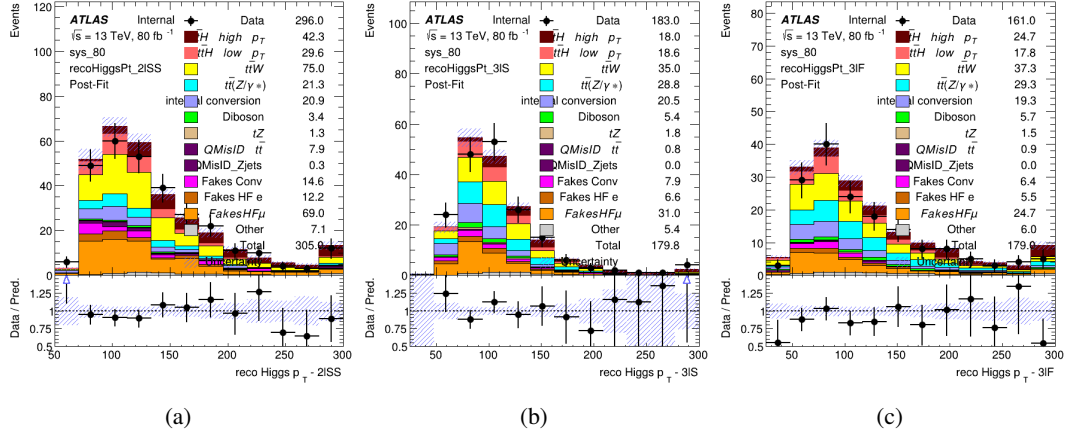


Figure 22.1: Post-fit distributions of the reconstructed Higgs p_T in the three signal regions, (a) 2ISS, (b) 3IS, and (c) 3IF, for 80 fb^{-1} of MC

1615

A post-fit summary of the fitted regions is shown in Figure 22.2.

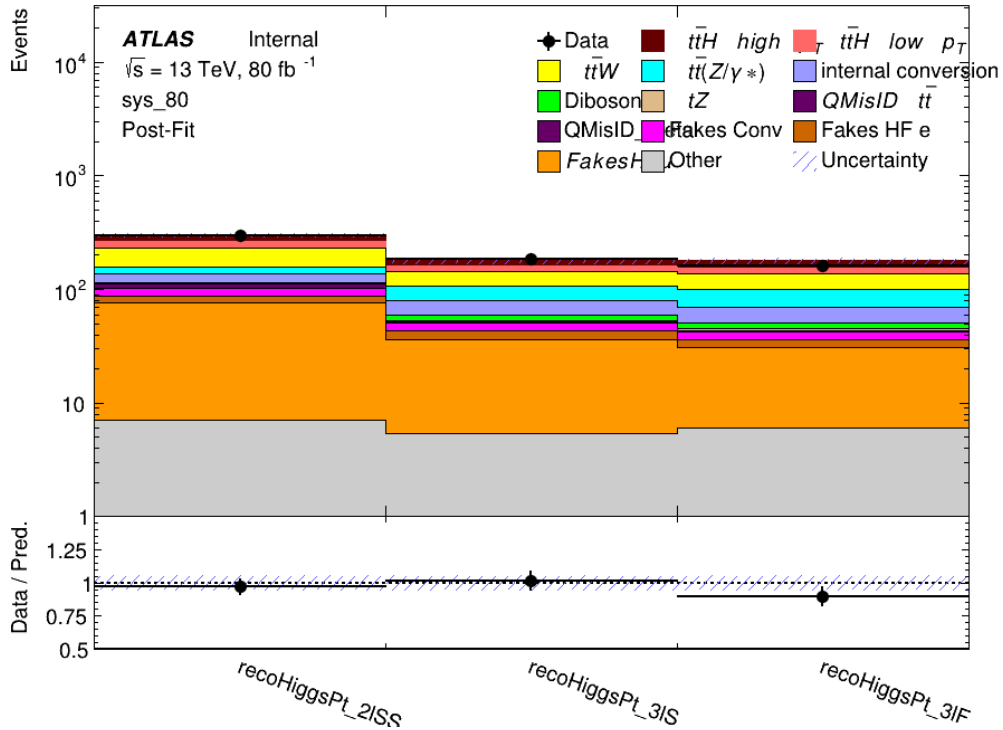


Figure 22.2: Post-fit summary of the yields in each signal region.

1616 The the measured μ values for high and low p_T Higgs production obtained from the fit
 1617 are shown in 49. A significance of 1.7σ is observed for $t\bar{t}H$ high p_T , and 2.1σ is measured for
 1618 $t\bar{t}H$ low p_T .

$$\mu_{t\bar{t}H \text{ high } p_T} = 2.1^{+0.62}_{-0.59}(\text{stat})^{+0.40}_{-0.43}(\text{sys})$$

$$\mu_{t\bar{t}H \text{ low } p_T} = 0.83^{+0.39}_{-0.40}(\text{stat})^{+0.51}_{-0.53}(\text{sys})$$

Table 49: Best fit μ values for $t\bar{t}H$ high p_T and $t\bar{t}H$ low p_T , where $\mu = \sigma_{\text{obs}}/\sigma_{\text{pred}}$

1619 The most prominent sources of systematic uncertainty, as measured by their impact on
 1620 $\mu_{t\bar{t}H \text{ high } p_T}$, are summarized in Table 50.

Uncertainty Source	$\Delta\mu$	
Jet Energy Scale	0.25	0.23
$t\bar{t}H$ cross-section (QCD scale)	-0.11	0.21
Luminosity	-0.13	0.14
Flavor Tagging	0.14	0.13
$t\bar{t}W$ cross-section (QCD scale)	-0.12	0.11
Higgs Branching Ratio	-0.1	0.11
$t\bar{t}H$ cross-section (PDF)	-0.07	0.08
Electron ID	-0.06	0.06
Non-prompt Muon Normalization	-0.05	0.06
$t\bar{t}Z$ cross-section (QCD scale)	-0.05	0.05
Diboson cross-section	-0.05	0.05
Fake muon modelling	-0.04	0.04
Total	0.40	0.43

Table 50: Summary of the most significant sources of systematic uncertainty on the measurement of $t\bar{t}H$ high p_T .

1621 The most significant sources of uncertainty on the measurement of $t\bar{t}H$ - low p_T are shown
 1622 in Table 51.

Uncertainty Source	$\Delta\mu$	
Internal Conversions	-0.26	0.26
Luminosity	-0.16	0.17
Non-prompt Muon Normalization	-0.16	0.16
t̄W cross-section (QCD scale)	-0.17	0.15
Jet Energy Scal	0.15	0.15
Non-prompt Electron Modelling	-0.13	0.14
Flavor Tagging	0.13	0.13
Non-prompt Muon Modelling	-0.12	0.13
Non-prompt Electron Normalization	-0.11	0.11
t̄Z cross-section (QCD scale)	-0.08	0.09
Diboson Cross-section	-0.07	0.07
Total	0.51	0.53

Table 51: Summary of the most significant sources of systematic uncertainty on the measurement of t̄H low p_T.

¹⁶²³ The ranking and impact of those nuisance parameters with the largest contribution to the
¹⁶²⁴ overall uncertainty is shown in Figure 22.3.

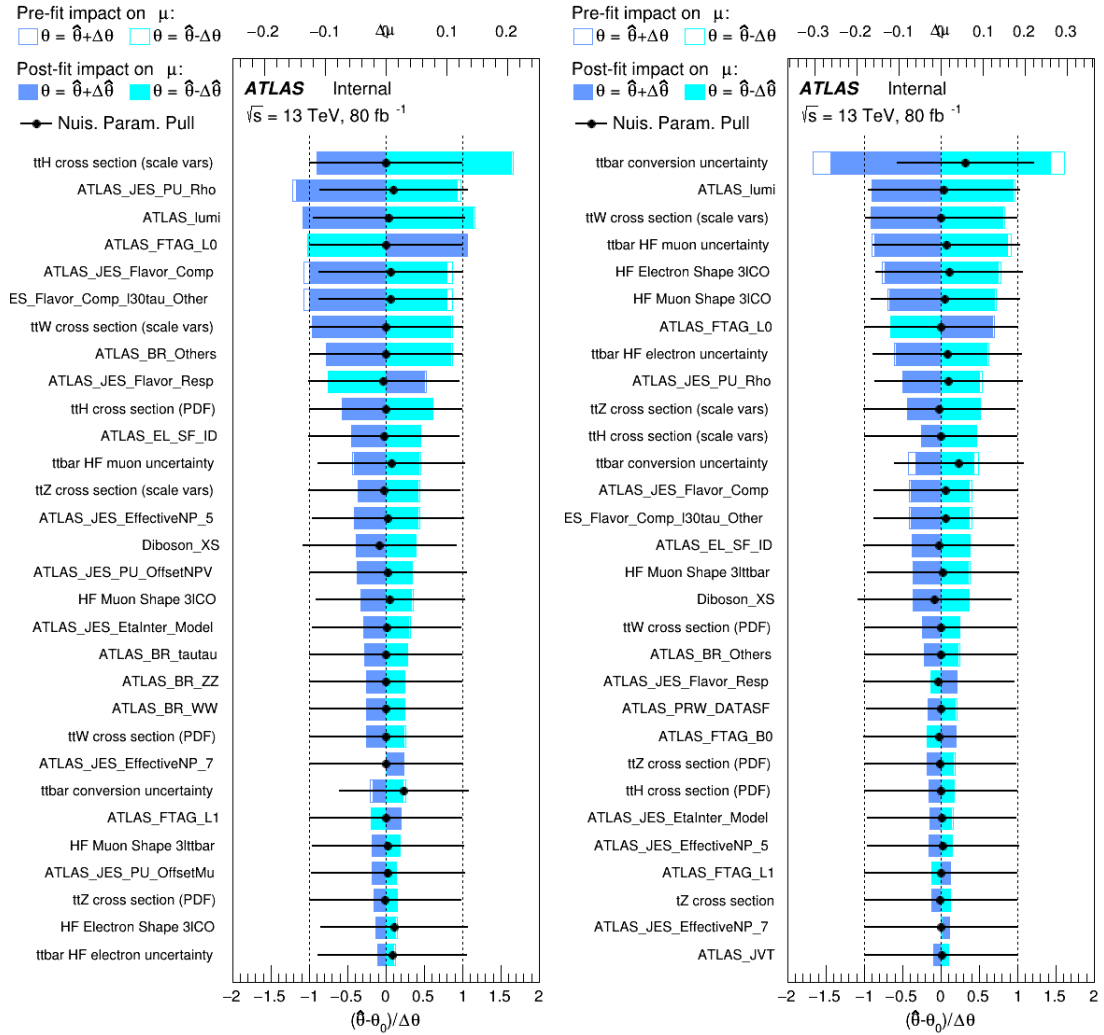


Figure 22.3: Impact of systematic uncertainties on the measurement of high p_T (left) and low p_T (right) $t\bar{t}H$ events

1625

The background composition of each of the fit regions is shown in Figure 22.4.

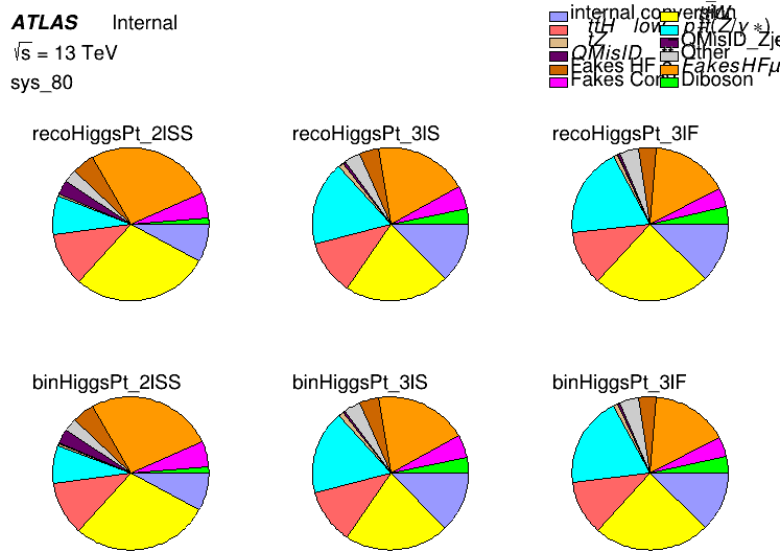


Figure 22.4: Background composition of the fit regions.

1626 **22.2 Projected Results - 140 fb^{-1}**

1627 As data collected in 2018 has not yet been unblinded for $t\bar{t}H$ – ML at the time of this note, data
1628 from that year remains blinded. Instead, an Asimov fit is performed - with the MC prediction
1629 being used both as the SM prediction as well as the data in the fit - in order to give expected
1630 results.

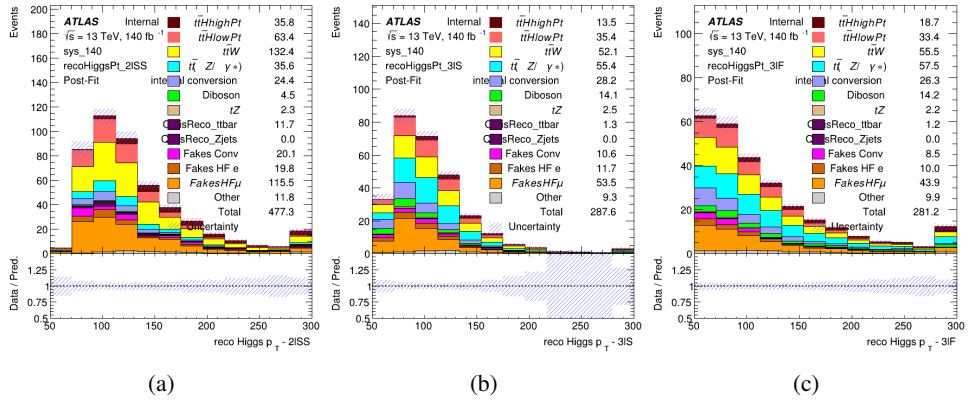


Figure 22.5: Blinded post-fit distributions of the reconstructed Higgs p_T in the three signal regions, (a) 2lSS, (b) 3lS, and (c) 3lF, for 140 fb^{-1} of data

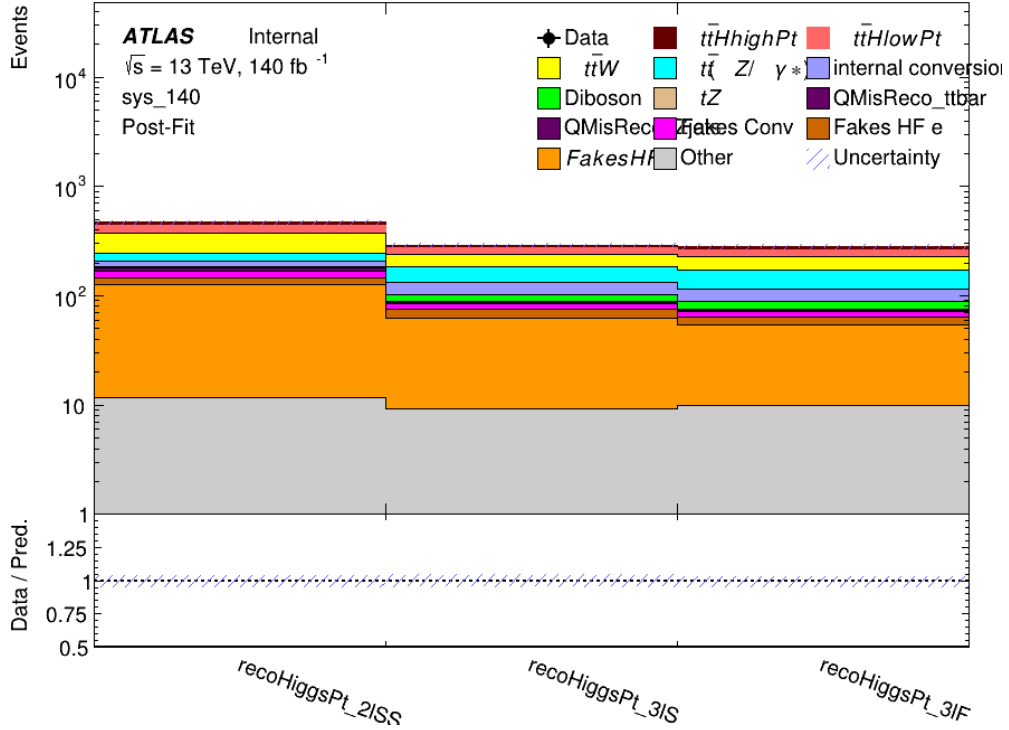


Figure 22.6: Post-fit summary of fit.

¹⁶³² shown in [52](#). A significance of 2.0σ is expected for $t\bar{t}H$ high p_T , and a projected significance

¹⁶³³ 2.3σ is extracted for $t\bar{t}H$ low p_T .

$$\mu_{t\bar{t}H \text{ high } p_T} = 1.00^{+0.45}_{-0.43}(\text{stat})^{+0.30}_{-0.31}(\text{sys})$$

$$\mu_{t\bar{t}H \text{ low } p_T} = 1.00^{+0.29}_{-0.30}(\text{stat})^{+0.48}_{-0.50}(\text{sys})$$

Table 52: Best fit μ values for $t\bar{t}H$ high p_T and $t\bar{t}H$ low p_T , where $\mu = \sigma_{\text{obs}}/\sigma_{\text{pred}}$

¹⁶³⁴ The most prominent sources of systematic uncertainty, as measured by their impact on

¹⁶³⁵ $\mu_{t\bar{t}H \text{ high } p_T}$, are summarized in Table ??.

Uncertainty Source	$\Delta\mu$	
Jet Energy Scale	0.19	0.17
$t\bar{t}W$ Cross-section (QCD Scale)	-0.12	0.11
Luminosity	-0.1	0.11
Flavor Tagging	0.1	0.1
$t\bar{t}H$ Cross-section (QCD Scale)	-0.05	0.1
$t\bar{t}Z$ Cross-section (QCD Scale)	-0.05	0.06
Non-prompt Muon Normalization	-0.05	0.05
Higgs Branching Ratio	-0.05	0.05
Diboson Cross-section	-0.04	0.05
Non-prompt Muon Modelling	-0.04	0.04
$t\bar{t}H$ Cross-section (PDF)	-0.03	0.04
Electron ID	-0.04	0.04
$t\bar{t}W$ Cross-section (PDF)	-0.03	0.03
Total	0.30	0.31

Table 53: Summary of the most significant sources of systematic uncertainty on the measurement of $t\bar{t}H$ high p_T .

¹⁶³⁶ The most significant sources of systematic uncertainty on $t\bar{t}H$ low p_T are summarized in

¹⁶³⁷ Table [54](#).

Uncertainty Source	$\Delta\mu$	
Internal Conversions	-0.18	0.2
Jet Energy Scale	0.19	0.16
Non-prompt Muon Normalization	-0.16	0.17
Luminosity	-0.15	0.17
t̄W Cross-section (QCD Scale)	-0.17	0.15
Non-prompt Electron Modelling	-0.13	0.14
Non-prompt Muon Modelling	-0.13	0.13
Flavor Tagging	0.13	0.12
Non-prompt Electron Normalization	-0.1	0.11
t̄Z Cross-section (QCD Scale)	-0.07	0.09
t̄H Cross-section (QCD Scale)	-0.05	0.1
Total	0.48	0.50

Table 54: Summary of the most significant sources of systematic uncertainty on the measurement of t̄H low p_T.

¹⁶³⁸ The ranking and impact of those nuisance parameters with the largest contribution to the
¹⁶³⁹ overall uncertainty is shown in Figure 22.7.

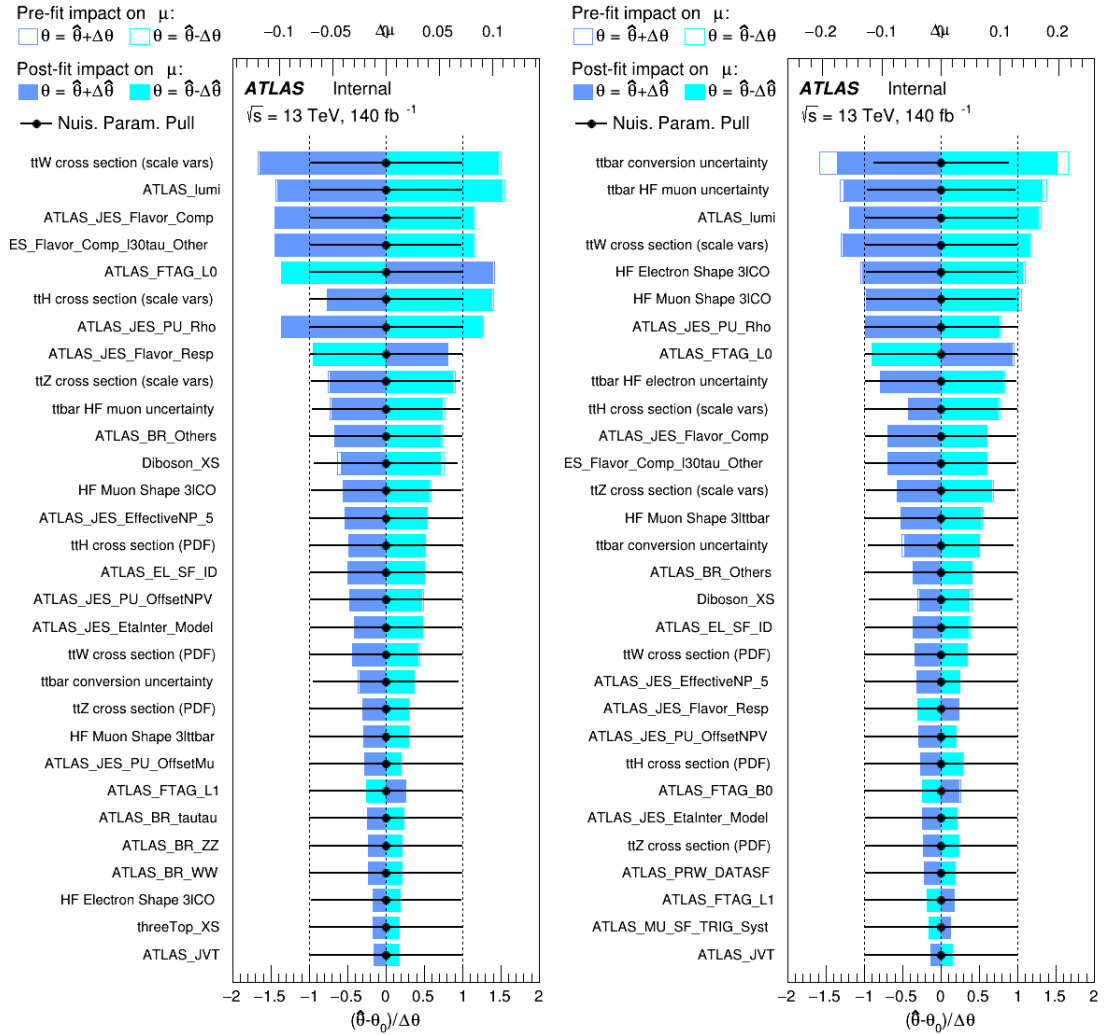


Figure 22.7: Impact of systematic uncertainties on the measurement of high p_T (left) and low p_T (right) $t\bar{t}H$ events

1640

The background composition of each of the fit regions is shown in Figure 22.8.

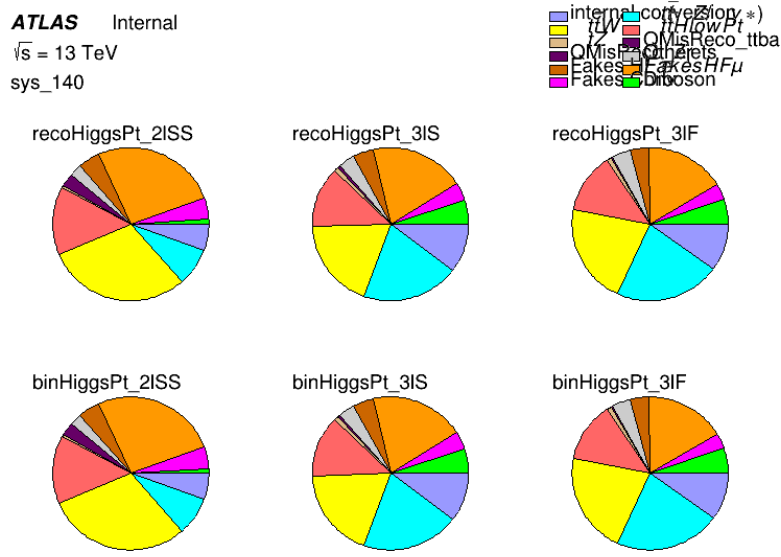


Figure 22.8: Background composition of the fit regions.

Part VI

Conclusion

As search for the effects of dimension-six operators on $t\bar{t}H$ production is performed. An effective field theory approach is used to parameterize the effects of high energy physics on the Higgs momentum spectrum. The momentum spectrum is reconstructed using various MVA techniques, and the limits on dimension-six operators are limited to X.

1647 References

- 1648 [1] R. Oerter, *The theory of almost everything : the Standard Model, the unsung triumph of*
1649 *modern physics*, Pi Press, 2006, ISBN: 978-0-13-236678-6.
- 1650 [2] P. W. Higgs, *Broken Symmetries and the Masses of Gauge Bosons*,
1651 Phys. Rev. Lett. 13 (Oct, 1964) 508-509 ().
- 1652 [3] J. Goldstone, A. Salam and S. Weinberg, *Broken Symmetries*,
1653 Phys. Rev. **127** (3 1962) 965,
1654 URL: <https://link.aps.org/doi/10.1103/PhysRev.127.965>.
- 1655 [4] J. Ellis, *Higgs Physics*,
1656 (2013) 117, 52 pages, 45 figures, Lectures presented at the ESHEP 2013 School of
1657 High-Energy Physics, to appear as part of the proceedings in a CERN Yellow Report,
1658 URL: <https://cds.cern.ch/record/1638469>.
- 1659 [5] *Evidence for the associated production of the Higgs boson and a top quark pair with the*
1660 *ATLAS detector*, tech. rep. ATLAS-CONF-2017-077, CERN, 2017,
1661 URL: <https://cds.cern.ch/record/2291405>.
- 1662 [6] A. M. Sirunyan et al., *Observation of $t\bar{t}H$ Production*,
1663 *Physical Review Letters* **120** (2018), ISSN: 1079-7114,
1664 URL: <http://dx.doi.org/10.1103/PhysRevLett.120.231801>.

- 1665 [7] B. Dumont, S. Fichet and G. von Gersdorff,
1666 *A Bayesian view of the Higgs sector with higher dimensional operators,*
1667 *Journal of High Energy Physics* **2013** (2013), ISSN: 1029-8479,
1668 URL: [http://dx.doi.org/10.1007/JHEP07\(2013\)065](http://dx.doi.org/10.1007/JHEP07(2013)065).
- 1669 [8] S. Banerjee, S. Mukhopadhyay and B. Mukhopadhyaya,
1670 *Higher dimensional operators and the LHC Higgs data: The role of modified kinematics,*
1671 *Physical Review D* **89** (2014), ISSN: 1550-2368,
1672 URL: <http://dx.doi.org/10.1103/PhysRevD.89.053010>.
- 1673 [9] M. Zinser, ‘The Large Hadron Collider’, *Search for New Heavy Charged Bosons and*
1674 *Measurement of High-Mass Drell-Yan Production in Proton—Proton Collisions,*
1675 Springer International Publishing, 2018 47, ISBN: 978-3-030-00650-1,
1676 URL: https://doi.org/10.1007/978-3-030-00650-1_4.
- 1677 [10] *Detector and Technology*, URL: <https://atlas.cern/discover/detector>.
- 1678 [11] M. Marjanovic, *ATLAS Tile calorimeter calibration and monitoring systems*, 2018.
- 1679 [12] M. Aaboud et al., *Observation of electroweak $W^\pm Z$ boson pair production in association*
1680 *with two jets in pp collisions at $\sqrt{s} = 13$ TeV with the ATLAS detector,*
1681 *Phys. Lett. B* **793** (2019) 469, arXiv: [1812.09740 \[hep-ex\]](https://arxiv.org/abs/1812.09740).
- 1682 [13] T. Gleisberg et al., *Event generation with SHERPA 1.1*, *JHEP* **02** (2009) 007,
1683 arXiv: [0811.4622 \[hep-ph\]](https://arxiv.org/abs/0811.4622).
- 1684 [14] R. D. Ball et al., *Parton distributions for the LHC Run II*, *JHEP* **04** (2015) 040,
1685 arXiv: [1410.8849 \[hep-ph\]](https://arxiv.org/abs/1410.8849).

- 1686 [15] H.-L. Lai et al., *New parton distributions for collider physics*,
 1687 [Phys. Rev. D](#) **82** (2010) 074024, arXiv: [1007.2241 \[hep-ph\]](#).
- 1688 [16] S. Frixione, G. Ridolfi and P. Nason,
 1689 *A positive-weight next-to-leading-order Monte Carlo for heavy flavour hadroproduction*,
 1690 [JHEP](#) **09** (2007) 126, arXiv: [0707.3088 \[hep-ph\]](#).
- 1691 [17] E. Re, *Single-top Wt-channel production matched with parton showers using the*
 1692 *POWHEG method*, [Eur. Phys. J. C](#) **71** (2011) 1547, arXiv: [1009.2450 \[hep-ph\]](#).
- 1693 [18] ATLAS Collaboration, *Electron efficiency measurements with the ATLAS detector using*
 1694 *the 2015 LHC proton–proton collision data*, ATLAS-CONF-2016-024, 2016,
 1695 URL: <https://cds.cern.ch/record/2157687>.
- 1696 [19] ATLAS Collaboration, *Measurement of the muon reconstruction performance of the*
 1697 *ATLAS detector using 2011 and 2012 LHC proton–proton collision data*,
 1698 [Eur. Phys. J. C](#) **74** (2014) 3130, arXiv: [1407.3935 \[hep-ex\]](#).
- 1699 [20] R. Narayan et al., *Measurement of the total and differential cross sections of a*
 1700 *top-quark-antiquark pair in association with a W boson in proton-proton collisions at a*
 1701 *centre-of-mass energy of 13 TeV with ATLAS detector at the Large Hadron Collider*,
 1702 tech. rep. ATL-COM-PHYS-2020-217, CERN, 2020,
 1703 URL: <https://cds.cern.ch/record/2712986>.
- 1704 [21] ATLAS Collaboration, *Jet Calibration and Systematic Uncertainties for Jets*
 1705 *Reconstructed in the ATLAS Detector at $\sqrt{s} = 13 \text{ TeV}$* , ATL-PHYS-PUB-2015-015,
 1706 2015, URL: <https://cds.cern.ch/record/2037613>.

- 1707 [22] ATLAS Collaboration,
1708 *Selection of jets produced in 13 TeV proton–proton collisions with the ATLAS detector,*
1709 ATLAS-CONF-2015-029, 2015, URL: <https://cds.cern.ch/record/2037702>.
- 1710 [23] ATLAS Collaboration, *Performance of pile-up mitigation techniques for jets in pp*
1711 *collisions at $\sqrt{s} = 8$ TeV using the ATLAS detector*, *Eur. Phys. J. C* **76** (2016) 581,
1712 arXiv: [1510.03823 \[hep-ex\]](https://arxiv.org/abs/1510.03823).
- 1713 [24] ATLAS Collaboration, *Performance of missing transverse momentum reconstruction*
1714 *with the ATLAS detector in the first proton–proton collisions at $\sqrt{s} = 13$ TeV,*
1715 ATL-PHYS-PUB-2015-027, 2015, URL: <https://cds.cern.ch/record/2037904>.
- 1716 [25] 2021, URL: https://twiki.cern.ch/twiki/bin/view/AtlasProtected/BTagCalibrationRecommendationsRelease21#Tools_for_Flavor_Tagging_Calibra.
- 1719 [26] P. S. A. Hoecker, *TMVA 4 Toolkit for Multivariate Data Analysis with ROOT*,
1720 arXiv:physics/0703039 (2013).
- 1721 [27] F. Cardillo et al., *Measurement of the fiducial and differential cross-section of a top*
1722 *quark pair in association with a Z boson at 13 TeV with the ATLAS detector*, (2019),
1723 URL: <https://cds.cern.ch/record/2672207>.
- 1724 [28] T. Chen and C. Guestrin, ‘XGBoost: A Scalable Tree Boosting System’,
1725 *Proceedings of the 22nd ACM SIGKDD International Conference on Knowledge*
1726 *Discovery and Data Mining*, KDD ’16, ACM, 2016 785, ISBN: 978-1-4503-4232-2,
1727 URL: <http://doi.acm.org/10.1145/2939672.2939785>.

- 1728 [29] ATLAS Collaboration, *Luminosity determination in pp collisions at $\sqrt{s} = 7 \text{ TeV}$ using*
1729 *the ATLAS detector at the LHC*, [Eur. Phys. J. C **71** \(2011\) 1630](#),
1730 arXiv: [1101.2185 \[hep-ex\]](#).
- 1731 [30] G. Avoni et al.,
1732 *The new LUCID-2 detector for luminosity measurement and monitoring in ATLAS*,
1733 [JINST **13** \(2018\) P07017](#).
- 1734 [31] G. Aad, T. Abajyan, B. Abbott and etal, *Jet energy resolution in proton-proton collisions*
1735 *at $\sqrt{s} = 7 \text{ TeV}$ recorded in 2010 with the ATLAS detector*,
1736 [The European Physical Journal C **73** \(2013\) 2306](#), ISSN: 1434-6052,
1737 URL: <https://doi.org/10.1140/epjc/s10052-013-2306-0>.
- 1738 [32] A. Collaboration, *Performance of b -jet identification in the ATLAS experiment*,
1739 [Journal of Instrumentation **11** \(2016\) P04008](#),
1740 URL: <http://stacks.iop.org/1748-0221/11/i=04/a=P04008>.
- 1741 [33] *Observation of the associated production of a top quark and a Z boson at 13 TeV with*
1742 *ATLAS*, (2020), URL: <https://cds.cern.ch/record/2722504>.

1743 List of contributions

1744

¹⁷⁴⁵ **Appendices**

¹⁷⁴⁶ **.1 Non-prompt lepton MVA**

1747 A lepton MVA has been developed to better reject non-prompt leptons than standard cut
1748 based selections based upon impact parameter, isolation and PID. The name of this MVA is
1749 **PromptLeptonIso**. The full set of studies and detailed explanation can be found in [20].

1750 The decays of W and Z bosons are commonly selected by the identification of one or two
1751 electrons or muons. The negligible lifetimes of these bosons mean that the leptons produced in the
1752 decay originate from the interaction vertex and are thus labelled “prompt”. Analyses using these
1753 light leptons impose strict reconstruction quality, isolation and impact parameter requirements
1754 to remove “fake” leptons. A significant source of the fake light leptons are non-prompt leptons
1755 produced in decays of hadrons that contain bottom (b) or charm (c) quarks. Such hadrons
1756 typically have microscopically significant lifetimes that can be detected experimentally.

1757 These non-prompt leptons can also pass the tight selection criteria. In analyses that
1758 involve top (t) quarks, which decay almost exclusively into a W boson and a b quark, non-
1759 prompt leptons from the semileptonic decay of bottom and charm hadrons can be a significant
1760 source of background events. This is particularly the case in the selection of same-sign dilepton
1761 and multilepton final states.

1762 The main idea is to identify non-prompt light leptons using lifetime information associated
1763 with a track jet that matches the selected light lepton. This lifetime information is computed
1764 using tracks contained within the jet. Typically, lepton lifetime is determined using the impact
1765 parameter of the track reconstructed by the inner tracking detector which is matched to the recon-
1766 structed lepton. Using additional reconstructed charged particle tracks increases the precision of

1767 identifying the displaced decay vertex of bottom or charm hadrons that produced a non-prompt
 1768 light lepton. The MVA also includes information related to the isolation of the lepton to reject
 1769 non-prompt leptons.

1770 **PromptLeptonIso** is a gradient boosted BDT. The training of the BDT is performed on
 1771 leptons selected from the PowHEG+PYTHIA6 non-allhad $t\bar{t}$ MC sample. Eight variables are used
 1772 to train the BDT in order to discriminate between prompt and non-prompt leptons. The track
 1773 jets that are matched to the non-prompt leptons correspond to jets initiated by b or c quarks, and
 1774 may contain a displaced vertex. Consequently, three of the selected variables are used to identify
 1775 b-tag jets by standard ATLAS flavour tagging algorithms. Two variables use the relationship
 1776 between the track jet and lepton: the ratio of the lepton p_T with respect to the track jet p_T and
 1777 ΔR between the lepton and the track jet axis. Finally three additional variables test whether the
 1778 reconstructed lepton is isolated: the number of tracks collected by the track jet and the lepton
 1779 track and calorimeter isolation variables. Table 55 describes the variables used to train the BDT
 1780 algorithm. The choice of input variables has been extensively discussed with Egamma, Muon,
 1781 Tracking, and Flavour Tagging CP groups.

Variable	Description
N_{track} in track jet	Number of tracks collected by the track jet
$\text{IP2 log}(P_b/P_{\text{light}})$	Log-likelihood ratio between the b and light jet hypotheses with the IP2D algorithm
$\text{IP3 log}(P_b/P_{\text{light}})$	Log-likelihood ratio between the b and light jet hypotheses with the IP3D algorithm
$N_{\text{TrkAtVtx}} \text{ SV + JF}$	Number of tracks used in the secondary vertex found by the SV1 algorithm in addition to the number of tracks from secondary vertices found by the JetFitter algorithm with at least two tracks
$p_T^{\text{lepton}}/p_T^{\text{track jet}}$	The ratio of the lepton p_T and the track jet p_T
$\Delta R(\text{lepton}, \text{track jet})$	ΔR between the lepton and the track jet axis
$p_T^{\text{VarCone30}}/p_T$	Lepton track isolation, with track collecting radius of $\Delta R < 0.3$
$E_T^{\text{TopoCone30}}/p_T$	Lepton calorimeter isolation, with topological cluster collecting radius of $\Delta R < 0.3$

Table 55: A table of the variables used in the training of **PromptLeptonIso**.

1782 The output distribution of the BDT is shown in Figure .1.

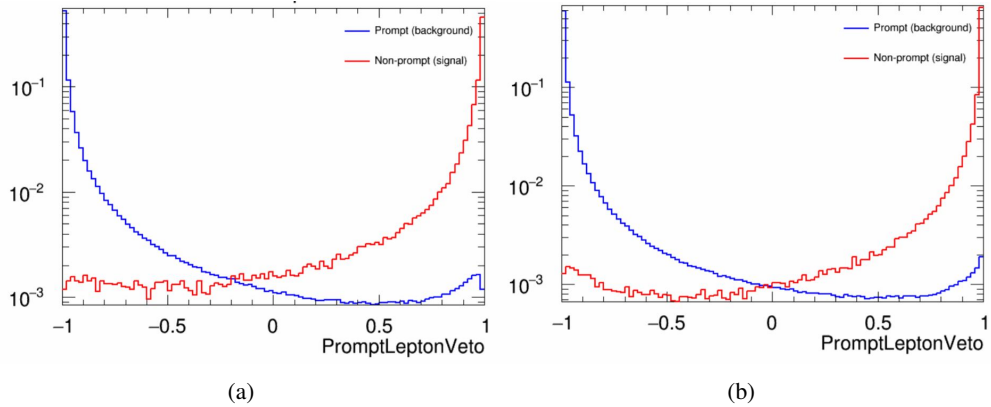


Figure .9: Distribution of the PLV BDT discriminant for (a) electrons and (b) muons

1783 The ROC curve for the BDT response, compared to the standard **FixedCutTight** WP, is
1784 shown in figure .1, which shows a clear improvement when using this alternate training.

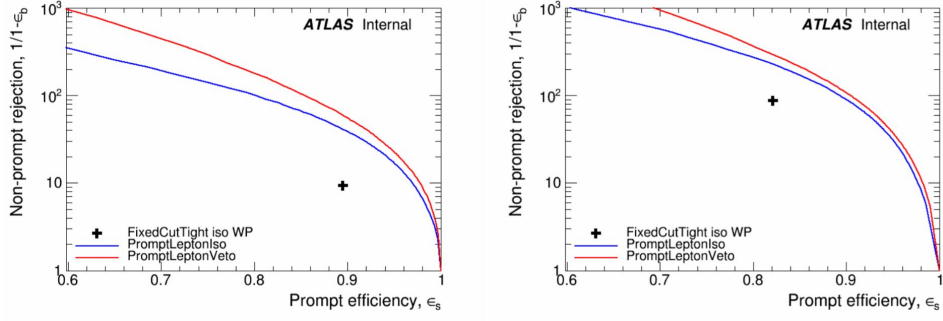


Figure .10: ROC curves for the PLV as well as the performance of the standard FixedCutTight WP for (left) electrons and (right) muons

A cutoff value of -0.7 for electrons and -0.5 for muons are chosen as the WPs for this
 MVA, based on an optimisation of S/\sqrt{B} performed in the preselection regions of the $t\bar{t}H - ML$
 analysis, which have a signature similar to that of this analysis.

1788 The efficiency of the tight `PromptLeptonIso` working point is measured using the tag
1789 and probe method with $Z \rightarrow \ell^+ \ell^-$ events. Such calibration are performed by analysers from
1790 this analysis in communication with the Egamma and Muon combined performance groups. The
1791 scale factor are approximately 0.92 for $10 < p_T < 15$ GeV, and averaging at 0.98 to 0.99 for
1792 higher p_T leptons. An extra systematic is applied to muons within $\Delta R < 0.6$ of a calorimeter
1793 jet, since there is a strong dependence on the scale factor due to the presence of these jets. For
1794 electrons, the dominant systematics is coming from pile-up dependence. Overall the systematics
1795 are a maximum of 3% at low p_T and decreasing at a function of p_T .

¹⁷⁹⁶ **.2 Non-prompt CR Modelling**

1797 In order to further validate the modeling in each of the non-prompt CRs, additional
 1798 kinematic plots are made in the Z+jets CR and $t\bar{t}$ CR in each of the continuous b-tag regions,
 1799 after the correction factors detailed in Section 12.3 have been applied.

1800 In the case of the Z+jets CR, the p_T spectrum of the lepton originating from the W
 1801 candidate is shown, as this is the distribution used to extract the scale factor applied to Z+jets.
 1802 These plots are shown in Figures .11 and .12.

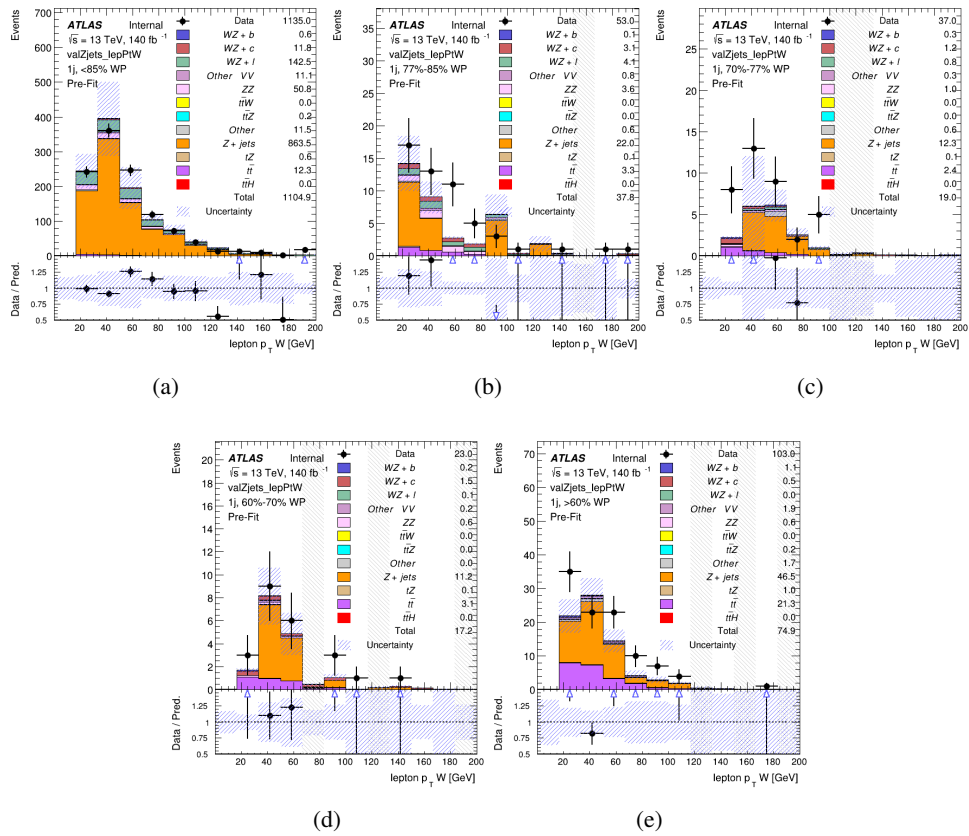


Figure .11: Comparisons between the data and MC distributions of the p_T of the lepton originating from the W-candidate in the Z+jets CR for each of the 1-jet b-tag working point regions

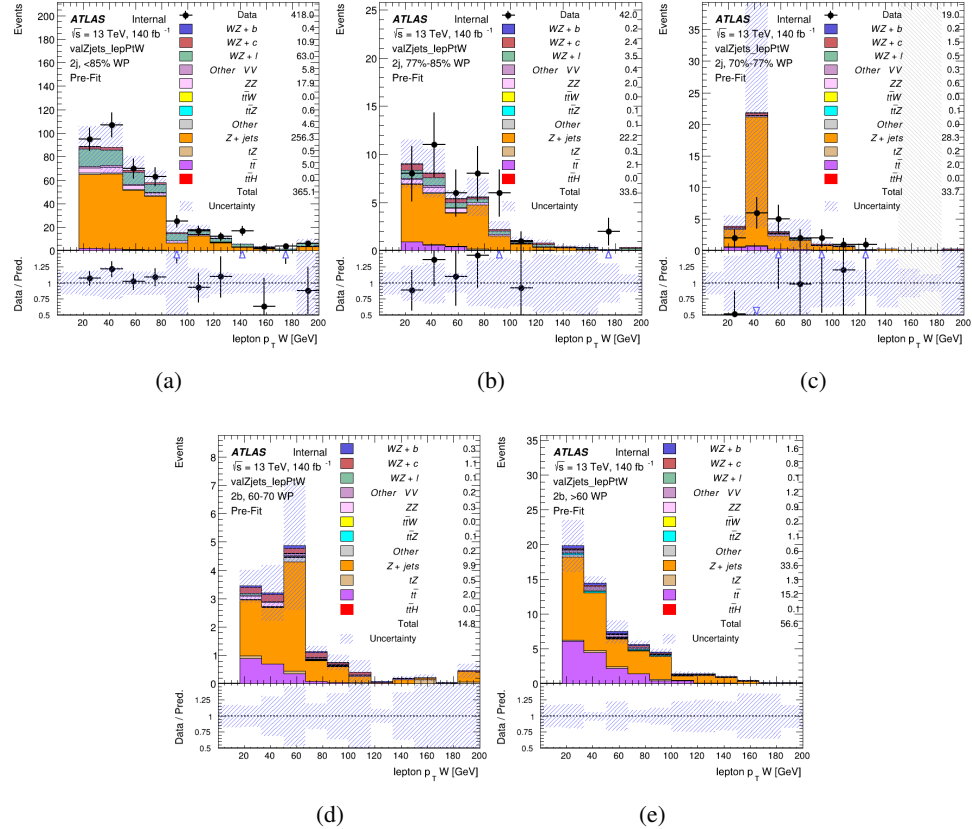


Figure .12: Comparisons between the data and MC distributions of the p_T of the lepton originating from the W-candidate in the Z+jets CR for each of the 2-jet b-tag working point regions

1803 The same is shown for the $t\bar{t}$ CR, but the p_T of the OS lepton is used instead as a
 1804 representation of the modeling, as the lepton from the W is not well defined for $t\bar{t}$ events. These
 1805 plots are shown in Figures .13 and .14.

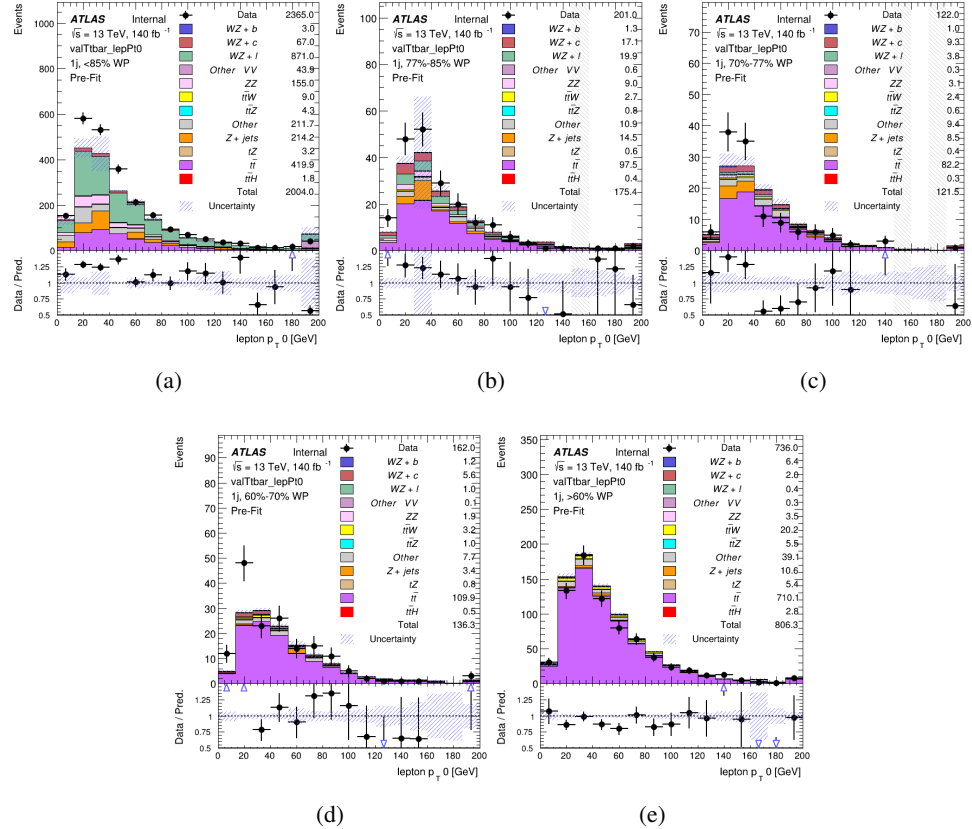


Figure .13: Comparisons between the data and MC distributions of the p_T of the OS lepton in the $t\bar{t}$ CR for each of the 1-jet b-tag working point regions

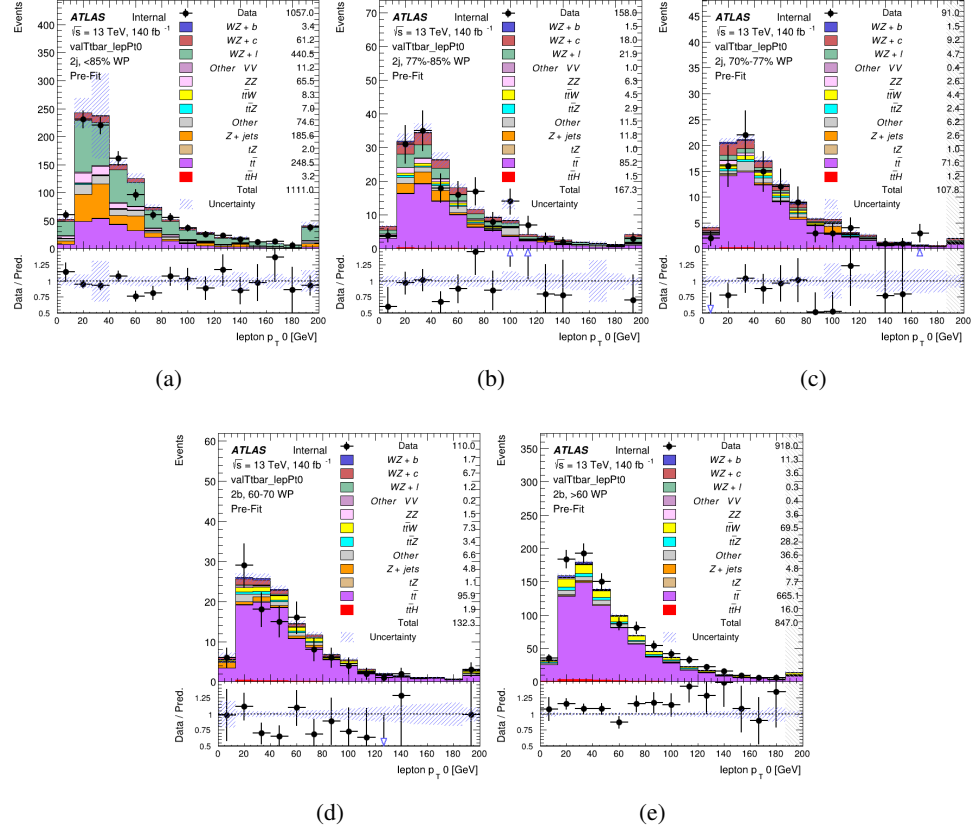


Figure 14: Comparisons between the data and MC distributions of the p_T of the OS lepton in the $t\bar{t}$ CR for each of the 2-jet b-tag working point regions

1806 .3 tZ Interference Studies

1807 Because it includes an on-shell Z boson as well as a b-jet and W from the top decay, tZ
1808 production represents an identical final state to WZ + b-jet. This implies the possibility of matrix
1809 level interference between these two processes not accounted for in the Monte Carlo simulations,
1810 which consider the two processes independently. Truth level studies are performed in order to
1811 estimate the impact of these interference effects.

1812 In order to estimate the matrix level interference effects between tZ and WZ + b-jet, two
1813 different sets of simulations are produced using MadGraph 5 [**Madgraph**] - one which simulates
1814 these two processes independently, and another where they are produced simultaneously, such
1815 that interference effects are present. These two sets of samples are then compared, and the
1816 difference between them can be taken to represent any interference effects.

1817 MadGraph simulations of 10,000 tZ and 10,000 WZ + b-jet events are produced, along
1818 with 20,000 events where both are present, in the fiducial region where three leptons and at least
1819 one jet are produced.

1820 A selection mimicking the preselection used in the main analysis is applied to the samples:
1821 The SS leptons are required to have $p_T > 20$ GeV, and > 10 GeV is required for the OS lepton.
1822 The associated b-jet is required to have $p_T > 25$ GeV, and all physics objects are required to fall
1823 in a range of $|\eta| < 2.5$.

1824 The kinematics of these samples after the selection has been applied are shown below:

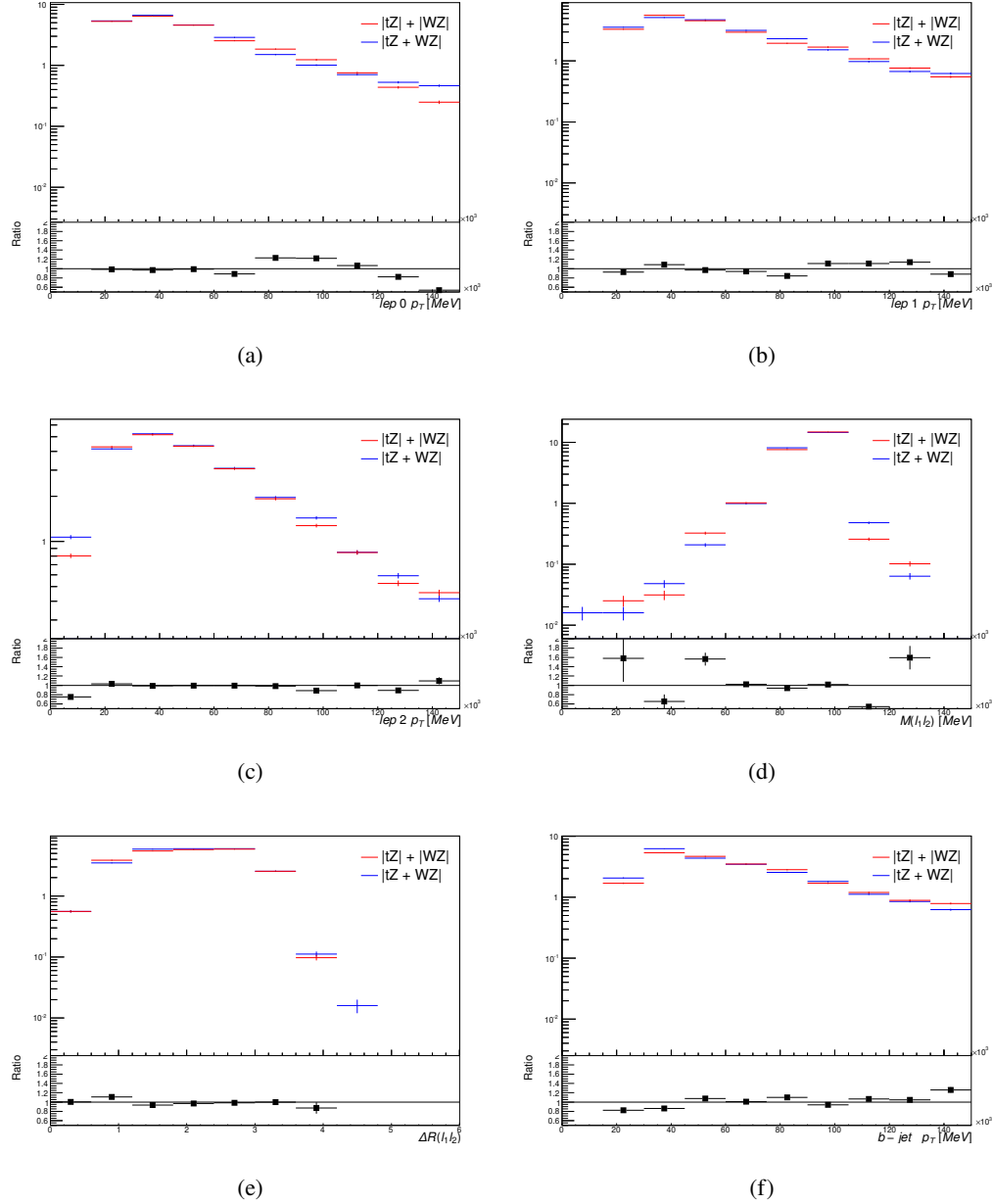


Figure .15: Comparisons between (a) the p_T of the lepton from the W, (b) and (c) show the p_T of the lepton from the Z, (d) the invariant mass of the Z-candidate, (e) ΔR of the leptons from the Z, and (f) the p_T of the b-jet, for WZ and tZ events generated with interference effects (blue) and without interference effects (red).

1825 The overall cross-section of the two methods agree within error, and no significant differ-
1826 ences in the kinematic distributions are seen. It is therefore concluded that interference effects
1827 do not significantly impact the results.

1828 **.4 Alternate tZ Inclusive Fit**

1829 **.4.1 tZ Inclusive Fit**

1830 While tZ is often considered as a distinct process from WZ + b, this could also be considered part
1831 of the signal. Alternate studies are performed where, using the same framework as the nominal
1832 analysis, a measurement of WZ + b is performed that includes tZ as part of WZ+b.

1833 Because of this change, the tZ CR is no longer necessary, and only the five pseudo-
1834 continuous b-tag regions are used in the fit. Further, systematics related to the tZ cross-section
1835 are removed from the fit, as they are now encompassed by the normalization measurement of
1836 WZ + b. All other systematic uncertainties are carried over from the nominal analysis.

1837 An expected WZ + b cross-section of $4.1^{+0.78}_{-0.74}(\text{stat})^{+0.53}_{-0.52}(\text{sys}) \text{ fb}$ is extracted from the fit,
1838 with an expected significance of 4.0σ .

1839 The impact of the predominate systematics are summarized in Table 56.

Uncertainty Source	$\Delta\mu$	
WZ + light cross-section	0.08	-0.08
Jet Energy Scale	-0.06	0.08
Luminosity	-0.05	0.06
WZ + charm cross-section	-0.04	0.05
Other Diboson + b cross-section	-0.04	0.04
WZ cross-section - QCD scale	-0.04	0.03
t̄t cross-section	-0.03	0.03
Jet Energy Resolution	-0.03	0.03
Flavor tagging	-0.03	0.03
Z+jets cross section	-0.02	0.02
Total Systematic Uncertainty	-0.15	0.16

Table 56: Summary of the most significant sources of systematic uncertainty on the measurement of WZ + b with exactly one associated jet.

1840 **.4.2 Floating tZ**

1841 In order to quantify the impact of the tZ uncertainty on the fit, an alternate fit strategy is used
1842 where the tZ normalization is allowed to float. This normalization factor replaces the cross-
1843 section uncertainty on tZ, and all other parameters of the fit remain the same.

1844 An uncertainty of 17% on the normalization of tZ is extracted from the fit, compared to a
1845 theory uncertainty of 15% applied to the tZ cross-section. The measured uncertainties on WZ
1846 remain the same.

1847 .5 DSID list

Data:

```
data15_13TeV.AllYear.physics_Main.PhysCont.DAOD_HIGG8D1.grp15_v01_p4134
data16_13TeV.AllYear.physics_Main.PhysCont.DAOD_HIGG8D1.grp16_v01_p4134
data17_13TeV.AllYear.physics_Main.PhysCont.DAOD_HIGG8D1.grp17_v01_p4134
data18_13TeV.AllYear.physics_Main.PhysCont.DAOD_HIGG8D1.grp18_v01_p4134
```

mc16a:

```
mc16_13TeV.361603.PowhegPy8EG_CT10nloME_AZNLOCTEQ6L1_ZZllll_mll4.deriv.DAOD_HIGG8D1.e4475_s3126_r9364_r9315_p4133
mc16_13TeV.361602.PowhegPy8EG_CT10nloME_AZNLOCTEQ6L1_WZlvvv_mll4.deriv.DAOD_HIGG8D1.e4054_s3126_r9364_r9315_p4133
mc16_13TeV.361604.PowhegPy8EG_CT10nloME_AZNLOCTEQ6L1_ZZvvll_mll4.deriv.DAOD_HIGG8D1.e4475_s3126_r9364_r9315_p4133
mc16_13TeV.361600.PowhegPy8EG_CT10nloME_AZNLOCTEQ6L1_WWlvvv.deriv.DAOD_HIGG8D1.e4616_s3126_r9364_r9315_p4133
mc16_13TeV.361605.PowhegPy8EG_CT10nloME_AZNLOCTEQ6L1_ZZvvvv_mll4.deriv.DAOD_HIGG8D1.e4054_s3126_s3136_r9364_r9315_p4133
mc16_13TeV.361601.PowhegPy8EG_CT10nloME_AZNLOCTEQ6L1_WZlVll_mll4.deriv.DAOD_HIGG8D1.e4475_s3126_r9364_r9315_p4133
mc16_13TeV.364286.Sherpa_222_NNPDF30NNLO_llvjj_ss_EW4.deriv.DAOD_HIGG8D1.e6055_e5984_s3126_r9364_r9315_p3983 mc16_13TeV.364285.Sherpa_222_NNPDF30NNLO_llvjj_EW6_OFPlus.deriv.DAOD_HIGG8D1.e7421_e5984_s3126_r9364_r9315_p4133
mc16_13TeV.364740.MGPy8EG_NNPDF30NLO_A14NNPDF23LO_lvlljj_EW6_SFPlus.deriv.DAOD_HIGG8D1.e7421_e5984_s3126_r9364_r9315_p4133
mc16_13TeV.364742.MGPy8EG_NNPDF30NLO_A14NNPDF23LO_lvlljj_EW6_SFPlus.deriv.DAOD_HIGG8D1.e7421_e5984_s3126_r9364_r9315_p4133
mc16_13TeV.364253.Sherpa_222_NNPDF30NNLO_llv.deriv.DAOD_HIGG8D1.e5916_s3126_r9364_r9315_p4133
mc16_13TeV.364250.Sherpa_222_NNPDF30NNLO_lll.deriv.DAOD_HIGG8D1.e5894_s3126_r9364_r9315_p4133
mc16_13TeV.364254.Sherpa_222_NNPDF30NNLO_llv.deriv.DAOD_HIGG8D1.e5916_s3126_r9364_r9315_p4133
mc16_13TeV.364255.Sherpa_222_NNPDF30NNLO_lvvv.deriv.DAOD_HIGG8D1.e5916_s3126_r9364_r9315_p4133
mc16_13TeV.410155.aMcAtNloPythia8EvtGen_MEN30NLO_A14N23LO_ttW.deriv.DAOD_HIGG8D1.e5070_s3126_r9364_r9315_p4133
mc16_13TeV.410156.aMcAtNloPythia8EvtGen_MEN30NLO_A14N23LO_ttZnunu.deriv.DAOD_HIGG8D1.e5070_s3126_r9364_r9315_p4133
mc16_13TeV.410157.aMcAtNloPythia8EvtGen_MEN30NLO_A14N23LO_ttZqq.deriv.DAOD_HIGG8D1.e5070_s3126_r9364_r9315_p4133
mc16_13TeV.410218.aMcAtNloPythia8EvtGen_MEN30NLO_A14N23LO_ttee.deriv.DAOD_HIGG8D1.e5070_s3126_r9364_r9315_p4133
mc16_13TeV.410219.aMcAtNloPythia8EvtGen_MEN30NLO_A14N23LO_ttmumu.deriv.DAOD_HIGG8D1.e5070_s3126_r9364_r9315_p4133
mc16_13TeV.410220.aMcAtNloPythia8EvtGen_MEN30NLO_A14N23LO_ttautau.deriv.DAOD_HIGG8D1.e5070_s3126_r9364_r9315_p4133
mc16_13TeV.412063.aMcAtNloPythia8EvtGen_tllq_NNPDF30_nf4_A14.deriv.DAOD_TOPQ1.e7054_e5984_s3126_r9364_r9315_p4174
mc16_13TeV.410276.aMcAtNloPythia8EvtGen_MEN30NLO_A14N23LO_ttee_mll_1_5.deriv.DAOD_HIGG8D1.e6087_e5984_s3126_r9364_r9315_p4133
mc16_13TeV.410277.aMcAtNloPythia8EvtGen_MEN30NLO_A14N23LO_ttmumu_mll_1_5.deriv.DAOD_HIGG8D1.e6087_e5984_s3126_r9364_r9315_p4133
mc16_13TeV.410278.aMcAtNloPythia8EvtGen_MEN30NLO_A14N23LO_ttautau_mll_1_5.deriv.DAOD_HIGG8D1.e6087_e5984_s3126_r9364_r9315_p4133
mc16_13TeV.410397.MadGraphPythia8EvtGen_ttbar_wbee_MEN30LO_A14N23LO.deriv.DAOD_HIGG8D1.e6086_e5984_s3126_r9364_r9315_p4133
```

mc16_13TeV.410398.MadGraphPythia8EvtGen_ttbar_wbmumu_MEN30LO_A14N23LO.deriv.DAOD_HIGG8D1.e6086_e5984_s3126_r9364_r9315_p4133
 mc16_13TeV.410399.MadGraphPythia8EvtGen_ttbar_wbtautau_MEN30LO_A14N23LO.deriv.DAOD_HIGG8D1.e6086_e5984_s3126_r9364_r9315_p4133
 mc16_13TeV.410658.PhPy8EG_A14_tchan_BW50_lept_top.deriv.DAOD_HIGG8D1.e6671_e5984_s3126_r9364_r9315_p4133
 mc16_13TeV.410659.PhPy8EG_A14_tchan_BW50_lept_antitop.deriv.DAOD_HIGG8D1.e6671_e5984_s3126_r9364_r9315_p4133
 mc16_13TeV.410644.PowhegPythia8EvtGen_A14_singletop_schan_lept_top.deriv.DAOD_HIGG8D1.e6527_e5984_s3126_r9364_r9315_p4133
 mc16_13TeV.410645.PowhegPythia8EvtGen_A14_singletop_schan_lept_antitop.deriv.DAOD_HIGG8D1.e6527_e5984_s3126_r9364_r9315_p4133
 mc16_13TeV.304014.MadGraphPythia8EvtGen_A14NNPDF23_3top_SM.deriv.DAOD_HIGG8D1.e4324_s3126_r9364_r9315_p4133
 mc16_13TeV.410080.MadGraphPythia8EvtGen_A14NNPDF23_4topSM.deriv.DAOD_HIGG8D1.e4111_s3126_r9364_r9315_p4133
 mc16_13TeV.410081.MadGraphPythia8EvtGen_A14NNPDF23_ttbarWW.deriv.DAOD_HIGG8D1.e4111_s3126_r9364_r9315_p4133
 mc16_13TeV.364100.Sherpa_221_NNPDF30NNLO_Zmumu_MAXHTPTV0_70_CVetoBVeto.deriv.DAOD_HIGG8D1.e5271_s3126_r9364_r9315_p4133
 mc16_13TeV.364101.Sherpa_221_NNPDF30NNLO_Zmumu_MAXHTPTV0_70_CFilterBVeto.deriv.DAOD_HIGG8D1.e5271_s3126_r9364_r9315_p4133
 mc16_13TeV.364102.Sherpa_221_NNPDF30NNLO_Zmumu_MAXHTPTV0_70_BFilter.deriv.DAOD_HIGG8D1.e5271_s3126_r9364_r9315_p4133
 mc16_13TeV.364103.Sherpa_221_NNPDF30NNLO_Zmumu_MAXHTPTV70_140_CVetoBVeto.deriv.DAOD_HIGG8D1.e5271_s3126_r9364_r9315_p4133
 mc16_13TeV.364104.Sherpa_221_NNPDF30NNLO_Zmumu_MAXHTPTV70_140_CFilterBVeto.deriv.DAOD_HIGG8D1.e5271_s3126_r9364_r9315_p4133
 mc16_13TeV.364106.Sherpa_221_NNPDF30NNLO_Zmumu_MAXHTPTV140_280_CVetoBVeto.deriv.DAOD_HIGG8D1.e5271_s3126_r9364_r9315_p4133
 mc16_13TeV.364107.Sherpa_221_NNPDF30NNLO_Zmumu_MAXHTPTV140_280_CFilterBVeto.deriv.DAOD_HIGG8D1.e5271_s3126_r9364_r9315_p4133
 mc16_13TeV.364108.Sherpa_221_NNPDF30NNLO_Zmumu_MAXHTPTV140_280_BFilter.deriv.DAOD_HIGG8D1.e5271_s3126_r9364_r9315_p4133
 mc16_13TeV.364109.Sherpa_221_NNPDF30NNLO_Zmumu_MAXHTPTV280_500_CVetoBVeto.deriv.DAOD_HIGG8D1.e5271_s3126_r9364_r9315_p4133
 mc16_13TeV.364110.Sherpa_221_NNPDF30NNLO_Zmumu_MAXHTPTV280_500_CFilterBVeto.deriv.DAOD_HIGG8D1.e5271_s3126_r9364_r9315_p4133
 mc16_13TeV.364111.Sherpa_221_NNPDF30NNLO_Zmumu_MAXHTPTV280_500_BFilter.deriv.DAOD_HIGG8D1.e5271_e5984_s3126_r9364_r9315_p4133
 mc16_13TeV.364111.Sherpa_221_NNPDF30NNLO_Zmumu_MAXHTPTV280_500_BFilter.deriv.DAOD_HIGG8D1.e5271_s3126_r9364_r9315_p4133
 mc16_13TeV.364112.Sherpa_221_NNPDF30NNLO_Zmumu_MAXHTPTV500_1000.deriv.DAOD_HIGG8D1.e5271_s3126_r9364_r9315_p4133
 mc16_13TeV.364113.Sherpa_221_NNPDF30NNLO_Zmumu_MAXHTPTV1000_E_CMS.deriv.DAOD_HIGG8D1.e5271_s3126_r9364_r9315_p4133
 mc16_13TeV.364114.Sherpa_221_NNPDF30NNLO_Zee_MAXHTPTV0_70_CVetoBVeto.deriv.DAOD_HIGG8D1.e5299_s3126_r9364_r9315_p4133
 mc16_13TeV.364115.Sherpa_221_NNPDF30NNLO_Zee_MAXHTPTV0_70_CFilterBVeto.deriv.DAOD_HIGG8D1.e5299_s3126_r9364_r9315_p4133
 mc16_13TeV.364116.Sherpa_221_NNPDF30NNLO_Zee_MAXHTPTV0_70_BFilter.deriv.DAOD_HIGG8D1.e5299_s3126_r9364_r9315_p4133
 mc16_13TeV.364117.Sherpa_221_NNPDF30NNLO_Zee_MAXHTPTV70_140_CVetoBVeto.deriv.DAOD_HIGG8D1.e5299_s3126_r9364_r9315_p4133
 mc16_13TeV.364118.Sherpa_221_NNPDF30NNLO_Zee_MAXHTPTV70_140_CFilterBVeto.deriv.DAOD_HIGG8D1.e5299_s3126_r9364_r9315_p4133
 mc16_13TeV.364119.Sherpa_221_NNPDF30NNLO_Zee_MAXHTPTV70_140_BFilter.deriv.DAOD_HIGG8D1.e5299_s3126_r9364_r9315_p4133
 mc16_13TeV.364120.Sherpa_221_NNPDF30NNLO_Zee_MAXHTPTV140_280_CVetoBVeto.deriv.DAOD_HIGG8D1.e5299_s3126_r9364_r9315_p4133
 mc16_13TeV.364121.Sherpa_221_NNPDF30NNLO_Zee_MAXHTPTV140_280_CFilterBVeto.deriv.DAOD_HIGG8D1.e5299_s3126_r9364_r9315_p4133

mc16_13TeV.364122.Sherpa_221_NNPDF30NNLO_Zee_MAXHTPTV140_280_BFilter.deriv.DAOD_HIGG8D1.e5299_s3126_r9364_r9315_p4133
 mc16_13TeV.364123.Sherpa_221_NNPDF30NNLO_Zee_MAXHTPTV280_500_CVetoBVeto.deriv.DAOD_HIGG8D1.e5299_s3126_r9364_r9315_p4133
 mc16_13TeV.364124.Sherpa_221_NNPDF30NNLO_Zee_MAXHTPTV280_500_CFilterBVeto.deriv.DAOD_HIGG8D1.e5299_s3126_r9364_r9315_p4133
 mc16_13TeV.364125.Sherpa_221_NNPDF30NNLO_Zee_MAXHTPTV280_500_BFilter.deriv.DAOD_HIGG8D1.e5299_s3126_r9364_r9315_p4133
 mc16_13TeV.364125.Sherpa_221_NNPDF30NNLO_Zee_MAXHTPTV280_500_BFilter.deriv.DAOD_HIGG8D1.e5299_e5984_s3126_r9364_r9315_p4133
 mc16_13TeV.364126.Sherpa_221_NNPDF30NNLO_Zee_MAXHTPTV500_1000.deriv.DAOD_HIGG8D1.e5299_s3126_r9364_r9315_p4133
 mc16_13TeV.364127.Sherpa_221_NNPDF30NNLO_Zee_MAXHTPTV1000_E_CMS.deriv.DAOD_HIGG8D1.e5299_s3126_r9364_r9315_p4133
 mc16_13TeV.364128.Sherpa_221_NNPDF30NNLO_Ztautau_MAXHTPTV0_70_CVetoBVeto.deriv.DAOD_HIGG8D1.e5307_s3126_r9364_r9315_p4133
 mc16_13TeV.364129.Sherpa_221_NNPDF30NNLO_Ztautau_MAXHTPTV0_70_CFilterBVeto.deriv.DAOD_HIGG8D1.e5307_s3126_r9364_r9315_p4133
 mc16_13TeV.364130.Sherpa_221_NNPDF30NNLO_Ztautau_MAXHTPTV0_70_BFilter.deriv.DAOD_HIGG8D1.e5307_s3126_r9364_r9315_p4133
 mc16_13TeV.364131.Sherpa_221_NNPDF30NNLO_Ztautau_MAXHTPTV70_140_CVetoBVeto.deriv.DAOD_HIGG8D1.e5307_s3126_r9364_r9315_p4133
 mc16_13TeV.364132.Sherpa_221_NNPDF30NNLO_Ztautau_MAXHTPTV70_140_CFilterBVeto.deriv.DAOD_HIGG8D1.e5307_s3126_r9364_r9315_p4133
 mc16_13TeV.364133.Sherpa_221_NNPDF30NNLO_Ztautau_MAXHTPTV70_140_BFilter.deriv.DAOD_HIGG8D1.e5307_s3126_r9364_r9315_p4133
 mc16_13TeV.364134.Sherpa_221_NNPDF30NNLO_Ztautau_MAXHTPTV140_280_CVetoBVeto.deriv.DAOD_HIGG8D1.e5307_s3126_r9364_r9315_p4133
 mc16_13TeV.364135.Sherpa_221_NNPDF30NNLO_Ztautau_MAXHTPTV140_280_CFilterBVeto.deriv.DAOD_HIGG8D1.e5307_s3126_r9364_r9315_p4133
 mc16_13TeV.364136.Sherpa_221_NNPDF30NNLO_Ztautau_MAXHTPTV140_280_BFilter.deriv.DAOD_HIGG8D1.e5307_s3126_r9364_r9315_p4133
 mc16_13TeV.364137.Sherpa_221_NNPDF30NNLO_Ztautau_MAXHTPTV280_500_CVetoBVeto.deriv.DAOD_HIGG8D1.e5307_e5984_s3126_r9364_r9315_p4133
 mc16_13TeV.364137.Sherpa_221_NNPDF30NNLO_Ztautau_MAXHTPTV280_500_CVetoBVeto.deriv.DAOD_HIGG8D1.e5307_s3126_r9364_r9315_p4133
 mc16_13TeV.364138.Sherpa_221_NNPDF30NNLO_Ztautau_MAXHTPTV280_500_CFilterBVeto.deriv.DAOD_HIGG8D1.e5313_s3126_r9364_r9315_p4133
 mc16_13TeV.364139.Sherpa_221_NNPDF30NNLO_Ztautau_MAXHTPTV280_500_BFilter.deriv.DAOD_HIGG8D1.e5313_s3126_r9364_r9315_p4133
 mc16_13TeV.364140.Sherpa_221_NNPDF30NNLO_Ztautau_MAXHTPTV500_1000.deriv.DAOD_HIGG8D1.e5307_s3126_r9364_r9315_p4133
 mc16_13TeV.364141.Sherpa_221_NNPDF30NNLO_Ztautau_MAXHTPTV1000_E_CMS.deriv.DAOD_HIGG8D1.e5307_s3126_r9364_r9315_p4133
 mc16_13TeV.364198.Sherpa_221_NN30NNLO_Zmm_Mll10_40_MAXHTPTV0_70_BVeto.deriv.DAOD_HIGG8D1.e5421_s3126_r9364_r9315_p4133
 mc16_13TeV.364199.Sherpa_221_NN30NNLO_Zmm_Mll10_40_MAXHTPTV0_70_BFilter.deriv.DAOD_HIGG8D1.e5421_s3126_r9364_r9315_p4133
 mc16_13TeV.364200.Sherpa_221_NN30NNLO_Zmm_Mll10_40_MAXHTPTV70_280_BVeto.deriv.DAOD_HIGG8D1.e5421_s3126_r9364_r9315_p4133
 mc16_13TeV.364201.Sherpa_221_NN30NNLO_Zmm_Mll10_40_MAXHTPTV70_280_BFilter.deriv.DAOD_HIGG8D1.e5421_s3126_r9364_r9315_p4133
 mc16_13TeV.364202.Sherpa_221_NN30NNLO_Zmm_Mll10_40_MAXHTPTV280_E_CMS_BVeto.deriv.DAOD_HIGG8D1.e5421_s3126_r9364_r9315_p4133
 mc16_13TeV.364203.Sherpa_221_NN30NNLO_Zmm_Mll10_40_MAXHTPTV280_E_CMS_BFilter.deriv.DAOD_HIGG8D1.e5421_s3126_r9364_r9315_p4133
 mc16_13TeV.364204.Sherpa_221_NN30NNLO_Zee_Mll10_40_MAXHTPTV0_70_BVeto.deriv.DAOD_HIGG8D1.e5421_s3126_r9364_r9315_p4133
 mc16_13TeV.364205.Sherpa_221_NN30NNLO_Zee_Mll10_40_MAXHTPTV0_70_BFilter.deriv.DAOD_HIGG8D1.e5421_s3126_r9364_r9315_p4133
 mc16_13TeV.364206.Sherpa_221_NN30NNLO_Zee_Mll10_40_MAXHTPTV70_280_BVeto.deriv.DAOD_HIGG8D1.e5421_s3126_r9364_r9315_p4133

mc16_13TeV.364207.Sherpa_221_NN30NNLO_Zee_Mll10_40_MAXHTPTV70_280_BFilter.deriv.DAOD_HIGG8D1.e5421_s3126_r9364_r9315_p4133
 mc16_13TeV.364208.Sherpa_221_NN30NNLO_Zee_Mll10_40_MAXHTPTV280_E_CMS_BVeto.deriv.DAOD_HIGG8D1.e5421_s3126_r9364_r9315_p4133
 mc16_13TeV.364209.Sherpa_221_NN30NNLO_Zee_Mll10_40_MAXHTPTV280_E_CMS_BFilter.deriv.DAOD_HIGG8D1.e5421_s3126_r9364_r9315_p4133
 mc16_13TeV.364210.Sherpa_221_NN30NNLO_Ztt_Mll10_40_MAXHTPTV0_70_BVeto.deriv.DAOD_HIGG8D1.e5421_s3126_r9364_r9315_p4133
 mc16_13TeV.364211.Sherpa_221_NN30NNLO_Ztt_Mll10_40_MAXHTPTV0_70_BFilter.deriv.DAOD_HIGG8D1.e5421_s3126_r9364_r9315_p4133
 mc16_13TeV.364212.Sherpa_221_NN30NNLO_Ztt_Mll10_40_MAXHTPTV70_280_BVeto.deriv.DAOD_HIGG8D1.e5421_s3126_r9364_r9315_p4133
 mc16_13TeV.364213.Sherpa_221_NN30NNLO_Ztt_Mll10_40_MAXHTPTV70_280_BFilter.deriv.DAOD_HIGG8D1.e5421_s3126_r9364_r9315_p4133
 mc16_13TeV.364214.Sherpa_221_NN30NNLO_Ztt_Mll10_40_MAXHTPTV280_E_CMS_BVeto.deriv.DAOD_HIGG8D1.e5421_s3126_r9364_r9315_p4133
 mc16_13TeV.364215.Sherpa_221_NN30NNLO_Ztt_Mll10_40_MAXHTPTV280_E_CMS_BFilter.deriv.DAOD_HIGG8D1.e5421_s3126_r9364_r9315_p4133
 mc16_13TeV.364156.Sherpa_221_NNPDF30NNLO_Wmunu_MAXHTPTV0_70_CVetoBVeto.deriv.DAOD_HIGG8D1.e5340_s3126_r9364_r9315_p4133
 mc16_13TeV.364157.Sherpa_221_NNPDF30NNLO_Wmunu_MAXHTPTV0_70_CFilterBVeto.deriv.DAOD_HIGG8D1.e5340_s3126_r9364_r9315_p4133
 mc16_13TeV.364157.Sherpa_221_NNPDF30NNLO_Wmunu_MAXHTPTV0_70_CFilterBVeto.deriv.DAOD_HIGG8D1.e5340_e5984_s3126_r9364_r9315_p4133
 mc16_13TeV.364158.Sherpa_221_NNPDF30NNLO_Wmunu_MAXHTPTV0_70_BFilter.deriv.DAOD_HIGG8D1.e5340_s3126_r9364_r9315_p4133
 mc16_13TeV.364159.Sherpa_221_NNPDF30NNLO_Wmunu_MAXHTPTV70_140_CVetoBVeto.deriv.DAOD_HIGG8D1.e5340_s3126_r9364_r9315_p4133
 mc16_13TeV.364160.Sherpa_221_NNPDF30NNLO_Wmunu_MAXHTPTV70_140_CFilterBVeto.deriv.DAOD_HIGG8D1.e5340_s3126_r9364_r9315_p4133
 mc16_13TeV.364161.Sherpa_221_NNPDF30NNLO_Wmunu_MAXHTPTV70_140_BFilter.deriv.DAOD_HIGG8D1.e5340_s3126_r9364_r9315_p4133
 mc16_13TeV.364162.Sherpa_221_NNPDF30NNLO_Wmunu_MAXHTPTV140_280_CVetoBVeto.deriv.DAOD_HIGG8D1.e5340_s3126_r9364_r9315_p4133
 mc16_13TeV.364163.Sherpa_221_NNPDF30NNLO_Wmunu_MAXHTPTV140_280_CFilterBVeto.deriv.DAOD_HIGG8D1.e5340_s3126_r9364_r9315_p4133
 mc16_13TeV.364163.Sherpa_221_NNPDF30NNLO_Wmunu_MAXHTPTV140_280_CFilterBVeto.deriv.DAOD_HIGG8D1.e5340_e5984_s3126_s3136_r9364_r9315_p4133
 mc16_13TeV.364164.Sherpa_221_NNPDF30NNLO_Wmunu_MAXHTPTV140_280_BFilter.deriv.DAOD_HIGG8D1.e5340_s3126_r9364_r9315_p4133
 mc16_13TeV.364165.Sherpa_221_NNPDF30NNLO_Wmunu_MAXHTPTV280_500_CVetoBVeto.deriv.DAOD_HIGG8D1.e5340_s3126_r9364_r9315_p4133
 mc16_13TeV.364166.Sherpa_221_NNPDF30NNLO_Wmunu_MAXHTPTV280_500_CFilterBVeto.deriv.DAOD_HIGG8D1.e5340_s3126_r9364_r9315_p4133
 mc16_13TeV.364167.Sherpa_221_NNPDF30NNLO_Wmunu_MAXHTPTV280_500_BFilter.deriv.DAOD_HIGG8D1.e5340_e5984_s3126_r9364_r9315_p4133
 mc16_13TeV.364167.Sherpa_221_NNPDF30NNLO_Wmunu_MAXHTPTV280_500_BFilter.deriv.DAOD_HIGG8D1.e5340_s3126_r9364_r9315_p4133
 mc16_13TeV.364168.Sherpa_221_NNPDF30NNLO_Wmunu_MAXHTPTV500_1000.deriv.DAOD_HIGG8D1.e5340_s3126_r9364_r9315_p4133
 mc16_13TeV.364169.Sherpa_221_NNPDF30NNLO_Wmunu_MAXHTPTV1000_E_CMS.deriv.DAOD_HIGG8D1.e5340_s3126_r9364_r9315_p4133
 mc16_13TeV.364170.Sherpa_221_NNPDF30NNLO_Wenu_MAXHTPTV0_70_CVetoBVeto.deriv.DAOD_HIGG8D1.e5340_s3126_r9364_r9315_p4133
 mc16_13TeV.364171.Sherpa_221_NNPDF30NNLO_Wenu_MAXHTPTV0_70_CFilterBVeto.deriv.DAOD_HIGG8D1.e5340_e5984_s3126_r9364_r9315_p4133
 mc16_13TeV.364171.Sherpa_221_NNPDF30NNLO_Wenu_MAXHTPTV0_70_CFilterBVeto.deriv.DAOD_HIGG8D1.e5340_s3126_r9364_r9315_p4133
 mc16_13TeV.364172.Sherpa_221_NNPDF30NNLO_Wenu_MAXHTPTV0_70_BFilter.deriv.DAOD_HIGG8D1.e5340_s3126_r9364_r9315_p4133
 mc16_13TeV.364173.Sherpa_221_NNPDF30NNLO_Wenu_MAXHTPTV70_140_CVetoBVeto.deriv.DAOD_HIGG8D1.e5340_s3126_r9364_r9315_p4133

mc16_13TeV.364174.Sherpa_221_NNPDF30NNLO_Wenu_MAXHTPTV70_140_CFilterBVeto.deriv.DAOD_HIGG8D1.e5340_s3126_r9364_r9315_p4133
 mc16_13TeV.364175.Sherpa_221_NNPDF30NNLO_Wenu_MAXHTPTV70_140_BFilter.deriv.DAOD_HIGG8D1.e5340_e5984_s3126_s3136_r9364_r9315_p4133
 mc16_13TeV.364175.Sherpa_221_NNPDF30NNLO_Wenu_MAXHTPTV70_140_BFilter.deriv.DAOD_HIGG8D1.e5340_s3126_r9364_r9315_p4133
 mc16_13TeV.364176.Sherpa_221_NNPDF30NNLO_Wenu_MAXHTPTV140_280_CVetoBVeto.deriv.DAOD_HIGG8D1.e5340_s3126_r9364_r9315_p4133
 mc16_13TeV.364177.Sherpa_221_NNPDF30NNLO_Wenu_MAXHTPTV140_280_CFilterBVeto.deriv.DAOD_HIGG8D1.e5340_s3126_r9364_r9315_p4133
 mc16_13TeV.364177.Sherpa_221_NNPDF30NNLO_Wenu_MAXHTPTV140_280_CFilterBVeto.deriv.DAOD_HIGG8D1.e5340_e5984_s3126_s3136_r9364_r9315_p4133
 mc16_13TeV.364178.Sherpa_221_NNPDF30NNLO_Wenu_MAXHTPTV140_280_BFilter.deriv.DAOD_HIGG8D1.e5340_s3126_r9364_r9315_p4133
 mc16_13TeV.364179.Sherpa_221_NNPDF30NNLO_Wenu_MAXHTPTV280_500_CVetoBVeto.deriv.DAOD_HIGG8D1.e5340_s3126_r9364_r9315_p4133
 mc16_13TeV.364180.Sherpa_221_NNPDF30NNLO_Wenu_MAXHTPTV280_500_CFilterBVeto.deriv.DAOD_HIGG8D1.e5340_s3126_r9364_r9315_p4133
 mc16_13TeV.364181.Sherpa_221_NNPDF30NNLO_Wenu_MAXHTPTV280_500_BFilter.deriv.DAOD_HIGG8D1.e5340_e5984_s3126_r9364_r9315_p4133
 mc16_13TeV.364181.Sherpa_221_NNPDF30NNLO_Wenu_MAXHTPTV280_500_BFilter.deriv.DAOD_HIGG8D1.e5340_s3126_r9364_r9315_p4133
 mc16_13TeV.364182.Sherpa_221_NNPDF30NNLO_Wenu_MAXHTPTV500_1000.deriv.DAOD_HIGG8D1.e5340_s3126_r9364_r9315_p4133
 mc16_13TeV.364183.Sherpa_221_NNPDF30NNLO_Wenu_MAXHTPTV1000_E_CMS.deriv.DAOD_HIGG8D1.e5340_s3126_r9364_r9315_p4133
 mc16_13TeV.364184.Sherpa_221_NNPDF30NNLO_Wtaunu_MAXHTPTV0_70_CVetoBVeto.deriv.DAOD_HIGG8D1.e5340_s3126_r9364_r9315_p4133
 mc16_13TeV.364185.Sherpa_221_NNPDF30NNLO_Wtaunu_MAXHTPTV0_70_CFilterBVeto.deriv.DAOD_HIGG8D1.e5340_e5984_s3126_r9364_r9315_p4133
 mc16_13TeV.364185.Sherpa_221_NNPDF30NNLO_Wtaunu_MAXHTPTV0_70_CFilterBVeto.deriv.DAOD_HIGG8D1.e5340_s3126_r9364_r9315_p4133
 mc16_13TeV.364186.Sherpa_221_NNPDF30NNLO_Wtaunu_MAXHTPTV0_70_BFilter.deriv.DAOD_HIGG8D1.e5340_s3126_r9364_r9315_p4133
 mc16_13TeV.364187.Sherpa_221_NNPDF30NNLO_Wtaunu_MAXHTPTV70_140_CVetoBVeto.deriv.DAOD_HIGG8D1.e5340_s3126_r9364_r9315_p4133
 mc16_13TeV.364188.Sherpa_221_NNPDF30NNLO_Wtaunu_MAXHTPTV70_140_CFilterBVeto.deriv.DAOD_HIGG8D1.e5340_s3126_r9364_r9315_p4133
 mc16_13TeV.364189.Sherpa_221_NNPDF30NNLO_Wtaunu_MAXHTPTV70_140_BFilter.deriv.DAOD_HIGG8D1.e5340_s3126_r9364_r9315_p4133
 mc16_13TeV.364190.Sherpa_221_NNPDF30NNLO_Wtaunu_MAXHTPTV140_280_CVetoBVeto.deriv.DAOD_HIGG8D1.e5340_e5984_s3126_r9364_r9315_p4133
 mc16_13TeV.364190.Sherpa_221_NNPDF30NNLO_Wtaunu_MAXHTPTV140_280_CVetoBVeto.deriv.DAOD_HIGG8D1.e5340_s3126_r9364_r9315_p4133
 mc16_13TeV.364191.Sherpa_221_NNPDF30NNLO_Wtaunu_MAXHTPTV140_280_CFilterBVeto.deriv.DAOD_HIGG8D1.e5340_s3126_r9364_r9315_p4133
 mc16_13TeV.364191.Sherpa_221_NNPDF30NNLO_Wtaunu_MAXHTPTV140_280_CFilterBVeto.deriv.DAOD_HIGG8D1.e5340_e5984_s3126_s3136_r9364_r9315_p4133
 mc16_13TeV.364192.Sherpa_221_NNPDF30NNLO_Wtaunu_MAXHTPTV140_280_BFilter.deriv.DAOD_HIGG8D1.e5340_s3126_r9364_r9315_p4133
 mc16_13TeV.364193.Sherpa_221_NNPDF30NNLO_Wtaunu_MAXHTPTV280_500_CVetoBVeto.deriv.DAOD_HIGG8D1.e5340_s3126_r9364_r9315_p4133
 mc16_13TeV.364193.Sherpa_221_NNPDF30NNLO_Wtaunu_MAXHTPTV280_500_CVetoBVeto.deriv.DAOD_HIGG8D1.e5340_e5984_s3126_s3136_r9364_r9315_p4133
 mc16_13TeV.364194.Sherpa_221_NNPDF30NNLO_Wtaunu_MAXHTPTV280_500_CFilterBVeto.deriv.DAOD_HIGG8D1.e5340_e5984_s3126_s3136_r9364_r9315_p4133
 mc16_13TeV.364195.Sherpa_221_NNPDF30NNLO_Wtaunu_MAXHTPTV280_500_BFilter.deriv.DAOD_HIGG8D1.e5340_s3126_r9364_r9315_p4133
 mc16_13TeV.364196.Sherpa_221_NNPDF30NNLO_Wtaunu_MAXHTPTV500_1000.deriv.DAOD_HIGG8D1.e5340_s3126_r9364_r9315_p4133

mc16_13TeV.364197.Sherpa_221_NNPDF30NNLO_Wtaunu_MAXHTPTV1000_E_CMS.deriv.DAOD_HIGG8D1.e5340_s3126_r9364_r9315_p4133
 mc16_13TeV.364500.Sherpa_222_NNPDF30NNLO_eegamma_pty_7_15.deriv.DAOD_HIGG8D1.e5928_e5984_s3126_r9364_r9315_p4133
 mc16_13TeV.364501.Sherpa_222_NNPDF30NNLO_eegamma_pty_15_35.deriv.DAOD_HIGG8D1.e5928_e5984_s3126_r9364_r9315_p4133
 mc16_13TeV.364502.Sherpa_222_NNPDF30NNLO_eegamma_pty_35_70.deriv.DAOD_HIGG8D1.e5928_e5984_s3126_r9364_r9315_p4133
 mc16_13TeV.364503.Sherpa_222_NNPDF30NNLO_eegamma_pty_70_140.deriv.DAOD_HIGG8D1.e5928_e5984_s3126_r9364_r9315_p4133
 mc16_13TeV.364504.Sherpa_222_NNPDF30NNLO_eegamma_pty_140_E_CMS.deriv.DAOD_HIGG8D1.e5928_e5984_s3126_r9364_r9315_p4133
 mc16_13TeV.364505.Sherpa_222_NNPDF30NNLO_mumugamma_pty_7_15.deriv.DAOD_HIGG8D1.e5928_e5984_s3126_r9364_r9315_p4133
 mc16_13TeV.364506.Sherpa_222_NNPDF30NNLO_mumugamma_pty_15_35.deriv.DAOD_HIGG8D1.e5988_e5984_s3126_r9364_r9315_p4133
 mc16_13TeV.364507.Sherpa_222_NNPDF30NNLO_mumugamma_pty_35_70.deriv.DAOD_HIGG8D1.e5928_e5984_s3126_r9364_r9315_p4133
 mc16_13TeV.364508.Sherpa_222_NNPDF30NNLO_mumugamma_pty_70_140.deriv.DAOD_HIGG8D1.e5928_e5984_s3126_r9364_r9315_p4133
 mc16_13TeV.364509.Sherpa_222_NNPDF30NNLO_mumugamma_pty_140_E_CMS.deriv.DAOD_HIGG8D1.e5928_e5984_s3126_r9364_r9315_p4133
 mc16_13TeV.364510.Sherpa_222_NNPDF30NNLO_tautaugamma_pty_7_15.deriv.DAOD_HIGG8D1.e5928_s3126_r9364_r9315_p4133
 mc16_13TeV.364511.Sherpa_222_NNPDF30NNLO_tautaugamma_pty_15_35.deriv.DAOD_HIGG8D1.e5928_s3126_r9364_r9315_p4133
 mc16_13TeV.364512.Sherpa_222_NNPDF30NNLO_tautaugamma_pty_35_70.deriv.DAOD_HIGG8D1.e5928_s3126_r9364_r9315_p4133
 mc16_13TeV.364513.Sherpa_222_NNPDF30NNLO_tautaugamma_pty_70_140.deriv.DAOD_HIGG8D1.e5982_s3126_r9364_r9315_p4133
 mc16_13TeV.364514.Sherpa_222_NNPDF30NNLO_tautaugamma_pty_140_E_CMS.deriv.DAOD_HIGG8D1.e5928_s3126_r9364_r9315_p4133
 mc16_13TeV.364521.Sherpa_222_NNPDF30NNLO_enugamma_pty_7_15.deriv.DAOD_HIGG8D1.e5928_s3126_r9364_r9315_p4133
 mc16_13TeV.364522.Sherpa_222_NNPDF30NNLO_enugamma_pty_15_35.deriv.DAOD_HIGG8D1.e5928_s3126_r9364_r9315_p4133
 mc16_13TeV.364523.Sherpa_222_NNPDF30NNLO_enugamma_pty_35_70.deriv.DAOD_HIGG8D1.e5928_s3126_r9364_r9315_p4133
 mc16_13TeV.364524.Sherpa_222_NNPDF30NNLO_enugamma_pty_70_140.deriv.DAOD_HIGG8D1.e5928_s3126_r9364_r9315_p4133
 mc16_13TeV.364525.Sherpa_222_NNPDF30NNLO_enugamma_pty_140_E_CMS.deriv.DAOD_HIGG8D1.e5928_s3126_r9364_r9315_p4133
 mc16_13TeV.364526.Sherpa_222_NNPDF30NNLO_munugamma_pty_7_15.deriv.DAOD_HIGG8D1.e5928_s3126_r9364_r9315_p4133
 mc16_13TeV.364527.Sherpa_222_NNPDF30NNLO_munugamma_pty_15_35.deriv.DAOD_HIGG8D1.e5928_s3126_r9364_r9315_p4133
 mc16_13TeV.364528.Sherpa_222_NNPDF30NNLO_munugamma_pty_35_70.deriv.DAOD_HIGG8D1.e5928_s3126_r9364_r9315_p4133
 mc16_13TeV.364529.Sherpa_222_NNPDF30NNLO_munugamma_pty_70_140.deriv.DAOD_HIGG8D1.e5928_s3126_r9364_r9315_p4133
 mc16_13TeV.364530.Sherpa_222_NNPDF30NNLO_munugamma_pty_140_E_CMS.deriv.DAOD_HIGG8D1.e5928_s3126_r9364_r9315_p4133
 mc16_13TeV.364530.Sherpa_222_NNPDF30NNLO_munugamma_pty_140_E_CMS.deriv.DAOD_HIGG8D1.e5928_e5984_s3126_r9364_r9315_p4133
 mc16_13TeV.364531.Sherpa_222_NNPDF30NNLO_taunugamma_pty_7_15.deriv.DAOD_HIGG8D1.e5928_s3126_r9364_r9315_p4133
 mc16_13TeV.364532.Sherpa_222_NNPDF30NNLO_taunugamma_pty_15_35.deriv.DAOD_HIGG8D1.e5928_s3126_r9364_r9315_p4133
 mc16_13TeV.364533.Sherpa_222_NNPDF30NNLO_taunugamma_pty_35_70.deriv.DAOD_HIGG8D1.e5928_s3126_r9364_r9315_p4133

mc16_13TeV.364534.Sherpa_222_NNPDF30NNLO_taunugamma_pty_70_140.deriv.DAOD_HIGG8D1.e5928_s3126_r9364_r9315_p4133
 mc16_13TeV.364535.Sherpa_222_NNPDF30NNLO_taunugamma_pty_140_E_CMS.deriv.DAOD_HIGG8D1.e5928_s3126_r9364_r9315_p4133
 mc16_13TeV.364535.Sherpa_222_NNPDF30NNLO_taunugamma_pty_140_E_CMS.deriv.DAOD_HIGG8D1.e5928_e5984_s3126_r9364_r9315_p4133
 mc16_13TeV.410560.MadGraphPythia8EvtGen_A14_tZ_4fl_tchan_noAllHad.deriv.DAOD_HIGG8D1.e5803_s3126_r9364_r9315_p4133
 mc16_13TeV.410013.PowhegPythiaEvtGen_P2012_Wt_inclusive_top.deriv.DAOD_HIGG8D1.e3753_s3126_r9364_r9315_p4133
 mc16_13TeV.410014.PowhegPythiaEvtGen_P2012_Wt_inclusive_antitop.deriv.DAOD_HIGG8D1.e3753_s3126_r9364_r9315_p4133
 mc16_13TeV.410408.aMcAtNloPythia8EvtGen_tWZ_Ztoll_minDR1.deriv.DAOD_HIGG8D1.e6423_e5984_s3126_r9364_r9315_p4133
 mc16_13TeV.364242.Sherpa_222_NNPDF30NNLO_WWW_3l3v_EW6.deriv.DAOD_HIGG8D1.e5887_s3126_r9364_r9315_p4133
 mc16_13TeV.364243.Sherpa_222_NNPDF30NNLO_WWZ_4l2v_EW6.deriv.DAOD_HIGG8D1.e5887_s3126_r9364_r9315_p4133
 mc16_13TeV.364244.Sherpa_222_NNPDF30NNLO_WWZ_2l4v_EW6.deriv.DAOD_HIGG8D1.e5887_s3126_r9364_r9315_p4133
 mc16_13TeV.364245.Sherpa_222_NNPDF30NNLO_WZZ_5l1v_EW6.deriv.DAOD_HIGG8D1.e5887_s3126_r9364_r9315_p4133
 mc16_13TeV.364246.Sherpa_222_NNPDF30NNLO_WZZ_3l3v_EW6.deriv.DAOD_HIGG8D1.e5887_s3126_r9364_r9315_p4133
 mc16_13TeV.364247.Sherpa_222_NNPDF30NNLO_ZZZ_6l0v_EW6.deriv.DAOD_HIGG8D1.e5887_s3126_r9364_r9315_p4133
 mc16_13TeV.364248.Sherpa_222_NNPDF30NNLO_ZZZ_4l2v_EW6.deriv.DAOD_HIGG8D1.e5887_s3126_r9364_r9315_p4133
 mc16_13TeV.364249.Sherpa_222_NNPDF30NNLO_ZZZ_2l4v_EW6.deriv.DAOD_HIGG8D1.e5887_s3126_r9364_r9315_p4133
 mc16_13TeV.342284.Pythia8EvtGen_A14NNPDF23LO_WH125_inc.deriv.DAOD_HIGG8D1.e4246_s3126_r9364_r9315_p4133
 mc16_13TeV.342285.Pythia8EvtGen_A14NNPDF23LO_ZH125_inc.deriv.DAOD_HIGG8D1.e4246_s3126_r9364_r9315_p4133
 mc16_13TeV.341998.aMcAtNloHppEG_UEEE5_CTEQ6L1_CT10ME_tWH125_gamgam_yt_plus1.deriv.DAOD_HIGG8D1.e4394_e5984_s3126_r9364_r9315_p4133
 mc16_13TeV.410389.MadGraphPythia8EvtGen_A14NNPDF23_ttgamma_nonallhadronic.deriv.DAOD_HIGG8D1.e6155_e5984_s3126_r9364_r9315_p4133
 mc16_13TeV.410470.PhPy8EG_A14_ttbar_hdamp258p75_nonallhad.deriv.DAOD_HIGG8D1.e6337_e5984_s3126_r9364_r9315_p4133
 mc16_13TeV.410472.PhPy8EG_A14_ttbar_hdamp258p75_dil.deriv.DAOD_HIGG8D1.e6348_e5984_s3126_r9364_r9315_p4133
 mc16_13TeV.346343.PhPy8EG_A14NNPDF23_NNPDF30ME_ttH125_allhad.deriv.DAOD_HIGG8D1.e7148_e5984_s3126_r9364_r9315_p4133
 mc16_13TeV.346344.PhPy8EG_A14NNPDF23_NNPDF30ME_ttH125_semilep.deriv.DAOD_HIGG8D1.e7148_e5984_s3126_r9364_r9315_p4133
 mc16_13TeV.346345.PhPy8EG_A14NNPDF23_NNPDF30ME_ttH125_dilep.deriv.DAOD_HIGG8D1.e7148_e5984_s3126_r9364_r9315_p4133

mc16d:

mc16_13TeV.364253.Sherpa_222_NNPDF30NNLO_lllv.deriv.DAOD_HIGG8D1.e5916_e5984_s3126_r10201_r10210_p4133
 mc16_13TeV.364250.Sherpa_222_NNPDF30NNLO_llll.deriv.DAOD_HIGG8D1.e5894_e5984_s3126_r10201_r10210_p4133
 mc16_13TeV.364254.Sherpa_222_NNPDF30NNLO_llvv.deriv.DAOD_HIGG8D1.e5916_e5984_s3126_r10201_r10210_p4133
 mc16_13TeV.364255.Sherpa_222_NNPDF30NNLO_lvvv.deriv.DAOD_HIGG8D1.e5916_e5984_s3126_r10201_r10210_p4133
 mc16_13TeV.410155.aMcAtNloPythia8EvtGen_MEN30NLO_A14N23LO_ttW.deriv.DAOD_HIGG8D1.e5070_e5984_s3126_r10201_r10210_p4133

mc16_13TeV.410156.aMcAtNloPythia8EvtGen_MEN30NLO_A14N23LO_ttZnunu.deriv.DAOD_HIGG8D1.e5070_e5984_s3126_r10201_r10210_p4133
 mc16_13TeV.410157.aMcAtNloPythia8EvtGen_MEN30NLO_A14N23LO_ttZqq.deriv.DAOD_HIGG8D1.e5070_e5984_s3126_r10201_r10210_p4133
 mc16_13TeV.410218.aMcAtNloPythia8EvtGen_MEN30NLO_A14N23LO_ttee.deriv.DAOD_HIGG8D1.e5070_e5984_s3126_r10201_r10210_p4133
 mc16_13TeV.410219.aMcAtNloPythia8EvtGen_MEN30NLO_A14N23LO_ttmumu.deriv.DAOD_HIGG8D1.e5070_e5984_s3126_r10201_r10210_p4133
 mc16_13TeV.410220.aMcAtNloPythia8EvtGen_MEN30NLO_A14N23LO_ttautau.deriv.DAOD_HIGG8D1.e5070_e5984_s3126_r10201_r10210_p4133
 mc16_13TeV.410276.aMcAtNloPythia8EvtGen_MEN30NLO_A14N23LO_ttee_mll_1_5.deriv.DAOD_HIGG8D1.e6087_e5984_s3126_r10201_r10210_p4133
 mc16_13TeV.410277.aMcAtNloPythia8EvtGen_MEN30NLO_A14N23LO_ttmumu_mll_1_5.deriv.DAOD_HIGG8D1.e6087_e5984_s3126_r10201_r10210_p4133
 mc16_13TeV.410278.aMcAtNloPythia8EvtGen_MEN30NLO_A14N23LO_ttautau_mll_1_5.deriv.DAOD_HIGG8D1.e6087_e5984_s3126_r10201_r10210_p4133
 mc16_13TeV.410397.MadGraphPythia8EvtGen_ttbar_wbee_MEN30LO_A14N23LO.deriv.DAOD_HIGG8D1.e6086_e5984_s3126_r10201_r10210_p4133
 mc16_13TeV.410398.MadGraphPythia8EvtGen_ttbar_wbmumu_MEN30LO_A14N23LO.deriv.DAOD_HIGG8D1.e6086_e5984_s3126_r10201_r10210_p4133
 mc16_13TeV.410399.MadGraphPythia8EvtGen_ttbar_wbttau_MEN30LO_A14N23LO.deriv.DAOD_HIGG8D1.e6086_e5984_s3126_r10201_r10210_p4133
 mc16_13TeV.410658.PhPy8EG_A14_tchan_BW50_lept_top.deriv.DAOD_HIGG8D1.e6671_e5984_s3126_r10201_r10210_p4133
 mc16_13TeV.410659.PhPy8EG_A14_tchan_BW50_lept_antitop.deriv.DAOD_HIGG8D1.e6671_e5984_s3126_r10201_r10210_p4133
 mc16_13TeV.410644.PowhegPythia8EvtGen_A14_singletop_schan_lept_top.deriv.DAOD_HIGG8D1.e6527_e5984_s3126_r10201_r10210_p4133
 mc16_13TeV.410645.PowhegPythia8EvtGen_A14_singletop_schan_lept_antitop.deriv.DAOD_HIGG8D1.e6527_s3126_r10201_r10210_p4133
 mc16_13TeV.412063.aMcAtNloPythia8EvtGen_tllq_NNPDF30_nf4_A14.deriv.DAOD_TOPQ1.e7054_e5984_s3126_r10201_r10210_p4174
 mc16_13TeV.304014.MadGraphPythia8EvtGen_A14NNPDF23_3top_SM.deriv.DAOD_HIGG8D1.e4324_e5984_s3126_r10201_r10210_p4133
 mc16_13TeV.410080.MadGraphPythia8EvtGen_A14NNPDF23_4topSM.deriv.DAOD_HIGG8D1.e4111_e5984_s3126_r10201_r10210_p4133
 mc16_13TeV.410081.MadGraphPythia8EvtGen_A14NNPDF23_ttbarWW.deriv.DAOD_HIGG8D1.e4111_e5984_s3126_r10201_r10210_p4133
 mc16_13TeV.364100.Sherpa_221_NNPDF30NNLO_Zmumu_MAXHTPTV0_70_CVetoBVeto.deriv.DAOD_HIGG8D1.e5271_s3126_r10201_r10210_p4133
 mc16_13TeV.364101.Sherpa_221_NNPDF30NNLO_Zmumu_MAXHTPTV0_70_CFfilterBVeto.deriv.DAOD_HIGG8D1.e5271_s3126_r10201_r10210_p4133
 mc16_13TeV.364101.Sherpa_221_NNPDF30NNLO_Zmumu_MAXHTPTV0_70_CFfilterBVeto.deriv.DAOD_HIGG8D1.e5271_e5984_s3126_r10201_r10210_p4133
 mc16_13TeV.364102.Sherpa_221_NNPDF30NNLO_Zmumu_MAXHTPTV0_70_BFilter.deriv.DAOD_HIGG8D1.e5271_s3126_r10201_r10210_p4133
 mc16_13TeV.364103.Sherpa_221_NNPDF30NNLO_Zmumu_MAXHTPTV70_140_CVetoBVeto.deriv.DAOD_HIGG8D1.e5271_s3126_r10201_r10210_p4133
 mc16_13TeV.364104.Sherpa_221_NNPDF30NNLO_Zmumu_MAXHTPTV70_140_CFfilterBVeto.deriv.DAOD_HIGG8D1.e5271_s3126_r10201_r10210_p4133
 mc16_13TeV.364106.Sherpa_221_NNPDF30NNLO_Zmumu_MAXHTPTV140_280_CVetoBVeto.deriv.DAOD_HIGG8D1.e5271_s3126_r10201_r10210_p4133
 mc16_13TeV.364107.Sherpa_221_NNPDF30NNLO_Zmumu_MAXHTPTV140_280_CFfilterBVeto.deriv.DAOD_HIGG8D1.e5271_s3126_r10201_r10210_p4133
 mc16_13TeV.364108.Sherpa_221_NNPDF30NNLO_Zmumu_MAXHTPTV140_280_BFilter.deriv.DAOD_HIGG8D1.e5271_e5984_s3126_r10201_r10210_p4133
 mc16_13TeV.364109.Sherpa_221_NNPDF30NNLO_Zmumu_MAXHTPTV280_500_CVetoBVeto.deriv.DAOD_HIGG8D1.e5271_e5984_s3126_r10201_r10210_p4133
 mc16_13TeV.364109.Sherpa_221_NNPDF30NNLO_Zmumu_MAXHTPTV280_500_CVetoBVeto.deriv.DAOD_HIGG8D1.e5271_s3126_r10201_r10210_p4133

mc16_13TeV.364110.Sherpa_221_NNPDF30NNLO_Zmumu_MAXHTPTV280_500_CFilterBVeto.deriv.DAOD_HIGG8D1.e5271_s3126_r10201_r10210_p4133
 mc16_13TeV.364111.Sherpa_221_NNPDF30NNLO_Zmumu_MAXHTPTV280_500_BFilter.deriv.DAOD_HIGG8D1.e5271_e5984_s3126_r10201_r10210_p4133
 mc16_13TeV.364111.Sherpa_221_NNPDF30NNLO_Zmumu_MAXHTPTV280_500_BFilter.deriv.DAOD_HIGG8D1.e5271_s3126_r10201_r10210_p4133
 mc16_13TeV.364112.Sherpa_221_NNPDF30NNLO_Zmumu_MAXHTPTV500_1000.deriv.DAOD_HIGG8D1.e5271_e5984_s3126_r10201_r10210_p4133
 mc16_13TeV.364112.Sherpa_221_NNPDF30NNLO_Zmumu_MAXHTPTV500_1000.deriv.DAOD_HIGG8D1.e5271_s3126_r10201_r10210_p4133
 mc16_13TeV.364113.Sherpa_221_NNPDF30NNLO_Zmumu_MAXHTPTV1000_E_CMS.deriv.DAOD_HIGG8D1.e5271_s3126_r10201_r10210_p4133
 mc16_13TeV.364114.Sherpa_221_NNPDF30NNLO_Zee_MAXHTPTV0_70_CVetoBVeto.deriv.DAOD_HIGG8D1.e5299_s3126_r10201_r10210_p4133
 mc16_13TeV.364115.Sherpa_221_NNPDF30NNLO_Zee_MAXHTPTV0_70_CFilterBVeto.deriv.DAOD_HIGG8D1.e5299_e5984_s3126_r10201_r10210_p4133
 mc16_13TeV.364116.Sherpa_221_NNPDF30NNLO_Zee_MAXHTPTV0_70_BFilter.deriv.DAOD_HIGG8D1.e5299_e5984_s3126_r10201_r10210_p4133
 mc16_13TeV.364117.Sherpa_221_NNPDF30NNLO_Zee_MAXHTPTV70_140_CVetoBVeto.deriv.DAOD_HIGG8D1.e5299_e5984_s3126_r10201_r10210_p4133
 mc16_13TeV.364118.Sherpa_221_NNPDF30NNLO_Zee_MAXHTPTV70_140_CFilterBVeto.deriv.DAOD_HIGG8D1.e5299_e5984_s3126_r10201_r10210_p4133
 mc16_13TeV.364119.Sherpa_221_NNPDF30NNLO_Zee_MAXHTPTV70_140_BFilter.deriv.DAOD_HIGG8D1.e5299_e5984_s3126_r10201_r10210_p4133
 mc16_13TeV.364120.Sherpa_221_NNPDF30NNLO_Zee_MAXHTPTV140_280_CVetoBVeto.deriv.DAOD_HIGG8D1.e5299_e5984_s3126_r10201_r10210_p4133
 mc16_13TeV.364121.Sherpa_221_NNPDF30NNLO_Zee_MAXHTPTV140_280_CFilterBVeto.deriv.DAOD_HIGG8D1.e5299_e5984_s3126_r10201_r10210_p4133
 mc16_13TeV.364122.Sherpa_221_NNPDF30NNLO_Zee_MAXHTPTV140_280_BFilter.deriv.DAOD_HIGG8D1.e5299_e5984_s3126_r10201_r10210_p4133
 mc16_13TeV.364123.Sherpa_221_NNPDF30NNLO_Zee_MAXHTPTV280_500_CVetoBVeto.deriv.DAOD_HIGG8D1.e5299_e5984_s3126_r10201_r10210_p4133
 mc16_13TeV.364124.Sherpa_221_NNPDF30NNLO_Zee_MAXHTPTV280_500_CFilterBVeto.deriv.DAOD_HIGG8D1.e5299_e5984_s3126_r10201_r10210_p4133
 mc16_13TeV.364125.Sherpa_221_NNPDF30NNLO_Zee_MAXHTPTV280_500_BFilter.deriv.DAOD_HIGG8D1.e5299_e5984_s3126_r10201_r10210_p4133
 mc16_13TeV.364126.Sherpa_221_NNPDF30NNLO_Zee_MAXHTPTV500_1000.deriv.DAOD_HIGG8D1.e5299_e5984_s3126_r10201_r10210_p4133
 mc16_13TeV.364127.Sherpa_221_NNPDF30NNLO_Zee_MAXHTPTV1000_E_CMS.deriv.DAOD_HIGG8D1.e5299_e5984_s3126_r10201_r10210_p4133
 mc16_13TeV.364128.Sherpa_221_NNPDF30NNLO_Ztautau_MAXHTPTV0_70_CVetoBVeto.deriv.DAOD_HIGG8D1.e5307_e5984_s3126_r10201_r10210_p4133
 mc16_13TeV.364129.Sherpa_221_NNPDF30NNLO_Ztautau_MAXHTPTV0_70_CFilterBVeto.deriv.DAOD_HIGG8D1.e5307_e5984_s3126_r10201_r10210_p4133
 mc16_13TeV.364130.Sherpa_221_NNPDF30NNLO_Ztautau_MAXHTPTV0_70_BFilter.deriv.DAOD_HIGG8D1.e5307_e5984_s3126_r10201_r10210_p4133
 mc16_13TeV.364131.Sherpa_221_NNPDF30NNLO_Ztautau_MAXHTPTV70_140_CVetoBVeto.deriv.DAOD_HIGG8D1.e5307_e5984_s3126_r10201_r10210_p4133
 mc16_13TeV.364132.Sherpa_221_NNPDF30NNLO_Ztautau_MAXHTPTV70_140_CFilterBVeto.deriv.DAOD_HIGG8D1.e5307_e5984_s3126_r10201_r10210_p4133
 mc16_13TeV.364133.Sherpa_221_NNPDF30NNLO_Ztautau_MAXHTPTV70_140_BFilter.deriv.DAOD_HIGG8D1.e5307_e5984_s3126_r10201_r10210_p4133
 mc16_13TeV.364134.Sherpa_221_NNPDF30NNLO_Ztautau_MAXHTPTV140_280_CVetoBVeto.deriv.DAOD_HIGG8D1.e5307_e5984_s3126_r10201_r10210_p4133
 mc16_13TeV.364135.Sherpa_221_NNPDF30NNLO_Ztautau_MAXHTPTV140_280_CFilterBVeto.deriv.DAOD_HIGG8D1.e5307_e5984_s3126_r10201_r10210_p4133
 mc16_13TeV.364136.Sherpa_221_NNPDF30NNLO_Ztautau_MAXHTPTV140_280_BFilter.deriv.DAOD_HIGG8D1.e5307_e5984_s3126_r10201_r10210_p4133
 mc16_13TeV.364137.Sherpa_221_NNPDF30NNLO_Ztautau_MAXHTPTV280_500_CVetoBVeto.deriv.DAOD_HIGG8D1.e5307_e5984_s3126_r10201_r10210_p4133
 mc16_13TeV.364138.Sherpa_221_NNPDF30NNLO_Ztautau_MAXHTPTV280_500_CFilterBVeto.deriv.DAOD_HIGG8D1.e5313_e5984_s3126_r10201_r10210_p4133

mc16_13TeV.364139.Sherpa_221_NNPDF30NNLO_Ztautau_MAXHTPTV280_500_BFilter.deriv.DAOD_HIGG8D1.e5313_e5984_s3126_r10201_r10210_p4133
 mc16_13TeV.364140.Sherpa_221_NNPDF30NNLO_Ztautau_MAXHTPTV500_1000.deriv.DAOD_HIGG8D1.e5307_e5984_s3126_r10201_r10210_p4133
 mc16_13TeV.364141.Sherpa_221_NNPDF30NNLO_Ztautau_MAXHTPTV1000_E_CMS.deriv.DAOD_HIGG8D1.e5307_e5984_s3126_r10201_r10210_p4133
 mc16_13TeV.364198.Sherpa_221_NN30NNLO_Zmm_Mll10_40_MAXHTPTV0_70_BVeto.deriv.DAOD_HIGG8D1.e5421_e5984_s3126_r10201_r10210_p4133
 mc16_13TeV.364199.Sherpa_221_NN30NNLO_Zmm_Mll10_40_MAXHTPTV0_70_BFilter.deriv.DAOD_HIGG8D1.e5421_e5984_s3126_r10201_r10210_p4133
 mc16_13TeV.364200.Sherpa_221_NN30NNLO_Zmm_Mll10_40_MAXHTPTV70_280_BVeto.deriv.DAOD_HIGG8D1.e5421_e5984_s3126_r10201_r10210_p4133
 mc16_13TeV.364201.Sherpa_221_NN30NNLO_Zmm_Mll10_40_MAXHTPTV70_280_BFilter.deriv.DAOD_HIGG8D1.e5421_e5984_s3126_r10201_r10210_p4133
 mc16_13TeV.364202.Sherpa_221_NN30NNLO_Zmm_Mll10_40_MAXHTPTV280_E_CMS_BVeto.deriv.DAOD_HIGG8D1.e5421_e5984_s3126_r10201_r10210_p4133
 mc16_13TeV.364203.Sherpa_221_NN30NNLO_Zmm_Mll10_40_MAXHTPTV280_E_CMS_BFilter.deriv.DAOD_HIGG8D1.e5421_e5984_s3126_r10201_r10210_p4133
 mc16_13TeV.364204.Sherpa_221_NN30NNLO_Zee_Mll10_40_MAXHTPTV0_70_BVeto.deriv.DAOD_HIGG8D1.e5421_e5984_s3126_r10201_r10210_p4133
 mc16_13TeV.364205.Sherpa_221_NN30NNLO_Zee_Mll10_40_MAXHTPTV0_70_BFilter.deriv.DAOD_HIGG8D1.e5421_e5984_s3126_r10201_r10210_p4133
 mc16_13TeV.364206.Sherpa_221_NN30NNLO_Zee_Mll10_40_MAXHTPTV70_280_BVeto.deriv.DAOD_HIGG8D1.e5421_e5984_s3126_r10201_r10210_p4133
 mc16_13TeV.364207.Sherpa_221_NN30NNLO_Zee_Mll10_40_MAXHTPTV70_280_BFilter.deriv.DAOD_HIGG8D1.e5421_e5984_s3126_r10201_r10210_p4133
 mc16_13TeV.364208.Sherpa_221_NN30NNLO_Zee_Mll10_40_MAXHTPTV280_E_CMS_BVeto.deriv.DAOD_HIGG8D1.e5421_e5984_s3126_r10201_r10210_p4133
 mc16_13TeV.364209.Sherpa_221_NN30NNLO_Zee_Mll10_40_MAXHTPTV280_E_CMS_BFilter.deriv.DAOD_HIGG8D1.e5421_e5984_s3126_r10201_r10210_p4133
 mc16_13TeV.364210.Sherpa_221_NN30NNLO_Ztt_Mll10_40_MAXHTPTV0_70_BVeto.deriv.DAOD_HIGG8D1.e5421_e5984_s3126_r10201_r10210_p4133
 mc16_13TeV.364211.Sherpa_221_NN30NNLO_Ztt_Mll10_40_MAXHTPTV0_70_BFilter.deriv.DAOD_HIGG8D1.e5421_e5984_s3126_r10201_r10210_p4133
 mc16_13TeV.364212.Sherpa_221_NN30NNLO_Ztt_Mll10_40_MAXHTPTV70_280_BVeto.deriv.DAOD_HIGG8D1.e5421_e5984_s3126_r10201_r10210_p4133
 mc16_13TeV.364213.Sherpa_221_NN30NNLO_Ztt_Mll10_40_MAXHTPTV70_280_BFilter.deriv.DAOD_HIGG8D1.e5421_e5984_s3126_r10201_r10210_p4133
 mc16_13TeV.364214.Sherpa_221_NN30NNLO_Ztt_Mll10_40_MAXHTPTV280_E_CMS_BVeto.deriv.DAOD_HIGG8D1.e5421_e5984_s3126_r10201_r10210_p4133
 mc16_13TeV.364215.Sherpa_221_NN30NNLO_Ztt_Mll10_40_MAXHTPTV280_E_CMS_BFilter.deriv.DAOD_HIGG8D1.e5421_e5984_s3126_r10201_r10210_p4133
 mc16_13TeV.364156.Sherpa_221_NNPDF30NNLO_Wmunu_MAXHTPTV0_70_CVetoBVeto.deriv.DAOD_HIGG8D1.e5340_s3126_r10201_r10210_p4133
 mc16_13TeV.364156.Sherpa_221_NNPDF30NNLO_Wmunu_MAXHTPTV0_70_CVetoBVeto.deriv.DAOD_HIGG8D1.e5340_e5984_s3126_s3136_r10201_r10210_p4133
 mc16_13TeV.364157.Sherpa_221_NNPDF30NNLO_Wmunu_MAXHTPTV0_70_CFilterBVeto.deriv.DAOD_HIGG8D1.e5340_e5984_s3126_s3136_r10201_r10210_p4133
 mc16_13TeV.364157.Sherpa_221_NNPDF30NNLO_Wmunu_MAXHTPTV0_70_CFilterBVeto.deriv.DAOD_HIGG8D1.e5340_s3126_r10201_r10210_p4133
 mc16_13TeV.364158.Sherpa_221_NNPDF30NNLO_Wmunu_MAXHTPTV0_70_BFilter.deriv.DAOD_HIGG8D1.e5340_e5984_s3126_s3136_r10201_r10210_p4133
 mc16_13TeV.364158.Sherpa_221_NNPDF30NNLO_Wmunu_MAXHTPTV0_70_BFilter.deriv.DAOD_HIGG8D1.e5340_s3126_r10201_r10210_p4133
 mc16_13TeV.364159.Sherpa_221_NNPDF30NNLO_Wmunu_MAXHTPTV70_140_CVetoBVeto.deriv.DAOD_HIGG8D1.e5340_s3126_r10201_r10210_p4133
 mc16_13TeV.364159.Sherpa_221_NNPDF30NNLO_Wmunu_MAXHTPTV70_140_CVetoBVeto.deriv.DAOD_HIGG8D1.e5340_e5984_s3126_r10201_r10210_p4133
 mc16_13TeV.364159.Sherpa_221_NNPDF30NNLO_Wmunu_MAXHTPTV70_140_CVetoBVeto.deriv.DAOD_HIGG8D1.e5340_e5984_s3126_s3136_r10201_r10210_p4133

mc16_13TeV.364160.Sherpa_221_NNPDF30NNLO_Wmunu_MAXHTPTV70_140_CFilterBVeto.deriv.DAOD_HIGG8D1.e5340_e5984_s3126_r10201_r10210_p4133
 mc16_13TeV.364160.Sherpa_221_NNPDF30NNLO_Wmunu_MAXHTPTV70_140_CFilterBVeto.deriv.DAOD_HIGG8D1.e5340_s3126_r10201_r10210_p4133
 mc16_13TeV.364161.Sherpa_221_NNPDF30NNLO_Wmunu_MAXHTPTV70_140_BFilter.deriv.DAOD_HIGG8D1.e5340_s3126_r10201_r10210_p4133
 mc16_13TeV.364161.Sherpa_221_NNPDF30NNLO_Wmunu_MAXHTPTV70_140_BFilter.deriv.DAOD_HIGG8D1.e5340_e5984_s3126_s3136_r10201_r10210_p4133
 mc16_13TeV.364162.Sherpa_221_NNPDF30NNLO_Wmunu_MAXHTPTV140_280_CVetoBVeto.deriv.DAOD_HIGG8D1.e5340_s3126_r10201_r10210_p4133
 mc16_13TeV.364162.Sherpa_221_NNPDF30NNLO_Wmunu_MAXHTPTV140_280_CVetoBVeto.deriv.DAOD_HIGG8D1.e5340_e5984_s3126_s3136_r10201_r10210_p4133
 mc16_13TeV.364163.Sherpa_221_NNPDF30NNLO_Wmunu_MAXHTPTV140_280_CFilterBVeto.deriv.DAOD_HIGG8D1.e5340_s3126_r10201_r10210_p4133
 mc16_13TeV.364163.Sherpa_221_NNPDF30NNLO_Wmunu_MAXHTPTV140_280_CFilterBVeto.deriv.DAOD_HIGG8D1.e5340_e5984_s3126_s3136_r10201_r10210_p4133
 mc16_13TeV.364163.Sherpa_221_NNPDF30NNLO_Wmunu_MAXHTPTV140_280_CFilterBVeto.deriv.DAOD_HIGG8D1.e5340_e5984_s3126_r10201_r10210_p4133
 mc16_13TeV.364164.Sherpa_221_NNPDF30NNLO_Wmunu_MAXHTPTV140_280_BFilter.deriv.DAOD_HIGG8D1.e5340_s3126_r10201_r10210_p4133
 mc16_13TeV.364164.Sherpa_221_NNPDF30NNLO_Wmunu_MAXHTPTV140_280_BFilter.deriv.DAOD_HIGG8D1.e5340_e5984_s3126_s3136_r10201_r10210_p4133
 mc16_13TeV.364165.Sherpa_221_NNPDF30NNLO_Wmunu_MAXHTPTV280_500_CVetoBVeto.deriv.DAOD_HIGG8D1.e5340_e5984_s3126_s3136_r10201_r10210_p4133
 mc16_13TeV.364166.Sherpa_221_NNPDF30NNLO_Wmunu_MAXHTPTV280_500_CFilterBVeto.deriv.DAOD_HIGG8D1.e5340_s3126_r10201_r10210_p4133
 mc16_13TeV.364166.Sherpa_221_NNPDF30NNLO_Wmunu_MAXHTPTV280_500_CFilterBVeto.deriv.DAOD_HIGG8D1.e5340_e5984_s3126_s3136_r10201_r10210_p4133
 mc16_13TeV.364167.Sherpa_221_NNPDF30NNLO_Wmunu_MAXHTPTV280_500_BFilter.deriv.DAOD_HIGG8D1.e5340_s3126_r10201_r10210_p4133
 mc16_13TeV.364167.Sherpa_221_NNPDF30NNLO_Wmunu_MAXHTPTV280_500_BFilter.deriv.DAOD_HIGG8D1.e5340_e5984_s3126_r10201_r10210_p4133
 mc16_13TeV.364168.Sherpa_221_NNPDF30NNLO_Wmunu_MAXHTPTV500_1000.deriv.DAOD_HIGG8D1.e5340_s3126_r10201_r10210_p4133
 mc16_13TeV.364168.Sherpa_221_NNPDF30NNLO_Wmunu_MAXHTPTV500_1000.deriv.DAOD_HIGG8D1.e5340_e5984_s3126_s3136_r10201_r10210_p4133
 mc16_13TeV.364169.Sherpa_221_NNPDF30NNLO_Wmunu_MAXHTPTV1000_E_CMS.deriv.DAOD_HIGG8D1.e5340_s3126_r10201_r10210_p4133
 mc16_13TeV.364169.Sherpa_221_NNPDF30NNLO_Wmunu_MAXHTPTV1000_E_CMS.deriv.DAOD_HIGG8D1.e5340_e5984_s3126_s3136_r10201_r10210_p4133
 mc16_13TeV.364170.Sherpa_221_NNPDF30NNLO_Wenu_MAXHTPTV0_70_CVetoBVeto.deriv.DAOD_HIGG8D1.e5340_e5984_s3126_s3136_r10201_r10210_p4133
 mc16_13TeV.364170.Sherpa_221_NNPDF30NNLO_Wenu_MAXHTPTV0_70_CVetoBVeto.deriv.DAOD_HIGG8D1.e5340_s3126_r10201_r10210_p4133
 mc16_13TeV.364171.Sherpa_221_NNPDF30NNLO_Wenu_MAXHTPTV0_70_CFilterBVeto.deriv.DAOD_HIGG8D1.e5340_e5984_s3126_r10201_r10210_p4133
 mc16_13TeV.364171.Sherpa_221_NNPDF30NNLO_Wenu_MAXHTPTV0_70_CFilterBVeto.deriv.DAOD_HIGG8D1.e5340_s3126_r10201_r10210_p4133
 mc16_13TeV.364171.Sherpa_221_NNPDF30NNLO_Wenu_MAXHTPTV0_70_CFilterBVeto.deriv.DAOD_HIGG8D1.e5340_e5984_s3126_s3136_r10201_r10210_p4133
 mc16_13TeV.364172.Sherpa_221_NNPDF30NNLO_Wenu_MAXHTPTV0_70_BFilter.deriv.DAOD_HIGG8D1.e5340_e5984_s3126_s3136_r10201_r10210_p4133
 mc16_13TeV.364172.Sherpa_221_NNPDF30NNLO_Wenu_MAXHTPTV0_70_BFilter.deriv.DAOD_HIGG8D1.e5340_e5984_s3126_r10201_r10210_p4133
 mc16_13TeV.364173.Sherpa_221_NNPDF30NNLO_Wenu_MAXHTPTV70_140_CVetoBVeto.deriv.DAOD_HIGG8D1.e5340_s3126_r10201_r10210_p4133
 mc16_13TeV.364173.Sherpa_221_NNPDF30NNLO_Wenu_MAXHTPTV70_140_CVetoBVeto.deriv.DAOD_HIGG8D1.e5340_e5984_s3126_r10201_r10210_p4133

mc16_13TeV.364174.Sherpa_221_NNPDF30NNLO_Wenu_MAXHTPTV70_140_CFilterBVeto.deriv.DAOD_HIGG8D1.e5340_s3126_r10201_r10210_p4133
 mc16_13TeV.364174.Sherpa_221_NNPDF30NNLO_Wenu_MAXHTPTV70_140_CFilterBVeto.deriv.DAOD_HIGG8D1.e5340_e5984_s3126_r10201_r10210_p4133
 mc16_13TeV.364175.Sherpa_221_NNPDF30NNLO_Wenu_MAXHTPTV70_140_BFilter.deriv.DAOD_HIGG8D1.e5340_e5984_s3126_r10201_r10210_p4133
 mc16_13TeV.364175.Sherpa_221_NNPDF30NNLO_Wenu_MAXHTPTV70_140_BFilter.deriv.DAOD_HIGG8D1.e5340_e5984_s3126_s3136_r10201_r10210_p4133
 mc16_13TeV.364175.Sherpa_221_NNPDF30NNLO_Wenu_MAXHTPTV70_140_BFilter.deriv.DAOD_HIGG8D1.e5340_s3126_r10201_r10210_p4133
 mc16_13TeV.364176.Sherpa_221_NNPDF30NNLO_Wenu_MAXHTPTV140_280_CVetoBVeto.deriv.DAOD_HIGG8D1.e5340_e5984_s3126_s3136_r10201_r10210_p4133
 mc16_13TeV.364176.Sherpa_221_NNPDF30NNLO_Wenu_MAXHTPTV140_280_CVetoBVeto.deriv.DAOD_HIGG8D1.e5340_s3126_r10201_r10210_p4133
 mc16_13TeV.364177.Sherpa_221_NNPDF30NNLO_Wenu_MAXHTPTV140_280_CFilterBVeto.deriv.DAOD_HIGG8D1.e5340_s3126_r10201_r10210_p4133
 mc16_13TeV.364177.Sherpa_221_NNPDF30NNLO_Wenu_MAXHTPTV140_280_CFilterBVeto.deriv.DAOD_HIGG8D1.e5340_e5984_s3126_s3136_r10201_r10210_p4133
 mc16_13TeV.364177.Sherpa_221_NNPDF30NNLO_Wenu_MAXHTPTV140_280_CFilterBVeto.deriv.DAOD_HIGG8D1.e5340_e5984_s3126_s3136_r10201_r10210_p4133
 mc16_13TeV.364177.Sherpa_221_NNPDF30NNLO_Wenu_MAXHTPTV140_280_CFilterBVeto.deriv.DAOD_HIGG8D1.e5340_e5984_s3126_r10201_r10210_p4133
 mc16_13TeV.364178.Sherpa_221_NNPDF30NNLO_Wenu_MAXHTPTV140_280_BFilter.deriv.DAOD_HIGG8D1.e5340_s3126_r10201_r10210_p4133
 mc16_13TeV.364179.Sherpa_221_NNPDF30NNLO_Wenu_MAXHTPTV280_500_CVetoBVeto.deriv.DAOD_HIGG8D1.e5340_s3126_r10201_r10210_p4133
 mc16_13TeV.364179.Sherpa_221_NNPDF30NNLO_Wenu_MAXHTPTV280_500_CVetoBVeto.deriv.DAOD_HIGG8D1.e5340_e5984_s3126_r10201_r10210_p4133
 mc16_13TeV.364180.Sherpa_221_NNPDF30NNLO_Wenu_MAXHTPTV280_500_CFilterBVeto.deriv.DAOD_HIGG8D1.e5340_e5984_s3126_s3136_r10201_r10210_p4133
 mc16_13TeV.364180.Sherpa_221_NNPDF30NNLO_Wenu_MAXHTPTV280_500_CFilterBVeto.deriv.DAOD_HIGG8D1.e5340_s3126_r10201_r10210_p4133
 mc16_13TeV.364181.Sherpa_221_NNPDF30NNLO_Wenu_MAXHTPTV280_500_BFilter.deriv.DAOD_HIGG8D1.e5340_e5984_s3126_r10201_r10210_p4133
 mc16_13TeV.364181.Sherpa_221_NNPDF30NNLO_Wenu_MAXHTPTV280_500_BFilter.deriv.DAOD_HIGG8D1.e5340_s3126_r10201_r10210_p4133
 mc16_13TeV.364182.Sherpa_221_NNPDF30NNLO_Wenu_MAXHTPTV500_1000.deriv.DAOD_HIGG8D1.e5340_s3126_r10201_r10210_p4133
 mc16_13TeV.364182.Sherpa_221_NNPDF30NNLO_Wenu_MAXHTPTV500_1000.deriv.DAOD_HIGG8D1.e5340_e5984_s3126_s3136_r10201_r10210_p4133
 mc16_13TeV.364183.Sherpa_221_NNPDF30NNLO_Wenu_MAXHTPTV1000_E_CMS.deriv.DAOD_HIGG8D1.e5340_e5984_s3126_r10201_r10210_p4133
 mc16_13TeV.364184.Sherpa_221_NNPDF30NNLO_Wtaunu_MAXHTPTV0_70_CVetoBVeto.deriv.DAOD_HIGG8D1.e5340_e5984_s3126_r10201_r10210_p4133
 mc16_13TeV.364184.Sherpa_221_NNPDF30NNLO_Wtaunu_MAXHTPTV0_70_CVetoBVeto.deriv.DAOD_HIGG8D1.e5340_s3126_r10201_r10210_p4133
 mc16_13TeV.364185.Sherpa_221_NNPDF30NNLO_Wtaunu_MAXHTPTV0_70_CFilterBVeto.deriv.DAOD_HIGG8D1.e5340_e5984_s3126_r10201_r10210_p4133
 mc16_13TeV.364186.Sherpa_221_NNPDF30NNLO_Wtaunu_MAXHTPTV0_70_BFilter.deriv.DAOD_HIGG8D1.e5340_e5984_s3126_r10201_r10210_p4133
 mc16_13TeV.364187.Sherpa_221_NNPDF30NNLO_Wtaunu_MAXHTPTV70_140_CVetoBVeto.deriv.DAOD_HIGG8D1.e5340_e5984_s3126_r10201_r10210_p4133
 mc16_13TeV.364188.Sherpa_221_NNPDF30NNLO_Wtaunu_MAXHTPTV70_140_CFilterBVeto.deriv.DAOD_HIGG8D1.e5340_e5984_s3126_r10201_r10210_p4133
 mc16_13TeV.364189.Sherpa_221_NNPDF30NNLO_Wtaunu_MAXHTPTV70_140_BFilter.deriv.DAOD_HIGG8D1.e5340_s3126_r10201_r10210_p4133
 mc16_13TeV.364190.Sherpa_221_NNPDF30NNLO_Wtaunu_MAXHTPTV140_280_CVetoBVeto.deriv.DAOD_HIGG8D1.e5340_s3126_r10201_r10210_p4133
 mc16_13TeV.364190.Sherpa_221_NNPDF30NNLO_Wtaunu_MAXHTPTV140_280_CVetoBVeto.deriv.DAOD_HIGG8D1.e5340_e5984_s3126_s3136_r10201_r10210_p4133

mc16_13TeV.364191.Sherpa_221_NNPDF30NNLO_Wtaunu_MAXHTPTV140_280_CFilterBVeto.deriv.DAOD_HIGG8D1.e5340_e5984_s3126_s3136_r10201_r10210_p4133
 mc16_13TeV.364191.Sherpa_221_NNPDF30NNLO_Wtaunu_MAXHTPTV140_280_CFilterBVeto.deriv.DAOD_HIGG8D1.e5340_s3126_r10201_r10210_p4133
 mc16_13TeV.364192.Sherpa_221_NNPDF30NNLO_Wtaunu_MAXHTPTV140_280_BFilter.deriv.DAOD_HIGG8D1.e5340_e5984_s3126_r10201_r10210_p4133
 mc16_13TeV.364193.Sherpa_221_NNPDF30NNLO_Wtaunu_MAXHTPTV280_500_CVetoBVeto.deriv.DAOD_HIGG8D1.e5340_e5984_s3126_r10201_r10210_p4133
 mc16_13TeV.364193.Sherpa_221_NNPDF30NNLO_Wtaunu_MAXHTPTV280_500_CVetoBVeto.deriv.DAOD_HIGG8D1.e5340_e5984_s3126_s3136_r10201_r10210_p4133
 mc16_13TeV.364194.Sherpa_221_NNPDF30NNLO_Wtaunu_MAXHTPTV280_500_CFilterBVeto.deriv.DAOD_HIGG8D1.e5340_e5984_s3126_r10201_r10210_p4133
 mc16_13TeV.364194.Sherpa_221_NNPDF30NNLO_Wtaunu_MAXHTPTV280_500_CFilterBVeto.deriv.DAOD_HIGG8D1.e5340_s3126_r10201_r10210_p4133
 mc16_13TeV.364194.Sherpa_221_NNPDF30NNLO_Wtaunu_MAXHTPTV280_500_BFilter.deriv.DAOD_HIGG8D1.e5340_e5984_s3126_r10201_r10210_p4133
 mc16_13TeV.364195.Sherpa_221_NNPDF30NNLO_Wtaunu_MAXHTPTV280_500_BFilter.deriv.DAOD_HIGG8D1.e5340_e5984_s3126_r10201_r10210_p4133
 mc16_13TeV.364195.Sherpa_221_NNPDF30NNLO_Wtaunu_MAXHTPTV280_500_BFilter.deriv.DAOD_HIGG8D1.e5340_s3126_r10201_r10210_p4133
 mc16_13TeV.364196.Sherpa_221_NNPDF30NNLO_Wtaunu_MAXHTPTV500_1000.deriv.DAOD_HIGG8D1.e5340_e5984_s3126_s3136_r10201_r10210_p4133
 mc16_13TeV.364196.Sherpa_221_NNPDF30NNLO_Wtaunu_MAXHTPTV500_1000.deriv.DAOD_HIGG8D1.e5340_s3126_r10201_r10210_p4133
 mc16_13TeV.364197.Sherpa_221_NNPDF30NNLO_Wtaunu_MAXHTPTV1000_E_CMS.deriv.DAOD_HIGG8D1.e5340_e5984_s3126_r10201_r10210_p4133
 mc16_13TeV.364500.Sherpa_222_NNPDF30NNLO_eegamma_pty_7_15.deriv.DAOD_HIGG8D1.e5928_e5984_s3126_r10201_r10210_p4133
 mc16_13TeV.364501.Sherpa_222_NNPDF30NNLO_eegamma_pty_15_35.deriv.DAOD_HIGG8D1.e5928_e5984_s3126_r10201_r10210_p4133
 mc16_13TeV.364502.Sherpa_222_NNPDF30NNLO_eegamma_pty_35_70.deriv.DAOD_HIGG8D1.e5928_e5984_s3126_r10201_r10210_p4133
 mc16_13TeV.364503.Sherpa_222_NNPDF30NNLO_eegamma_pty_70_140.deriv.DAOD_HIGG8D1.e5928_e5984_s3126_r10201_r10210_p4133
 mc16_13TeV.364504.Sherpa_222_NNPDF30NNLO_eegamma_pty_140_E_CMS.deriv.DAOD_HIGG8D1.e5928_e5984_s3126_r10201_r10210_p4133
 mc16_13TeV.364505.Sherpa_222_NNPDF30NNLO_mumugamma_pty_7_15.deriv.DAOD_HIGG8D1.e5928_e5984_s3126_r10201_r10210_p4133
 mc16_13TeV.364506.Sherpa_222_NNPDF30NNLO_mumugamma_pty_15_35.deriv.DAOD_HIGG8D1.e5928_e5984_s3126_r10201_r10210_p4133
 mc16_13TeV.364507.Sherpa_222_NNPDF30NNLO_mumugamma_pty_35_70.deriv.DAOD_HIGG8D1.e5928_e5984_s3126_r10201_r10210_p4133
 mc16_13TeV.364508.Sherpa_222_NNPDF30NNLO_mumugamma_pty_70_140.deriv.DAOD_HIGG8D1.e5928_e5984_s3126_r10201_r10210_p4133
 mc16_13TeV.364509.Sherpa_222_NNPDF30NNLO_mumugamma_pty_140_E_CMS.deriv.DAOD_HIGG8D1.e5928_e5984_s3126_r10201_r10210_p4133
 mc16_13TeV.364510.Sherpa_222_NNPDF30NNLO_tautaugamma_pty_7_15.deriv.DAOD_HIGG8D1.e5928_e5984_s3126_r10201_r10210_p4133
 mc16_13TeV.364511.Sherpa_222_NNPDF30NNLO_tautaugamma_pty_15_35.deriv.DAOD_HIGG8D1.e5928_e5984_s3126_r10201_r10210_p4133
 mc16_13TeV.364512.Sherpa_222_NNPDF30NNLO_tautaugamma_pty_35_70.deriv.DAOD_HIGG8D1.e5928_e5984_s3126_r10201_r10210_p4133
 mc16_13TeV.364513.Sherpa_222_NNPDF30NNLO_tautaugamma_pty_70_140.deriv.DAOD_HIGG8D1.e5982_e5984_s3126_r10201_r10210_p4133
 mc16_13TeV.364513.Sherpa_222_NNPDF30NNLO_tautaugamma_pty_70_140.deriv.DAOD_HIGG8D1.e5928_e5984_s3126_r10201_r10210_p4133
 mc16_13TeV.364514.Sherpa_222_NNPDF30NNLO_tautaugamma_pty_140_E_CMS.deriv.DAOD_HIGG8D1.e5928_e5984_s3126_r10201_r10210_p4133
 mc16_13TeV.364521.Sherpa_222_NNPDF30NNLO_enugamma_pty_7_15.deriv.DAOD_HIGG8D1.e5928_e5984_s3126_r10201_r10210_p4133
 mc16_13TeV.364522.Sherpa_222_NNPDF30NNLO_enugamma_pty_15_35.deriv.DAOD_HIGG8D1.e5928_e5984_s3126_r10201_r10210_p4133

mc16_13TeV.364523.Sherpa_222_NNPDF30NNLO_enugamma_pty_35_70.deriv.DAOD_HIGG8D1.e5928_e5984_s3126_r10201_r10210_p4133
 mc16_13TeV.364524.Sherpa_222_NNPDF30NNLO_enugamma_pty_70_140.deriv.DAOD_HIGG8D1.e5928_e5984_s3126_r10201_r10210_p4133
 mc16_13TeV.364525.Sherpa_222_NNPDF30NNLO_enugamma_pty_140_E_CMS.deriv.DAOD_HIGG8D1.e5928_e5984_s3126_r10201_r10210_p4133
 mc16_13TeV.364526.Sherpa_222_NNPDF30NNLO_munugamma_pty_7_15.deriv.DAOD_HIGG8D1.e5928_e5984_s3126_r10201_r10210_p4133
 mc16_13TeV.364527.Sherpa_222_NNPDF30NNLO_munugamma_pty_15_35.deriv.DAOD_HIGG8D1.e5928_e5984_s3126_r10201_r10210_p4133
 mc16_13TeV.364528.Sherpa_222_NNPDF30NNLO_munugamma_pty_35_70.deriv.DAOD_HIGG8D1.e5928_e5984_s3126_r10201_r10210_p4133
 mc16_13TeV.364529.Sherpa_222_NNPDF30NNLO_munugamma_pty_70_140.deriv.DAOD_HIGG8D1.e5928_e5984_s3126_r10201_r10210_p4133
 mc16_13TeV.364530.Sherpa_222_NNPDF30NNLO_munugamma_pty_140_E_CMS.deriv.DAOD_HIGG8D1.e5928_e5984_s3126_r10201_r10210_p4133
 mc16_13TeV.364531.Sherpa_222_NNPDF30NNLO_taunugamma_pty_7_15.deriv.DAOD_HIGG8D1.e5928_e5984_s3126_r10201_r10210_p4133
 mc16_13TeV.364532.Sherpa_222_NNPDF30NNLO_taunugamma_pty_15_35.deriv.DAOD_HIGG8D1.e5928_e5984_s3126_r10201_r10210_p4133
 mc16_13TeV.364533.Sherpa_222_NNPDF30NNLO_taunugamma_pty_35_70.deriv.DAOD_HIGG8D1.e5928_e5984_s3126_r10201_r10210_p4133
 mc16_13TeV.364534.Sherpa_222_NNPDF30NNLO_taunugamma_pty_70_140.deriv.DAOD_HIGG8D1.e5928_e5984_s3126_r10201_r10210_p4133
 mc16_13TeV.364535.Sherpa_222_NNPDF30NNLO_taunugamma_pty_140_E_CMS.deriv.DAOD_HIGG8D1.e5928_e5984_s3126_r10201_r10210_p4133
 mc16_13TeV.410560.MadGraphPythia8EvtGen_A14_tZ_4fl_tchan_noAllHad.deriv.DAOD_HIGG8D1.e5803_e5984_s3126_r10201_r10210_p4133
 mc16_13TeV.410013.PowhegPythiaEvtGen_P2012_Wt_inclusive_top.deriv.DAOD_HIGG8D1.e3753_s3126_r10201_r10210_p4133
 mc16_13TeV.410014.PowhegPythiaEvtGen_P2012_Wt_inclusive_antitop.deriv.DAOD_HIGG8D1.e3753_s3126_r10201_r10210_p4133
 mc16_13TeV.410408.aMcAtNloPythia8EvtGen_tWZ_Ztoll_minDR1.deriv.DAOD_HIGG8D1.e6423_e5984_s3126_r10201_r10210_p4133
 mc16_13TeV.364242.Sherpa_222_NNPDF30NNLO_WWW_3l3v_EW6.deriv.DAOD_HIGG8D1.e5887_e5984_s3126_r10201_r10210_p4133
 mc16_13TeV.364243.Sherpa_222_NNPDF30NNLO_WWZ_4l2v_EW6.deriv.DAOD_HIGG8D1.e5887_e5984_s3126_r10201_r10210_p4133
 mc16_13TeV.364244.Sherpa_222_NNPDF30NNLO_WWZ_2l4v_EW6.deriv.DAOD_HIGG8D1.e5887_e5984_s3126_r10201_r10210_p4133
 mc16_13TeV.364245.Sherpa_222_NNPDF30NNLO_WZZ_5l1v_EW6.deriv.DAOD_HIGG8D1.e5887_e5984_s3126_r10201_r10210_p4133
 mc16_13TeV.364246.Sherpa_222_NNPDF30NNLO_WZZ_3l3v_EW6.deriv.DAOD_HIGG8D1.e5887_e5984_s3126_r10201_r10210_p4133
 mc16_13TeV.364247.Sherpa_222_NNPDF30NNLO_ZZZ_6l0v_EW6.deriv.DAOD_HIGG8D1.e5887_e5984_s3126_r10201_r10210_p4133
 mc16_13TeV.364248.Sherpa_222_NNPDF30NNLO_ZZZ_4l2v_EW6.deriv.DAOD_HIGG8D1.e5887_e5984_s3126_r10201_r10210_p4133
 mc16_13TeV.364249.Sherpa_222_NNPDF30NNLO_ZZZ_2l4v_EW6.deriv.DAOD_HIGG8D1.e5887_e5984_s3126_r10201_r10210_p4133
 mc16_13TeV.342284.Pythia8EvtGen_A14NNPDF23LO_WH125_inc.deriv.DAOD_HIGG8D1.e4246_e5984_s3126_r10201_r10210_p4133
 mc16_13TeV.342285.Pythia8EvtGen_A14NNPDF23LO_ZH125_inc.deriv.DAOD_HIGG8D1.e4246_e5984_s3126_r10201_r10210_p4133
 mc16_13TeV.341998.aMcAtNloHppEG_UEEE5_CTEQ6L1_CT10ME_tWH125_gamgam_yt_plus1.deriv.DAOD_HIGG8D1.e4394_e5984_s3126_r10201_r10210_p4133
 mc16_13TeV.410470.PhPy8EG_A14_ttbar_hdamp258p75_nonallhad.deriv.DAOD_HIGG8D1.e6337_e5984_s3126_r10201_r10210_p4133
 mc16_13TeV.410472.PhPy8EG_A14_ttbar_hdamp258p75_dil.deriv.DAOD_HIGG8D1.e6348_e5984_s3126_r10201_r10210_p4133
 mc16_13TeV.346343.PhPy8EG_A14NNPDF23_NNPDF30ME_ttH125_allhad.deriv.DAOD_HIGG8D1.e7148_e5984_s3126_r10201_r10210_p4133

mc16_13TeV.346344.PhPy8EG_A14NNPDF23_NNPDF30ME_ttH125_semilep.deriv.DAOD_HIGG8D1.e7148_e5984_a875_r10201_r10210_p4133

mc16_13TeV.346345.PhPy8EG_A14NNPDF23_NNPDF30ME_ttH125_dilep.deriv.DAOD_HIGG8D1.e7148_e5984_a875_r10201_r10210_p4133

mc16e:

mc16_13TeV.361605.PowhegPy8EG_CT10nloME_AZNLOCTEQ6L1_ZZvvvv_mll4.deriv.DAOD_HIGG8D1.e4054_e5984_s3126_r10724_r10726_p4133

mc16_13TeV.361602.PowhegPy8EG_CT10nloME_AZNLOCTEQ6L1_WZlvvv_mll4.deriv.DAOD_HIGG8D1.e4054_e5984_s3126_r10724_r10726_p4133

mc16_13TeV.361601.PowhegPy8EG_CT10nloME_AZNLOCTEQ6L1_WZlvl_l_mll4.deriv.DAOD_HIGG8D1.e4475_e5984_s3126_r10724_r10726_p4133

mc16_13TeV.361600.PowhegPy8EG_CT10nloME_AZNLOCTEQ6L1_WWlvvv.deriv.DAOD_HIGG8D1.e4616_e5984_s3126_r10724_r10726_p4133

mc16_13TeV.361603.PowhegPy8EG_CT10nloME_AZNLOCTEQ6L1_ZZllll_mll4.deriv.DAOD_HIGG8D1.e4475_e5984_s3126_r10724_r10726_p4133

mc16_13TeV.361604.PowhegPy8EG_CT10nloME_AZNLOCTEQ6L1_ZZvvll_mll4.deriv.DAOD_HIGG8D1.e4475_e5984_s3126_r10724_r10726_p4133

mc16_13TeV.364288.Sherpa_222_NNPDF30NNLO_llll_lowMllPtComplement.deriv.DAOD_HIGG8D1.e6096_s3126_r10724_p3983 mc16_13TeV.364287.Sherpa_222_NNPDF

mc16_13TeV.364285.Sherpa_222_NNPDF30NNLO_llvjj_EW6.deriv.DAOD_HIGG8D1.e6055_e5984_s3126_r10724_r10726_p3983

mc16_13TeV.364284.Sherpa_222_NNPDF30NNLO_llvjj_EW6.deriv.DAOD_HIGG8D1.e6055_s3126_r10724_p3983

mc16_13TeV.364283.Sherpa_222_NNPDF30NNLO_lllljj_EW6.deriv.DAOD_HIGG8D1.e6055_s3126_r10724_p3983

mc16_13TeV.364739.MGPy8EG_NNPDF30NLO_A14NNPDF23LO_lvlljjEW6_OFMinus.deriv.DAOD_HIGG8D1.e7421_e5984_s3126_r10724_r10726_p4133

mc16_13TeV.364742.MGPy8EG_NNPDF30NLO_A14NNPDF23LO_lvlljjEW6_SFPlus.deriv.DAOD_HIGG8D1.e7421_e5984_s3126_r10724_r10726_p4133

mc16_13TeV.364740.MGPy8EG_NNPDF30NLO_A14NNPDF23LO_lvlljjEW6_OFPlus.deriv.DAOD_HIGG8D1.e7421_e5984_s3126_r10724_r10726_p4133

mc16_13TeV.364741.MGPy8EG_NNPDF30NLO_A14NNPDF23LO_lvlljjEW6_SFMinus.deriv.DAOD_HIGG8D1.e7421_e5984_s3126_r10724_r10726_p4133

mc16_13TeV.364253.Sherpa_222_NNPDF30NNLO_llv.deriv.DAOD_HIGG8D1.e5916_e5984_s3126_r10724_r10726_p4133

mc16_13TeV.364250.Sherpa_222_NNPDF30NNLO_llll.deriv.DAOD_HIGG8D1.e5894_e5984_s3126_r10724_r10726_p4133

mc16_13TeV.364254.Sherpa_222_NNPDF30NNLO_llv.deriv.DAOD_HIGG8D1.e5916_e5984_s3126_r10724_r10726_p4133

mc16_13TeV.364255.Sherpa_222_NNPDF30NNLO_lvvv.deriv.DAOD_HIGG8D1.e5916_e5984_s3126_r10724_r10726_p4133

mc16_13TeV.410155.aMcAtNloPythia8EvtGen_MEN30NLO_A14N23LO_ttW.deriv.DAOD_HIGG8D1.e5070_e5984_s3126_r10724_r10726_p4133

mc16_13TeV.410156.aMcAtNloPythia8EvtGen_MEN30NLO_A14N23LO_ttZnuuu.deriv.DAOD_HIGG8D1.e5070_e5984_s3126_r10724_r10726_p4133

mc16_13TeV.410157.aMcAtNloPythia8EvtGen_MEN30NLO_A14N23LO_ttZqq.deriv.DAOD_HIGG8D1.e5070_e5984_s3126_r10724_r10726_p4133

mc16_13TeV.410218.aMcAtNloPythia8EvtGen_MEN30NLO_A14N23LO_ttee.deriv.DAOD_HIGG8D1.e5070_e5984_s3126_r10724_r10726_p4133

mc16_13TeV.410219.aMcAtNloPythia8EvtGen_MEN30NLO_A14N23LO_ttmumu.deriv.DAOD_HIGG8D1.e5070_e5984_s3126_r10724_r10726_p4133

mc16_13TeV.410220.aMcAtNloPythia8EvtGen_MEN30NLO_A14N23LO_ttautau.deriv.DAOD_HIGG8D1.e5070_e5984_s3126_r10724_r10726_p4133

mc16_13TeV.410276.aMcAtNloPythia8EvtGen_MEN30NLO_A14N23LO_ttee_mll_1_5.deriv.DAOD_HIGG8D1.e6087_e5984_s3126_r10724_r10726_p4133

mc16_13TeV.410277.aMcAtNloPythia8EvtGen_MEN30NLO_A14N23LO_ttmumu_mll_1_5.deriv.DAOD_HIGG8D1.e6087_e5984_s3126_r10724_r10726_p4133

mc16_13TeV.410278.aMcAtNloPythia8EvtGen_MEN30NLO_A14N23LO_ttautau_mll_1_5.deriv.DAOD_HIGG8D1.e6087_e5984_s3126_r10724_r10726_p4133

mc16_13TeV.410397.MadGraphPythia8EvtGen_ttbar_wbee_MEN30LO_A14N23LO.deriv.DAOD_HIGG8D1.e6086_e5984_s3126_r10724_r10726_p4133
 mc16_13TeV.410398.MadGraphPythia8EvtGen_ttbar_wbmumu_MEN30LO_A14N23LO.deriv.DAOD_HIGG8D1.e6086_e5984_s3126_r10724_r10726_p4133
 mc16_13TeV.410399.MadGraphPythia8EvtGen_ttbar_wbttau_MEN30LO_A14N23LO.deriv.DAOD_HIGG8D1.e6086_e5984_s3126_r10724_r10726_p4133
 mc16_13TeV.410658.PhPy8EG_A14_tchan_BW50_lept_top.deriv.DAOD_HIGG8D1.e6671_e5984_s3126_s3136_r10724_r10726_p4133
 mc16_13TeV.410659.PhPy8EG_A14_tchan_BW50_lept_antitop.deriv.DAOD_HIGG8D1.e6671_e5984_s3126_s3136_r10724_r10726_p4133
 mc16_13TeV.410644.PowhegPythia8EvtGen_A14_singletop_schan_lept_top.deriv.DAOD_HIGG8D1.e6527_e5984_s3126_r10724_r10726_p4133
 mc16_13TeV.410645.PowhegPythia8EvtGen_A14_singletop_schan_lept_antitop.deriv.DAOD_HIGG8D1.e6527_e5984_s3126_r10724_r10726_p4133
 mc16_13TeV.412063.aMcAtNloPythia8EvtGen_llq_NNPDF30_nf4_A14.deriv.DAOD_TOPQ1.e7054_e5984_s3126_r10724_r10726_p4174
 mc16_13TeV.304014.MadGraphPythia8EvtGen_A14NNPDF23_3top_SM.deriv.DAOD_HIGG8D1.e4324_e5984_s3126_r10724_r10726_p4133
 mc16_13TeV.410080.MadGraphPythia8EvtGen_A14NNPDF23_4topSM.deriv.DAOD_HIGG8D1.e4111_e5984_s3126_r10724_r10726_p4133
 mc16_13TeV.410081.MadGraphPythia8EvtGen_A14NNPDF23_ttbarWW.deriv.DAOD_HIGG8D1.e4111_e5984_s3126_r10724_r10726_p4133
 mc16_13TeV.364100.Sherpa_221_NNPDF30NNLO_Zmumu_MAXHTPTV0_70_CVetoBVeto.deriv.DAOD_HIGG8D1.e5271_e5984_s3126_s3136_r10724_r10726_p4133
 mc16_13TeV.364100.Sherpa_221_NNPDF30NNLO_Zmumu_MAXHTPTV0_70_CVetoBVeto.deriv.DAOD_HIGG8D1.e5271_e5984_s3126_r10724_r10726_p4133
 mc16_13TeV.364101.Sherpa_221_NNPDF30NNLO_Zmumu_MAXHTPTV0_70_CFilterBVeto.deriv.DAOD_HIGG8D1.e5271_e5984_s3126_r10724_r10726_p4133
 mc16_13TeV.364102.Sherpa_221_NNPDF30NNLO_Zmumu_MAXHTPTV0_70_BFilter.deriv.DAOD_HIGG8D1.e5271_e5984_s3126_s3136_r10724_r10726_p4133
 mc16_13TeV.364102.Sherpa_221_NNPDF30NNLO_Zmumu_MAXHTPTV0_70_BFilter.deriv.DAOD_HIGG8D1.e5271_e5984_s3126_r10724_r10726_p4133
 mc16_13TeV.364103.Sherpa_221_NNPDF30NNLO_Zmumu_MAXHTPTV70_140_CVetoBVeto.deriv.DAOD_HIGG8D1.e5271_e5984_s3126_r10724_r10726_p4133
 mc16_13TeV.364103.Sherpa_221_NNPDF30NNLO_Zmumu_MAXHTPTV70_140_CVetoBVeto.deriv.DAOD_HIGG8D1.e5271_e5984_s3126_s3136_r10724_r10726_p4133
 mc16_13TeV.364104.Sherpa_221_NNPDF30NNLO_Zmumu_MAXHTPTV70_140_CFilterBVeto.deriv.DAOD_HIGG8D1.e5271_e5984_s3126_r10724_r10726_p4133
 mc16_13TeV.364104.Sherpa_221_NNPDF30NNLO_Zmumu_MAXHTPTV70_140_CFilterBVeto.deriv.DAOD_HIGG8D1.e5271_e5984_s3126_s3136_r10724_r10726_p4133
 mc16_13TeV.364106.Sherpa_221_NNPDF30NNLO_Zmumu_MAXHTPTV140_280_CVetoBVeto.deriv.DAOD_HIGG8D1.e5271_e5984_s3126_s3136_r10724_r10726_p4133
 mc16_13TeV.364107.Sherpa_221_NNPDF30NNLO_Zmumu_MAXHTPTV140_280_CFilterBVeto.deriv.DAOD_HIGG8D1.e5271_e5984_s3126_r10724_r10726_p4133
 mc16_13TeV.364107.Sherpa_221_NNPDF30NNLO_Zmumu_MAXHTPTV140_280_CFilterBVeto.deriv.DAOD_HIGG8D1.e5271_e5984_s3126_s3136_r10724_r10726_p4133
 mc16_13TeV.364108.Sherpa_221_NNPDF30NNLO_Zmumu_MAXHTPTV140_280_BFilter.deriv.DAOD_HIGG8D1.e5271_e5984_s3126_r10724_r10726_p4133
 mc16_13TeV.364109.Sherpa_221_NNPDF30NNLO_Zmumu_MAXHTPTV280_500_CVetoBVeto.deriv.DAOD_HIGG8D1.e5271_e5984_s3126_r10724_r10726_p4133
 mc16_13TeV.364110.Sherpa_221_NNPDF30NNLO_Zmumu_MAXHTPTV280_500_CFilterBVeto.deriv.DAOD_HIGG8D1.e5271_e5984_s3126_r10724_r10726_p4133
 mc16_13TeV.364110.Sherpa_221_NNPDF30NNLO_Zmumu_MAXHTPTV280_500_CFilterBVeto.deriv.DAOD_HIGG8D1.e5271_e5984_s3126_s3136_r10724_r10726_p4133
 mc16_13TeV.364111.Sherpa_221_NNPDF30NNLO_Zmumu_MAXHTPTV280_500_BFilter.deriv.DAOD_HIGG8D1.e5271_e5984_s3126_s3136_r10724_r10726_p4133
 mc16_13TeV.364111.Sherpa_221_NNPDF30NNLO_Zmumu_MAXHTPTV280_500_BFilter.deriv.DAOD_HIGG8D1.e5271_e5984_s3126_r10724_r10726_p4133
 mc16_13TeV.364112.Sherpa_221_NNPDF30NNLO_Zmumu_MAXHTPTV500_1000.deriv.DAOD_HIGG8D1.e5271_e5984_s3126_r10724_r10726_p4133

mc16_13TeV.364113.Sherpa_221_NNPDF30NNLO_Zmumu_MAXHTPTV1000_E_CMS.deriv.DAOD_HIGG8D1.e5271_e5984_s3126_r10724_r10726_p4133
 mc16_13TeV.364113.Sherpa_221_NNPDF30NNLO_Zmumu_MAXHTPTV1000_E_CMS.deriv.DAOD_HIGG8D1.e5271_e5984_s3126_s3136_r10724_r10726_p4133
 mc16_13TeV.364114.Sherpa_221_NNPDF30NNLO_Zee_MAXHTPTV0_70_CVetoBVeto.deriv.DAOD_HIGG8D1.e5299_e5984_s3126_s3136_r10724_r10726_p4133
 mc16_13TeV.364114.Sherpa_221_NNPDF30NNLO_Zee_MAXHTPTV0_70_CVetoBVeto.deriv.DAOD_HIGG8D1.e5299_e5984_s3126_r10724_r10726_p4133
 mc16_13TeV.364115.Sherpa_221_NNPDF30NNLO_Zee_MAXHTPTV0_70_CFilterBVeto.deriv.DAOD_HIGG8D1.e5299_e5984_s3126_s3136_r10724_r10726_p4133
 mc16_13TeV.364115.Sherpa_221_NNPDF30NNLO_Zee_MAXHTPTV0_70_CFilterBVeto.deriv.DAOD_HIGG8D1.e5299_e5984_s3126_r10724_r10726_p4133
 mc16_13TeV.364116.Sherpa_221_NNPDF30NNLO_Zee_MAXHTPTV0_70_BFilter.deriv.DAOD_HIGG8D1.e5299_e5984_s3126_r10724_r10726_p4133
 mc16_13TeV.364117.Sherpa_221_NNPDF30NNLO_Zee_MAXHTPTV70_140_CVetoBVeto.deriv.DAOD_HIGG8D1.e5299_e5984_s3126_s3136_r10724_r10726_p4133
 mc16_13TeV.364117.Sherpa_221_NNPDF30NNLO_Zee_MAXHTPTV70_140_CVetoBVeto.deriv.DAOD_HIGG8D1.e5299_e5984_s3126_r10724_r10726_p4133
 mc16_13TeV.364118.Sherpa_221_NNPDF30NNLO_Zee_MAXHTPTV70_140_CFilterBVeto.deriv.DAOD_HIGG8D1.e5299_e5984_s3126_s3136_r10724_r10726_p4133
 mc16_13TeV.364118.Sherpa_221_NNPDF30NNLO_Zee_MAXHTPTV70_140_CFilterBVeto.deriv.DAOD_HIGG8D1.e5299_e5984_s3126_r10724_r10726_p4133
 mc16_13TeV.364119.Sherpa_221_NNPDF30NNLO_Zee_MAXHTPTV70_140_BFilter.deriv.DAOD_HIGG8D1.e5299_e5984_s3126_r10724_r10726_p4133
 mc16_13TeV.364120.Sherpa_221_NNPDF30NNLO_Zee_MAXHTPTV140_280_CVetoBVeto.deriv.DAOD_HIGG8D1.e5299_e5984_s3126_r10724_r10726_p4133
 mc16_13TeV.364121.Sherpa_221_NNPDF30NNLO_Zee_MAXHTPTV140_280_CFilterBVeto.deriv.DAOD_HIGG8D1.e5299_e5984_s3126_r10724_r10726_p4133
 mc16_13TeV.364122.Sherpa_221_NNPDF30NNLO_Zee_MAXHTPTV140_280_BFilter.deriv.DAOD_HIGG8D1.e5299_e5984_s3126_s3136_r10724_r10726_p4133
 mc16_13TeV.364122.Sherpa_221_NNPDF30NNLO_Zee_MAXHTPTV140_280_BFilter.deriv.DAOD_HIGG8D1.e5299_e5984_s3126_r10724_r10726_p4133
 mc16_13TeV.364123.Sherpa_221_NNPDF30NNLO_Zee_MAXHTPTV280_500_CVetoBVeto.deriv.DAOD_HIGG8D1.e5299_e5984_s3126_r10724_r10726_p4133
 mc16_13TeV.364124.Sherpa_221_NNPDF30NNLO_Zee_MAXHTPTV280_500_CFilterBVeto.deriv.DAOD_HIGG8D1.e5299_e5984_s3126_r10724_r10726_p4133
 mc16_13TeV.364125.Sherpa_221_NNPDF30NNLO_Zee_MAXHTPTV280_500_BFilter.deriv.DAOD_HIGG8D1.e5299_e5984_s3126_s3136_r10724_r10726_p4133
 mc16_13TeV.364125.Sherpa_221_NNPDF30NNLO_Zee_MAXHTPTV280_500_BFilter.deriv.DAOD_HIGG8D1.e5299_e5984_s3126_r10724_r10726_p4133
 mc16_13TeV.364126.Sherpa_221_NNPDF30NNLO_Zee_MAXHTPTV500_1000.deriv.DAOD_HIGG8D1.e5299_e5984_s3126_r10724_r10726_p4133
 mc16_13TeV.364126.Sherpa_221_NNPDF30NNLO_Zee_MAXHTPTV500_1000.deriv.DAOD_HIGG8D1.e5299_e5984_s3126_s3136_r10724_r10726_p4133
 mc16_13TeV.364127.Sherpa_221_NNPDF30NNLO_Zee_MAXHTPTV1000_E_CMS.deriv.DAOD_HIGG8D1.e5299_e5984_s3126_s3136_r10724_r10726_p4133
 mc16_13TeV.364127.Sherpa_221_NNPDF30NNLO_Zee_MAXHTPTV1000_E_CMS.deriv.DAOD_HIGG8D1.e5299_e5984_s3126_r10724_r10726_p4133
 mc16_13TeV.364128.Sherpa_221_NNPDF30NNLO_Ztautau_MAXHTPTV0_70_CVetoBVeto.deriv.DAOD_HIGG8D1.e5307_e5984_s3126_s3136_r10724_r10726_p4133
 mc16_13TeV.364128.Sherpa_221_NNPDF30NNLO_Ztautau_MAXHTPTV0_70_CVetoBVeto.deriv.DAOD_HIGG8D1.e5307_e5984_s3126_r10724_r10726_p4133
 mc16_13TeV.364129.Sherpa_221_NNPDF30NNLO_Ztautau_MAXHTPTV0_70_CFilterBVeto.deriv.DAOD_HIGG8D1.e5307_e5984_s3126_r10724_r10726_p4133
 mc16_13TeV.364129.Sherpa_221_NNPDF30NNLO_Ztautau_MAXHTPTV0_70_CFilterBVeto.deriv.DAOD_HIGG8D1.e5307_e5984_s3126_s3136_r10724_r10726_p4133
 mc16_13TeV.364130.Sherpa_221_NNPDF30NNLO_Ztautau_MAXHTPTV0_70_BFilter.deriv.DAOD_HIGG8D1.e5307_e5984_s3126_s3136_r10724_r10726_p4133
 mc16_13TeV.364130.Sherpa_221_NNPDF30NNLO_Ztautau_MAXHTPTV0_70_BFilter.deriv.DAOD_HIGG8D1.e5307_e5984_s3126_r10724_r10726_p4133
 mc16_13TeV.364131.Sherpa_221_NNPDF30NNLO_Ztautau_MAXHTPTV70_140_CVetoBVeto.deriv.DAOD_HIGG8D1.e5307_e5984_s3126_r10724_r10726_p4133

mc16_13TeV.364132.Sherpa_221_NNPDF30NNLO_Ztautau_MAXHTPTV70_140_CFilterBVeto.deriv.DAOD_HIGG8D1.e5307_e5984_s3126_r10724_r10726_p4133
 mc16_13TeV.364132.Sherpa_221_NNPDF30NNLO_Ztautau_MAXHTPTV70_140_CFilterBVeto.deriv.DAOD_HIGG8D1.e5307_e5984_s3126_s3136_r10724_r10726_p4133
 mc16_13TeV.364133.Sherpa_221_NNPDF30NNLO_Ztautau_MAXHTPTV70_140_BFilter.deriv.DAOD_HIGG8D1.e5307_e5984_s3126_r10724_r10726_p4133
 mc16_13TeV.364134.Sherpa_221_NNPDF30NNLO_Ztautau_MAXHTPTV140_280_CVetoBVeto.deriv.DAOD_HIGG8D1.e5307_e5984_s3126_r10724_r10726_p4133
 mc16_13TeV.364135.Sherpa_221_NNPDF30NNLO_Ztautau_MAXHTPTV140_280_CFilterBVeto.deriv.DAOD_HIGG8D1.e5307_e5984_s3126_r10724_r10726_p4133
 mc16_13TeV.364135.Sherpa_221_NNPDF30NNLO_Ztautau_MAXHTPTV140_280_CFilterBVeto.deriv.DAOD_HIGG8D1.e5307_e5984_s3126_s3136_r10724_r10726_p4133
 mc16_13TeV.364136.Sherpa_221_NNPDF30NNLO_Ztautau_MAXHTPTV140_280_BFilter.deriv.DAOD_HIGG8D1.e5307_e5984_s3126_r10724_r10726_p4133
 mc16_13TeV.364137.Sherpa_221_NNPDF30NNLO_Ztautau_MAXHTPTV280_500_CVetoBVeto.deriv.DAOD_HIGG8D1.e5307_e5984_s3126_r10724_r10726_p4133
 mc16_13TeV.364138.Sherpa_221_NNPDF30NNLO_Ztautau_MAXHTPTV280_500_CFilterBVeto.deriv.DAOD_HIGG8D1.e5313_e5984_s3126_s3136_r10724_r10726_p4133
 mc16_13TeV.364138.Sherpa_221_NNPDF30NNLO_Ztautau_MAXHTPTV280_500_CFilterBVeto.deriv.DAOD_HIGG8D1.e5313_e5984_s3126_r10724_r10726_p4133
 mc16_13TeV.364139.Sherpa_221_NNPDF30NNLO_Ztautau_MAXHTPTV280_500_BFilter.deriv.DAOD_HIGG8D1.e5313_e5984_s3126_r10724_r10726_p4133
 mc16_13TeV.364139.Sherpa_221_NNPDF30NNLO_Ztautau_MAXHTPTV280_500_BFilter.deriv.DAOD_HIGG8D1.e5313_e5984_s3126_s3136_r10724_r10726_p4133
 mc16_13TeV.364140.Sherpa_221_NNPDF30NNLO_Ztautau_MAXHTPTV500_1000.deriv.DAOD_HIGG8D1.e5307_e5984_s3126_r10724_r10726_p4133
 mc16_13TeV.364140.Sherpa_221_NNPDF30NNLO_Ztautau_MAXHTPTV500_1000.deriv.DAOD_HIGG8D1.e5307_e5984_s3126_s3136_r10724_r10726_p4133
 mc16_13TeV.364141.Sherpa_221_NNPDF30NNLO_Ztautau_MAXHTPTV1000_E_CMS.deriv.DAOD_HIGG8D1.e5307_e5984_s3126_s3136_r10724_r10726_p4133
 mc16_13TeV.364141.Sherpa_221_NNPDF30NNLO_Ztautau_MAXHTPTV1000_E_CMS.deriv.DAOD_HIGG8D1.e5307_e5984_s3126_r10724_r10726_p4133
 mc16_13TeV.364198.Sherpa_221_NN30NNLO_Zmm_Mll10_40_MAXHTPTV0_70_BVeto.deriv.DAOD_HIGG8D1.e5421_e5984_s3126_r10724_r10726_p4133
 mc16_13TeV.364199.Sherpa_221_NN30NNLO_Zmm_Mll10_40_MAXHTPTV0_70_BFilter.deriv.DAOD_HIGG8D1.e5421_e5984_s3126_r10724_r10726_p4133
 mc16_13TeV.364200.Sherpa_221_NN30NNLO_Zmm_Mll10_40_MAXHTPTV70_280_BVeto.deriv.DAOD_HIGG8D1.e5421_e5984_s3126_r10724_r10726_p4133
 mc16_13TeV.364201.Sherpa_221_NN30NNLO_Zmm_Mll10_40_MAXHTPTV70_280_BFilter.deriv.DAOD_HIGG8D1.e5421_e5984_s3126_r10724_r10726_p4133
 mc16_13TeV.364202.Sherpa_221_NN30NNLO_Zmm_Mll10_40_MAXHTPTV280_E_CMS_BVeto.deriv.DAOD_HIGG8D1.e5421_e5984_s3126_r10724_r10726_p4133
 mc16_13TeV.364203.Sherpa_221_NN30NNLO_Zmm_Mll10_40_MAXHTPTV280_E_CMS_BFilter.deriv.DAOD_HIGG8D1.e5421_e5984_s3126_r10724_r10726_p4133
 mc16_13TeV.364204.Sherpa_221_NN30NNLO_Zee_Mll10_40_MAXHTPTV0_70_BVeto.deriv.DAOD_HIGG8D1.e5421_e5984_s3126_r10724_r10726_p4133
 mc16_13TeV.364205.Sherpa_221_NN30NNLO_Zee_Mll10_40_MAXHTPTV0_70_BFilter.deriv.DAOD_HIGG8D1.e5421_e5984_s3126_r10724_r10726_p4133
 mc16_13TeV.364206.Sherpa_221_NN30NNLO_Zee_Mll10_40_MAXHTPTV70_280_BVeto.deriv.DAOD_HIGG8D1.e5421_e5984_s3126_r10724_r10726_p4133
 mc16_13TeV.364207.Sherpa_221_NN30NNLO_Zee_Mll10_40_MAXHTPTV70_280_BFilter.deriv.DAOD_HIGG8D1.e5421_e5984_s3126_r10724_r10726_p4133
 mc16_13TeV.364208.Sherpa_221_NN30NNLO_Zee_Mll10_40_MAXHTPTV280_E_CMS_BVeto.deriv.DAOD_HIGG8D1.e5421_e5984_s3126_r10724_r10726_p4133
 mc16_13TeV.364209.Sherpa_221_NN30NNLO_Zee_Mll10_40_MAXHTPTV280_E_CMS_BFilter.deriv.DAOD_HIGG8D1.e5421_e5984_s3126_r10724_r10726_p4133
 mc16_13TeV.364210.Sherpa_221_NN30NNLO_Ztt_Mll10_40_MAXHTPTV0_70_BVeto.deriv.DAOD_HIGG8D1.e5421_e5984_s3126_r10724_r10726_p4133
 mc16_13TeV.364211.Sherpa_221_NN30NNLO_Ztt_Mll10_40_MAXHTPTV0_70_BFilter.deriv.DAOD_HIGG8D1.e5421_e5984_s3126_r10724_r10726_p4133
 mc16_13TeV.364212.Sherpa_221_NN30NNLO_Ztt_Mll10_40_MAXHTPTV70_280_BVeto.deriv.DAOD_HIGG8D1.e5421_e5984_s3126_r10724_r10726_p4133

mc16_13TeV.364213.Sherpa_221_NN30NNLO_Ztt_Mll10_40_MAXHTPTV70_280_BFilter.deriv.DAOD_HIGG8D1.e5421_e5984_s3126_r10724_r10726_p4133
 mc16_13TeV.364214.Sherpa_221_NN30NNLO_Ztt_Mll10_40_MAXHTPTV280_E_CMS_BVeto.deriv.DAOD_HIGG8D1.e5421_e5984_s3126_r10724_r10726_p4133
 mc16_13TeV.364215.Sherpa_221_NN30NNLO_Ztt_Mll10_40_MAXHTPTV280_E_CMS_BFilter.deriv.DAOD_HIGG8D1.e5421_e5984_s3126_r10724_r10726_p4133
 mc16_13TeV.364156.Sherpa_221_NNPDF30NNLO_Wmunu_MAXHTPTV0_70_CVetoBVeto.deriv.DAOD_HIGG8D1.e5340_e5984_s3126_r10724_r10726_p4133
 mc16_13TeV.364157.Sherpa_221_NNPDF30NNLO_Wmunu_MAXHTPTV0_70_CFilterBVeto.deriv.DAOD_HIGG8D1.e5340_e5984_s3126_r10724_r10726_p4133
 mc16_13TeV.364158.Sherpa_221_NNPDF30NNLO_Wmunu_MAXHTPTV0_70_BFilter.deriv.DAOD_HIGG8D1.e5340_e5984_s3126_s3136_r10724_r10726_p4133
 mc16_13TeV.364158.Sherpa_221_NNPDF30NNLO_Wmunu_MAXHTPTV0_70_BFilter.deriv.DAOD_HIGG8D1.e5340_e5984_s3126_r10724_r10726_p4133
 mc16_13TeV.364159.Sherpa_221_NNPDF30NNLO_Wmunu_MAXHTPTV70_140_CVetoBVeto.deriv.DAOD_HIGG8D1.e5340_e5984_s3126_s3136_r10724_r10726_p4133
 mc16_13TeV.364160.Sherpa_221_NNPDF30NNLO_Wmunu_MAXHTPTV70_140_CFilterBVeto.deriv.DAOD_HIGG8D1.e5340_e5984_s3126_s3136_r10724_r10726_p4133
 mc16_13TeV.364160.Sherpa_221_NNPDF30NNLO_Wmunu_MAXHTPTV70_140_CFilterBVeto.deriv.DAOD_HIGG8D1.e5340_e5984_s3126_r10724_r10726_p4133
 mc16_13TeV.364161.Sherpa_221_NNPDF30NNLO_Wmunu_MAXHTPTV70_140_BFilter.deriv.DAOD_HIGG8D1.e5340_e5984_s3126_r10724_r10726_p4133
 mc16_13TeV.364162.Sherpa_221_NNPDF30NNLO_Wmunu_MAXHTPTV140_280_CVetoBVeto.deriv.DAOD_HIGG8D1.e5340_e5984_s3126_r10724_r10726_p4133
 mc16_13TeV.364163.Sherpa_221_NNPDF30NNLO_Wmunu_MAXHTPTV140_280_CFilterBVeto.deriv.DAOD_HIGG8D1.e5340_e5984_s3126_s3136_r10724_r10726_p4133
 mc16_13TeV.364163.Sherpa_221_NNPDF30NNLO_Wmunu_MAXHTPTV140_280_CFilterBVeto.deriv.DAOD_HIGG8D1.e5340_e5984_s3126_r10724_r10726_p4133
 mc16_13TeV.364164.Sherpa_221_NNPDF30NNLO_Wmunu_MAXHTPTV140_280_BFilter.deriv.DAOD_HIGG8D1.e5340_e5984_s3126_r10724_r10726_p4133
 mc16_13TeV.364165.Sherpa_221_NNPDF30NNLO_Wmunu_MAXHTPTV280_500_CVetoBVeto.deriv.DAOD_HIGG8D1.e5340_e5984_s3126_r10724_r10726_p4133
 mc16_13TeV.364165.Sherpa_221_NNPDF30NNLO_Wmunu_MAXHTPTV280_500_CVetoBVeto.deriv.DAOD_HIGG8D1.e5340_e5984_s3126_s3136_r10724_r10726_p4133
 mc16_13TeV.364166.Sherpa_221_NNPDF30NNLO_Wmunu_MAXHTPTV280_500_CFilterBVeto.deriv.DAOD_HIGG8D1.e5340_e5984_s3126_s3136_r10724_r10726_p4133
 mc16_13TeV.364166.Sherpa_221_NNPDF30NNLO_Wmunu_MAXHTPTV280_500_CFilterBVeto.deriv.DAOD_HIGG8D1.e5340_e5984_s3126_r10724_r10726_p4133
 mc16_13TeV.364167.Sherpa_221_NNPDF30NNLO_Wmunu_MAXHTPTV280_500_BFilter.deriv.DAOD_HIGG8D1.e5340_e5984_s3126_r10724_r10726_p4133
 mc16_13TeV.364167.Sherpa_221_NNPDF30NNLO_Wmunu_MAXHTPTV280_500_BFilter.deriv.DAOD_HIGG8D1.e5340_e5984_s3126_s3136_r10724_r10726_p4133
 mc16_13TeV.364168.Sherpa_221_NNPDF30NNLO_Wmunu_MAXHTPTV500_1000.deriv.DAOD_HIGG8D1.e5340_e5984_s3126_r10724_r10726_p4133
 mc16_13TeV.364168.Sherpa_221_NNPDF30NNLO_Wmunu_MAXHTPTV500_1000.deriv.DAOD_HIGG8D1.e5340_e5984_s3126_s3136_r10724_r10726_p4133
 mc16_13TeV.364169.Sherpa_221_NNPDF30NNLO_Wmunu_MAXHTPTV1000_E_CMS.deriv.DAOD_HIGG8D1.e5340_e5984_s3126_s3136_r10724_r10726_p4133
 mc16_13TeV.364169.Sherpa_221_NNPDF30NNLO_Wmunu_MAXHTPTV1000_E_CMS.deriv.DAOD_HIGG8D1.e5340_e5984_s3126_r10724_r10726_p4133
 mc16_13TeV.364170.Sherpa_221_NNPDF30NNLO_Wenu_MAXHTPTV0_70_CVetoBVeto.deriv.DAOD_HIGG8D1.e5340_e5984_s3126_r10724_r10726_p4133
 mc16_13TeV.364171.Sherpa_221_NNPDF30NNLO_Wenu_MAXHTPTV0_70_CFilterBVeto.deriv.DAOD_HIGG8D1.e5340_e5984_s3126_r10724_r10726_p4133
 mc16_13TeV.364172.Sherpa_221_NNPDF30NNLO_Wenu_MAXHTPTV0_70_BFilter.deriv.DAOD_HIGG8D1.e5340_e5984_s3126_r10724_r10726_p4133
 mc16_13TeV.364173.Sherpa_221_NNPDF30NNLO_Wenu_MAXHTPTV70_140_CVetoBVeto.deriv.DAOD_HIGG8D1.e5340_e5984_s3126_s3136_r10724_r10726_p4133
 mc16_13TeV.364174.Sherpa_221_NNPDF30NNLO_Wenu_MAXHTPTV70_140_CFilterBVeto.deriv.DAOD_HIGG8D1.e5340_e5984_s3126_r10724_r10726_p4133
 mc16_13TeV.364175.Sherpa_221_NNPDF30NNLO_Wenu_MAXHTPTV70_140_BFilter.deriv.DAOD_HIGG8D1.e5340_e5984_s3126_s3136_r10724_r10726_p4133

mc16_13TeV.364176.Sherpa_221_NNPDF30NNLO_Wenu_MAXHTPTV140_280_CVetoBVeto.deriv.DAOD_HIGG8D1.e5340_e5984_s3126_r10724_r10726_p4133
 mc16_13TeV.364177.Sherpa_221_NNPDF30NNLO_Wenu_MAXHTPTV140_280_CFilterBVeto.deriv.DAOD_HIGG8D1.e5340_e5984_s3126_r10724_r10726_p4133
 mc16_13TeV.364177.Sherpa_221_NNPDF30NNLO_Wenu_MAXHTPTV140_280_CFilterBVeto.deriv.DAOD_HIGG8D1.e5340_e5984_s3126_s3136_r10724_r10726_p4133
 mc16_13TeV.364178.Sherpa_221_NNPDF30NNLO_Wenu_MAXHTPTV140_280_BFilter.deriv.DAOD_HIGG8D1.e5340_e5984_s3126_r10724_r10726_p4133
 mc16_13TeV.364179.Sherpa_221_NNPDF30NNLO_Wenu_MAXHTPTV280_500_CVetoBVeto.deriv.DAOD_HIGG8D1.e5340_e5984_s3126_r10724_r10726_p4133
 mc16_13TeV.364179.Sherpa_221_NNPDF30NNLO_Wenu_MAXHTPTV280_500_CVetoBVeto.deriv.DAOD_HIGG8D1.e5340_e5984_s3126_s3136_r10724_r10726_p4133
 mc16_13TeV.364180.Sherpa_221_NNPDF30NNLO_Wenu_MAXHTPTV280_500_CFilterBVeto.deriv.DAOD_HIGG8D1.e5340_e5984_s3126_s3136_r10724_r10726_p4133
 mc16_13TeV.364180.Sherpa_221_NNPDF30NNLO_Wenu_MAXHTPTV280_500_CFilterBVeto.deriv.DAOD_HIGG8D1.e5340_e5984_s3126_r10724_r10726_p4133
 mc16_13TeV.364181.Sherpa_221_NNPDF30NNLO_Wenu_MAXHTPTV280_500_BFilter.deriv.DAOD_HIGG8D1.e5340_e5984_s3126_s3136_r10724_r10726_p4133
 mc16_13TeV.364181.Sherpa_221_NNPDF30NNLO_Wenu_MAXHTPTV280_500_BFilter.deriv.DAOD_HIGG8D1.e5340_e5984_s3126_r10724_r10726_p4133
 mc16_13TeV.364182.Sherpa_221_NNPDF30NNLO_Wenu_MAXHTPTV500_1000.deriv.DAOD_HIGG8D1.e5340_e5984_s3126_s3136_r10724_r10726_p4133
 mc16_13TeV.364182.Sherpa_221_NNPDF30NNLO_Wenu_MAXHTPTV500_1000.deriv.DAOD_HIGG8D1.e5340_e5984_s3126_r10724_r10726_p4133
 mc16_13TeV.364183.Sherpa_221_NNPDF30NNLO_Wenu_MAXHTPTV1000_E_CMS.deriv.DAOD_HIGG8D1.e5340_e5984_s3126_r10724_r10726_p4133
 mc16_13TeV.364183.Sherpa_221_NNPDF30NNLO_Wenu_MAXHTPTV1000_E_CMS.deriv.DAOD_HIGG8D1.e5340_e5984_s3126_s3136_r10724_r10726_p4133
 mc16_13TeV.364184.Sherpa_221_NNPDF30NNLO_Wtaunu_MAXHTPTV0_70_CVetoBVeto.deriv.DAOD_HIGG8D1.e5340_e5984_s3126_r10724_r10726_p4133
 mc16_13TeV.364185.Sherpa_221_NNPDF30NNLO_Wtaunu_MAXHTPTV0_70_CFilterBVeto.deriv.DAOD_HIGG8D1.e5340_e5984_s3126_r10724_r10726_p4133
 mc16_13TeV.364186.Sherpa_221_NNPDF30NNLO_Wtaunu_MAXHTPTV0_70_BFilter.deriv.DAOD_HIGG8D1.e5340_e5984_s3126_s3136_r10724_r10726_p4133
 mc16_13TeV.364186.Sherpa_221_NNPDF30NNLO_Wtaunu_MAXHTPTV0_70_BFilter.deriv.DAOD_HIGG8D1.e5340_e5984_s3126_r10724_r10726_p4133
 mc16_13TeV.364187.Sherpa_221_NNPDF30NNLO_Wtaunu_MAXHTPTV70_140_CVetoBVeto.deriv.DAOD_HIGG8D1.e5340_e5984_s3126_r10724_r10726_p4133
 mc16_13TeV.364188.Sherpa_221_NNPDF30NNLO_Wtaunu_MAXHTPTV70_140_CFilterBVeto.deriv.DAOD_HIGG8D1.e5340_e5984_s3126_r10724_r10726_p4133
 mc16_13TeV.364189.Sherpa_221_NNPDF30NNLO_Wtaunu_MAXHTPTV70_140_BFilter.deriv.DAOD_HIGG8D1.e5340_e5984_s3126_r10724_r10726_p4133
 mc16_13TeV.364189.Sherpa_221_NNPDF30NNLO_Wtaunu_MAXHTPTV70_140_BFilter.deriv.DAOD_HIGG8D1.e5340_e5984_s3126_s3136_r10724_r10726_p4133
 mc16_13TeV.364190.Sherpa_221_NNPDF30NNLO_Wtaunu_MAXHTPTV140_280_CVetoBVeto.deriv.DAOD_HIGG8D1.e5340_e5984_s3126_r10724_r10726_p4133
 mc16_13TeV.364190.Sherpa_221_NNPDF30NNLO_Wtaunu_MAXHTPTV140_280_CVetoBVeto.deriv.DAOD_HIGG8D1.e5340_e5984_s3126_s3136_r10724_r10726_p4133
 mc16_13TeV.364191.Sherpa_221_NNPDF30NNLO_Wtaunu_MAXHTPTV140_280_CFilterBVeto.deriv.DAOD_HIGG8D1.e5340_e5984_s3126_r10724_r10726_p4133
 mc16_13TeV.364191.Sherpa_221_NNPDF30NNLO_Wtaunu_MAXHTPTV140_280_CFilterBVeto.deriv.DAOD_HIGG8D1.e5340_e5984_s3126_s3136_r10724_r10726_p4133
 mc16_13TeV.364192.Sherpa_221_NNPDF30NNLO_Wtaunu_MAXHTPTV140_280_BFilter.deriv.DAOD_HIGG8D1.e5340_e5984_s3126_s3136_r10724_r10726_p4133
 mc16_13TeV.364192.Sherpa_221_NNPDF30NNLO_Wtaunu_MAXHTPTV140_280_BFilter.deriv.DAOD_HIGG8D1.e5340_e5984_s3126_r10724_r10726_p4133
 mc16_13TeV.364193.Sherpa_221_NNPDF30NNLO_Wtaunu_MAXHTPTV280_500_CVetoBVeto.deriv.DAOD_HIGG8D1.e5340_e5984_s3126_r10724_r10726_p4133
 mc16_13TeV.364193.Sherpa_221_NNPDF30NNLO_Wtaunu_MAXHTPTV280_500_CVetoBVeto.deriv.DAOD_HIGG8D1.e5340_e5984_s3126_s3136_r10724_r10726_p4133
 mc16_13TeV.364194.Sherpa_221_NNPDF30NNLO_Wtaunu_MAXHTPTV280_500_CFilterBVeto.deriv.DAOD_HIGG8D1.e5340_e5984_s3126_s3136_r10724_r10726_p4133

mc16_13TeV.364194.Sherpa_221_NNPDF30NNLO_Wtaunu_MAXHTPTV280_500_CFilterBVeto.deriv.DAOD_HIGG8D1.e5340_e5984_s3126_r10724_r10726_p4133
 mc16_13TeV.364195.Sherpa_221_NNPDF30NNLO_Wtaunu_MAXHTPTV280_500_BFilter.deriv.DAOD_HIGG8D1.e5340_e5984_s3126_s3136_r10724_r10726_p4133
 mc16_13TeV.364195.Sherpa_221_NNPDF30NNLO_Wtaunu_MAXHTPTV280_500_BFilter.deriv.DAOD_HIGG8D1.e5340_e5984_s3126_r10724_r10726_p4133
 mc16_13TeV.364196.Sherpa_221_NNPDF30NNLO_Wtaunu_MAXHTPTV500_1000.deriv.DAOD_HIGG8D1.e5340_e5984_s3126_s3136_r10724_r10726_p4133
 mc16_13TeV.364196.Sherpa_221_NNPDF30NNLO_Wtaunu_MAXHTPTV500_1000.deriv.DAOD_HIGG8D1.e5340_e5984_s3126_r10724_r10726_p4133
 mc16_13TeV.364197.Sherpa_221_NNPDF30NNLO_Wtaunu_MAXHTPTV1000_E_CMS.deriv.DAOD_HIGG8D1.e5340_e5984_s3126_s3136_r10724_r10726_p4133
 mc16_13TeV.364197.Sherpa_221_NNPDF30NNLO_Wtaunu_MAXHTPTV1000_E_CMS.deriv.DAOD_HIGG8D1.e5340_e5984_s3126_r10724_r10726_p4133
 mc16_13TeV.364500.Sherpa_222_NNPDF30NNLO_eegamma_pty_7_15.deriv.DAOD_HIGG8D1.e5928_e5984_s3126_r10724_r10726_p4133
 mc16_13TeV.364501.Sherpa_222_NNPDF30NNLO_eegamma_pty_15_35.deriv.DAOD_HIGG8D1.e5928_e5984_s3126_r10724_r10726_p4133
 mc16_13TeV.364502.Sherpa_222_NNPDF30NNLO_eegamma_pty_35_70.deriv.DAOD_HIGG8D1.e5928_e5984_s3126_r10724_r10726_p4133
 mc16_13TeV.364503.Sherpa_222_NNPDF30NNLO_eegamma_pty_70_140.deriv.DAOD_HIGG8D1.e5928_e5984_s3126_r10724_r10726_p4133
 mc16_13TeV.364504.Sherpa_222_NNPDF30NNLO_eegamma_pty_140_E_CMS.deriv.DAOD_HIGG8D1.e5928_e5984_s3126_r10724_r10726_p4133
 mc16_13TeV.364505.Sherpa_222_NNPDF30NNLO_mumugamma_pty_7_15.deriv.DAOD_HIGG8D1.e5928_e5984_s3126_r10724_r10726_p4133
 mc16_13TeV.364506.Sherpa_222_NNPDF30NNLO_mumugamma_pty_15_35.deriv.DAOD_HIGG8D1.e5928_e5984_s3126_r10724_r10726_p4133
 mc16_13TeV.364507.Sherpa_222_NNPDF30NNLO_mumugamma_pty_35_70.deriv.DAOD_HIGG8D1.e5928_e5984_s3126_r10724_r10726_p4133
 mc16_13TeV.364508.Sherpa_222_NNPDF30NNLO_mumugamma_pty_70_140.deriv.DAOD_HIGG8D1.e5928_e5984_s3126_r10724_r10726_p4133
 mc16_13TeV.364509.Sherpa_222_NNPDF30NNLO_mumugamma_pty_140_E_CMS.deriv.DAOD_HIGG8D1.e5928_e5984_s3126_r10724_r10726_p4133
 mc16_13TeV.364511.Sherpa_222_NNPDF30NNLO_tautaugamma_pty_15_35.deriv.DAOD_HIGG8D1.e5928_e5984_s3126_r10724_r10726_p4133
 mc16_13TeV.364512.Sherpa_222_NNPDF30NNLO_tautaugamma_pty_35_70.deriv.DAOD_HIGG8D1.e5928_e5984_s3126_r10724_r10726_p4133
 mc16_13TeV.364513.Sherpa_222_NNPDF30NNLO_tautaugamma_pty_70_140.deriv.DAOD_HIGG8D1.e5982_e5984_s3126_r10724_r10726_p4133
 mc16_13TeV.364514.Sherpa_222_NNPDF30NNLO_tautaugamma_pty_140_E_CMS.deriv.DAOD_HIGG8D1.e5928_e5984_s3126_r10724_r10726_p4133
 mc16_13TeV.364522.Sherpa_222_NNPDF30NNLO_enugamma_pty_15_35.deriv.DAOD_HIGG8D1.e5928_e5984_s3126_r10724_r10726_p4133
 mc16_13TeV.364523.Sherpa_222_NNPDF30NNLO_enugamma_pty_35_70.deriv.DAOD_HIGG8D1.e5928_e5984_s3126_r10724_r10726_p4133
 mc16_13TeV.364524.Sherpa_222_NNPDF30NNLO_enugamma_pty_70_140.deriv.DAOD_HIGG8D1.e5928_e5984_s3126_r10724_r10726_p4133
 mc16_13TeV.364525.Sherpa_222_NNPDF30NNLO_enugamma_pty_140_E_CMS.deriv.DAOD_HIGG8D1.e5928_e5984_s3126_r10724_r10726_p4133
 mc16_13TeV.364527.Sherpa_222_NNPDF30NNLO_munugamma_pty_15_35.deriv.DAOD_HIGG8D1.e5928_e5984_s3126_r10724_r10726_p4133
 mc16_13TeV.364528.Sherpa_222_NNPDF30NNLO_munugamma_pty_35_70.deriv.DAOD_HIGG8D1.e5928_e5984_s3126_r10724_r10726_p4133
 mc16_13TeV.364529.Sherpa_222_NNPDF30NNLO_munugamma_pty_70_140.deriv.DAOD_HIGG8D1.e5928_e5984_s3126_r10724_r10726_p4133
 mc16_13TeV.364530.Sherpa_222_NNPDF30NNLO_munugamma_pty_140_E_CMS.deriv.DAOD_HIGG8D1.e5928_e5984_s3126_r10724_r10726_p4133
 mc16_13TeV.364532.Sherpa_222_NNPDF30NNLO_taunugamma_pty_15_35.deriv.DAOD_HIGG8D1.e5928_e5984_s3126_r10724_r10726_p4133
 mc16_13TeV.364533.Sherpa_222_NNPDF30NNLO_taunugamma_pty_35_70.deriv.DAOD_HIGG8D1.e5928_e5984_s3126_r10724_r10726_p4133

mc16_13TeV.364534.Sherpa_222_NNPDF30NNLO_taunugamma_pty_70_140.deriv.DAOD_HIGG8D1.e5928_e5984_s3126_r10724_r10726_p4133
 mc16_13TeV.364535.Sherpa_222_NNPDF30NNLO_taunugamma_pty_140_E_CMS.deriv.DAOD_HIGG8D1.e5928_e5984_s3126_r10724_r10726_p4133
 mc16_13TeV.410560.MadGraphPythia8EvtGen_A14_tZ_4fl_tchan_noAllHad.deriv.DAOD_HIGG8D1.e5803_e5984_s3126_r10724_r10726_p4133
 mc16_13TeV.410408.aMcAtNloPythia8EvtGen_tWZ_Ztoll_minDR1.deriv.DAOD_HIGG8D1.e6423_e5984_s3126_r10724_r10726_p4133
 mc16_13TeV.364242.Sherpa_222_NNPDF30NNLO_WWW_3l3v_EW6.deriv.DAOD_HIGG8D1.e5887_e5984_s3126_r10724_r10726_p4133
 mc16_13TeV.364243.Sherpa_222_NNPDF30NNLO_WWZ_4l2v_EW6.deriv.DAOD_HIGG8D1.e5887_e5984_s3126_r10724_r10726_p4133
 mc16_13TeV.364244.Sherpa_222_NNPDF30NNLO_WWZ_2l4v_EW6.deriv.DAOD_HIGG8D1.e5887_e5984_s3126_r10724_r10726_p4133
 mc16_13TeV.364245.Sherpa_222_NNPDF30NNLO_WZZ_5l1v_EW6.deriv.DAOD_HIGG8D1.e5887_e5984_s3126_r10724_r10726_p4133
 mc16_13TeV.364246.Sherpa_222_NNPDF30NNLO_WZZ_3l3v_EW6.deriv.DAOD_HIGG8D1.e5887_e5984_s3126_r10724_r10726_p4133
 mc16_13TeV.364247.Sherpa_222_NNPDF30NNLO_ZZZ_6l0v_EW6.deriv.DAOD_HIGG8D1.e5887_e5984_s3126_r10724_r10726_p4133
 mc16_13TeV.364248.Sherpa_222_NNPDF30NNLO_ZZZ_4l2v_EW6.deriv.DAOD_HIGG8D1.e5887_e5984_s3126_r10724_r10726_p4133
 mc16_13TeV.364249.Sherpa_222_NNPDF30NNLO_ZZZ_2l4v_EW6.deriv.DAOD_HIGG8D1.e5887_e5984_s3126_r10724_r10726_p4133
 mc16_13TeV.342284.Pythia8EvtGen_A14NNPDF23LO_WH125_inc.deriv.DAOD_HIGG8D1.e4246_e5984_s3126_r10724_r10726_p4133
 mc16_13TeV.342285.Pythia8EvtGen_A14NNPDF23LO_ZH125_inc.deriv.DAOD_HIGG8D1.e4246_e5984_s3126_r10724_r10726_p4133
 mc16_13TeV.341998.aMcAtNloHppEG_UEEE5_CTEQ6L1_CT10ME_tWH125_gamgam_yt_plus1.deriv.DAOD_HIGG8D1.e4394_e5984_s3126_r10724_r10726_p4133
 mc16_13TeV.410389.MadGraphPythia8EvtGen_A14NNPDF23_ttgamma_nonallhadronic.deriv.DAOD_HIGG8D1.e6155_e5984_s3126_r10724_r10726_p4133
 mc16_13TeV.410470.PhPy8EG_A14_ttbar_hdamp258p75_nonallhad.deriv.DAOD_HIGG8D1.e6337_e5984_s3126_r10724_r10726_p4133
 mc16_13TeV.410472.PhPy8EG_A14_ttbar_hdamp258p75_dil.deriv.DAOD_HIGG8D1.e6348_e5984_s3126_r10724_r10726_p4133
 mc16_13TeV.346343.PhPy8EG_A14NNPDF23_NNPDF30ME_ttH125_allhad.deriv.DAOD_HIGG8D1.e7148_e5984_s3126_r10724_r10726_p4133
 mc16_13TeV.346343.PhPy8EG_A14NNPDF23_NNPDF30ME_ttH125_allhad.deriv.DAOD_HIGG8D1.e7148_e5984_a875_r10724_r10726_p4133
 mc16_13TeV.346344.PhPy8EG_A14NNPDF23_NNPDF30ME_ttH125_semilep.deriv.DAOD_HIGG8D1.e7148_e5984_a875_r10724_r10726_p4133
 mc16_13TeV.346344.PhPy8EG_A14NNPDF23_NNPDF30ME_ttH125_semilep.deriv.DAOD_HIGG8D1.e7148_e5984_s3126_r10724_r10726_p4133
 mc16_13TeV.346345.PhPy8EG_A14NNPDF23_NNPDF30ME_ttH125_dilep.deriv.DAOD_HIGG8D1.e7148_e5984_a875_r10724_r10726_p4133
 mc16_13TeV.346345.PhPy8EG_A14NNPDF23_NNPDF30ME_ttH125_dilep.deriv.DAOD_HIGG8D1.e7148_e5984_s3126_r10724_r10726_p4133

1848 **A Machine Learning Models**

1849 The following section provides details of the various MVAs as well as a few studies performed
1850 in support of this analysis, exploring alternate decisions and strategies.

1851 **A.1 Higgs Reconstruction Models**

1852 **A.1.1 b-jet Identification Features - 2lSS**

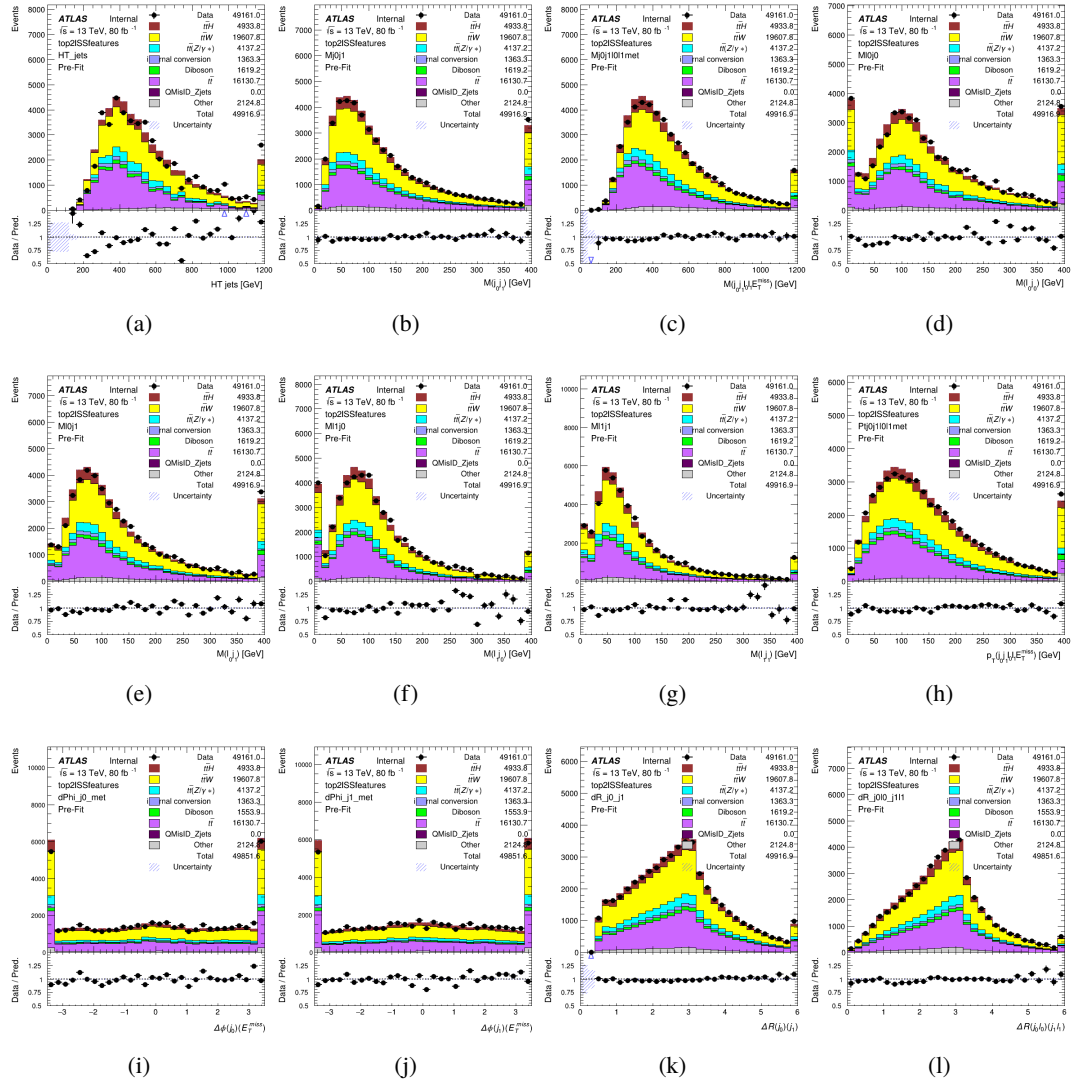


Figure A.1: Input features for top2lSS

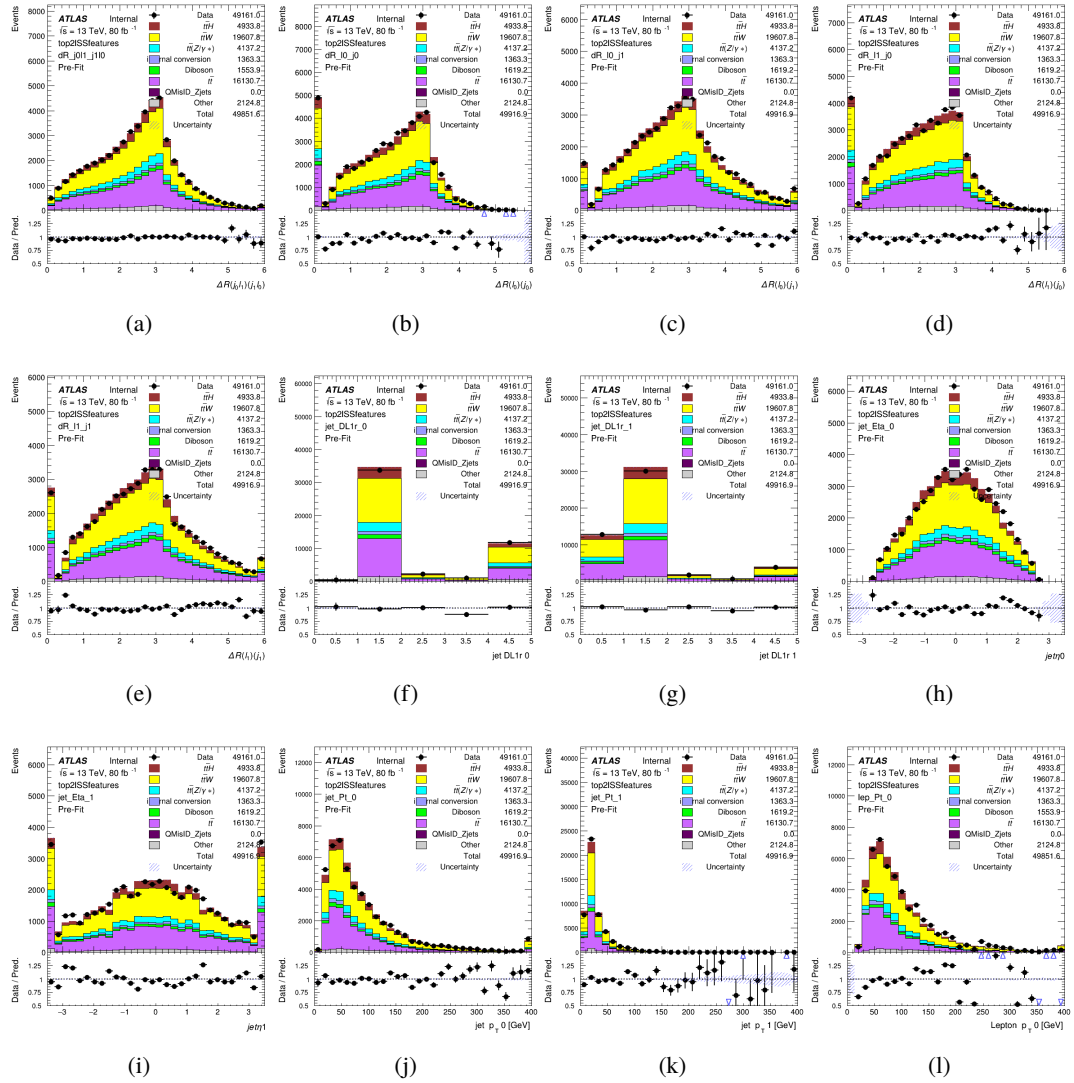


Figure A.2: Input features for top2lSS

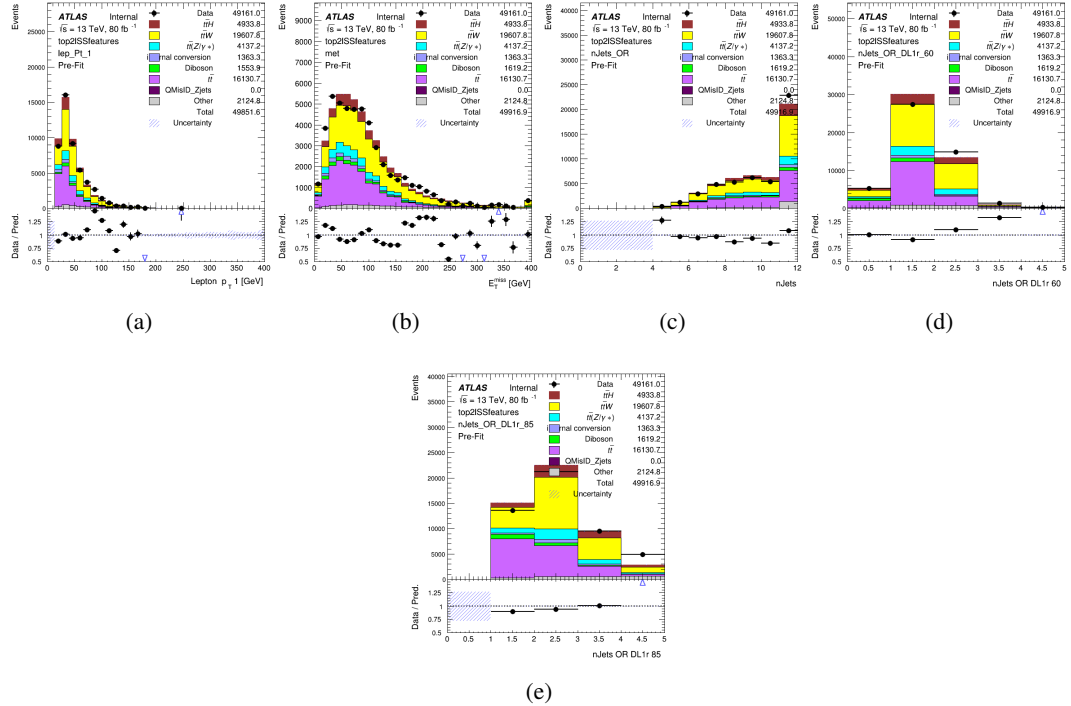


Figure A.3: Input features for top2ISS

1853 **A.1.2 b-jet Identification Features - 3l**

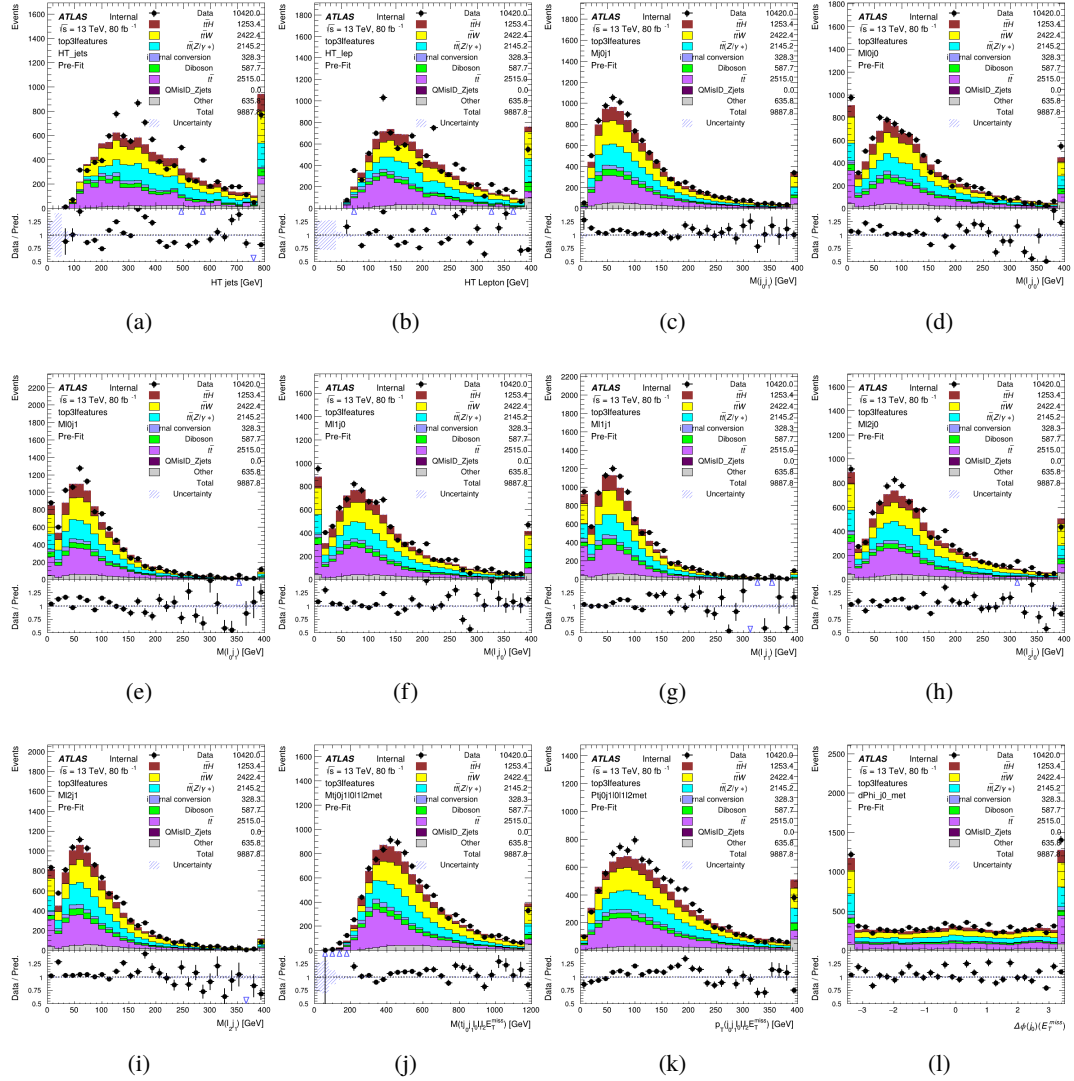


Figure A.4: Input features for top31

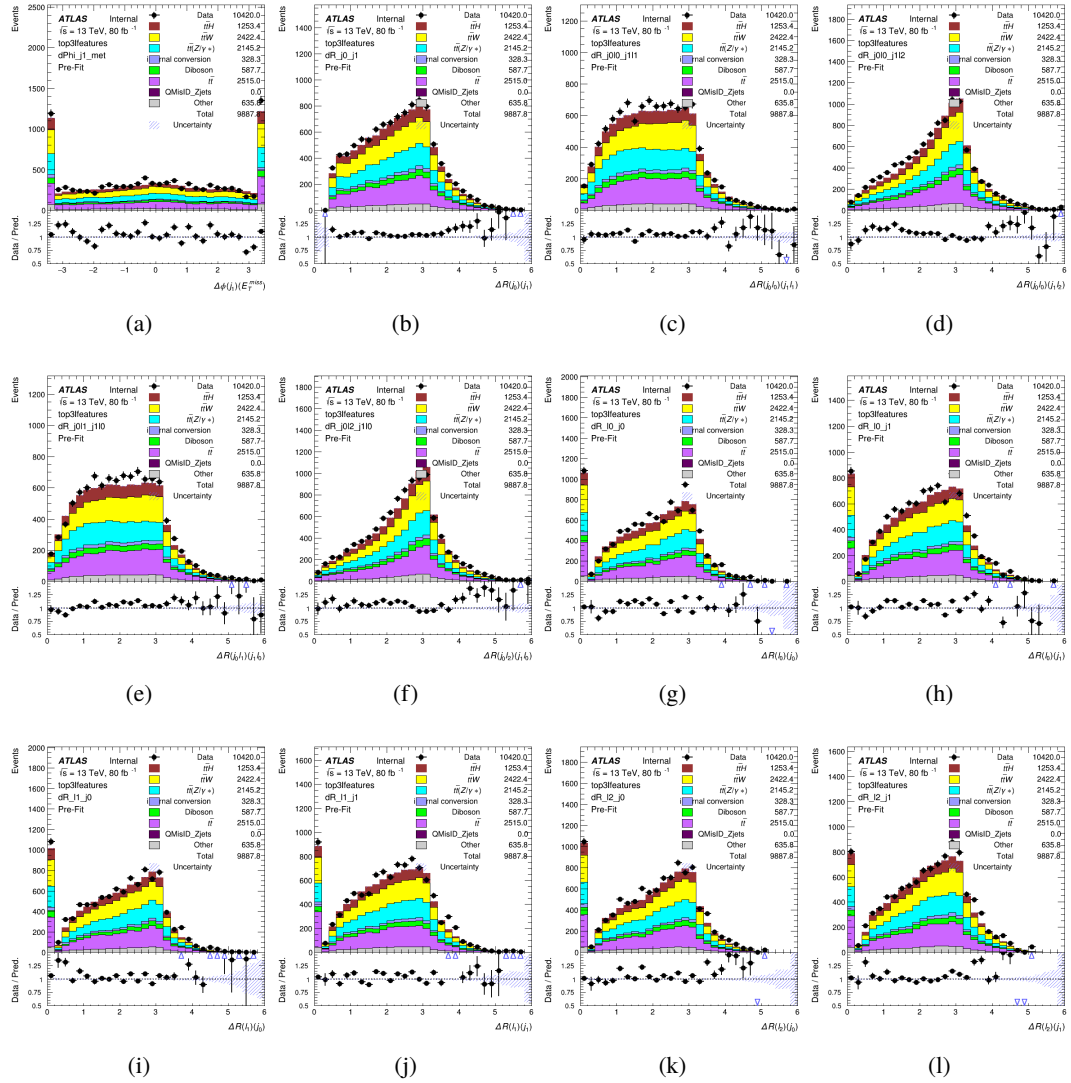


Figure A.5: Input features for top31

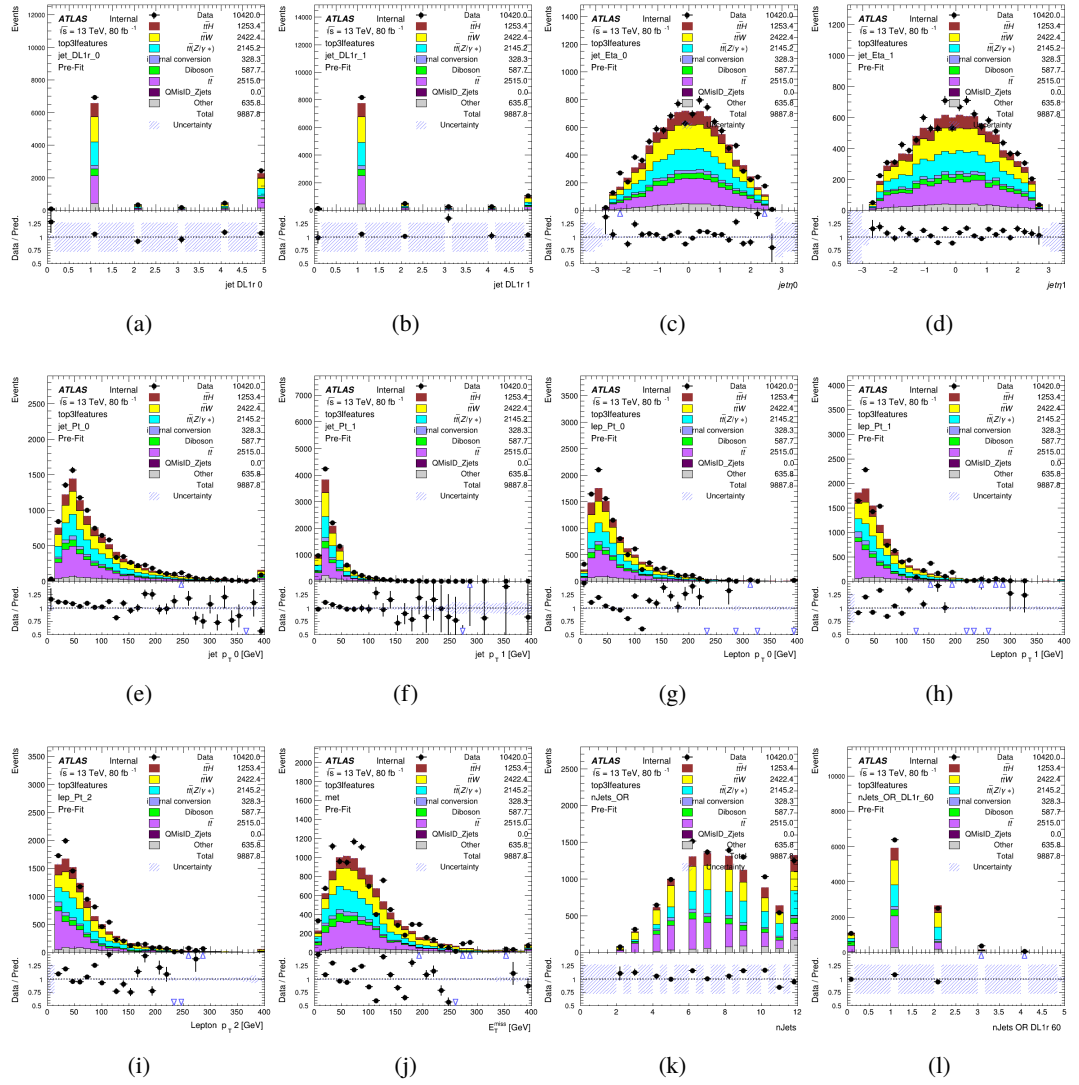
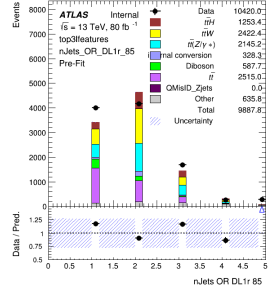


Figure A.6: Input features for top31



(a)

Figure A.7: Input features for top31

1854 **A.1.3 Higgs Reconstruction Features - 2lSS**

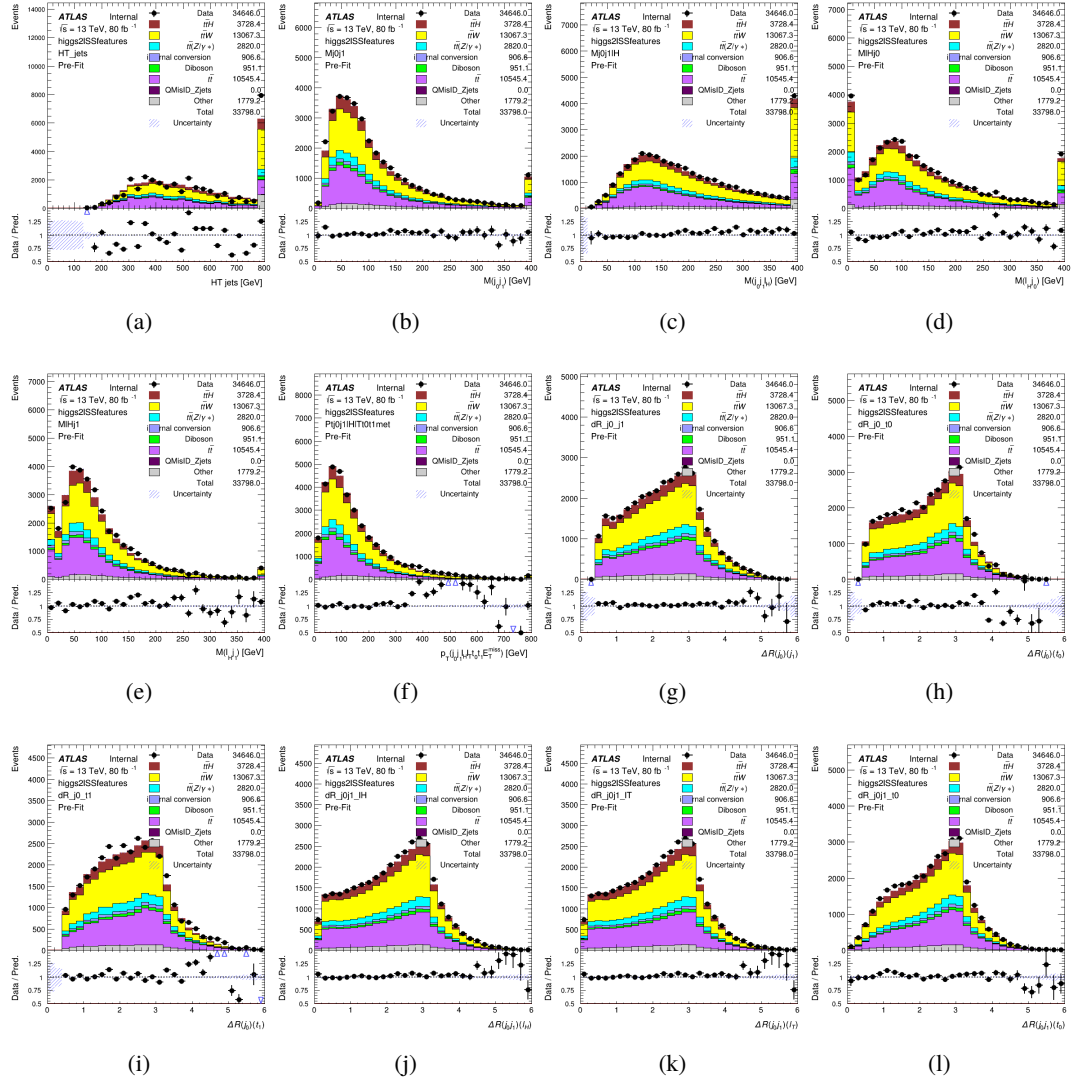


Figure A.8: Input features for higgs2lSS

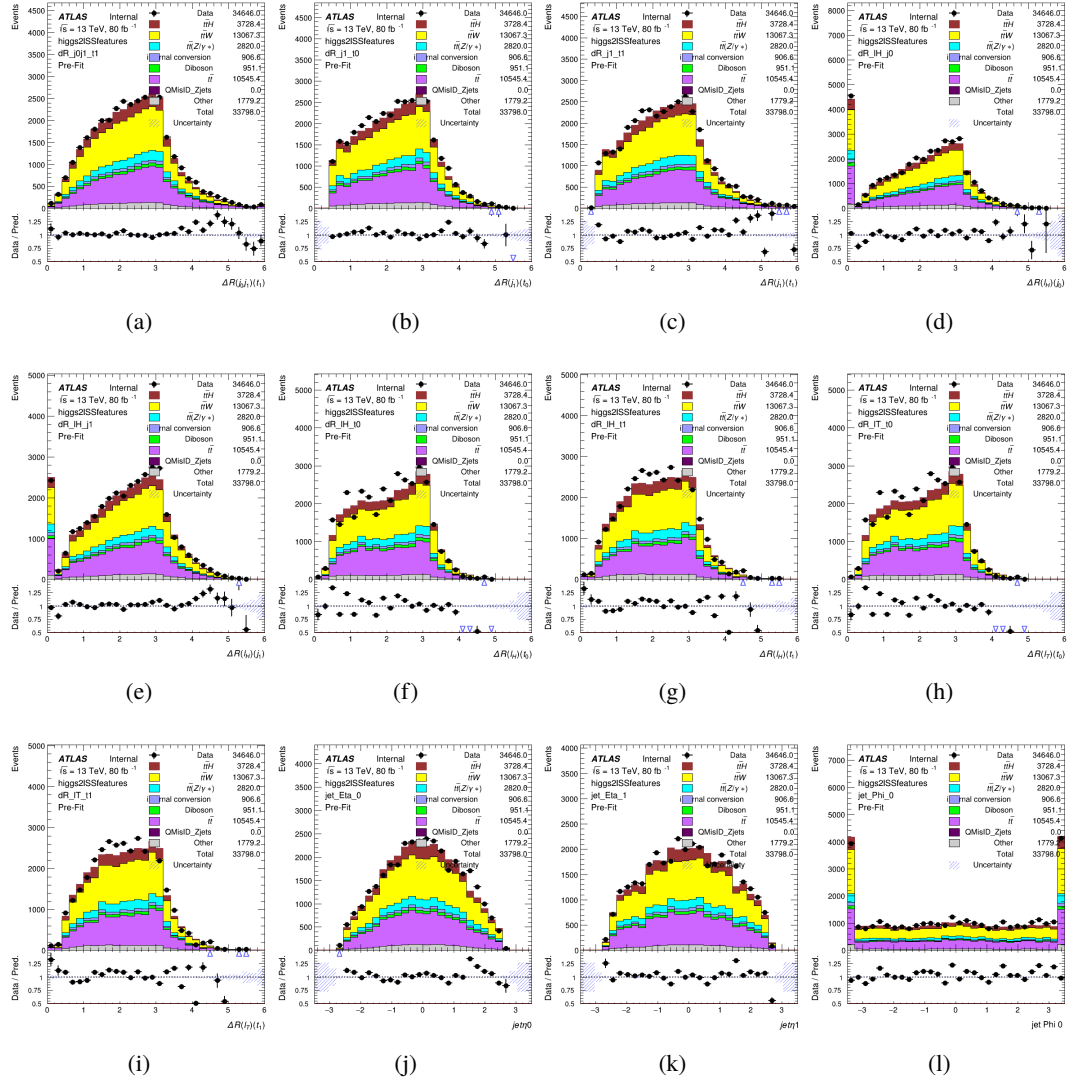


Figure A.9: Input features for higgs2lSS

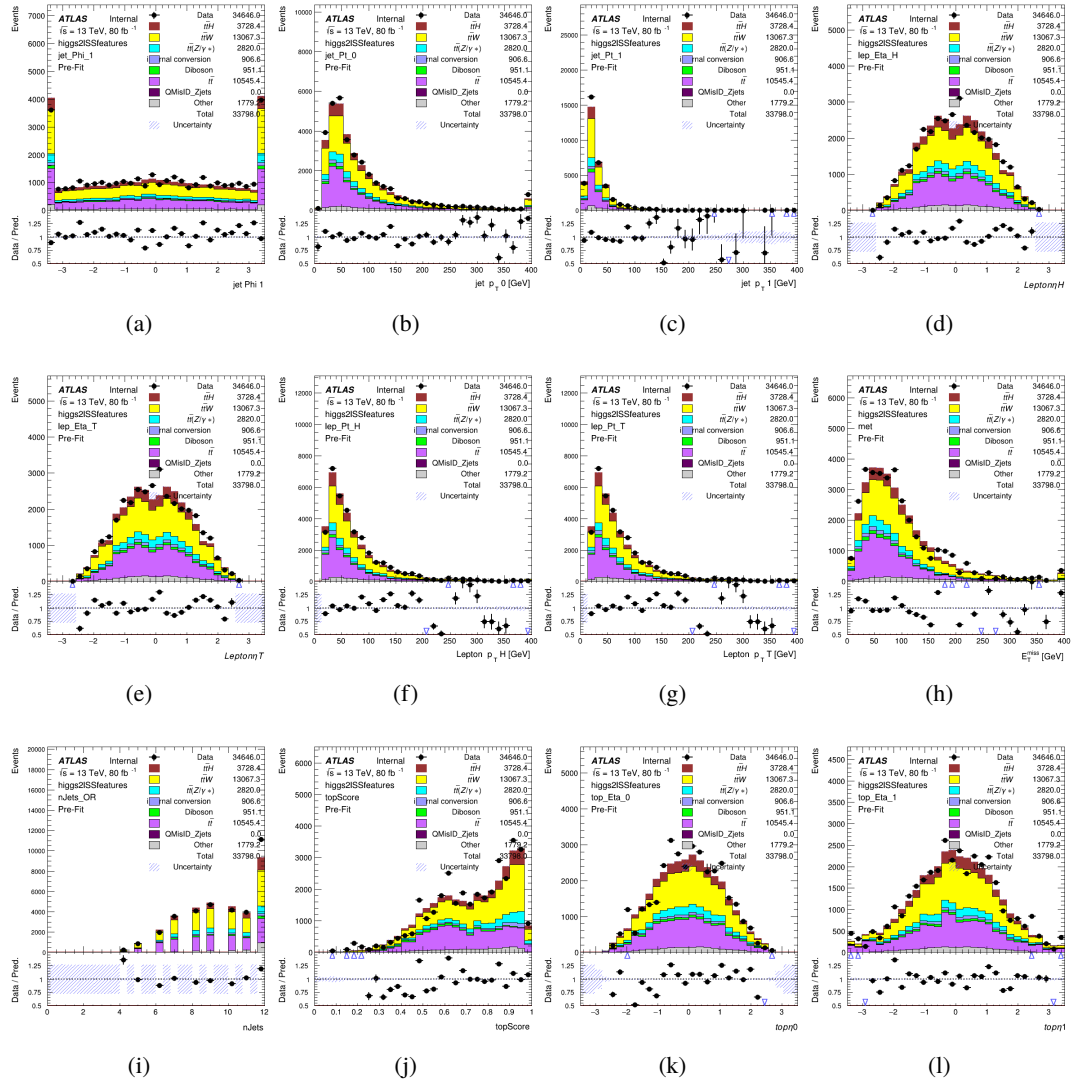


Figure A.10: Input features for higgs2IS

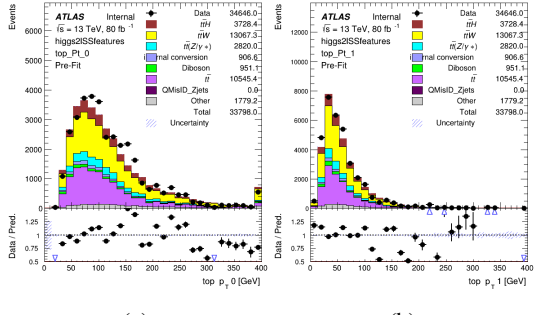


Figure A.11: Input features for higgs2lSS

1855 **A.1.4 Higgs Reconstruction Features - 3lS**

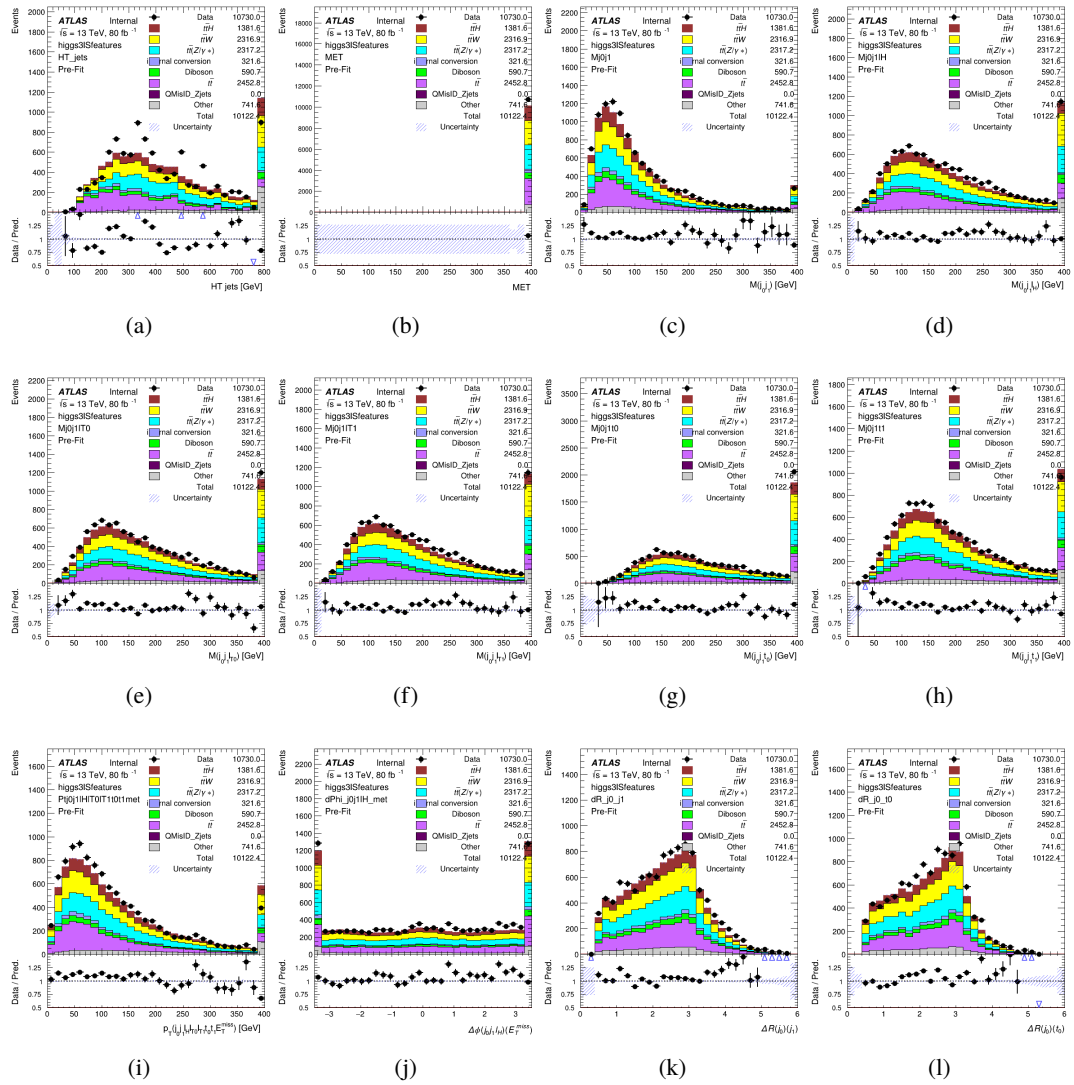


Figure A.12: Input features for higgs3lS

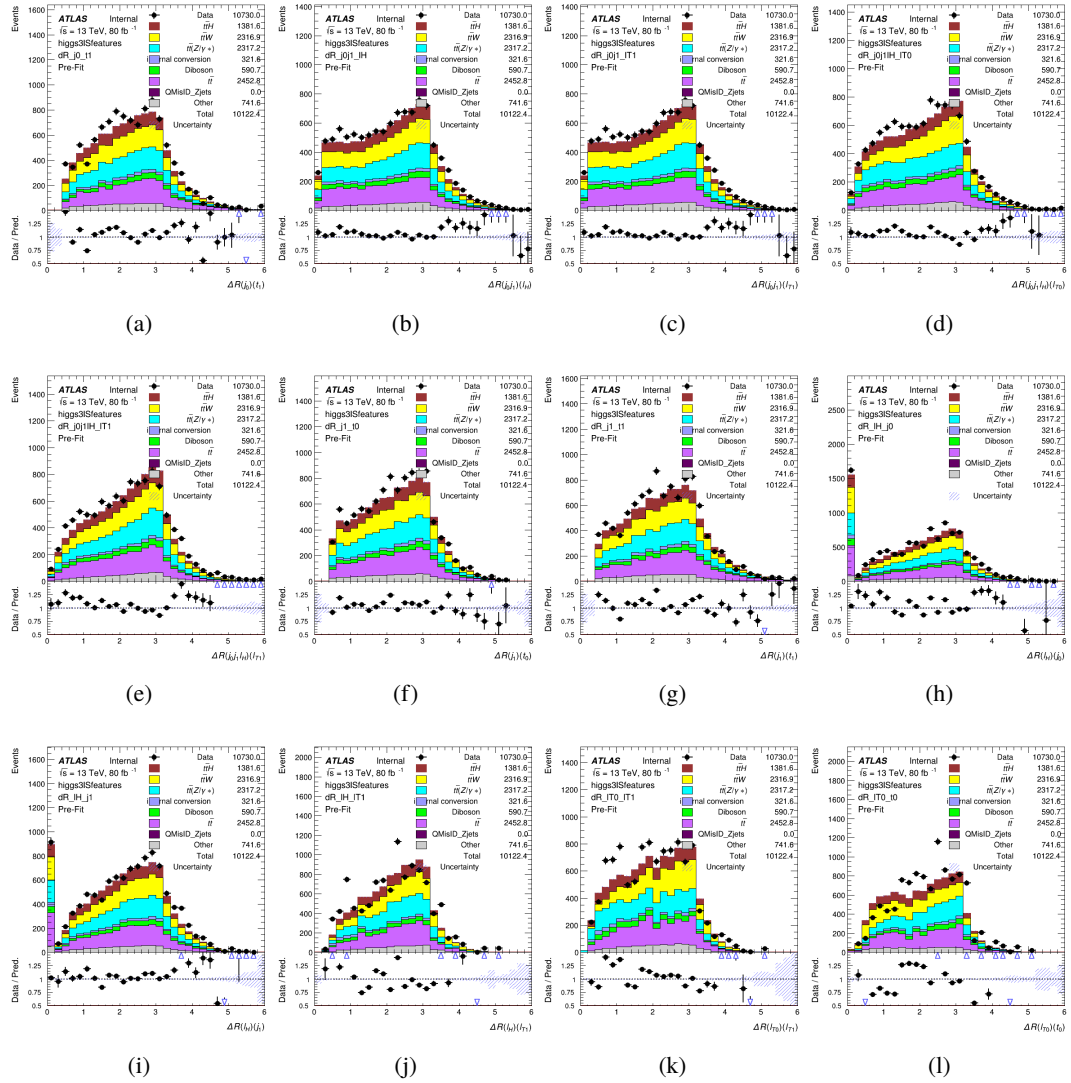


Figure A.13: Input features for higgs3IS

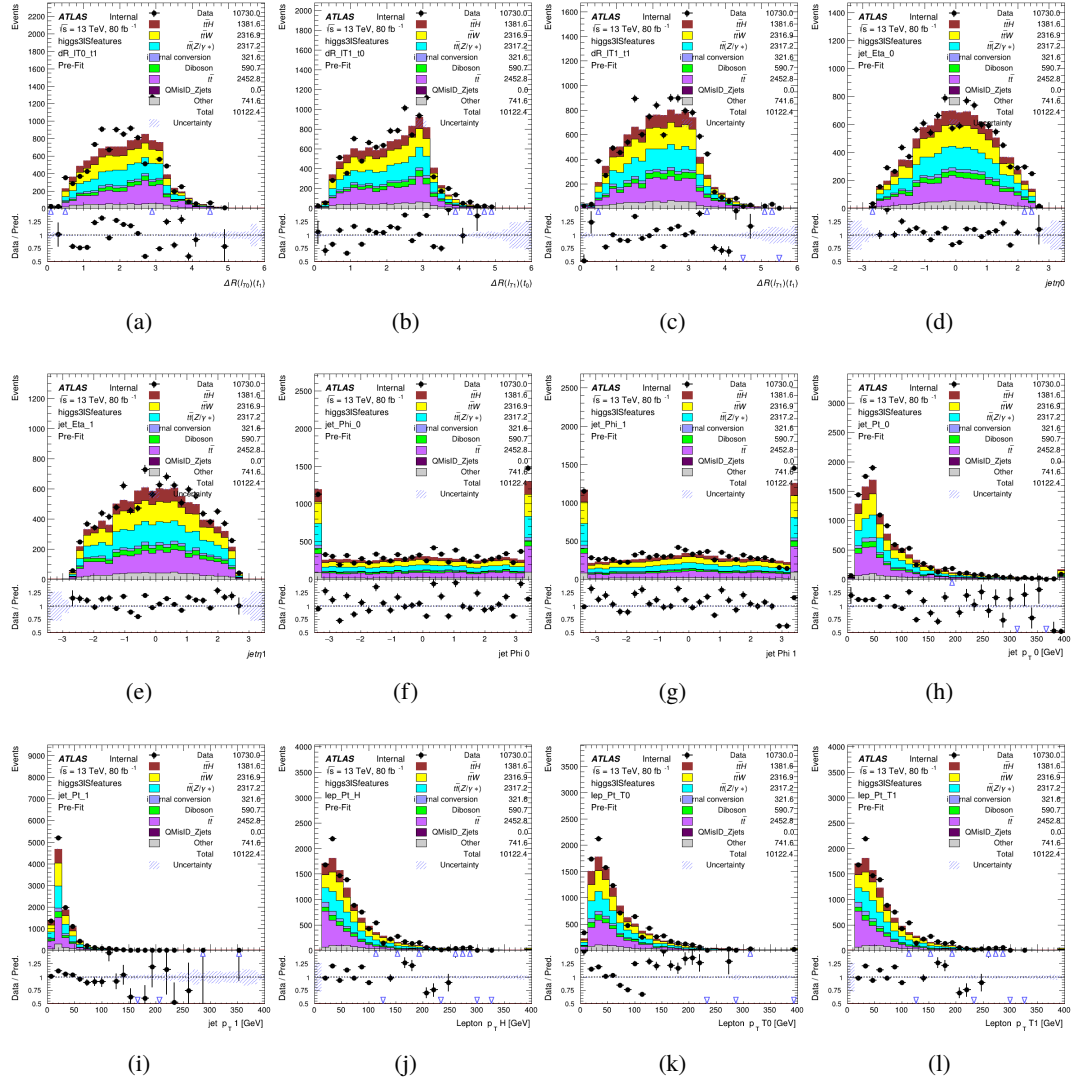


Figure A.14: Input features for higgs3IS

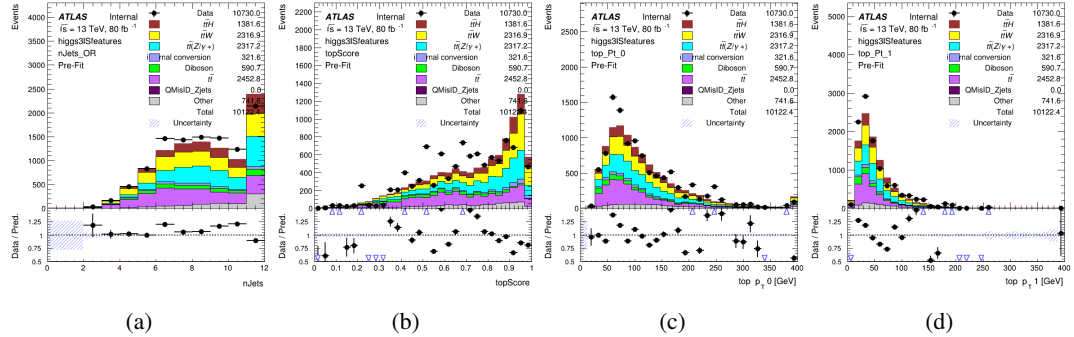


Figure A.15: Input features for higgs3IS

1856 **A.1.5 Higgs Reconstruction Features - 3lF**

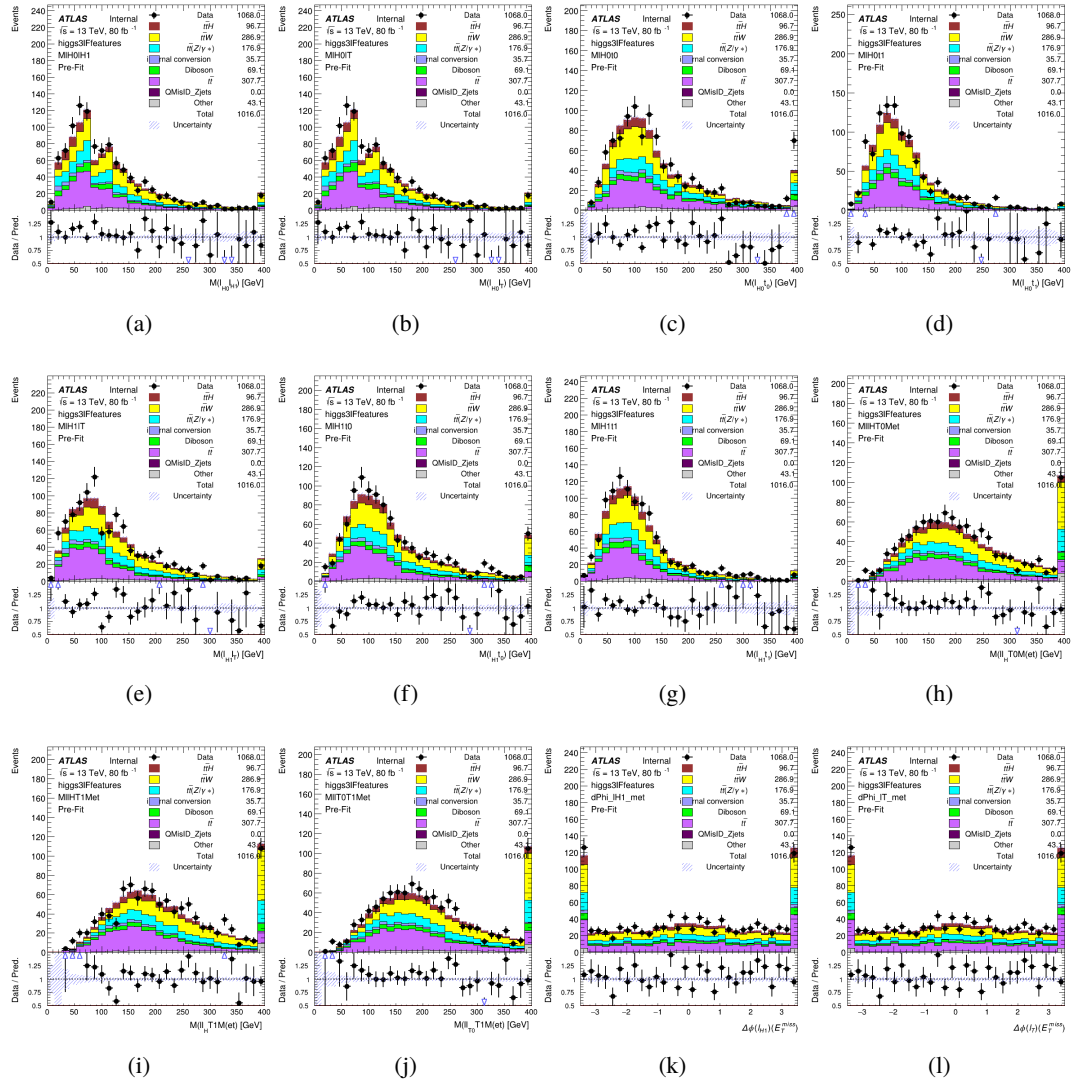


Figure A.16: Input features for higgs3IF

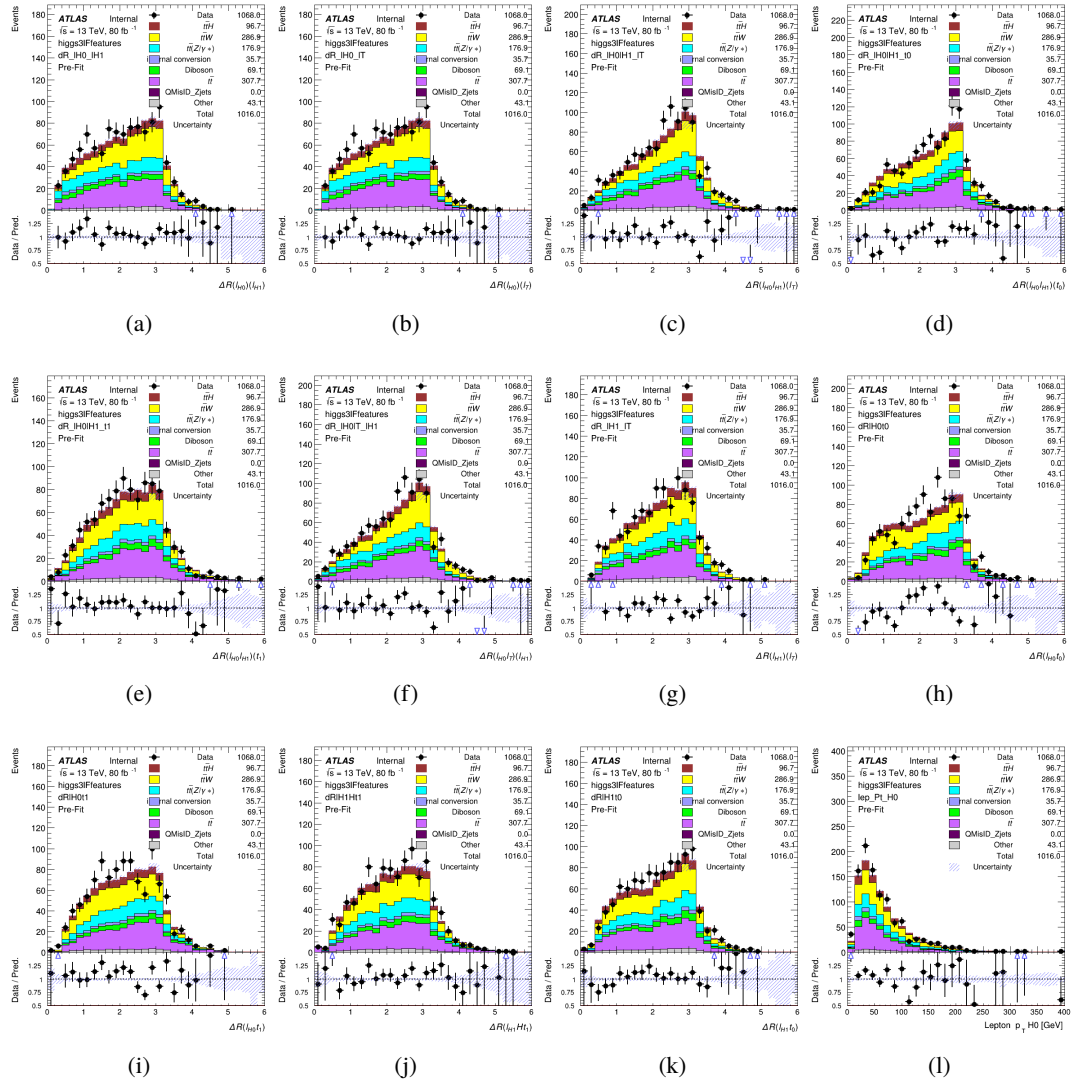


Figure A.17: Input features for higgs3lF

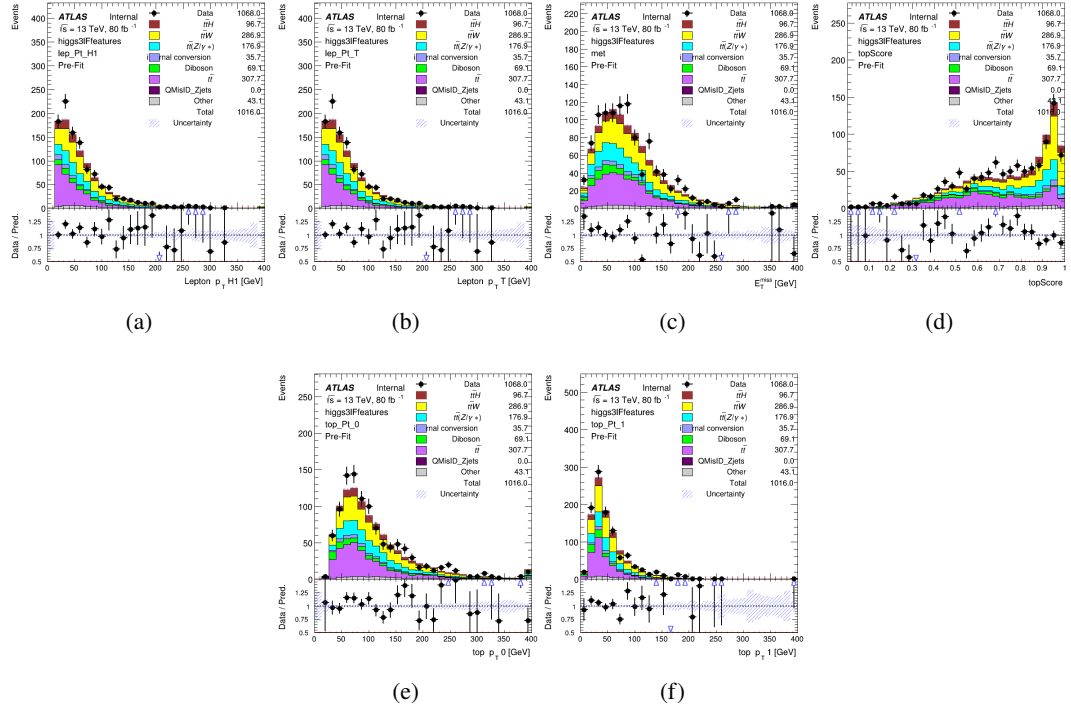


Figure A.18: Input features for higgs3lF

1857 **A.2 Background Rejection MVAs**

1858 **A.2.1 Background Rejection MVA Features - 2lSS**

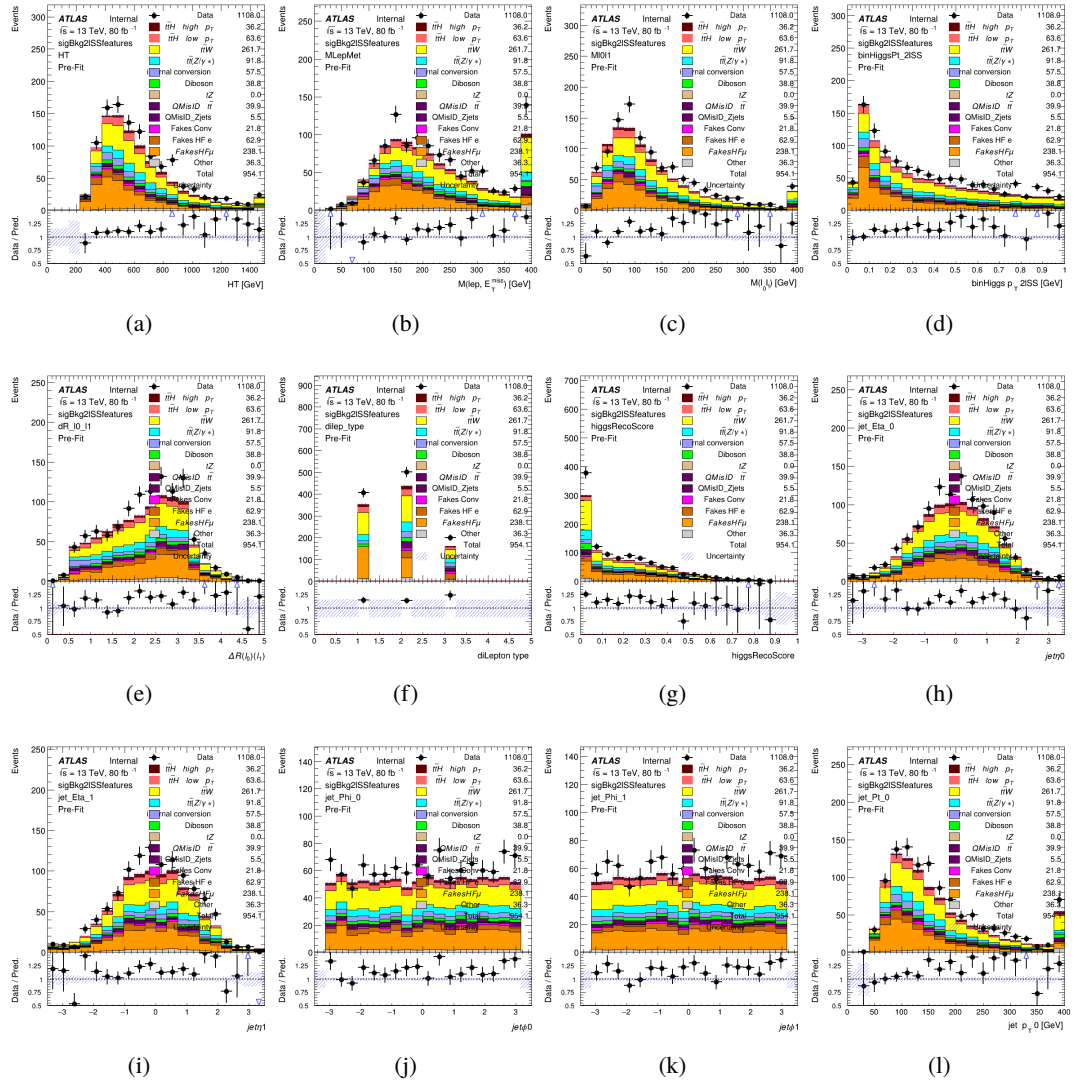
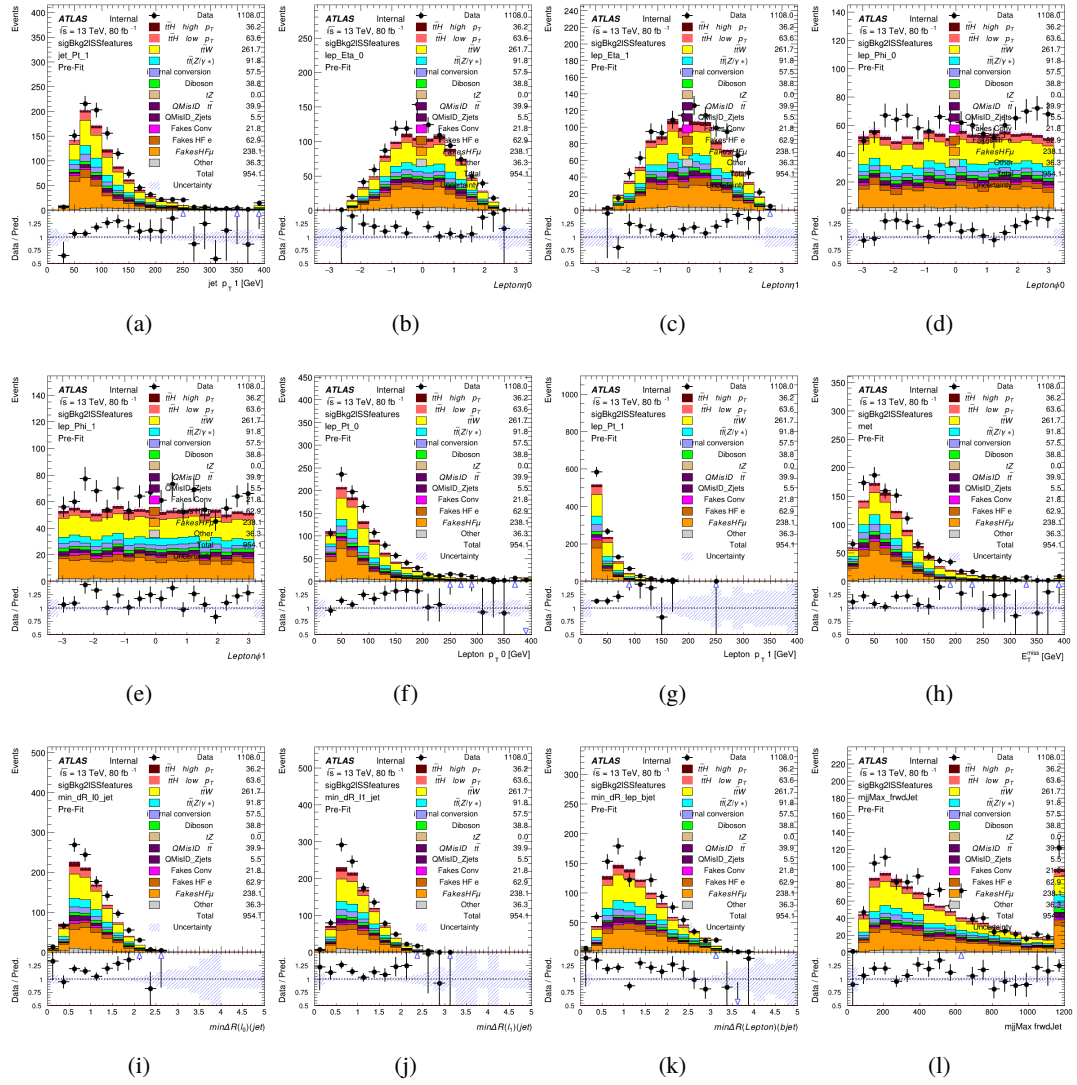


Figure A.19: Input features for sigBkg2lSS

Figure A.20: Input features for `sigBkg2lSS`

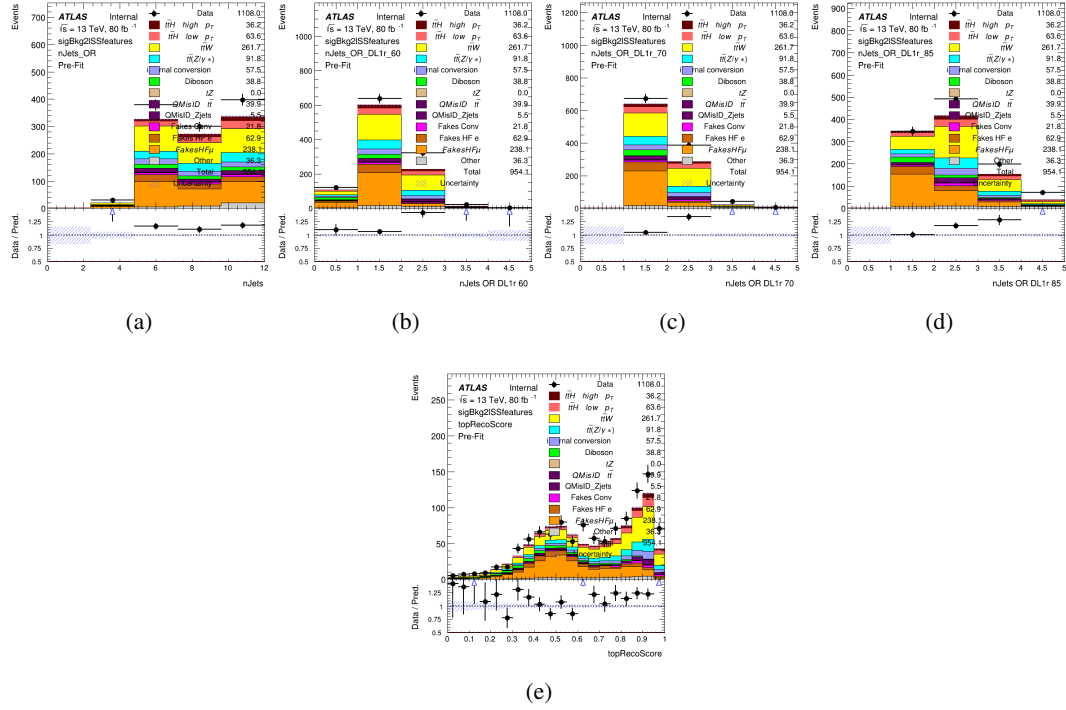


Figure A.21: Input features for sigBkg2lSS

1859 **A.2.2 Background Rejection MVA Features - 3l**

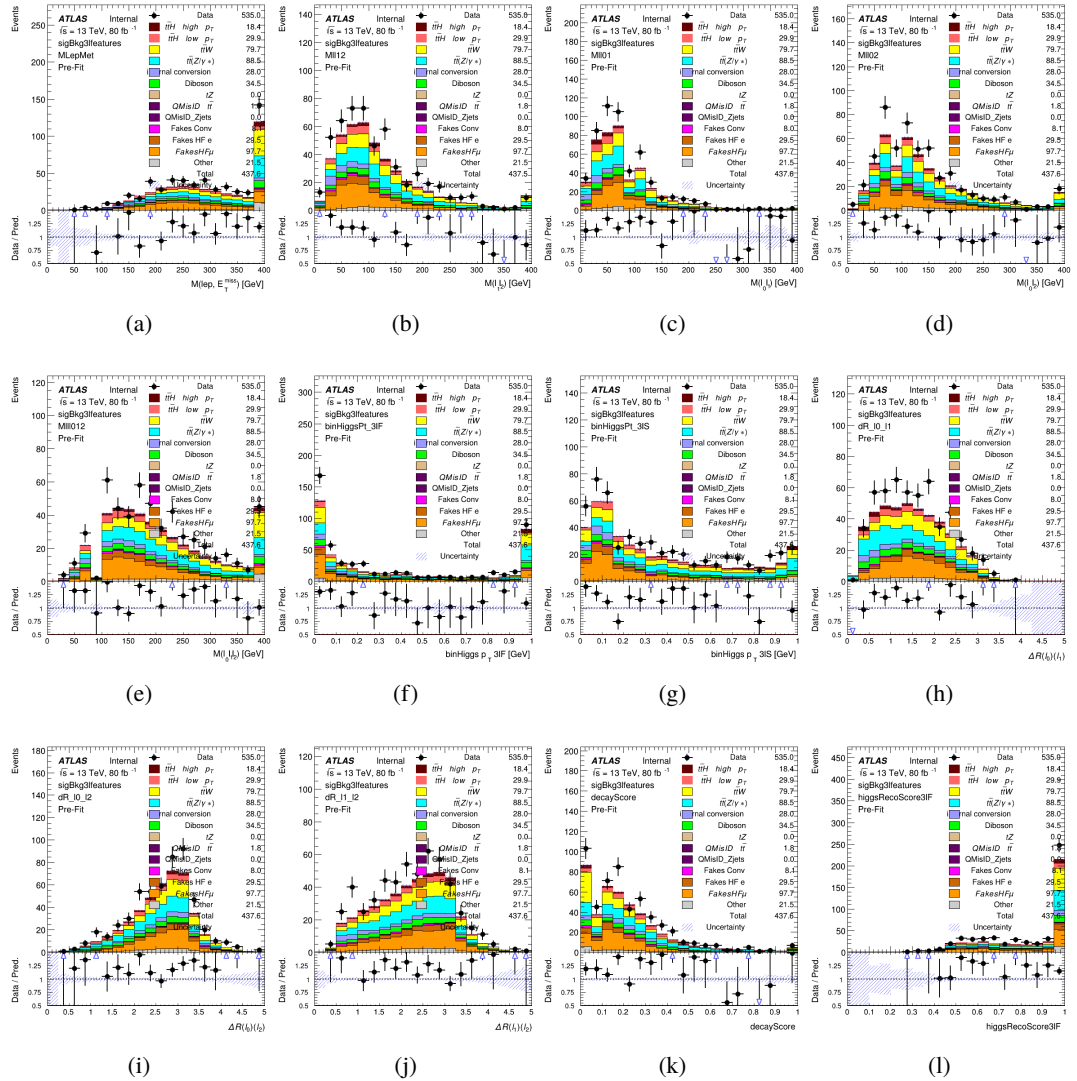


Figure A.22: Input features for sigBkg3l

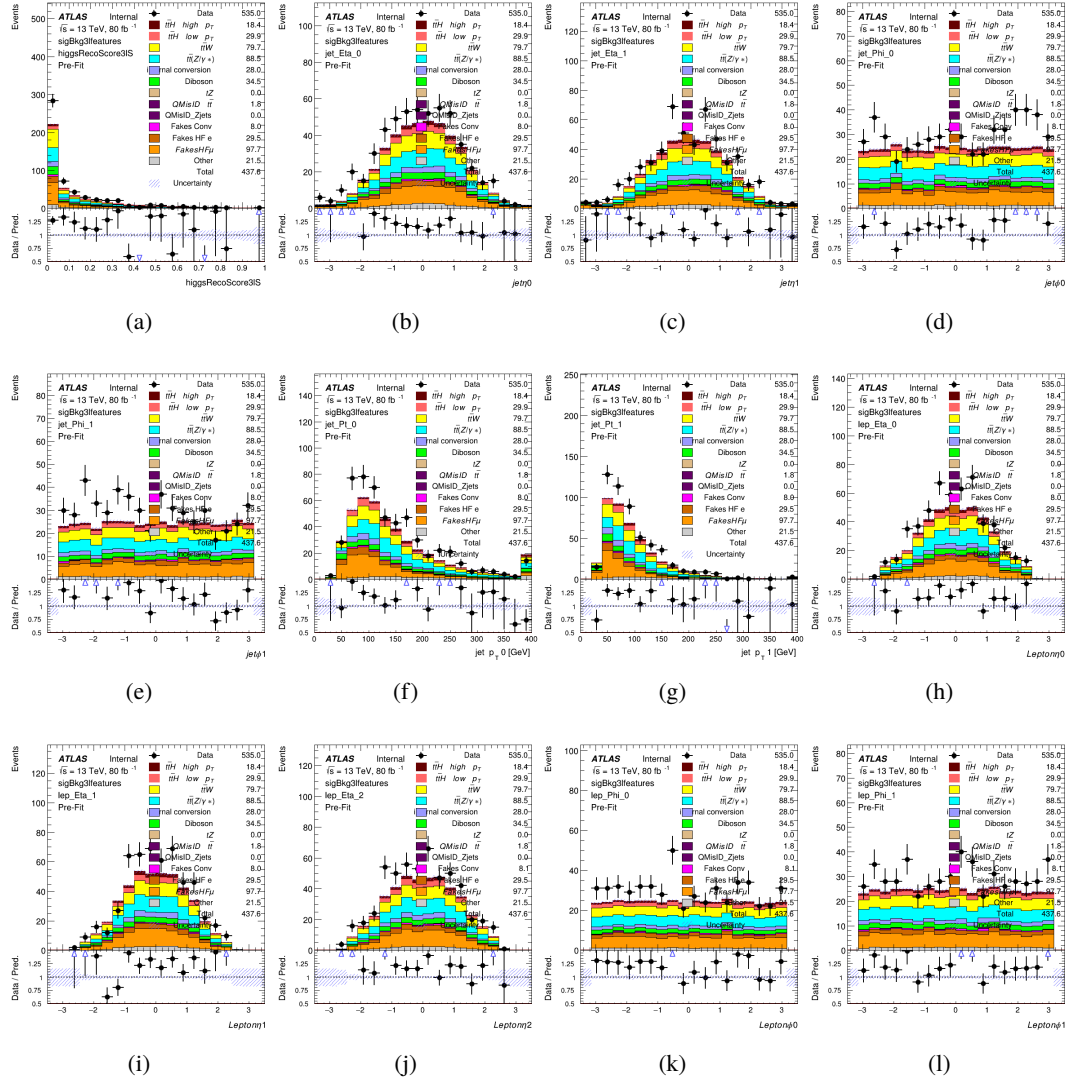


Figure A.23: Input features for sigBkg3l

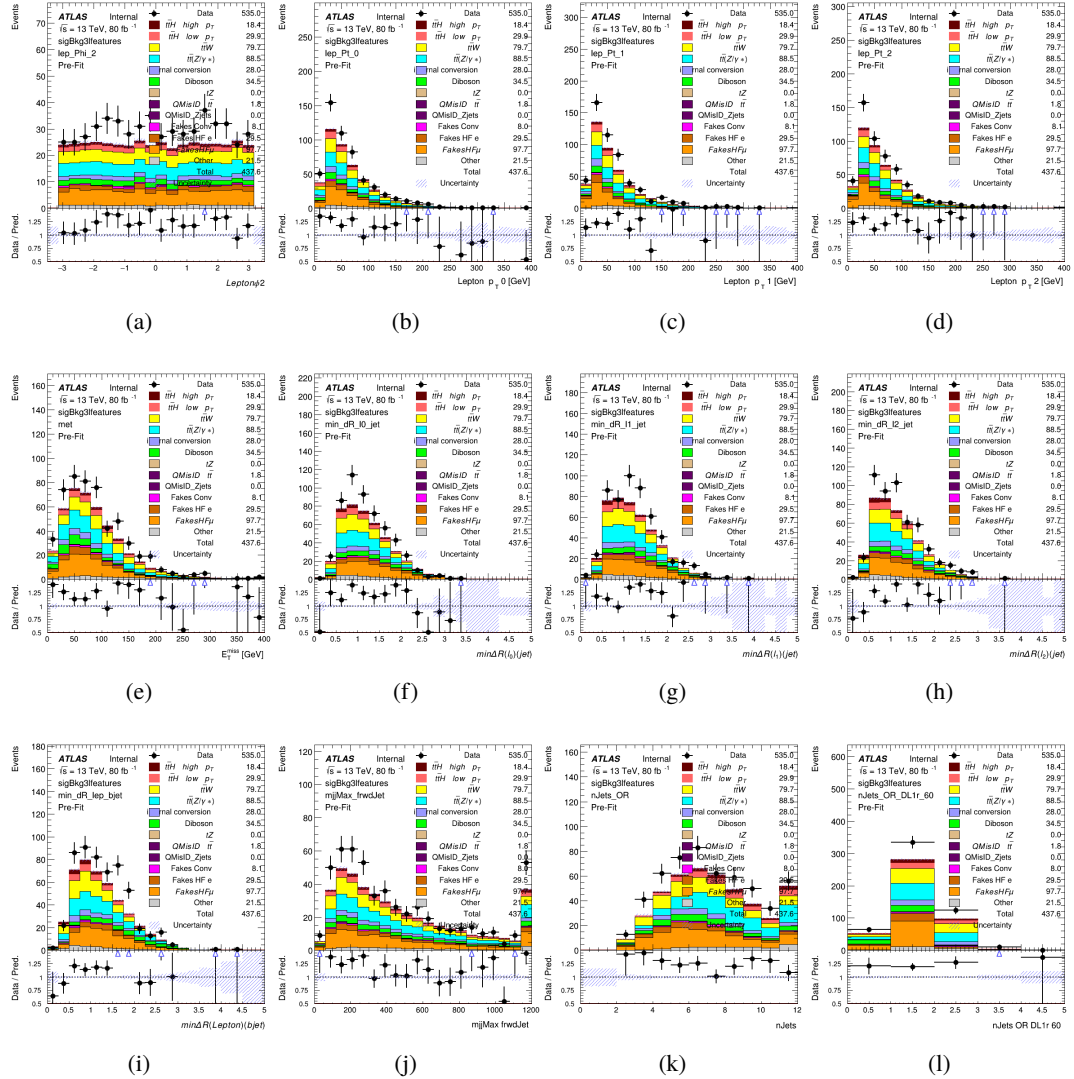


Figure A.24: Input features for sigBkg3l

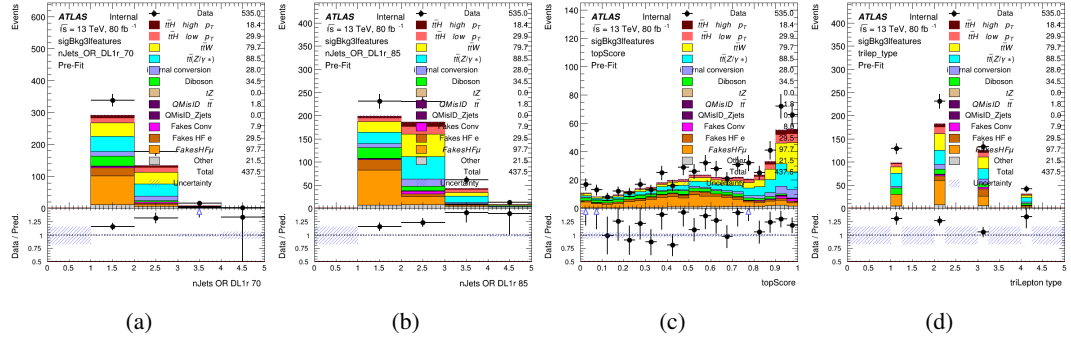


Figure A.25: Input features for sigBkg3l

1860 **A.3 Alternate b-jet Identification Algorithm**

1861 The nominal analysis reconstructs the b-jets by considering different combinations of jets, and
1862 asking a neural network to determine whether each combination consists of b-jets from top quark
1863 decays. An alternate approach would be to give the neural network about all of the jets in an event
1864 at once, and train it to select which two are most likely to be the b-jets from top decay. It was
1865 hypothesized that this could perform better than considering each combination independently, as
1866 the neural network could consider the event as a whole. While this is not found to be the case,
1867 these studies are documented here as a point of interest and comparison.

1868 For these studies, the kinematics of the 10 highest p_T jets in each event are used for
1869 training. This includes the vast majority of truth b-jets. Specifically the p_T , η , ϕ , E , and DL1r
1870 score of each jet are used. For events with fewer than 10 jets, these values are substituted with 0.
1871 The p_T , η , ϕ , and E of the leptons and E_T^{miss} are included as well. Categorical cross entropy is
1872 used as the loss function.

Table 58: Accuracy of the NN in identifying b-jets from tops in 2lSS events for the alternate categorical method compared to the nominal method.

Channel	Categorical	Nominal
2lSS	70.6%	73.9%
3l	76.1%	79.8%

1873 **A.4 Binary Classification of the Higgs p_T**

1874 A two bin fit of the Higgs momentum is used because statistics are insufficient for any finer
 1875 resolution. This means separating high and low p_T events is sufficient for this analysis. As
 1876 such, rather than attempting the reconstruct the full Higgs p_T spectrum, a binary classification
 1877 approach is explored.

1878 A model is built to determine whether $t\bar{t}H$ events include a high p_T (>150 GeV) or low
 1879 p_T (<150 GeV) Higgs Boson. While this is now a classification model, it uses the same input
 1880 features described in section 18.4. Binary crossentropy is used as the loss function.

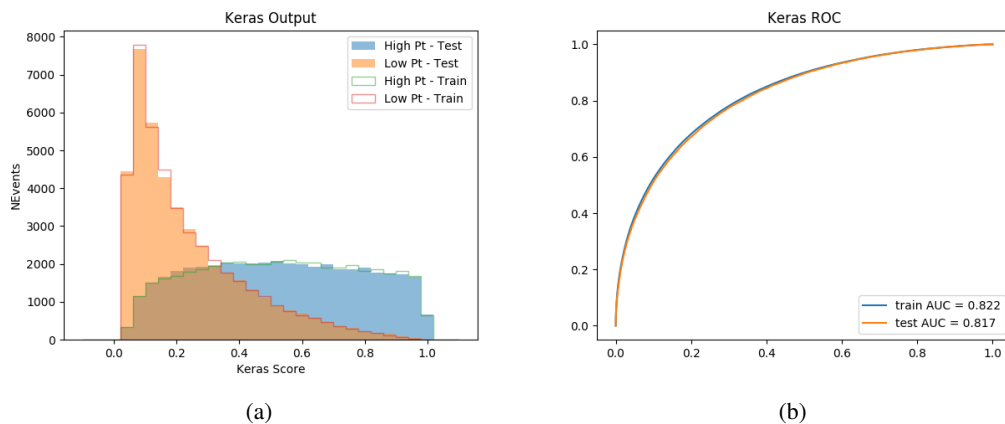


Figure A.26:

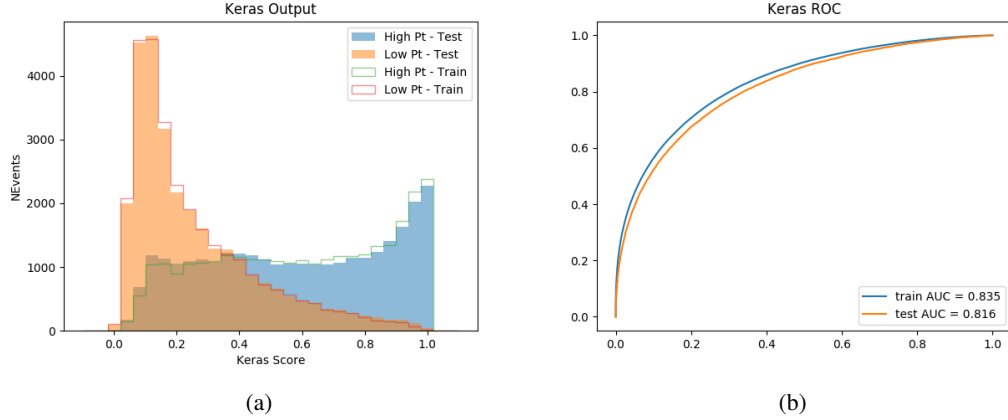


Figure A.27:

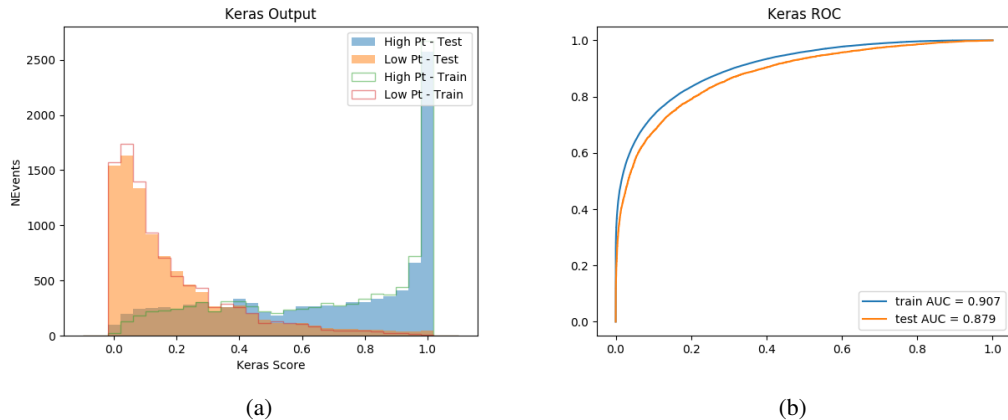


Figure A.28:

1881 A.5 Impact of Alternative Jet Selection

1882 A relatively low p_T threshold of 15 GeV is used to determine jet candidates, as the jets originating
 1883 from the Higgs decay are found to fall between 15 and 25 GeV a large fraction of the time. The
 1884 impact of different jet p_T cuts on our ability to reconstruct the Higgs p_T is explored here. The

1885 performance of the Higgs p_T prediction models is evaluated for jet p_T cuts of 10, 15, 20, and 25

1886 GeV.

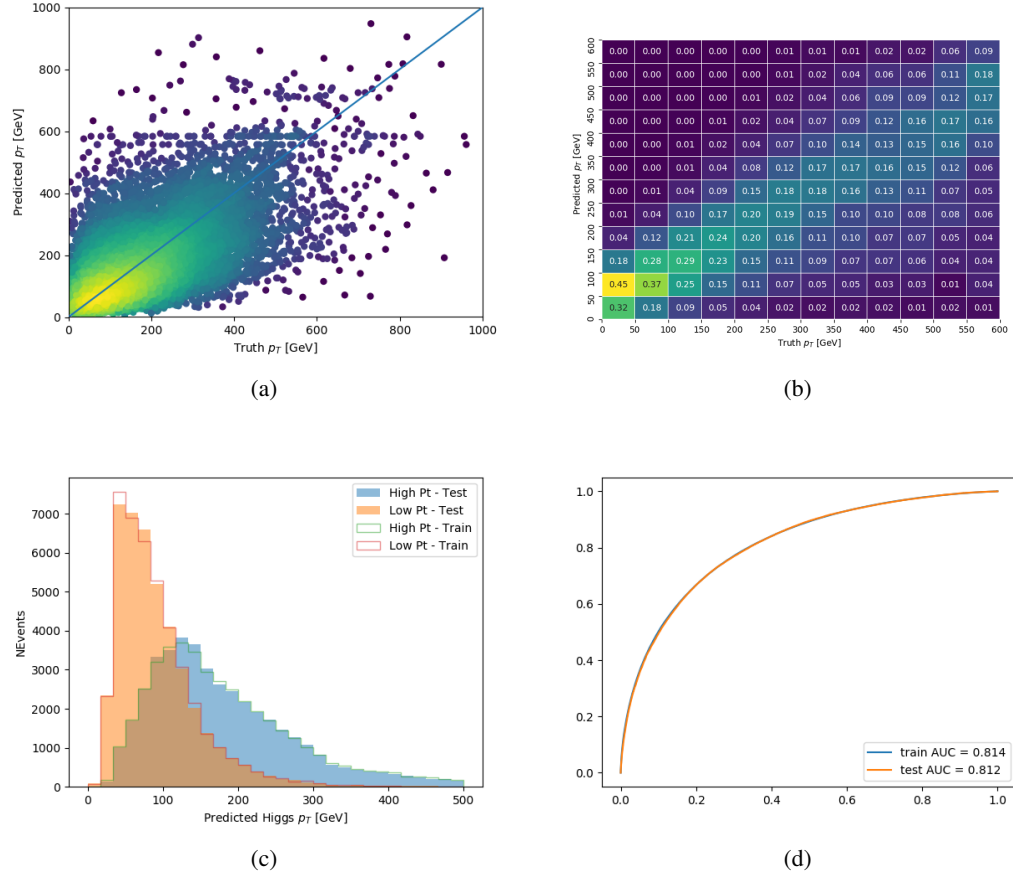


Figure A.29:

1887 **B**